Ollscoil na hÉireann, Corcaigh

National University of Ireland, Cork

ucc

Coláiste na hOllscoile Corcaigh, Éire
University College Cork, Ireland

An Evaluation of some Commercially-available Thin TiO_2 Films and TiO_2 Films Grown by Atomic Layer Deposition for Potential Photocatalytic Applications.

Thesis presented by

Harry Manley

for the degree of

Doctor of Philosophy

University College Cork

School of Chemistry

Head of School: Professor Justin Holmes

Supervisors: Professor Martyn Pemble, Dr Ian Povey

09/2018

Contents

Declaration

This is to certify that the work I am submitting is my own and has not been submitted for another degree, either at University College Cork or elsewhere. All external references and sources are clearly acknowledges and identified within the content. I have read and understood the regulations of University College Cork concerning plagiarism.

I hereby declare that I have written this thesis independently, but with help from my supervisors, colleagues and permitted aids only. There has not been any assistance from any prohibited means.

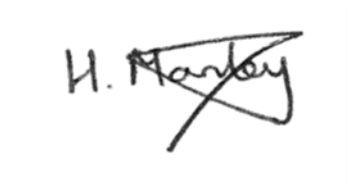

Harry Manley

September 2018

Acknowledgements

Firstly, I would like to thank my supervisor Professor Martyn Pemble for providing the opportunity to undertake the research for this PhD, and his support and assistance throughout. Secondly, I would like to thank my co-supervisor Dr. Ian Povey for his assistance and knowledge. Additionally, I am grateful to the rest of my past and present co-workers in the Advanced Materials and Surface Group (ASMG) and across the rest of the Tyndall National Institute and University College Cork, especially Professor Jim Greer, Dr. Michael Schmidt, Dr. Mircea Modreanu and Vince Lodge.

Furthermore, I would also like to thank Dr. Fathima Laffir from the Materials and Surface Science Institute at the University of Limerick for her continued assistance.

Foremost, I would like to thank my husband, Ross, for his unwavering support, love, belief in my ability and for putting up with my continued absences (we can have our weekends back now). As well as my family and close friends, old and new, for their understanding, support and laughter over the previous five years.

This work was supported by SFI PI Grant No.11/PI/1117 and SFI IA Grant No.15/IA/3015.

Abstract

Atomic Layer Deposition (ALD) was utilized to synthesize nominally undoped titanium dioxide (TiO_2) and a range of doped TiO_2 films ($Ti_{1-x}O_2:M_x$) on quartz substrates, separately accommodating aluminium, gallium, hafnium, silver, tin and vanadium as nanolaminate dopants. The synthesized TiO_2 and $Ti_{1-x}O_2:M_x$ films provided varying photocatalytic activities dependent on differing degrees of crystalline morphology, Ti^{3+} concentrations and dopant used.

Nominally undoped TiO_2 was mainly amorphous, showing only minimal evidence of polycrystalline anatase structures and contained around 20 % Ti^{3+}, providing a time to bleach (ttb) of 11 minutes 4 seconds ±35 seconds with respect to basic blue ink. In comparison to the nominally undoped TiO_2 film, only the $Ti_{1-x}O_2:Ag_x$ (19:1) and $Ti_{1-x}O_2:Sn_x$ (19:1) films provided any photocatalytic improvement, recording basic blue 66 ink ttb values of 6 minutes 4 seconds and 5 minutes 12 seconds ±1 minute 13 seconds, respectively. This near halving of the ttb previously observed for the nominally undoped TiO_2 film, probably originated from higher bulk Ti^{3+} concentrations (52 and 31 %) for the $Ti_{1-x}O_2:Ag_x$ and $Ti_{1-x}O_2:Sn_x$ films, respectively.

Additionally, a novel approach was utilized, through which the effect of Irish hospital cleaning agents (Actichlor Plus™, ChloraPrep™, SteriClean™, and Virusolve+™) on the photocatalytic activity of both the commercially available Pilkington Activ™ and ALD-grown $Ti_{1-x}O_2:Sn_x$ films was examined. On different cleaning agent treatment, the photocatalytic activity of both films was found to decrease in respect to basic blue 66 and resazurin ink photodegradation, as well as increasing water contact angle hydrophobicity under UV light irradiation. However, the permanent damage to photocatalytic activity decrease was not incremental after multiple treatments for the non-residue creating cleaning agents (SteriClean™ and Virusolve+™) and cleaning agent treatment was shown to not mechanically degrade film morphology. Furthermore, both the Pilkington Activ™ and $Ti_{1-x}O_2:Sn_x$ films showed inconclusive results for microbiological exposure with a complex interplay between *E.coli* colony attachment and photocatalytic destruction detected.

Chapter 1. An introduction to ALD (Atomic Layer Deposition) of doped titanium dioxide films for photocatalytic applications

TiO_2, zinc oxide (ZnO) and tin dioxide (SnO_2) are wide band gap (3-3.6 eV) [1-3] semiconducting metal oxides undergoing activation through UV (ultraviolet) light irradiation and are either typically utilized as photocatalytic surfaces or as various functional layers in photovoltaic devices. UV light absorption in semiconducting metal oxides generates exciton charged pairs through band gap electron excitation. These excitons subsequently diffuse to surface regions and react with adsorbed water or oxygen molecules, generating Reactive Oxide Species (ROS). ROS (hydroxyl and superoxide radicals) further interact with surface contaminants or biological species to provide photocatalytic effects, namely: self-cleaning, anti-fogging and antibacterial properties. However, photocatalytic surfaces dependent on UV light irradiation are not optimal, as UV light;

- Lacks presence within indoor environments,
- Occurs in minimal daylight concentrations (4-5 %),
- Is a human health hazard [4].

Visible light utilization is therefore required to increase device and photocatalytic surface efficiency, as well as providing increased utilization across varied indoor (with negligible UV irradiation) and outdoor environments. Hospitals are a particular example, presenting significant and increasing surface-based antimicrobial resistance [5-7], but with the potential to provide antibacterial degradation under light irradiation and TiO_2 application [8]. However, utilization of commercial UV light activated films is unsuitable due to human health concerns. Surfaces and equipment coated with corrosion resistant, visible light active, antimicrobial metal oxide coatings could provide microbial and dirt degradation under visible light wavelength irradiation, assisting with microbial colony reduction alongside normal hospital cleaning routines.

All three semiconducting oxides (TiO_2, ZnO and SnO_2) possess potential conductive and photocatalytic properties, however, this thesis focuses specifically on TiO_2. TiO_2 is a non-toxic and abundant material [9] with a large band gap (3-3.4 eV) dependent on crystallization into three main polymorphs; anatase (tetragonal), rutile (tetragonal) and brookite (orthorhombic) [10]. Anatase TiO_2 possesses the greatest photoactivity, growing at temperatures between 250 and 400 ^oC under ALD conditions and consists of spherical upward protruding grains [11]. Rutile TiO_2 possesses the greatest thermal stability, growing at temperatures < 400 ^oC under ALD conditions and consists of flat, facetted grains [11]. Brookite TiO_2 is less studied through vapour deposition processes, but has been indicated to grow oblong and elongated grains through sol-gel processes at similar growth temperatures to rutile [12]. Below temperatures of 250 ^oC, amorphous TiO_2 films are usually synthesized through ALD [11].

TiO_2 undergoes UV wavelength light activation, as initially indicated by Fujishima and Honda in 1972 [13] and through subsequent correlation to photocatalysis by Frank and Bard in 1977 [14, 15]. As of writing, commercial TiO_2 photocatalytic degradation under UV light wavelength irradiation can be observed from a range of products, for example;

- Pilkington Activ^{TM} films, which are anatase TiO_2 grown by Chemical Vapour Deposition (CVD) [16].
- Degussa (Evonik) P25^{TM} powders, which are typically mixed 70 : 30, anatase : amorphous/rutile TiO_2 photocatalysts [17].

TiO_2 also undergoes visible light photoactivation [18], with on-going research focusing on development of reliable visible light TiO_2 activation [19, 20]. Typically, attempts to induce visible light activity focus on varying metallic [21, 22] and non-metallic [19, 23] dopant incorporation, effectively decreasing band gap size though mid-band gap state insertion. This originates either directly from dopants or indirectly through charge compensating defect generation.

Furthermore, TiO_2 also possesses n-type semiconductivity with naturally occurring oxygen vacancies ($V_{O^{\cdot\cdot}}$) providing excess electron density. Increased electron

density in the conduction band is also observed on UV light activation with excess excited electrons assisting current creation [24]. TiO_2 has therefore been studied for numerous applications, resulting in: anti-fogging devices [25], biosensors [26], Transparent Conducting Oxides (TCO's) [27], Dye Sensitized Solar Cells (DSSC's) [24], antibacterial coatings [8] and self-cleaning surfaces [28, 29]. However, TiO_2 film photocatalysis and conductivity are the focus of this research, and so are discussed in detail below.

1.1 Photocatalysis

On illumination with light of wavelengths <410 nm, TiO_2 valence band (filled oxygen 2p orbitals) electrons are excited by absorbed photon energies (equalling or exceeding band gap energy). Excited electrons are energetically promoted across the band gap to the conduction band (unfilled titanium 3d orbital) states, leaving a hole within valence band states. Subsequently, both excited electron and hole are bound as in identical molecular orbitals, creating an exciton (figure 1.1).

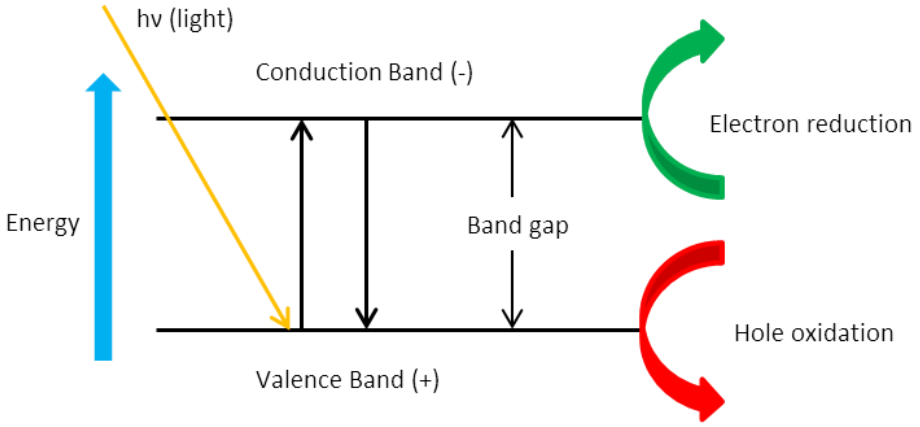

Figure 1.1: Light absorption and exciton generation [30]

Electron and hole band states within excitons undergo attraction through repulsive electrostatic coulomb forces. These forces are generated by increased electron concentrations surrounding an unbound charged pair and provide a lower energy, increased stability state on exciton creation [31]. Automatic recombination is subsequently hindered through resonance stabilization of overlapping charge pair wave functions, extending exciton lifetimes [31]. Additionally, exciton constituents can undergo dissociation into charge carriers to diffuse throughout TiO_2 and

become trapped within surface groups and impurities [32, 33], or potentially undergo radiative recombination resulting in relaxation and photon emission [34] as shown in equation 1.1.

$$e^-_{CB} + h^+_{VB} \rightarrow MO_x + h\nu \qquad \text{Equation 1.1}$$

However, both initial excitation and eventual recombination of charge carriers are dependent on band gap size with absorption of light wavelengths ≤410 nm resulting from the TiO_2 crystal morphology. TiO_2 also possesses either a direct or indirect band gap (figure 1.2) typically between 3 and 3.4 eV dependent on disparate crystalline morphologies;

- Anatase: 3.2 eV (<387 nm) [1] and can be a direct or indirect transition [35],
- Rutile: 3.0 eV (<410 nm) direct [1],
- Brookite: within 3.1-3.4 eV and is either a direct or an indirect transition due to limited consensus on possessed properties [1, 12, 36],
- Amorphous: 3.37 eV [2].

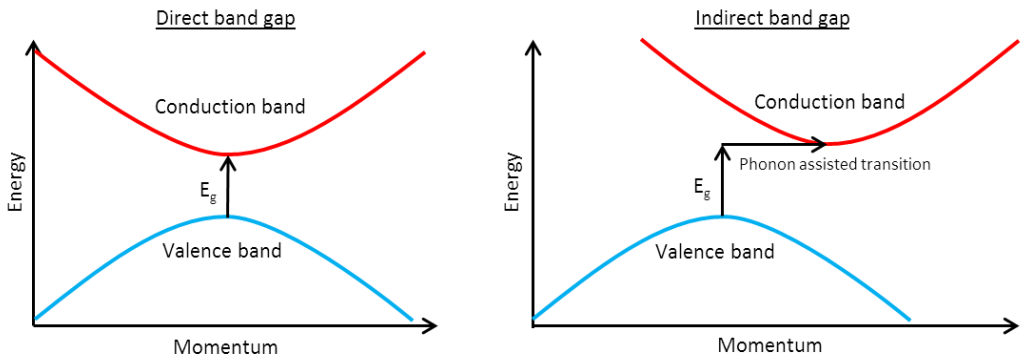

Figure 1.2: Direct and indirect band gaps [35]

As established in figure 1.2, the indirect TiO_2 anatase band gap requires phonon momentum (phonon assisted transition) to complete exciton charge pair creation through electron excitation across an electric dipole forbidden transition [35]. Phonon addition subsequently alters both energy and momentum of exciton pairs during the transition, weakening both adsorption (requiring initial longer excited electron lifetimes) and emission [35]. Excited conduction band electrons are also unable to directly combine with valence band holes as both electron wave vectors

differ at the conduction and valence bands, resulting in longer exciton lifetimes [37].

Additionally, anatase TiO_2 morphology is suggested to possesses the lightest effective mass of electrons and holes as compared to rutile or brookite, increasing exciton bulk to surface diffusion, whilst reducing recombination [37]. Alternatively, the direct TiO_2 rutile band gap generates increasing radiative recombination in comparable time frames, resulting in greater recombination rates.

Typically, recombination effectively reverses charged pair generation with electrons relaxing radiatively (emitting a photon) or non-radiatively (emitting a phonon) to restore valence band states [38, 39], thereby reducing the TiO_2 photoactivity. Energetically, recombination occurs at high mid-band gap state concentrations in band gap regions, typically generated by intrinsic or extrinsic defects [40-44]. In contrast, recombination physically transpires at TiO_2 trapping centres, namely; crystalline grain boundaries, intrinsic or extrinsic defects and surface regions [45, 46]. Furthermore, in trapping centres (either shallow or bulk), recombination is a quick process equating to; 1-10 ps and >20 ns for shallow and deep traps, respectively [47].

However, charge pair diffusion towards surface regions results in trapping and/or reactions with surface adsorbed water, hydroxyl and oxygen species, generating hydroxyl [33, 48, 49] and superoxide [32] radicals (ROS) for photocatalysis (figure 1.3). In particular, holes can undergo transfer through either a surface trapped hole species or hydroxyl radical formation [33, 48, 49].

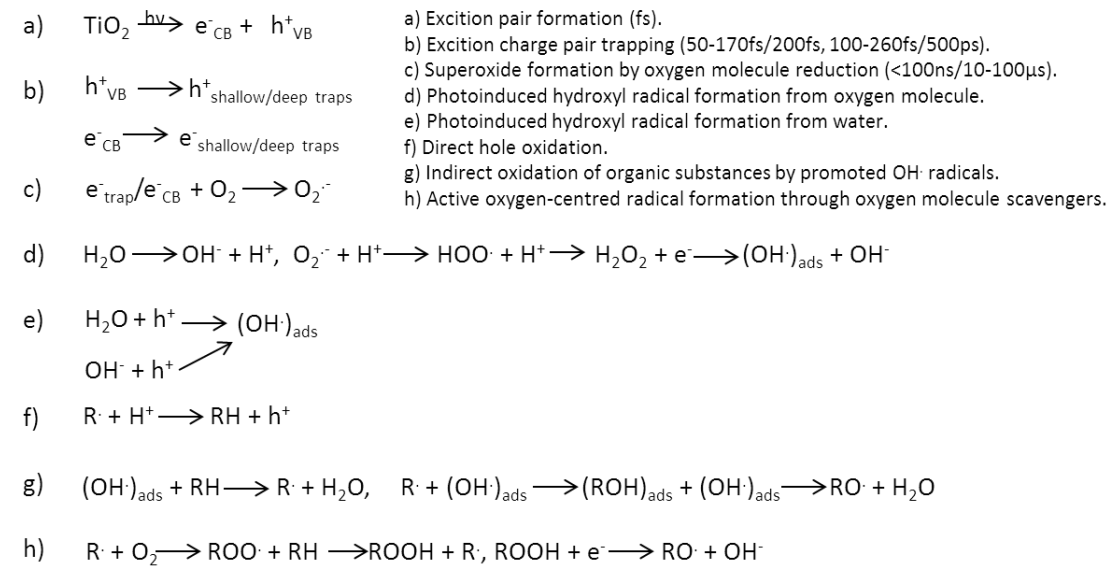

Figure 1.3: Surface radical generation [32, 33, 48-53]

As indicated in figure 1.3, molecular oxygen acts as an electron scavenger producing superoxide radicals (c) [32, 53], initiating absorbed water promoted free-radical chain reactions to provide hydroxyl radical formation (d) [51, 52]. Hydroxyl radicals are also created through adsorbed water or hydroxide ion hole oxidation (e), subsequently sourced from excitons.

Hydroxide radicals oxidize surface adsorbed organics (g) alongside molecular surface oxygen. This ensures reactions with organic radical species (h) and direct organic radical hole oxidation (f), eventually providing decomposition to simpler organic molecules, water and carbon dioxide (under complete demineralization). However, on replenishment of molecular oxygen, titanol ($TiOH^{+\cdot}$) surface groups act as principal oxidizing agents [50].

For these reasons, photocatalysis is frequently described utilizing a Mars Van Krevelen type mechanism (figure 1.4) [54-56], especially under oxygen deficient conditions. In a Mars Van Krevelen type mechanism, the absence of surface adsorbed oxygen generates lattice oxygen removal for radical initiation to decompose surface adsorbed organics. The remaining surface $V_O^{\cdot\cdot}$ undergo replenishment by molecular oxygen or water surface adsorption. Comparatively,

oxygen rich conditions typically favour using surface dissolved oxygen or water, over $Vo^{\cdot\cdot}$.

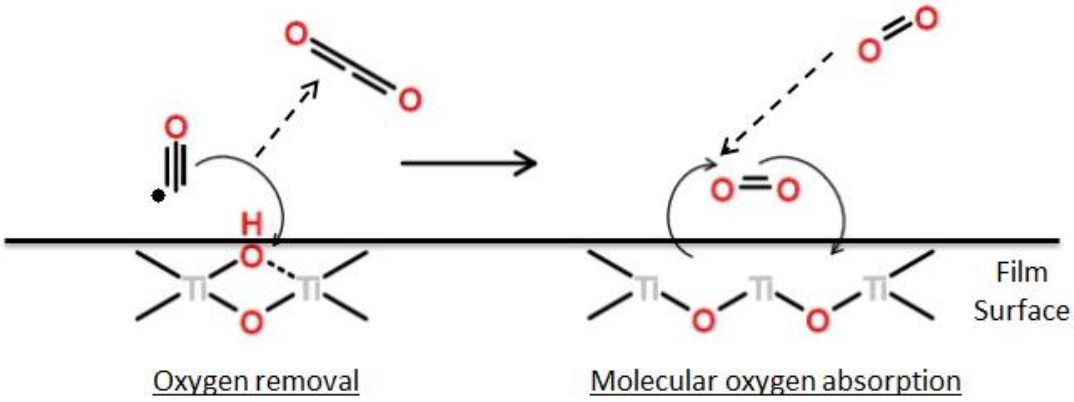

Figure 1.4: A simplified Mars Van Krevelen type mechanism [54-56]

Furthermore, two major competitions over excitons exist during photocatalysis between varying reactions [57, 58]:

- Exciton trapping versus recombination,
- Interfacial charge transfer versus trapped species recombination.

This competition for increased exciton lifetime correlates to photocatalytic efficiency with dissociation into strongly reducing/oxidizing conduction/valence band electrons/holes (+0.5 to -1.5 V / +1 to +3.5 V vs a normal hydrogen electrode) [30] and further reaction or recombination to produce ROS or photon emission. Extended trapping lifetimes are observed for photogenerated excitons due to defect states present in the TiO_2 band gap. Therefore, increased photocatalytic reaction efficiency results from improved free radical creation, similarly dependent on a greater capability for longer-lived exciton generation.

Furthermore, surface species can also affect photocatalytic efficiency with both adsorbed pollutant and surface hydroxyl radical concentrations determining decomposition rate kinetics [59-61]. Specifically, diffusion/adsorption of water molecules towards $V_O^{\cdot\cdot}$ sites can also limit the reaction rate of hydroxyl radical formation [62].

1.1.1 Antimicrobial photodegradation

Both surface absorbed microbiological species and organic compounds undergo photocatalytic decomposition on reaction with surface free charge carriers and ROS (f, g and h figure 1.3) [63]. Furthermore, surface water rinsing after photocatalysis reconstitutes ROS, subsequently increasing decomposite removal through greater water run-off from superhydrophilic effects [64, 65]. Greater water run-off also assists in bacteria and biofilm surface adhesion prevention [64].

However, major bacterial decomposition mechanisms through surface ROS are predominately speculative. Typically, the literature [66-68] agrees that ROS initially damage cell membranes resulting in internal component leakage with further oxidization by photocatalytic reactions and complete mineralization to CO_2 and H_2O [66, 68, 69]. Contrastingly, different bacterial decomposition mechanisms or greater mechanism specificity has been suggested by other researchers:

- Matsunga [70, 71] observed respiration suppression through CoA enzyme inhibition with membrane and cell wall damage through lipid peroxidation, indicating a doubly-destructive effect.
- Sunada [63] proposed a three step mechanism; an initial ROS attack of cell walls, followed by creation of internal cytoplasmic membrane disorder and subsequent bacterial cell death and decomposition.
- Kubacka [72, 73] through researching bacterial gene difference on UV light TiO_2 photoactivation, suggested the following;
    - Rapid cell inactivation at regulatory and signalling levels,
    - Decreasing co-enzyme dependent respiratory chain concentrations,
    - Decreased ability to assimilate and transport iron and phosphorus,
    - Decreased capacity for heme (Fe-S cluster) group synthesis.

  Additionally, bacterial shock and adaptability were also detected with greater lipid production for cell membranes to compensate cell wall disruption by hydroxyl radicals.
- Hidaka [4] detected RNA damage through hydroxyl radical attack.
- Multiple sources [74-79] showed potassium ion leakage with cell viability decrease.

- Multiple sources [77, 80-82] also indicated cell disruption resulting from lipid peroxidation or direct oxidation by ROS.

Overall, greater TiO_2 photocatalytic effectiveness in gram negative bacteria decomposition results from different cell wall structure and thinner peptidoglycan (figure 1.5).

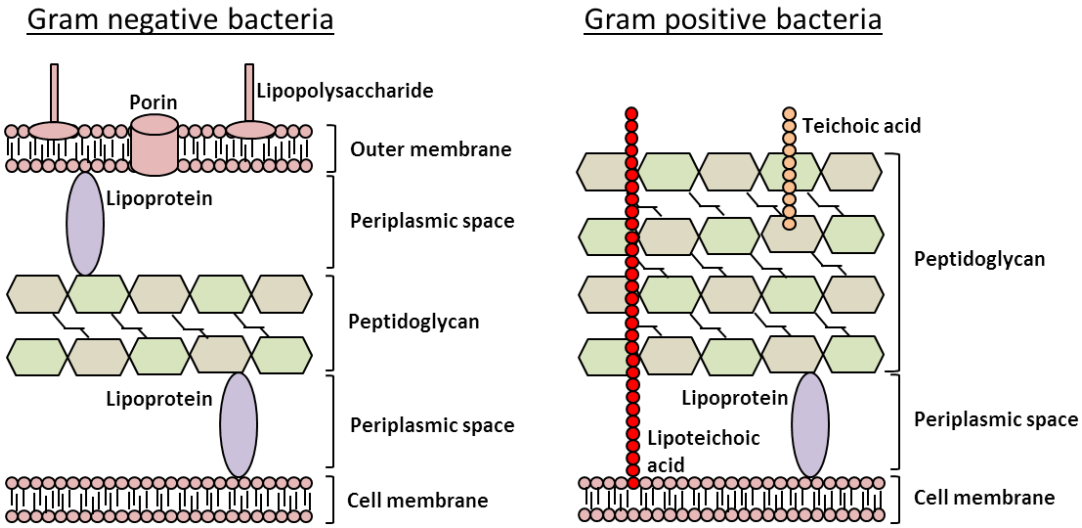

Figure 1.5: Cell wall structure of gram positive and negative bacteria [83]

Typically, both the gram negative *Escherichia coli* (*E.coli*) and the gram positive *Staphylococcus aureus* (*S.aureus*) undergo decomposition on TiO_2 under UVA light, as has been described previously [84-88]. Studies of bacterial colonies suggested cell viability decrease with potassium ion leakage; however, *E.coli* underwent greater cell decomposition with plasmolysis, intracellular vacuoles and cell debris detected. Contrastingly, *S.aureus* colonies presented lower decomposition rates, incorporating cytoplasmic membrane and peptidoglycan layer separation, as well as cell distortion.

Another study [89], indicated similar results between *E.coli* and *S.aureus* destruction with 100 % and 90 % bacterial inactivation indicated respectively after UV irradiation for one hour on 1 gL^{-1} TiO_2 nanoparticles. Additionally, *S.aureus* colonies underwent 31 % inactivation under UV light irradiation alone indicating both higher UV sensitivity and photoactive TiO_2 resistance compared to *E.coli* (0 % inactivation under UV light irradiation). Furthermore, gram positive *Bacillus subtilis*

(*B.subtilis*) and gram negative *Pseudomonas aeruginosa* (*P.aeruginosa*) also underwent 100 % and 0 % inactivation respectively under identical conditions. *B.subtilis*, similar to S.*aureus*, indicates high UV sensitivity (67 % inactivation), however, *P.aeruginosa,* dissimilar to *E.coli*, indicates resistivity to photoactive TiO_2 and UV light. Greater *P.aeruginosa* resistivity possibly originates from a thicker outer membrane or "biofilm". This outer membrane consists of an extracellular polymeric substance, namely: 50-90 % high molecular weight polysaccharides and protein compounds including minimal lipid, DNA and humic substances. However, increased UV light intensity or exposure time could potentially destroy biofilms and inactivate bacteria [90].

Additionally, UV light independently possesses antimicrobial properties and is utilized for sterilization [4]. In particular, UV-C (100-280 nm) is utilized in sterilization, being absent from natural environments due to the ozone layer. However, TiO_2 films are typically photo-activated by UV-A (315-400 nm) exposure, with UV-A occurring naturally and generating minimal bacterial cell damage. Negligible UV-A also exists in indoor environments containing increased human pathogen levels (hospitals). For effective continual photocatalytic sterilization to be introduced in these environments, developing highly active TiO_2 through varying crystallinity or defect/dopant addition towards visible light utilization is a priority.

1.2 Crystallinity

TiO_2 crystallinity indicates varied effects on photocatalytic ability. Anatase is the most photocatalytically active polymorph [91-93], resulting from superior exciton charge pair mobility (reducing radiative recombination) and increased surface hydroxyl density (figure 1.6). Comparatively, the photocatalytic activity of rutile is restricted due to higher recombination rates and decreased surface hydroxyl density [94]. Additionally, surface Ti-O-Ti bonding undergoes hole attack in both anatase and rutile morphologies, with anatase typically forming hydroxyl radicals from water. However, rutile typically absorbs another trapped hole and forms Ti-peroxo (Ti-O-O-Ti) surface groups to subsequently generate hydroxyl radicals from water (figure 1.6) [95].

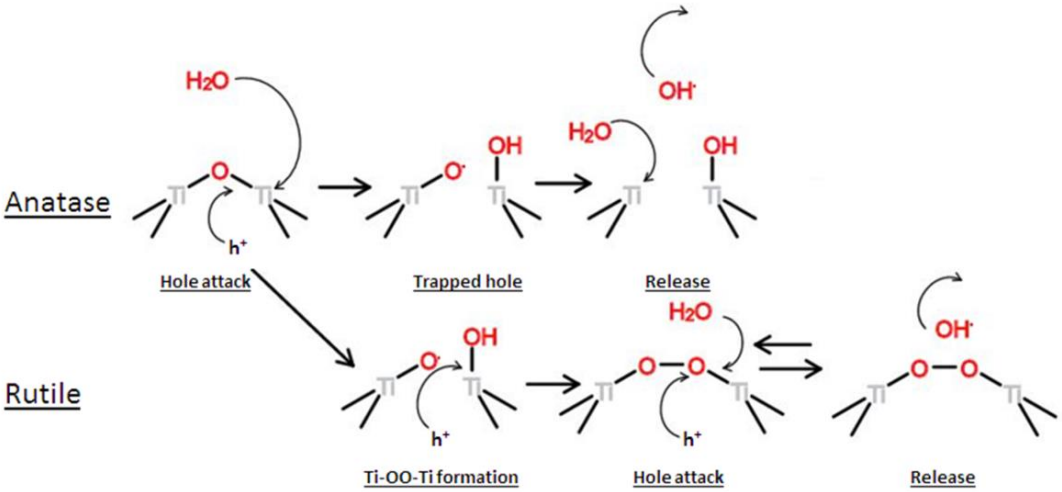

Figure 1.6: Hydroxyl radical generation on anatase and rutile TiO_2 [95]

Radiative recombination also occurs in rutile as a result of its direct band gap (figure 1.2), providing increased charge carrier/exciton recombination without requiring phonon absorption, dissimilar to anatase. However, a majority anatase and minimal rutile polymorph mixture is believed to produce the best photocatalytic activity through band gap combination [96, 97]. Correspondingly, Nakajima [98] confirmed greater luminescence efficiency for a combined anatase and rutile morphology, compared to single crystal rutile TiO_2. A combined anatase and rutile morphology leads to excited anatase conduction band electron trapping in an energetically lower rutile conduction band, combating recombination by extending excited electron lifetimes.

Comparatively, brookite has not been so thoroughly studied for contrasting photoactivity, with alternative TiO_2 polymorphs [99] showing negligible photocatalytic activity. Amorphous TiO_2 also indicates negligible photocatalytic activity [30] from TiO_2 structure randomization, thereby decreasing exciton charge pair mobility, whilst increasing deep trapping states for recombination.

1.3 Defects

In the previous sections, completely crystalline or amorphous, pure TiO_2 film generation was considered. However, in reality, TiO_2 film composition possesses greater complexity with crystallographic, intrinsic and extrinsic defects altering the TiO_2 properties from those of the assumed “ideal” TiO_2 film.

Defect concentrations ($N_{defects}$) and associated available defect sites (N_{sites}) are both dependent on change in formation energy (ΔE^f) as shown in equation 1.2, with greater defect concentrations at equilibrium resulting from lower energy requirements [100, 101]. Additionally, lattice formation energies influence defect equilibrium concentrations and therefore the subsequent metal and oxygen chemical potentials with the individual chemical potentials being dependent on metal or oxygen rich growth conditions [100].

$$N_{defects}/N_{sites} = \exp(-\Delta E^f_m/k_BT) \qquad \text{Equation 1.2}$$

However, in contrast to the particular ZnO study, TiO_2 films naturally (synthesis-dependent) possess greater $V_{O^{\cdot\cdot}}$ concentrations as primary defects through oxygen diffusion mechanisms and incorporate minimal titanium interstitials ($Ti_{i^{\cdots}}$), producing n-type semiconductivity [102-104].

Correspondingly, lower intrinsic and extrinsic defect concentrations energetically assist activation and diffusion processes by providing mid-band gap defect states for electron trapping, decreasing TiO_2 recombination rates [105]. Contrastingly, excess intrinsic and extrinsic defect concentrations assist recombination through increased mid-band gap defect state generation. This effectively creates a lower energy system suitable for faster recombination rates [106], and suggests a possible optimal defect concentration.

Furthermore, the defect spatial distribution also affects activation and recombination processes. Surface defects improve activation through trapping dissociated excitons and therefore initialize reactive oxidizing species generation. However, bulk defects escalate recombination by providing deep excition trapping centres subsequent to bulk-surface diffusion [107]. Contrastingly, crystallographic defects provide intrinsic and extrinsic defect agglomeration [108, 109] resulting in voids or precipitates, increasing recombination.

1.3.1 Crystallographic defects

Crystallographic defects include grain boundaries, which induce negative effects on TiO_2 film properties [110, 111]. Grain boundaries are boundaries between

crystalline grain growth phases, known as notorious recombination centres [11, 112] with deep trapping effects for diffusing charge carrier pairs and dopant ions. Dopant ions (extrinsic defects) can diffuse throughout doped TiO_2 films and tend to precipitate as dopant oxides at grain boundaries, especially following film annealing, further distorting electrical and photocatalytic properties. Grain boundaries are also indicated to "deflect" charged ion diffusion away from film surfaces, increasing deep recombination [109].

Although not technically "crystallographic" defects; amorphous regions within crystalline TiO_2 films also distort charge carrier diffusion and contain increased intrinsic defect concentrations to provide deep traps, thereby increasing recombination rates [113].

1.3.2 Intrinsic defects

Intrinsic defects are associated with pure TiO_2 film elements, namely: titanium vacancies (V_{Ti}''''), $Ti_i^{\cdots}$ and $V_O^{\cdot\cdot}$, resulting from imperfect TiO_2 film growth. Typically, oxygen deficient growth conditions generate $Ti_i^{\cdots}$ (titanium ions situated between TiO_2 lattice atoms) and $V_O^{\cdot\cdot}$, whereas V_{Ti}'''' creation occurs during oxygen-rich synthesis.

Increasing annealing or growth temperatures, increases $V_O^{\cdot\cdot}$ and $Ti_i^{\cdots}$ concentrations through oxygen diffusion loss [30, 105], producing reduced TiO_2 (Table 1.1). Oxygen diffusion results in a bulk to surface gradient, replacing lost surface oxygen and generating subsurface $V_O^{\cdot\cdot}$.

	Average annealing temperatures			
	<400 °C	>400 °C	>700 °C	>1000 °C
Surface	TiO_2	TiO_{2-x} (Ti^{3+})	TiO	Ti
Subsurface	TiO_2	TiO_{2-x} (Ti^{3+})	TiO_{2-x} (Ti^{3+})	TiO
Bulk	TiO_2	TiO_2	TiO_{2-x} (Ti^{3+})	$Ti_{1+x}O_2$

Table 1.1: Oxygen diffusion loss with increasing anneal temperature [114]

In Table 1.1, TiO_2 lattice structure undergoes degradation on increasing annealing temperatures and continual surface oxygen loss. $Ti_{i}^{\cdots}$ ($Ti_{1+x}O_2$) are also generated on surface to bulk titanium ion diffusion (subsequently increasing the Ti:O ratio at the surface regions). Oxygen interstitials (O_{i}'') can also be generated, but are unstable within TiO_2 lattices and diffuse out at increased temperatures.

Additionally, defect state (F-centre) recombination results in specific wavelength emission, as detected through photoluminescence. Jin [115] detected 600 nm (red) and 515 nm (green) emissions from anatase TiO_2 photoluminescence, correlating $V_O^{\cdot\cdot}$ to the green emission and reduced Ti^{3+} ions to the red emission. An increase in green emission was subsequently detected on annealing in an oxygen deficient atmosphere.

Previously, Mathew [116] assigned the 534 nm emission to $V_O^{\cdot\cdot}$ with two emission categories: 421, 491, 573 nm for lower Ti^{3+} 3d vibronic state relaxation to deep trap states and 533, 612 nm for lower $V_O^{\cdot\cdot}$ vibronic state in relation to the ground state. Also, Abazovic [117] suggested 2.8, 2.7, 2.56 and 2.34 eV as shallow trap states, and associated emissions equated to $V_O^{\cdot\cdot}$ in various anatase and rutile mixed phase films. Furthermore, $V_O^{\cdot\cdot}$ states in TiO_2 would decrease overall band gap energy, providing potential visible light wavelength absorption.

A combination of several studies [40, 41, 44] generates a TiO_2 band gap defect energy level diagram (figure 1.6), indicating shallow $V_O^{\cdot\cdot}$ and $Ti_{i}^{\cdots}$ (0.89 and 0.78 eV respectively) and deep trapping V_{Ti}'''' (1.15-1.44 eV) defect positions. Shallow defects stabilize exciton charge carriers near film surfaces, providing active sites for hydroxyl radical generation. In contrast, deep defects trap excited electrons, increasing recombination. Therefore oxygen deficient synthesis conditions seem beneficial towards TiO_2 film generation within surface diffusion regions producing $V_O^{\cdot\cdot}$ and $Ti_{i}^{\cdots}$. However, initial TiO_2 film synthesis possibly requires oxygen concentration parity to remove spatially deep defects beneath surface diffusion distances, removing deep trapping recombination centres from any potential defect source.

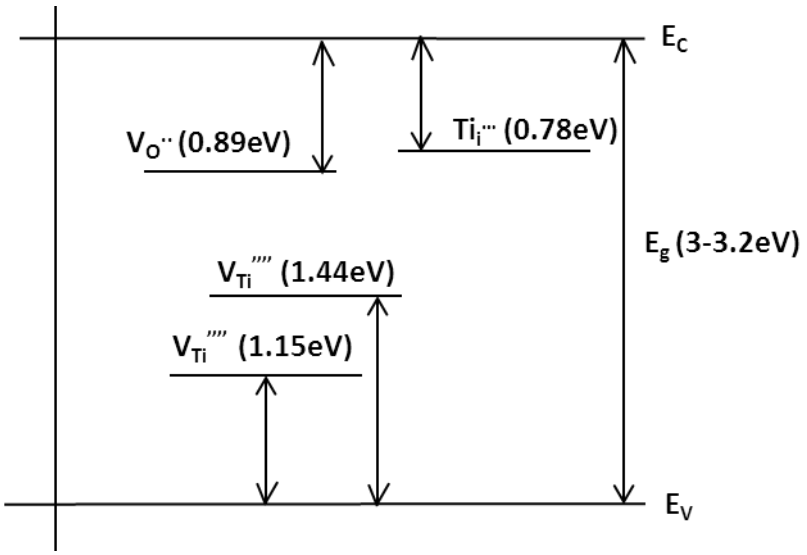

Figure 1.7: TiO_2 band gap defect energy level diagram [40, 41, 44]

Additionally, the excess electron density around a $V_O^{\cdot\cdot}$ between two Ti^{4+} atoms generates Ti^{3+} centres (equation 1.3). Both Ti^{3+} and $V_O^{\cdot\cdot}$ create mid-band gap states (figure 1.7) [118], effectively decreasing overall band gap size, but increase recombination in greater densities.

$$O_o \leftrightarrow V_O^{\cdot\cdot} + \tfrac{1}{2}O_2\,(g) + 2e^-,\ 2Ti^{4+} + 2e^- \rightarrow 2Ti^{3+} \qquad \text{Equation 1.3}$$

The presence of $V_O^{\cdot\cdot}$ in significant densities introduces mid-band gap states 0.4-1.18 eV beneath the TiO_2 conduction band [105, 119, 120] (figure 1.7). Ti^{3+} centres created by excess electron redistribution [121], also result in shallow conduction band donor states with a continuum of states around conduction band energies in highly deficient anatase [122]. Both $V_O^{\cdot\cdot}$ and Ti^{3+} centres effectively decrease the overall band gap size for >378 nm light wavelength absorption, subsequently increasing photocatalytic activity through visible light excitation of electrons to conduction band states. Additionally, greater excited electron density can further increase Ti^{3+} concentrations or create greater surface ROS.

Geometrically, the presence of $V_O^{\cdot\cdot}$ results in a lattice contraction [123, 124] with titanium atoms relaxing away from vacancies, strengthening lattice bonding. Surface $V_O^{\cdot\cdot}$ provide excess electron density generating favourable oxygen and dissociated water absorption conditions [125-127]. $V_O^{\cdot\cdot}$ are oxidized by adsorbed

oxide species undergoing subsequent reduction to one superoxide and two hydroxyl radicals per $V_O^{\cdot\cdot}$, improving photocatalytic reactions.

However, bulk TiO_2 $V_O^{\cdot\cdot}$ serve as photoinduced exciton recombination centres, reducing photocatalytic activity [128]. Conflicting literary opinions exist as to whether $V_O^{\cdot\cdot}$ predominately act as recombination centres hindering [129-131] or trapping centres facilitating [132, 133] charge separation and exciton synthesis for both photovoltaic and photocatalytic properties.

Surface defects are suggested to provide absorption sites and exciton charge pair traps with charge transfer to absorbed species helping to prevent recombination [107, 134]. However, surface $V_O^{\cdot\cdot}$ are unstable to oxidation with atmospheric oxygen absorption on excessively negatively charged surfaces. This absorption is provided by surface/subsurface photo-excited electrons or $V_O^{\cdot\cdot}$ (-0.94 eV or -2.52 eV) [126], slowly regenerating oxygen under ambient atmospheric conditions. Water molecule adsorption and dissociation can also occur on $V_O^{\cdot\cdot}$ associated defective sites [125], synthesizing two hydroxyl groups from one vacancy. Contrastingly, bulk $V_O^{\cdot\cdot}$ trap [107, 129, 131, 134] exciton charge pairs leading to recombination, and are generated through dopant or impurity charge compensation. Therefore an oxygen deficient film (possessing higher $V_O^{\cdot\cdot}$ concentration) is only desirable within exciton surface diffusion distance to prevent greater recombination rates.

It is therefore apparent that the optimisation of $V_O^{\cdot\cdot}$ concentration would result in a controlled recombination and charge transfer dominance. Optimal $V_O^{\cdot\cdot}$ concentrations would provide shallow donor states, to reduce the overall band gap and increase excited electron trapping rate. Beyond optimal amounts or with deep donor state presence, recombination processes dominate [105] and are favoured through greater excited electron concentrations possessing energies closer in proximity to the valence band.

1.3.3 Extrinsic defects

Intrinsic defects are usually incidental and created by varying environmental or synthesis stressors. In contrast, extrinsic defects are composed of disparate elements incorporated into host matrices. Extrinsic defects are either;

- Impurities, undergoing accidental addition during film synthesis and are commonly carbon or nitrogen from precursor ligand decomposition, or
- Dopants, purposefully added impurities in minimal amounts.

Extrinsic defects can potentially improve; light absorption [135-137] electronic [14, 94, 138] or chemical [61, 139, 140] properties. Additionally, extrinsic defects can greatly vary TiO_2 film properties and are location dependent in surface, shallow or deep bulk regions [42]. Extrinsic defects (similar to intrinsic defects) possess advantages and disadvantages in relation to photocatalysis which are dependent on specific defect; ionic radii, charge, oxide band gap, concentration and inclusion type (substitutional or interstitial) [19, 141].

As discussed, TiO_2 presents a matrix predominately consisting of Ti^{4+} and O^{2-} ions with associated intrinsic defects (frequently naturally occurring $V_{O}^{\cdot\cdot}$) in amorphous TiO_2 or a crystalline (anatase, rutile or brookite) TiO_2 polymorph. Titanium (IV) presents an octahedral environment ionic radii of 74.5 pm (Ti^{4+}), increasing on electron addition to 81 pm (Ti^{3+}) and oxygen presents ionic radii of 126 pm (O^{2-}) [142]. TiO_2 band gap also varies (3-3.4 eV) dependent on morphology, therefore photocatalytic activation typically proceeds by utilizing light wavelengths possessing energies greater than or equal to the band gap possessed by the material (corresponding to 387 nm for anatase TiO_2).

Extrinsic defect addition into a TiO_2 lattice can therefore occur through either substituting Ti^{4+} or O^{2-} ions resulting in M_{Ti} or M_O sites, or interstitial insertion between ions by lattice O^{2-} to create M_i sites. However, Hume-Rothery solubilisation rules [143, 144] define extrinsic defect (solute) incorporation to a TiO_2 lattice (solvent) similar to generating a solid solution with final concentrations dependent on specific extrinsic defect properties. For substitutional extrinsic defect addition, Hume-Rothery rules are:

- A ≤15 % disparity in ionic radii size,
- An identical oxide crystal structure,
- Similar electronegativities and valences between the defect and the substituted ion.

Similar electronegativity and valency rules also apply on interstitial extrinsic defect addition, alongside the possession of smaller extrinsic defect ionic radii than the TiO_2 interstitial lattice sites. Furthermore, extrinsic defects can also undergo both substitutional and interstitial incorporation into TiO_2 lattices. X-ray Photoelectron Spectroscopy (XPS) is able to separate disparate additions, as indicated in $TiO_{2-x}:N_x$; substitutional N_{2p} (0.14 eV) and interstitial N-O π^* (0.73 eV) [145].

Hume-Rothery rules define extrinsic defect concentration limits in a single homogeneous phase prior to TiO_2 lattice distortion. Incorporation of extrinsic defects with larger ionic radii generates strain in TiO_2 lattices, increasing distortion [145] and potentially also crystalline defect concentrations. Contrastingly, the probability of interstitial extrinsic defect addition increases with reduced ionic radii size, but subsequently accumulates greater intrinsic defect generation [146]. Optimal extrinsic defects (dopants) would therefore align with only a ≤15 % disparity in ionic radii and assume minimal lattice strain generation for crystalline integrity.

Additionally, Hume-Rothery rules also dictate valency disparity between typically charged extrinsic defects. Greater aliovalent (n/p-type) defect charge difference results in a lower solubility amongst nominally undoped TiO_2 lattice ions:

- Aliovalent defects:
    - n-type: possess increased charge and provide excess electron donation on substitution into TiO_2, producing states beneath the TiO_2 conduction band.
    - p-type: possess decreased charge and provide excess hole donation on substitution into TiO_2, generating states above the TiO_2 valence band.
- Isovalent defects result in no excess charge carrier addition.

Extrinsic defect incorporation therefore potentially introduces mid-band gap states into TiO_2, effectively decreasing the overall band gap size. Subsequently, band gap reduction could generate TiO_2 photoactivation with >387 nm light wavelengths, increasing photocatalytic efficiency within natural and artificial environments under visible light [60, 137, 147-149]. As an example, transition metal doping can generate mid-band gap d-orbital energy states, providing an absorption red shift [43]. However, transition metal dopant addition can also generate:

- Burstein-Moss effects [150, 151], resulting in lowest conduction band state occupation by dopant electrons, blocking low energy transitions and expanding overall band gap sizes.
- Increased exciton pair recombination rates and secondary defect generation after titanium site substitution, lowering TiO_2 photocatalytic activity despite typically optimal dopant concentrations [152-154].

Additionally, Bloh [155] suggested 0.01-1 % optimal concentration for any metallic dopant with resulting $Ti_{1-x}O_2{:}M_x$ photocatalytic improvement dependent on particle size or film thickness and not on specific dopant oxide properties. Therefore, beyond 0.01-1 % concentrations, metallic dopant solubility begins to vary with dopant properties providing detrimental effects on photocatalytic activity. Further solubility also begins to vary, blocking active photoreaction surface sites and decreasing photocatalytic activity [30].

Regardless, aliovalent dopant addition generates charge compensation mechanisms relative to both dopant concentration and charge difference between dopant and replaced lattice ions. Charge compensation neutralises overall lattice charge through defect formation. Aliovalent dopants possessing decreased positive charge versus substituted ions (Ga^{3+} substituted for Ti^{4+}) generate $V_O^{\cdot\cdot}$. However, aliovalent dopants possessing greater positive charge versus substituted ions (V^{5+} substituted for Ti^{4+}) generate $V_{Ti}^{''''}$ (equation 1.4).

$$Ti^{4+} + Ga^{3+} + 4O^{2-} + \tfrac{1}{2}V_O^{\cdot\cdot} = \text{Neutrality}$$

$$2Ti^{4+} + 3O^{2-} + N^{3-} + \tfrac{1}{2}V_O^{\cdot\cdot} = \text{Neutrality}$$

$$Ti^{4+} + V^{5+} + 4O^{2-} + ¼V_{Ti}'''' = Neutrality$$

$$2Ti^{4+} + 3O^{2-} + F^{-} + ¼V_{Ti}'''' = Neutrality \quad \text{Equation 1.4}$$

Multiple oxidation state dopant addition possesses favourable transition through photoinduced reduction, and can also result in $V_O^{\cdot\cdot}$ stabilization to retain photocatalytic activity. Photoinduced reduction; Fe^{3+} to Fe^{2+} (equation 1.5) provides a recombination pathway and indicates active metal reduction with excess $V_O^{\cdot\cdot}$ [156].

$$Fe^{III}{}_2O_3 \rightarrow 2Fe^{II}{}_{Ti} + 3O_O + V_O = Neutrality \quad \text{Equation 1.5}$$

Additionally, nominally undoped TiO_2 naturally possesses low $V_O^{\cdot\cdot}$ concentrations. This suggests that charge compensation requires decreased n-type or increased p-type (to overcome initial n-type nature) dopant addition before reaching an optimal limit.

Furthermore, increasing strain or defect concentrations can also promote anatase conversion into increasingly stable rutile morphology at suitable temperatures. The anatase to rutile transition (ART) [110, 157-159] differs with charge compensating vacancy generation on disparate aliovalent dopant addition into TiO_2 lattices. Dopant cations below a +4 oxidation state accelerate ART, providing a $V_O^{\cdot\cdot}$ creation mechanism and subsequently enhance atom transport in anatase morphologies accelerating phase transitions [160]. Comparatively, dopant cations above +4 oxidation states decelerate ART through generating $Ti_i^{\cdot\cdot\cdot\cdot}$ and suppressing atomic transport [146]. Annealing TiO_2 also naturally accelerates ART though oxygen ion removal via diffusion and subsequent $V_O^{\cdot\cdot}$ creation [161, 162].

1.4 Single dopant systems

In this section a non-exhaustive review of specific dopants undergoing incorporation into TiO_2 films and subsequent variation in photocatalytic activity is discussed.

1.4.1 Metals

Previous research into TiO_2 films with metallic dopants (M) is discussed here in terms of both theories of dopant addition (as described in further detail in chapter 2) and the resulting properties. These theories are namely; metal ion addition through either; direct substitution of a titanium site (M_{Ti}) or interstitial insertion (M_i) into the TiO_2 film, or metal oxide formation (MOx) in a nanolaminate layer. Initially, dopants and doped TiO_2 materials similar to those utilized within this research are described below.

For aluminium doping, several studies [163-166] indicate Al^{3+} (67.5 pm) undergoes either interstitial ($Al_i^{\cdots}$) or substitution ($Al_{Ti'}$) doping into a TiO_2 film with associated charge compensating $V_O^{\cdot\cdot}$ creation. Literature reports of $Ti_{1-x}O_2$:Al_x photocatalytic activity are inconsistent, with both increasing and decreasing activity indicated, depending on variable synthesis procedures and aluminium concentrations.

Choi [45] initially reported decreased $Ti_{1-x}O_2$:Al_x photocatalytic activity compared to nominally undoped TiO_2. However, further studies by Navas and de los Santos [167, 168], Liu [169] and Murashkina [170] reported greater photocatalytic activity (phenol/dye degradation). Whereas Gesenhues [171], Maeda [172] and Paulauskas [173] all reported decreased photocatalytic activity, in contrast to nominally undoped TiO_2. Photocatalytic activity suppression was indicated independent of Al_2O_3 concentrations across the range of 1-8 mol% [171]. However, concentrations of 0.1-1 mol% were found to be optimal as indicated for any metal dopant under theoretical modelling by Bloh [155], providing greater photocatalytic activity. Similar optimal dopant values were also observed alongside photocatalytic activity increase in $Ti_{1-x}O_2$:Al_x [167-170]. This suggested that photocatalytic activity was independent of aluminium doping with charge compensating $V_O^{\cdot\cdot}$ generation providing increased photocatalytic activity. Furthermore, photocatalytic activity suppression was subsequently detected at greater aluminium concentrations [171-173].

Therefore, it is believed suppression of photocatalytic activity results from Al^{3+} acting as deep traps [45], capturing electrons or holes prior to surface migration.

Al^{3+} also adopt an uniform distribution by diffusing throughout $Ti_{1-x}O_2:Al_x$ films [164]. Additionally Al_2O_3 possesses a 6.4 eV band gap suggesting mid-band gap states within $Ti_{1-x}O_2:Al_x$ originate from charge compensating $V_{O^{\cdot\cdot}}$. Aluminium doping is also suggested to reduce ART [174] with lower rutile growth rates subsequent to Al^{3+} incorporation from decreased TiO_2 precursor chemisorption [164]. Overall, previous studies of $Ti_{1-x}O_2:Al_x$ suggest photocatalytic activity suppression from Al^{3+} as deep traps in $Ti_{1-x}O_2:Al_x$ lattices.

Similarly, gallium doped systems could utilize a nanolaminate Ga_2O_3 system, with Ga_2O_3 possessing a 4.9 eV band gap [175], suggesting UV light photocatalytic activity [176]. However, minimal direct reduction may be observed on $Ti_{1-x}O_2:Ga_x$ generation, with charge compensating $V_{O^{\cdot\cdot}}$ creation expected to decrease the $Ti_{1-x}O_2:Ga_x$ band gap size. In the literature, Banerjee [177] synthesized $Ti_{1-x}O_2:Ga_x$ nanoparticles, which generated 90 % Rhodamine B dye degradation over three hours UV irradiation. $V_{O^{\cdot\cdot}}$ mid-band gap states and exciton trapping centres were further indicated in $Ti_{1-x}O_2:Ga_x$ nanoparticles through the presence of surface Ti^{3+} and titanol (Ti-OH) groups. These groups resulted in improved UV photocatalytic activity, in comparison to nominally undoped TiO_2 nanoparticles. Additionally, $Ga_{Ti'}$ generated strain in $Ti_{1-x}O_2:Ga_x$ nanoparticles despite minimal ionic radii disparity (Ga^{3+}: 76 pm).

Liu [178] synthesized $Ti_{1-x}O_2:Ga_x$ powders providing methyl orange photocatalytic decolourization under visible light irradiation through absorption by mid band gap states formed from charge compensating $V_{O^{\cdot\cdot}}$ [179]. Additionally, Ga^{3+} are believed to act as electron traps, enhancing exciton generation and stabilization, and increasing surface hydroxyl group $Ti_{1-x}O_2:Ga_x$ concentration across the range of x = 0.01-0.06. Furthermore, greater Ga^{3+} concentrations resulted in decreasing photocatalytic activity with excess Ga^{3+} acting as recombination centres [180, 181].

In summary, $Ti_{1-x}O_2:Ga_x$ is expected to show increased photocatalytic activity resulting from secondary $V_{O^{\cdot\cdot}}/Ti^{3+}$ defect creation on minimal gallium incorporation, with Ga^{3+} inclusion enhancing excition generation and hydroxyl concentrations.

Hafnium is yet another dopant researched within this study. Hafnium possesses a dominant +4 oxidation state and 85 pm Hf^{4+} ionic size, synthesizing hafnium dioxide with a subsequent 5.3-5.7 eV band gap. As a nanolaminate dopant in $Ti_{1-x}O_2:Hf_x$ possessing an identical oxidation state and increased size in contrast to Ti^{4+}, Hf_{Ti} formation could result in negligible charge compensating defect concentrations and significant lattice strain.

Fang [182] described a lowering of photocatalytic activity, compared to undoped TiO_2, with mixed $Ti_{1-x}O_2:Hf_x$ anatase/amorphous morphologies. Furthermore, $V_{O}^{\cdot\cdot}$ were undetected, indicating consistent harder and denser film generation with better band gap stability (immobile conduction and valence band states) on hafnium doping [183, 184]. Contrastingly, Meng [185] suggested visible light photocatalysis, resulting in water splitting, with band gap red shift (2.65 eV) occurring on mixed oxide ($TiHf_2O_6$) generation.

Overall, minimal research into $Ti_{1-x}O_2:Hf_x$ for photocatalytic activity improvement is detected in literature, with only Meng [185] indicating increased TiO_2 photocatalytic activity.

Silver doped TiO_2 ($Ti_{1-x}O_2:Ag_x$) film synthesis was also attempted in this research with silver frequently generating a stable Ag^{+} oxidation state to create Ag_2O. Structurally, Ag_2O possesses cubic crystallinity with a 1.46 eV band gap, suggesting possible visible light wavelength absorption and therefore potential mid-band gap state creation on doping into TiO_2. However, similar to copper (below), transitions to and mixing with the filled Ag 4d-orbital may be difficult. Ag^{+} possesses almost double the ionic radii (129 pm) of Ti^{4+}, suggesting $Ag_{Ti}^{\prime\prime\prime}$ would cause significant strain and excess grain boundary formation, if substitution occurs outside Hume-Rothery solubilisation rules [144]. Significant charge compensation defects could also result from substitutional doping due to charge variation between Ag^{+} and Ti^{4+} ions.

In TiO_2, silver can trap electrons [186], delaying exciton recombination through interfacial charge transfer, thereby producing greater concentrations of surface hydroxyl radicals [187] and decreasing recombination [186, 188]. Increased surface

TiO_2 bridging complex weakening is also detected with silver ions encouraging ART during film growth [189] and band gap extension to visible light ranges [186, 190, 191], both of which increase the photocatalytic activity. Additionally, greater excited electron lifetimes could potentially occur from silver surface plasmon resonances, [187] further increasing hydroxyl radical generation or recombination. Surface plasmon resonances fundamentally result from TiO_2 incident light absorption near a colloidal silver nanoparticle and energy interaction with free metal electrons, generating oscillating electric fields. These electron field oscillations then resonate with the incident light altering the silver nanoparticle electrical field distribution. In turn a local field effect can be propagated, resulting in greater excited electron lifetimes.

Additionally, silver possesses antimicrobial properties with silver ions binding to thiol groups in enzymes causing deactivation [192, 193]. Silver also binds to cell membranes [192], causing transmembrane energy generation and ion transport disruption [194]. Silver ions also catalyse oxidation reactions, generating excess water and disulphide bond formation [195]. Yamanaka [193] showed silver ions bound to 30S ribosomal subunit proteins and succinyl coenzyme A synthease prevented protein translation and ATP/energy production for cell respiration, eventually resulting in death.

$Ti_{1-x}O_2:Sn_x$ films were also synthesized within this research, with tin capable of doping TiO_2 via two potential ions; Sn^{4+} and Sn^{2+}. However, Sn^{4+} is typically utilized on account of a similar oxide crystal structure and an electronically lower energy conduction band [196]. Nevertheless, physically substituting larger tin ions (Sn^{2+}: 136 pm and Sn^{4+}: 83 pm) into Ti^{4+} sites (Sn_{Ti}) increases the lattice cell volume. Sn^{4+} substitution retains an anatase morphology, but induces lattice deformation and distortion, thereby increasing surface defect concentrations [145, 197] and consequently varies photocatalytic activity. However, opinion varies on the extent of lattice deformation resulting from Sn^{4+} concentration with Harunsani [198] suggesting lower tin concentrations hinder anatase formation and Duan [145] observing no structural variation under 1% incorporation.

Furthermore, greater strain and charge compensation defects would assumedly occur on Sn^{2+} substitution with greater surface Sn^{2+} sites detected on increasing tin incorporation [198, 199].

SnO_2 also possesses a similarly sized 3.6 eV band gap (as TiO_2) with a conveniently lower energy conduction band (-0.34 and 0.07 eV respectively, versus a normal hydrogen electrode) [200]. This facilitates excited electron transfer between the TiO_2 and SnO_2 conduction bands and reverse hole transport between the valence bands (Equation 1.6).

$$(TiO_2)e^-_{CB} \rightarrow (SnO_2)e^-_{CB} \ , \ (SnO_2)h^+_{VB} \rightarrow (TiO_2)h^+_{VB} \qquad \text{Equation 1.6}$$

Excited charged carrier transfers into the conduction band of SnO_2 or mid- TiO_2 band gap Sn^{4+} states subsequently increases both the charge carrier trapping and lifetime. This simultaneously generates decreased band gap size (red wavelength absorbance shift) [197] and greater ROS concentrations, improving photocatalytic activity. In particular, excited electrons in the SnO_2 conduction bands capture oxygen molecules, generating superoxide radicals and accelerating charge carrier separation [197]. Additionally, strong $Sn^{(4+/2+)}$ 5s hybridization with O 2p states and Sn 5s/5p lone pair states also provide antibonding states above $Ti_{1-x}O_2{:}Sn_x$ valence band energies capable of inducing visible light activity [198, 201]. However, if optimal Sn^{4+} concentrations (2-3 %) are exceeded, greater Ti^{3+} and Sn^{2+} site formation is instigated. This decreases surface hydroxyl concentrations [196, 200] with lower tin concentrations also resulting in photocatalytic activity inhibition [199]. Photocatalytic activity therefore significantly improves with tin doping [202] and $Ti_{1-x}O_2{:}Sn_x$ has been used in the degradation of:

- Malachite green dye [197], directly oxidized through photogenerated valence band holes.
- Methylene blue [201] under visible light irradiation after surface Sn^{4+} to Sn^{2+} conversion.
- Methyl orange under both UV and visible light irradiation [199].

- 4-chlorophenol [203] under UV light, with 6 mol% SnO_2 showing maximum photocatalytic activity,
- Penicillin [200].

Additionally, Sn^{4+} incorporation potentially increases photocatalytic activity by inducing rutile crystallite formation [200]. This encourages both mixed anatase/rutile TiO_2 morphology growth, and catalytically improved anatase crystallization with little or no variation in grain size [204]. However, Sn^{4+} doping also removes the natural TiO_2 oxygen deficiency on annealing, subsequently decreasing Ti^{3+} defect concentrations [198] and therefore associated photocatalytic activity.

Overall, $Ti_{1-x}O_2:Sn_x$ is expected to garner greater photocatalytic activity as compared to nominally undoped TiO_2 with decreasing effective band gap size towards visible light absorption and greater surface ROS concentrations.

Vanadium, namely as V^{4+} was also utilized as a dopant for synthesizing $Ti_{1-x}O_2:V_x$ films in the research presented here. Vanadium possesses three main oxidation states; V^{+3}, V^{+4} and V^{+5} typically appearing in three disparate oxides: V_2O_3, VO_2 and V_2O_5 respectively. Each oxide typically possesses different band gap sizes; 0.6, 0.6/2.4 and 2.3 eV, morphology; corundum, rutile/monoclinic and orthorhombic and ionic size; 78, 72 and 68 pm (octahedral), respectively. Therefore, $Ti_{1-x}O_2:V_x$ film synthesis would suggest:

- Negligible strain generation on substitutional doping from comparable ionic radii.
- Potential mid band gap state creation on charge compensation from V^{3+} or V^{5+} incorporation leading to decreased overall band gap size. However, V^{4+} substitutional doping would not be expected to generate charge compensation defects.

Choi [45] suggested increased photocatalytic activity from $Ti_{1-x}O_2:V_x$ in contrast to nominally undoped films. Shen [205] subsequently observed a 55 nm absorption wavelength red shift into visible light regions with $Ti_{1-x}O_2:V_x$ synthesized by liquid

injection ALD. For $Ti_{1-x}O_2:V_x$, photocatalytic activity increased 400-500 % with methylene blue degradation rate compared to nominally undoped TiO_2. 5 and 10 atm% doping concentrations with V^{4+} substitution for Ti^{4+} was detected with no resulting charge compensation defects. Doping also reduced the band gap through V^{4+} 3d orbital and TiO_2 conduction band overlap with V^{4+} favouring charge pair separation.

Overall, $Ti_{1-x}O_2:V_x$ suggests promise for increasing TiO_2 film photocatalytic activities, especially under visible light irradiation. Further research is required into variances between disparate vanadium oxidation states on doping, especially V^{4+} stabilization with respect to dissociation.

Additional dopant and dopant systems reviewed below are not subsequently studied in the research presented here. Despite this, these dopants and doped TiO_2 materials are included to round out the overall picture of research present within the literature.

Niobium possesses a dominant +5 oxidation state generating orthogonal Nb_2O_5 during nanolaminate TiO_2 film doping [206]. Nb_2O_5 maintains a 3.3-3.4 eV band gap [207, 208] suggesting mid-band gap state generation originating from V_{Ti}'''' defect charge compensation. Burstein-Moss effects are also detected in $Ti_{1-x}O_2:Nb_x$ films to provide a band gap increase (3.49-3.56 eV) [112] [209].

Nb_2O_5 easily undergoes reduction to NbO_2 (+4, distorted rutile structure) or NbO (+2, defective rock salt structure), possibly through oxygen diffusion during annealing. However, $Nb^{5/4+}$ substitution into a Ti^{4+} site ($Nb_{Ti}^{\cdot}$) would incorporate strain from greater ionic radii 78/82 pm respectively, as compared to Ti^{4+}. So on speculation, Nb^{4+} substitution would show the greater promise for doping than Nb^{5+}, with potential provision of minimal strain and a 0.5-1.2 eV NbO_2 band gap [210, 211]. Therefore, NbO_2 inclusion suggests possible mid-band gap state creation on without charge compensation defects. However, as the time of writing, no $Ti_{1-x}O_2:Nb_x$ photocatalytic analysis has been performed suggesting a potential future research avenue.

Tantalum maintains a dominant +5 oxidation state (78 pm) generating Ta_2O_5, which can be produced as either one of two existing orthorhombic polymorphs, and could provide a band gap of 3.8-5.3 eV [212, 213]. Direct TiO_2 mid-band gap state creation is therefore unlikely, but could indirectly occur through charge compensation defect formation. In contrast, theoretically calculated 2.3-3.8 eV band gaps [214, 215] suggest potential mid-band gap state creation with minimal strain for $Ta_{Ti}^{\cdot}$. At the time of writing, no $Ti_{1-x}O_2$:Ta_x film photocatalytic analysis has been performed [216].

Chromium possesses multiple oxidation states; +2, +3, +4 and +6 and therefore multiple d orbital states having energies within TiO_2 band gap regions. Frequently observed, corundum crystalline Cr_2O_3 shows increased atmospheric stability compared to alternative oxidation states with polycrystalline Cr_2O_3 possessing a 3-3.2 eV band gap similar to TiO_2 [217, 218]. Chromium ion loading [218-220] is indicated to be directly proportional to band gap narrowing, suggesting mid band gap state generation from chromium oxidation state energy orbitals. However, chromium ions only trap photogenerated electrons [160], resulting in a lower activity compared to dual charge carrier trapping dopants, and so is less favoured for photocatalytic research.

Molybdenum possesses two major oxidation states: Mo^{+4} (79 pm) and Mo^{+6} (73 pm), which occur in MoO_2 and MoO_3 with monoclinic/orthorhombic (α-phase) or monoclinic (β-phase) morphology, respectively. Greater photocatalytic activity [45] in $Ti_{1-x}O_2$:Mo_x is generated through electronic donor state creation near the TiO_2 conduction band, probably originating from a varied 2.75-2.89 eV or 3.1 eV MoO_3 band gap [221-223]. MoO_3 is also thought to possess antibacterial activity with H^+ generation on H_2O interaction [224], suggesting direct $Ti_{1-x}O_2$:Mo_x film band gap reduction and indirect charge compensating defect creation. At the time of writing, no reports exist detailing photocatalytic activity measurements of $Ti_{1-x}O_2$:Mo_x, suggesting possible future research avenues.

For manganese doping of TiO_2, multiple stable Mn^{+2}, Mn^{+3}, Mn^{+4} and Mn^{+7} oxidation states can produce abundant possible d-d energy orbital transitions

within the TiO_2 band gap energy ranges [225]. Of these rock salt MnO and rutile MnO_2 both possess an indirect 2.33 eV band gap [226, 227]. However, MnO_2 exhibits a decreasing band gap to 1.3 eV by spin dependent hybridization between Mn 3d and O 2p states, providing exchange O 2p state splitting and multiple Ti/Mn_{3d} states [225]. For nanolaminate or homogeneously doped $Ti_{1-x}O_2:Mn_x$ generation, mid-band gap states could initiate visible light photocatalytic activity with no charge compensation defects on Mn^{4+} substitution.

Sellers [228], synthesized $Ti_{1-x}O_2:Mn_x$ films with 1.2 and 2.4 atm% dopant concentrations, but with no photocatalytic activity measurements. Additionally, substitutional manganese doping (Mn_{Ti}) induced some light surface roughing and grain boundary increase on comparison to nominally undoped TiO_2 with divalent $Mn^{2/3+}$ detected in polycrystalline anatase. Furthermore, Li [139] proposed that manganese ions can separately trap both charge carriers by using multiple $Mn^{2/3+}$ oxidation states, increasing charge carrier lifetimes.

In summary, $Ti_{1-x}O_2:Mn_x$ films indicated enhanced surface area and anatase morphology, as well as Mn^{x+} trapping of both charge carriers, providing potential for greater UV and visible photocatalytic activity. Therefore, $Ti_{1-x}O_2:Mn_x$ material systems warrant further research.

Iron retains two major oxidation states: Fe^{+2} and Fe^{+3}, which could produce FeO, Fe_2O_3 and Fe_3O_4 on nanolaminate doped TiO_2. Specifically, Fe_2O_3 (corundum α-Fe_2O_3 (hematite) or cubic γ-Fe_2O_3 (maghemite)) possesses a band gap of 2.1-2.2 eV [229-231]. Fe_2O_3 accommodation within the TiO_2 band gap range could provide potential visible light photocatalytic activity generation on TiO_2 doping. Additionally, on substitution of Ti^{4+} sites, possible Fe_{Ti}'' site generation would result in minimal overall strain increase with similar ionic radii; Fe^{3+}: 69/78.5 pm (low spin/high spin (hs)) and Fe^{2+}: 75pm compared to Ti^{4+}. However, Fe^{2+}: 92 pm (hs) would incorporate significant strain in Fe_{Ti}'' site formation.

Choi [45], indicated increased $Ti_{1-x}O_2:Fe_x$ photocatalytic activity compared to nominally undoped TiO_2, through greater charge carrier trapping on Fe_2O_3 valance and conduction band states near the TiO_2 valence and conduction bands. Wu [160]

also suggested greater photocatalytic activities were a result of observed electron and hole charge carrier trapping by Fe ions.

Later, Yu [232] synthesized Fe(III) grafted TiO_2. Visible light absorption was generated from interfacial charge transfer to Fe^{3+} surface species from accumulated TiO_2 conduction band electrons, creating photoreduced Fe^{2+} species. Furthermore, switching between $Fe^{2+/3+}$ oxidation states was detected on photoexcited electron absorption, suggesting multiple electron oxygen reduction catalyst generation. Therefore, minimal doping would potentially offset charge compensation effects, effectively creating surface ROS with negligible recombination. To summarize, $Ti_{1-x}O_2$:Fe_x possess great potential for visible light photocatalytic activity, suggesting further research is required.

At the time of writing there have been no reported studies of the photocatalytic activity of $Ti_{1-x}O_2$:Co_x films. Cobalt presents two stable oxidation states: Co^{2+} (79/88.5 pm (hs)) and Co^{3+} (68.5/75 pm (hs)) subsequently able to generate three oxides: rock salt CoO, trigonal Co_2O_3 and spinel Co_3O_4, respectively. CoO and Co_3O_4 possess band gaps of 2.4 eV and 1.6-1.96 eV [233] respectively, suggesting doping TiO_2 with cobalt could produce mid-band gap states and hence induce visible light absorption. However, $V_{O^{\cdot\cdot}}$ generation in bulk regions may present recombination issues, with further research obviously required.

Nickel possesses a dominant +2 oxidation state, and could generate a rock salt structured nickel (I) oxide on nanolaminate doping of TiO_2 with a corresponding 3.6 eV band gap for Ni_2O [234, 235]. In contrast, nickel (III) oxide (Ni_2O_3) is not well characterised. Interestingly, Ni^{3+} (Ni_2O_3) [236] as a potential Ni_{Ti}'' would generate minimal lattice strain in octahedral environments due to possession of a nearly identical 74 pm ionic radii size to Ti^{4+} (unless low spin Ni^{3+} (70 pm) is present).

Tian [237] synthesized $Ti_{1-x}O_2$:Ni_x films through a sol-gel technique and subsequent annealing. Ni^{2+} and $V_{O^{\cdot\cdot}}$ formation were indicated by XPS, suggesting Ni_{Ti}'' formation and subsequent charge compensation. Furthermore, strain on substituting increased Ni^{2+} ionic radii (83 pm) into Ti^{4+} sites supported hypotheses of greater charge compensation effects and lattice deformation. Additionally, ART was

catalysed by Ni^{2+} presence, providing reductions to both Ti-O bond rupturing and ART activation energy, as indicated with ≥7 mol% $Ti_{1-x}O_2:Ni_x$ films generating a purely rutile structure. Additionally, Hosny NM [238] described an initially anatase $Ti_{1-x}O_2:Ni_x$ film possessing a 3.56 eV band gap with a decrease in band gap to 3.34 eV, correlating to increasing nickel content up to 10 %.

In summary, for Ni^{2+} inclusion a band gap decrease resulting from direct mid band gap state introduction is not implicated, with nickel ions only trapping electrons [160]. The resulting $Ti_{1-x}O_2:Ni_x$ therefore possesses lower photocatalytic activity as compared to other doped TiO_2 materials. However, Ni^{2+} ions also promote ART and therefore minimal Ni^{2+} concentrations could result in greater photocatalytic activity. Further research is subsequently required in order to determine the photocatalytic activity potential of $Ti_{1-x}O_2:Ni_x$ materials.

Copper possesses dominant Cu^+ and Cu^{2+} oxidation states providing generation of both Cu_2O and CuO, respectively in nanolaminate TiO_2 doping. Structurally, Cu_2O adopts a cubic crystalline structure with a 2.1 eV band gap [239] and in comparison, CuO possesses a monoclinic crystalline structure with a 1.9 eV band gap [240]. For Ti^{4+} site substitution, both ionic radii of Cu^+ (91 pm) and Cu^{2+} (87 pm) are greater than Ti^{4+} with potential Cu_{Ti}''' sites possibly creating significant $Ti_{1-x}O_2:Cu_x$ strain and excess grain boundaries. TiO_2 and CuO/Cu_2O band gap mixing would potentially generate mid-band gap states, decreasing the overall TiO_2 band gap and creating visible light photoactivity. However, transitions to and mixing with filled Cu^+ 3d orbitals may negate this hypothesis.

Choi [45] suggested copper doping creates additional charge carrier trapping states near both the valence and conduction bands of TiO_2. Wu [160] further confirmed this hypothesis, proposing copper ion doping traps exciton charge pairs. Hashimoto [241] subsequently synthesized Cu (II) grafted TiO_2 possessing visible light activity, generated through interfacial electron charge transfer to Cu^{2+}. The Cu^{2+} then undergo reduction to Cu^+ by reaction with conduction band electrons.

Additionally, copper has antimicrobial properties and is capable of preventing microbial colony growth. Varied antimicrobial mechanisms for copper have been

suggested in the literature [242]. However, copper ions frequently bind with cell membranes, causing rupturing and subsequent nutrient leakage. Copper is thought to short circuit the transmembrane potential (voltage between inside and outside of a cell), resulting in greater membrane hole density [21]. Copper ions are also believed to generate oxidative stress through H_2O_2 generation (Fenton-type reaction) and inappropriately bind to enzymes [243], both eventually leading to cell death.

Bacterial cell destruction requires copper ions to be positioned within film surface diffusion regions. Physical contact of copper ions and microbes is necessary for microbial destruction through cell wall attack [242] or by diffusing into cells to simultaneously attack DNA and enzymes [242]. Further research is required to examine specific copper doping on TiO_2 film properties.

For zinc doped TiO_2, zinc commonly presents a Zn^{2+} able to undergo substitution into TiO_2 sites ($Zn_{Ti''}$). Additionally, for nanolaminate ZnO doping, ZnO has a 3.2 eV band gap, nearly identical to that of nominally undoped anatase TiO_2. Therefore $Ti_{1-x}O_2$:Zn_x films would comparably undergo negligible band gap decrease as compared to undoped TiO_2, whilst maintaining significant visible light transmittance. However, photocatalytic activity at UV wavelengths is expected to increase as a result of;

- Greater exciton lifetimes from excited electrons “hopping” into the ZnO conduction band, further reducing recombination rates.
- Charge compensation from zinc dopant inclusion resulting in surface $V_{O}^{\cdot\cdot}$ generation for hydroxyl radical creation [244].
- Zn^{2+} incorporation creating exciton traps, decreasing recombination rates in lower concentrations [245].

Additionally, charge compensating $V_{O}^{\cdot\cdot}$ in low concentrations may provide mid-band gap states for visible light transitions [244]. However, $Zn_{Ti''}$ substitution to form $V_{O}^{\cdot\cdot}$ undergoes difficulties from ionic size dissimilarities (Zn^{2+}: 88 pm vs Ti^{4+}: 75.4 pm) generating strain on Zn^{2+} incorporation [244].

$Ti_{1-x}O_2:Zn_x$ nanoparticles have been previously studied. Zhao [244] initially produced highly photocatalytic $Ti_{1-x}O_2:Zn_x$ with 99.4 % Rhodamine B ink degradation detected in under 30 minutes visible light irradiation, contrasting to the 63.5 % degradation observed for nominally undoped TiO_2. Thanh Binh [245] also generated $Ti_{1-x}O_2:Zn_x$ (x = 0.03-0.1) nanoparticles, which indicated 91.4 % methylene blue photocatalytic degradation, as compared to 46.4 % for nominally undoped TiO_2, subsequent to four hours UV light irradiation. In contrast, Chauhan [246] and Wattanawikkam [247] generated $Ti_{1-x}O_2:Zn_x$ nanoparticles, with Chauhan reporting a slight band gap shift towards higher wavelength absorption.

Comparatively, Arunachalam [248] produced $Ti_{1-x}O_2:Zn_x$ films possessing 85 % visible light transmittance and negligible band gap shrinkage. Furthermore, $Ti_{1-x}O_2:Zn_x$ also suggested significant antimicrobial activity towards *bacillus subtilis* colonies.

To summarize, zinc ion addition to TiO_2 represents a potential avenue for further research with disparate $Ti_{1-x}O_2:Zn_x$ properties resulting, dependent on oxygen concentration during film synthesis. In particular:

- Photocatalytic activity increases under UV irradiation, through addition of excess holes and a reduction in defects [245].
- Photocatalytic activity increases with effective bandgap decrease under visible light irradiation [244], suggesting increased charge compensation from defect formation in an oxygen deficient environment.
- Synthesis in an oxygen rich environment generates high visible light transmittance [248] with Zn^{2+} in Zn_{Ti}'' providing antibacterial activity by surface diffusion.

Europium possesses a dominant Eu^{3+} ion with greater size (108.7 pm) compared to Ti^{4+} (74.5 pm), suggesting significant strain induction on potential Eu_{Ti}''' substitution and therefore potentially results in excess grain boundary generation. Lower nanolaminate growth rates from differing nucleation sites could potentially occur, as Eu_2O_3 possesses monoclinic and cubic crystalline morphologies. However, europium possesses significant 4f orbital concentrations resulting in discrete and

narrow emission bands throughout the near IR, visible and UV electromagnetic spectrum regions with relatively long excited state lifetimes [249]. Eu_2O_3 potentially provides TiO_2 mid-band gap $^5L_6$, $^5D_{(0-3)}$ and $^7F_{(0-6)}$ states (table 1.2).

Energy State	Level (eV)
$^5L_6$	3.15
$^5D_3$	3.02
$^5D_2$	2.67
$^5D_1$	2.36
$^5D_0$	2.14
$^7F_6$	0.62
$^7F_5$	0.49
$^7F_4$	0.35
$^7F_3$	0.23
$^7F_2$	0.12
$^7F_1$	0.04
$^7F_0$	0.00

Table 1.2: Energy state type versus TiO_2 band gap energy [250]

Corresponding radiative emissions from the $^5D_0$ energy state equal to visible light wavelengths and beyond ($^7F_{5-6}$) are discussed by Wakefield [250] (table 1.3).

$^5D_0$ transition	$^7F_6$	$^7F_5$	$^7F_4$	$^7F_3$	$^7F_2$	$^7F_1$	$^7F_0$
Emission (nm)	815	751	692	649	613	590	579

Table 1.3: $^5D_0$ to $^7F_{0-6}$ transitions and associated emissions [249]

Furthermore, Wang [249] describe a wider luminescence emission range with visible light emissions resulting in colours from differing $^5D_{0-3}$ to $^7F_{0-6}$ states [251];

- Red: $^5D_0$ to ^7F_J (J = 1, 2, 3, 4).
- Green: $^5D_1$ to ^7F_J (J = 0, 1, 2).
- Dark blue/green: $^5D_2$ to $^7F_3$.
- Violet: $^5D_3$ to ^7F_J (J = 0, 1, 2).
- UV: $^5H_{3-7}$, $^5G_{2-6}$ and $^5L_6$ to $^7F_0$.

Thus, if TiO_2 was successfully doped with Eu^{3+}, potential visible light activity could result from corresponding photon wavelength absorption, generating excitons and subsequent surface reactive oxide species.

Europium would aliovalently (Eu^{3+}) substitute Ti^{4+} lattice sites (Eu_{Ti}), providing excess holes and a greater p-type conductive nature. Charge compensating $V_{O}^{\cdot\cdot}$ could be generated, which may counteract the potential p-type natures and also potentially produce visible light photocatalytic activity with 515 ($V_{O}^{\cdot\cdot}$) and 600 nm (Ti^{3+}) emissions indicated [115]. Hansen [251, 252] synthesized europium titanium oxide ($Eu_xTi_yO_z$) films through ALD and subsequently studied the luminescent properties of the films. In $Ti_{1-x}O_2$:Eu_x films, TiO_2 and Eu_2O_3 were shown to provide beneficial roles with TiO_2 controlling UV absorption and Eu_2O_3 governing luminescence. Additionally, the highest luminescence efficiency was dependent on specific concentration of Eu_2O_3 and TiO_2.

Overall, $Ti_{1-x}O_2$:Eu_x films could provide greater photocatalytic activity as compared to nominally undoped TiO_2. This could occur through secondary $V_{O}^{\cdot\cdot}$ generation for ROS generation and via europium energetic state presence within the TiO_2 band gap. However, the ionic radius of Eu^{3+} is significantly larger as compared to Ti^{4+} and so would be outside Hume-Rothery rules for solid solubilisation, providing great difficulty in creating $Ti_{1-x}O_2$:Eu_x, without relying on Eu_2O_3 nanolaminate doping approaches.

Furthermore, upconversion [253, 254] is also a possibility with $Ti_{1-x}O_2$:Eu_x films, with Eu^{3+} providing sequential absorption of two or more inbound lower energy (visible) photons, to result in subsequent emission of a higher energy (UV) photon. This higher energy UV photon could potentially photocatalytically activate the TiO_2

providing visible light activity, however, this is outside the scope of the presented research.

1.4.2 Non-Metals

Non-metals typically enhance visible-light photocatalytic activity through anionic doping ($TiO_{2-x}:M_x$). This generally provides greater photocatalytic efficiency through reducing the number of recombination centres as compared to cationic metal doping [30]. Although not explicitly studied within this research, non-metal dopants within TiO_2 materials commonly occur as impurities (hydrogen, carbon and nitrogen). Therefore non-metal dopants are reviewed here to show the effect these impurities could impart if present in the synthesized $Ti_{1-x}O_2:M_x$ films.

Theoretically, hydrogen impurities were initially suggested by Park [255], to generate OH^- in bulk TiO_2 through H_i attachment to a non-bonding oxygen p-orbital. Park also showed hydrogen impurity levels occurred above the TiO_2 conduction band maximum for both anatase and rutile morphologies. Additionally, Mehta [256] further theorized that atomic hydrogen could occupy $V_{O^{\cdot\cdot}}$ sites in nominally undoped TiO_2, enhancing visible light absorption through stabilization of Ti^{3+} states.

Experimentally, Mo [257] confirmed rutile TiO_2 hydrogenation either resulted in $V_{O^{\cdot\cdot}}$ site occupation or H_i formation, subsequently creating weak O-H bonding. Additionally, Ataei [258] suggested that hydrogen impurities enhanced both visible and infrared wavelength absorption, providing potential for future research. Contrastingly, Deng [259] reported formaldehyde photo-oxidation by nominally undoped anatase TiO_2 was outperformed by amorphous hydrated TiO_2 ($Ti_{(2-x/2)}(OH)_x$). The improved $Ti_{(2-x/2)}(OH)_x$ photocatalytic activity was believed to result from greater terminal and surface OH^- density and not $V_{O^{\cdot\cdot}}/Ti^{3+}$ concentrations, with Ti-OH group condensation creating Ti-O-Ti at greater temperatures.

Additionally, carbon can undergo both substitutional ($C_{O''}$) and interstitial ($C_{i^{\cdots\cdot}}$) doping depending on synthesis conditions (oxygen partial pressure). Carbon also shows possible electron transfer from an oxidized interstitial to reduced substitutional species [260]. Both $C_{O''}$ and $C_{i^{\cdots\cdot}}$ result in isolated C 2p and mid-band gap states located 0.26 eV [94] above valence band energies with differing

electronegativities (2.55 and 3.44 respectively) providing negligible O 2p and C 2p state mixing. C 2p states, $V_{O}^{\cdot\cdot}$ and subsequent Ti^{3+} formation further suggest that visible light absorption is possible [261-264].

Sakthivel [261] initially demonstrated TiO_{2-x}:C_x film photocatalysis under daylight illumination with further research [94, 260, 263, 264] suggesting significant photocatalytic improvement as compared to nominally undoped TiO_2. Additionally, antibacterial results indicate *S.aureus* visible light inactivation at anatase-brookite heterojunctions via additional carbonate ion energy states within TiO_{2-x}:C_x films [94]. Overall, TiO_{2-x}:C_x films usually occur unintentionally as a result of precursor decomposition impurities ($C_{i}^{\cdots}$), but intentional low carbon concentrations suggest a significant photocatalytic improvement into visible light ranges may be possible.

TiO_{2-x}:N_x films are commonly synthesized for applications requiring visible light photocatalytic activity [9, 265-267]. Sato [268] initially reported visible light activity after nitrogen incorporation into a TiO_2 sol. N^{3-} ions usually incorporate into TiO_2 lattices through oxygen lattice site substitution ($N_{O}^{\cdot}$) with significant proportions also undergoing interstitial site substitution ($N_{i}^{\cdots}$). In contrast, Pore [267] only observed $N_{i}^{\cdots}$ doping across TiO_2 lattices. $N_{O}^{\cdot}$ generates isolated N 2p states (with negligible mixing resulting from differing electronegativity (nitrogen: 3.04 and oxygen: 3.44)) 0.14 eV above the valence band [269]. In comparison, $N_{i}^{\cdots}$ induces N-O bonding with localized antibonding impurity states 0.73 eV above the valence band [270, 271] to generate visible light absorption [272, 273]. Contrastingly, other researchers [262, 274] proposed band gap narrowing and subsequent visible light absorption from surface adsorbed NO_x and NH_x groups.

Nitrogen doping is also believed to induce visible light absorption through stabilizing $V_{O}^{\cdot\cdot}$ formation [275]. Doped nitrogen initiates electron transfer between higher energy Ti^{3+} states to lower energy nitrogen states [276], subsequently producing an absorption red shift towards visible light regions (2.25 eV) [277]. Higher stability resulting from the comparable ionic sizes of nitrogen (N^{3-}: 132 pm) and oxygen (O^{2-}: 124 pm) is associated with $N_{O}^{\cdot}$ formation. However, Ti-N bonding

negatively affects band gap narrowing and therefore decreases photocatalytic activity [278, 279].

$TiO_{2-x}:N_x$ frequently exhibits an anatase dominated morphology, incorporating increasing rutile concentration with film thickness. Greatest photoactivity was detected in anatase dominant films containing minimal rutile, as in nominally undoped TiO_2 [98]. However, $TiO_{2-x}:N_x$ films containing significant rutile phase possessed lower energy N 2p states. Valence band energies therefore were decreased by 0.05 eV versus nominally undoped rutile TiO_2 films, effectively providing band gap widening and blue-shifting absorption wavelengths [280, 281].

$TiO_{2-x}:N_x$ films indicate superhydrophilicity (<15 ^{o} contact angle) under UV or visible irradiation, and therefore potential photocatalytic activity, present from significant $N_{i}^{\cdots}$ concentrations [267, 282]. $TiO_{2-x}:N_x$ surface pollutant molecular degradation of the following species has been previously studied:

- For salicylic acid decomposition [265], increased photocatalytic activity was detected at pH 6 for both nominally undoped TiO_2 and $TiO_{2-x}:N_x$ films with higher degradation rates obtained for nominally undoped TiO_2 (85 %), compared to $TiO_{2-x}:N_x$ (75 %). Additionally, $TiO_{2-x}:N_x$ showed increased absorption around 250-300 nm.
- For methylene blue decomposition [9], $TiO_{2-x}:N_x$ films containing increased nitrogen concentrations indicated greater levels of degradation after four hours of visible light exposure.
- For stearic acid decomposition [267, 283, 284], greater degradation efficiency was shown for nominally undoped TiO_2 films under UV light irradiation, indicating decreasing photoactivity with increasing nitrogen concentration. Additionally, the $TiO_{2-x}:N_x$ films indicated visible light activation as a result of interstitial nitrogen ($N_{i}^{\cdots}$) or annealing, resulting in complete stearic acid removal after 160 hours for an approximate rate of 1.4 $molcm^{-2}h^{-1}$.

- For 4-cholophenol decomposition, $TiO_{2-x}:N_x$ films underwent photocatalytic activation and greater levels of degradation under solar irradiation, in contrast to nominally undoped TiO_2 [280].
- For 100 % DDT (dichlorodiphenyltrichloroethane) decomposition, a greater degradation rate was observed under visible light irradiation as compared to UV light irradiation [285].
- For RR4 dye photodegradation [286], $Ti_{1-x}O_2:N_x$ films containing interstitial nitrogen from urea addition during synthesis provided complete degradation after 60 minutes under LED irradiation.

Without photocatalytic activity measurement standardization, comparability difficulties exist. However, literature indicates greater $TiO_{2-x}:N_x$ photoactivity overall as compared to nominally undoped TiO_2 under visible light and subsequent decomposition of a variety of model pollutants.

Phosphorus and sulphur ions are potential surface contaminants from treatment with cleaning agents in this research. Therefore, both phosphorus and sulphur doped systems were also reviewed with the view of the potential effect these impurities could impart if present on $Ti_{1-x}O_2:M_x$ surfaces.

Phosphorus doping can occur through substitution of both titanium and oxygen, dependent on the phosphorus ion oxidation state. P^{5+} can substitute Ti^{4+} sites ($P_{Ti}^{\cdot}$), resulting in $V_{Ti}^{''''}$ generation and P^{3-} can substitute O^{2-} sites ($P_{O}^{'}$), resulting in $V_O^{\cdot\cdot}$ creation. Iwase [287, 288] indicated P^{3-} substitution generated increased band gap narrowing via P 3p states and $V_O^{\cdot\cdot}$ formation, as compared to P^{5+} substitution. However, the formation of $V_O^{\cdot\cdot}$ resulted in no visible light activity and further suggested P 3p states solely produce visible light active sites. Additionally, the photocatalytic decomposition of acetaldehyde and phenol under visible light was observed for $Ti_{1-x}O_2:P_x$ films. Improved visible light activity resulted from inhibited rutile crystalline growth occurring upon phosphorus ion incorporation. Furthermore, Han [289] suggested phosphorus inclusion suppressed TiO_2 ART and surface crystallite growth, potentially improving photocatalytic activity through greater surface area production.

Additionally, sulphur has been incorporated in TiO_2 lattices as S^{6+}, S^{4+} or S^{2-} ions [290-292]. However, lattice strain is detected on substitution through either; S^{2-} possessing greater ionic radii (184 pm) [293] in contrast to O^{2-} (124 pm) or $S^{6/4+}$ ions possessing lower ionic radii (43/51 pm) as compared to Ti^{4+}, with potential for S_i creation. Visible light absorption is therefore explained through S 3p dopant mid-band gap states located 0.38 eV above the TiO_2 valence band [294]. (However, S 3p and O 2p orbital mixing is contentious, from electronegativity differences (2.58 vs 3.44 respectively)) [291, 295]. Overall, $Ti_{1-x}O_{2-y}:S_{x/y}$ films exhibit increased 2-propanol and methylene blue visible light photocatalytic decomposition. This suggested a photocatalytic improvement as compared to nominally undoped TiO_2 films, potentially resulting from S 3p mid-band gap states.

Furthermore, other non-metallic TiO_2 dopants, namely; boron, fluorine and iodine, have also been reviewed with respect to how doped TiO_2 film properties are altered with the addition of these specific dopants.

Boron undergoes interstitial (B_i) [296] doping into TiO_2 with B^{3+} (41 pm) creating oxidized borate species bound to Ti^{3+} centres [297]. Both $V_{O^{\cdot\cdot}}$ and B_{2p} mid-band gap energy states are subsequently generated, narrowing the TiO_2:B band gap and achieving visible light photocatalytic activity. Furthermore, TiO_2:B has been previously shown to actively decompose a range of organic pollutants under visible light irradiation [298-301], suggesting further research potential.

When doped, fluorine [302-307] undergoes substitution into oxygen sites ($F_{O'}$) causing Ti^{4+} reduction (Ti^{3+}) through strong fluorine ion electronegativity [308]. Additionally, subsequent band-gap narrowing from $V_{O^{\cdot\cdot}}$ formation generates visible light photocatalytic activity, as indicated by increased X-3B dye photodegradation [309], suggesting further research possibilities. Furthermore, fluorine doping stabilizes anatase TiO_2 (001) facets [310, 311] possessing greatest photo-reactivity. Also F^- possesses similar ionic size (119 pm) to O^{2-} (124 pm) lowering potential lattice strain, which may improve $TiO_{2-x}:F_x$ stability.

In comparison, iodine doping generates anatase $TiO_{2-x}:I_x$, which provides a band gap reduction resulting from the expected lattice strain on I^- (206 pm) substitution

($I_{O'}$) [312] and inducing <550 nm absorption. Furthermore, subsequent strain removal upon surface iodine doping extends absorption and therefore also the photocatalytic activity to <800 nm [313]. Contrastingly, Liu [313] also detected I^{7+}, possibly resulting in decreased strain (67 pm) for Ti^{4+} substitution ($I_{Ti}^{\cdots\cdots}$).

Additionally, multivalent I^{7+}/I^{-} $Ti_{1-x}O_{2-y}:I_{x/y}$ films were also synthesized, which showed suppression of recombination through electron trapping site generation [314]. Multivalent doping results in the creation of two mid-band gap states; I-O-Ti near the valence band and I-O-I [313] near the conduction band. Both created states effectively decrease $Ti_{1-x}O_{2-y}:I_{x/y}$ band gap size, increasing absorption under visible light irradiation. $Ti_{1-x}O_{2-y}:I_{x/y}$ films also resulted in methylene blue [315], 4-chlorophenol [313] and CO_2 [316] decomposition, indicating greater photocatalytic ability as compared to nominally undoped TiO_2 and therefore suggesting a potential avenue for further research.

1.5 Co-dopant systems

Co-doping provides potential for both electron donor and hole acceptor species incorporation. One dopant typically induces visible light absorption properties and another compensates for lattice defect formation in order to decrease recombination centres [317], both therefore simultaneously improving photocatalytic activity. Additionally, initial dopant inclusion is suggested to favour second dopant introduction [317, 318].

$Ti_{1-x}O_{2-y}:N_y/S_{x/y}$ indicated enhanced visible light photocatalytic activity as compared to separately doped $TiO_{2-x}:N_x$ or $Ti_{1-x}O_{2-y}:S_{x/y}$. Periyat [319] detected N-O species, surface chemisorbed nitrogen and S^{6+} states generating band gap narrowing with highly reactive (001) facet exposures for increased photocatalytic activity [320].

Additionally, Rengifo-Herrera [321] indicated ROS generation on $Ti_{1-x}O_{2-y}:N_y/S_{x/y}$ surfaces with photocatalytic activity being affected by a combination of; the doping nature (N_O· and $N_i^{\cdots}$ and/or S_{Ti} or S_O), the initial surface hydroxylation and the $Ti_{1-x}O_{2-y}:N_y/S_{x/y}$ particle size. Furthermore, mid-band gap S 3p, N 2p and π^*N-O state creation provided visible light excited electrons for the formation of superoxide radicals and singlet oxygen [322, 323], and holes for creating hydroxyl radicals [66],

increasing photocatalytic activity. However, direct hydroxyl radical creation from adsorbed water molecules and holes is indicated to be preferable for *E.coli* colony inactivation [321] in comparison to O_2^- or $^1O_2$ generation from $Ti_{1-x}O_{2-y}:N_x/S_{x/y}$.

Comparatively, $TiO_{2-x}:C_x/N_x$ exhibited increased visible light (<700 nm) [324] photocatalytic degradation of; stearic acid, Bisphenol A, Microcystin-LR and Rhodamine-B dye, as compared to commercial nominally undoped TiO_2 [325-328].

In addition, $TiO_{2-x}:F_x/N_x$ shows greater photocatalytic activity, decomposing 6-hydroxymethyl uracil [329], in contrast to nominally undoped TiO_2, $Ti_{1-x}O_{2-y}:F_y/P_x$ and $TiO_{2-x}:S_x$. Enhanced photocatalytic activity was possibly generated by opposite n and p-type dopants, $N_{O^{\cdot}}$ and $F_{O'}$ respectively, interacting through spatially extended charge transfer. Fluorine dopants induced $V_{O^{\cdot\cdot}}$ formation and subsequent Ti^{3+} mid-band gap state generation with nitrogen (N 2p) mid-band gap state addition generating an excited electron cycle [330]. Furthermore, $TiO_{2-x}:F_x/N_x$ synthesis by Pelaez [331] indicated a 2.85 eV overall band gap, but with increased photocatalytic efficiency, possibly relating to inter-particle electron transfer across heterojunctions between anatase and brookite crystallites. $TiO_{2-x}:F_x/N_x$ films have also been shown to be active in atrazine elimination under visible light irradiation [332, 333]. Additionally, $TiO_{2-x}:C_x/F_x$ has also indicated styrene degradation under visible light irradiation [334].

Also, $TiO_{2-x}:B/N_x$ microspheres have been shown to possess a surface 1.94 eV band gap with visible light absorption extension to 700 nm. Initial boron pre-doping generated Ti-O bond weakening to result in greater nitrogen solubility [335], suggesting synergistic dopant effects.

Furthermore, Wang [336] synthesized triple doped $TiO_{2-x}:C_x/N_x/S_x$, which showed band gap reduction to 2.67 eV with subsequent visible light photocatalytic activity providing 68 % carbamazepine removal in 120 minutes.

Breault [337] synthesized $Ti_{1-x}O_{2-y}:Nb_x/N_y$ which showed a 7-fold greater visible light photocatalytic activity as compared to undoped TiO_2.

Additionally, co-doped $Ti_{1-x}O_{2-y}:Ga_x/D_{x/y}$ films have indicated greater photocatalytic activities through synergistic effects as compared to $Ti_{1-x}O_2:Ga_x$ [179, 317, 338-341]. Song [339] and Li [317] co-doped non-metallic elements (iodine and nitrogen respectively) with resulting films indicating synergistic effects between I 5p or N 2p and gallium-doped charge-compensated $V_O^{\cdot\cdot}$. Deng [341] and Hirano [338] synthesized $Ti_{1-x}O_2:Ga_x/V_x$ and $Ti_{1-x}O_2:Ga_x/Nb_x$ respectively creating p-d hybridization between metal mid-band gap states producing a red-shift in absorption and improving photocatalytic activity. Li [317] synthesized $Ti_{1-x}O_{2-y}:Ga_x/N_y$. Nitrogen inclusion introduced N 2p mid-band gap states, increasing visible light photocatalysis and generating excess $V_O^{\cdot\cdot}$. However, gallium incorporation improved initial $V_O^{\cdot\cdot}$ generation, induced through p-type nitrogen doping, to create additional electron trapping centres. $Ti_{1-x}O_{2-y}:Ga_x/N_y$ co-doped films also showed greater levels of H_2 evolution in contrast to nominally undoped or singly doped TiO_2 films under a water splitting process.

In comparison, Li [318] indicated similarly enhanced synergetic photocatalytic activity on $Ti_{1-x}O_{2-y}:C_y/Mo_x$ generation. Mo_{Ti} sites provided overall band gap narrowing, synergistically extending photogenerated excition lifetimes with surface absorbed carbon.

Furthermore, $Ti_{1-x}O_{2-y}:Cu_x/F_Y$ produced by Leyland [342] showed significant antimicrobial properties under visible light irradiation, reducing *S.aureus* populations. Fluorine incorporation minimized exciton recombination on $F_O^{\prime}$ creation, with charge compensation inducing the formation of $V_O^{\cdot\cdot}$ and Ti^{3+}. Additionally, copper improved oxygen deficient defect concentrations and assisted in hydroxyl radical production at surface regions through a Fenton-type reaction. However, independent of photocatalytic interactions, surface copper ions also generated cell membrane rupture providing antimicrobial activity in dark conditions.

In summary, co-doped TiO_2 generally results in greater photocatalytic activity through synergy typically between organic and charge compensated $V_O^{\cdot\cdot}/Ti^{3+}$ mid-band gap energy states. These mid-band gap energy states, reduce band gaps and

facilitate visible light wavelength absorption. The interplay between non-metal and TiO_2 defects also provides greater exciton pair trapping centres, increasing charge pair lifetimes and ROS formation on reaction with surface oxygen containing groups. Both of which could potentially increase photocatalytic activity, as compared to nominally undoped TiO_2.

1.6 Photovoltaics

Many semiconductors are also used in photovoltaic devices, which exploit identical or similar phenomena to those that underpin photocatalytic activity. Excitons are created from light irradiation, undergo subsequent dissociation and result in excited electron diffusion throughout the semiconductor, creating current. In the case of TiO_2, light conversion efficiencies are typically low with absorption only occurring from light possessing equal or greater energies compared to the semiconductor band gap [30]. Doping can increase absorption efficiency towards visible light wavelengths, but also provides a loss in transparency [343], sometimes limiting the use of the materials towards further layers into the photovoltaic device.

TCO layers provide both an ohmic contact for electron transport and high transparency for light penetration. Therefore, TCO substrates utilized in photovoltaic devices typically possess [344]:

- 80% or greater visible light transparency.
- Resistivity in orders of $<10^{-3}$ Ω.cm [27] for efficient carrier transport.
- Minimal 10^{20} cm^{-3} carrier concentrations for low resistivity.
- n-type conductivity.
- A band gap >3.2 eV to avoid visible light absorption.

Doped TiO_2 and ZnO suggest possession of these properties, providing potential for utilization as cheaper TCO substrates compared to industrially standard 2 x 10^{-4} Ω.cm ITO (tin doped indium oxide) [345]. However, comparatively high resistivities are reported for pure metal oxides with nominally undoped anatase TiO_2 possessing maximum resistivity magnitudes of 1 x 10^{-1} Ω.cm [27]. In contrast,

chemically sensitive wurtzite ZnO possesses a maximum resistivity of 2.35 x 10^{-3} Ω.cm [346]. Therefore intrinsic and extrinsic defects have been utilized to lower resistivity of TCO layers, whilst retaining high transparency.

1.6.1 Dopants and defects

As previously discussed, dopant incorporation can decrease the metal oxide band gap. Therefore TCO efficiency can be improved through generating either donor states near the conduction band minimum or acceptor states near the valence band maximum, dependent on the dopant utilized.

TCO's typically contain significant electron density from donating defects (M_i and $V_{O^{\cdot\cdot}}$) (M = metal) with film growth typically occurring in reducing environments to suppress V_M creation and provide n-type conduction characteristics [345]. $V_{O^{\cdot\cdot}}$ and M_i further generate mid-band gap states just beneath the conduction band minimum [40, 41, 44], both generating electron-rich sources [121] for increasing n-type conduction characteristics. ITO films provide an example of this, with each $V_{O^{\cdot\cdot}}$ trapping two electrons, to further stabilize neighbouring In^{3+} 5s orbitals from oxygen bond removal, generating mid-band gap states 0.03 eV beneath the ITO conduction band [345].

Additionally, recombination rates are directly proportional to lattice defect concentrations with greater electron trapping preventing current conduction and decreasing film current densities. Specifically, recombination is related to deeper traps, significantly resulting from V_M creation [40, 41, 44].

Both dopants and defects also increase charge scattering cross sections versus their neutral lattice counterparts with heavily doped metal oxides undergoing significant intra-grain scattering. This could provide decreased charge carrier mobility [347] and lower electrical conductivity. Comparatively, nominally undoped metal oxides are dominated by scattering at grain boundaries and other crystallographic defects (point defects, dislocations and stacking faults). Scattering is shown to be directly affected by crystalline defect density [348], decreasing the electrical conductivity.

Therefore, an optimal dopant concentration would ideally decrease grain boundary scattering, resulting in greater charge carrier grain boundary tunnelling without intra-grain scattering and increasing the electrical conductivity. 10^{20} cm^{-3} carrier concentrations are suggested [347] as optimal concentrations for decreased grain boundary scattering with negligible intra-grain scattering. Correspondingly, Edwards [349] created a model assuming a parabolic conduction band and doping levels above the Mott Criterion as shown in equation 1.7. Where a_H^* is ground state mean Bohr radius and n_c is minimal dopant concentration.

$$n_c^{1/3} a_H^* = 0.26 \pm 0.05 \qquad \text{Equation 1.7}$$

On satisfying the Mott criterion, metal oxides typically experience an induced composition state transition from semiconducting to metallic and become conductive [350]. However, an optimal dopant balance is required for maximum efficiency, satisfying the Mott Criterion, but minimalizing recombination with dopant incorporation at solid solubility limits. Additionally, barrier layer utilization to passivate surface doped metal oxide layer sites can also decrease recombination rates [351] and increase efficiency.

Single crystalline films or polycrystalline films containing large grains and subsequently minimal grain boundaries are preferable for TCO films [348]. Specifically in TiO_2 films, anatase is preferred over rutile for TCO applications, since it possesses both higher carrier concentration (>10^{21} cm^{-3}) [27] and $V_O^{\cdot\cdot}$ incorporation. For example; in TNO ($Ti_{1-x}O_2$:Nb_x) films [352], anatase generated a strongly hybridized niobium 4d orbital across the conduction band resulting in one electron being transported per Nb^{5+}. Whereas rutile generated shallow Nb 4d impurity states.

However, both greater charge carrier, and $V_O^{\cdot\cdot}$ concentrations increase visible light wavelength absorption, decreasing transparency. Additionally, thicker TCO films tend to possess lower transparency, presenting difficulties in terms of light penetration. A range of specific TCO materials already utilized for photovoltaic applications are discussed below.

1.6.2 Doped TCO materials

Tin doped indium oxide (ITO) consists of a transparent and colourless solid solution typically of around 90 % indium (III) oxide and 10 % tin (IV) oxide ($In_{1.8}Sn_{0.2}O_3$) [344, 345, 353]. ITO possesses a large 4 eV band gap, providing visible light transparency. However, ITO is opaque under UV and near IR irradiation due to band-to band absorption (UV photon electron excitation from valence to conduction bands) and free carrier absorption (IR photon electron excitation within the conduction band), respectively. ITO films typically possess low resistivity values around 2 x 10^{-4} Ω.cm with 90 % transmittance and good chemical moisture resistance. ITO films are also grown in reducing environments, producing significant $V_O^{\cdot\cdot}$ concentrations and increasing electron concentration.

However, ITO layers are fragile and lack flexibility and there is limited supply with an associated high cost of indium. Therefore research has progressed towards synthesizing new TCO materials without indium.

Fluorine doped tin oxide or FTO [353, 354] is an n-type semiconductor, consisting of a transparent and colourless $SnO_{2-x}:F_x$ film, which is typically deposited on glass substrate, as part of the glass manufacturing process [353, 355-357]. In the literature, polycrystalline FTO has been synthesized by Suh [358] through CVD, resulting in a film resistivity of 8.2x10^{-4} Ω.cm with 75 % transparency. Additionally, Proscia [359] and Maruyama [360] utilized atmospheric pressure CVD (APCVD) synthesis routes to produce polycrystalline films with recorded resistivities of 5.92x10^{-4} Ω.cm. Additionally, Kim [353] grew predominately polycrystalline FTO from pulsed laser deposition (PLD), providing a resistivity of 5 x 10^{-4} Ω.cm dependent on oxygen pressures during synthesis. Furthermore, these films additionally showed 87 % visible light transparency, 15 $cm^2V^{-1}s^{-1}$ carrier mobilities and a 4.25 eV band gap.

FTO, unlike ITO, is an inexpensive, chemically and thermally stable material, but possesses greater average resistivity and marginally lower transparency in photovoltaic devices. Furthermore, tantalum, niobium and antimony have been utilized as tin oxide dopants for TCO's indicating high electrical conductivity [361].

Doped ZnO [344, 362-364] namely; $Zn_{1-x}O:Al_x$ (AZO), $Zn_{1-x}O:Ga_x$ (GZO) [365] and $Zn_{x-1}O:Al_x/Ga_x$ (AGZO) [366] were synthesized by Lin [362] and all adopted a hexagonal wurtzite structure with >80 % transparency. GZO with 3 % gallium possessed the best electrical properties (resistivity; 3.18 x 10^{-4} Ω.cm, mobility; 27.8 $cm^2V^{-1}s^{-1}$ and carrier concentration; 11.05 x 10^{20}). This was followed closely by AZO containing 2% aluminium (resistivity; 4.31 x 10^{-4} Ω.cm, mobility; 22.0 $cm^2V^{-1}s^{-1}$ and carrier concentration; 11.09 x 10^{20} cm^{-3}). Finally AGZO incorporated 0.5 % aluminium and 1.165 % gallium (resistivity; 8.14 x 10^{-4} Ω.cm, mobility; 13.5 $cm^2V^{-1}s^{-1}$ and carrier concentration; 6.35 x 10^{20} cm^{-3}).

AZO films are frequently utilized as TCO's [363, 364, 367-369] incorporating an optimal 5 atm% aluminium concentration. However, Maeng [369] proposed a 2.5 atm% optimal concentration with; 2.6 x 10^{19} cm^3 carrier concentration, 4.2 Ω.cm resistivity and a 3.3 eV band gap. In contrast Myong [370], generated a lower resistivity of 6.2 x 10^{-4} Ω.cm in AZO films fourteen years prior with an identical magnitude to ITO. However, as already mentioned, Lin [362] also synthesized AZO films containing 2 % aluminium, further improving electrical conductivity.

GZO films are also studied for TCO applications [371], with GZO grown through CVD by Ataev [372] initially exhibiting a resistivity of 1.2 x 10^{-4} Ω.cm, and thereby equalling ITO film conductivity magnitudes. Further GZO film synthesis by Assuncao [373] and Lin [362] through r.f magnetron sputtering generated resistivities of 2.6 x 10^{-4} Ω.cm and 3.18 x 10^{-4} Ω.cm, respectively. Assuncao also reported 90 % transmittance and Lin reported 27.8 $cm^2V^{-1}s^{-1}$ mobility and 11.05 x 10^{20} cm^{-3} carrier concentrations. Contrastingly, Gabas [374-376] achieved even lower GZO resistivities of: 6.3 x 10^{-4} Ω.cm.

Furthermore, IGZO (Indium gallium zinc oxide) [366] films and other potential zinc oxide film dopants including; sodium [377] and molybdenum [378], were also studied for potential TCO utilization.

However, with indium scarcity and difficulties in generating p-type ZnO, doped TiO_2 is a potential candidate for TCO materials. Nominally undoped TiO_2 is abundant, possesses increased chemical stability [9], a wide 3-3.37 eV band gap [10] for visible

light transparency, and can provide n-type conductivity from $V_{O}^{\cdot\cdot}$ defects [119, 122, 379].

Nominally undoped TiO_2 is typically utilized as barrier or blocking layers at interfaces between metal oxide layers and electrolyte/dye/TCO in DSSC's [380, 381]. Doped TiO_2 should possess greater charge carrier density and therefore conductivity, with an ideal TiO_2 dopant for TCO applications generating:

- Additional charge carriers either directly from dopant addition or indirectly from charge compensation defects, for improved n- or p-type conduction characteristics.
- Negligible effects on film morphology, corresponding to favourable solid solubility conditions with similar substituted ionic size, subsequently reducing strain and grain boundary dopant accumulation.

Correspondingly, previous studies of doped TiO_2 for potential TCO applications are commented on below.

Niobium doped TiO_2 [352] or $Ti_{1-x}O_2:Nb_x$ indicates comparable electrical and optical properties to ITO films including a large refractive index, high infra-red (IR) transmittance and chemical stability in reducing atmospheres [352]. $Ti_{1-x}O_2:Nb_x$ films typically incorporate Nb^{5+} through substitution, generating $V_{Ti}^{''''}$ and releasing electrons with 90 % efficiency ($x \geq 0.06$).

Initially, Furubayashi [382, 383] grew single crystal anatase $Ti_{1-x}O_2:Nb_x$ ($x = 0.002$-0.2) onto $SrTiO_3$ by sol-gel methods followed by hydrogen gas annealing, and resulting in 2.3×10^{-4} Ω.cm resistivity and 97 % transmittance ($x = 0.3$). Additional PLD synthesis on glass generated samples possessing resistivities of 4.6×10^{-4} and 9.5×10^{-4} Ω.cm for polycrystalline and anatase films respectively [384, 385], with 75 % visible light transmittance.

$Ti_{0.94}Nb_{0.06}O_2$ on glass was further synthesized by sol-gel dip coating [112] and sputtering [27]. Dip coating produced highly resistive polycrystalline anatase films (19.3 Ω.cm), after annealing in air and subsequent vacuum (4×10^{-4} Pa) at 550 ^{o}C. Sputtered anatase films achieved 2.3×10^{-4} Ω.cm resistivities and 95 % visible light

transmittance. Contrastingly, sputtered polycrystalline films generated slightly increased 6.4 x 10^{-4} Ω.cm resistivities.

Additionally, Hung [386] synthesized $Ti_{1-x}O_2:Nb_x$ (x = 0-0.52) films from titanium and niobium metal target reactive co-sputtering. Synthesized films were amorphous and insulating, with annealing in hydrogen gas at 600 ^oC generating anatase or mixed phase anatase and rutile morphology as well as conductivity. The pure anatase phase generated a resistivity of 9.2 x 10^{-4} Ω.cm and > 70 % visible light transparency (for x = 0.39 in $Ti_{1-x}O_2:Nb_x$), whereas mixed anatase-rutile phase films showed an increased resistivity of: 1.2 x 10^{-1} Ω.cm. It was suggested that this greater resistivity possibly evolved through increased grain boundary density between different crystallites, highlighting single crystal growth as being preferable for decreased resistivity, allowing less charge carrier deflection.

Furthermore, $Ti_{1-x}O_2:Nb_x$ films were synthesized through ALD by Niemela [206] generating anatase after post-deposition reductive (H_2/N_2 atmosphere) annealing. These $Ti_{1-x}O_2:Nb_x$ films subsequently became conductive after annealing, possessing a minimal 1.4 x 10^{-3} Ω.cm resistivity on 25 % Nb doping, with 1.1 x 10^{21} cm^{-3} charge carrier density and 22 $cm^2V^{-1}s^{-1}$ electron mobilities. However, minimal strain was indicated on $Nb_{Ti}^{\cdot}$ substitution with an increase in the d_{101} interplanar spacing.

Tantalum doped TiO_2 or $Ti_{1-x}O_2:Ta_x$ was sputter grown by Hitosugi [387] and indicated similar film properties as $Ti_{1-x}O_2:Nb_x$. Choi [216] later synthesized several $Ti_{1-x}O_2:Ta_x$ films with varied 1.2-4.9 atm% tantalum, generating anatase with homogeneous $Ta_{Ti}^{\cdot}$ substitution and resulting in charge compensation through V_{Ti}'''' creation.

Furthermore, other metal dopants have also been (or possess potential to be) utilized as TCO's:

- $Ti_{1-x}O_2:Ga_x$ [388] indicated an oxygen stoichiometry dependence in terms of n/p-type conductivity. p-type conduction characteristics were generated from oxygen rich synthesis and holes from Ga^{3+} inclusion. Alternatively n-

type conduction characteristics were created through charge compensating $V_{O}^{\cdot\cdot}$ under oxygen deficient conditions.

- Nickel has potential for TiO_2 doping with increasing Ni^{3+} in NiO (p-type semiconductor) systems lowering resistivity from monovalent atom addition or V_{Ni}'' and $O_i^{\cdot\cdot}$ formation in NiO crystallites [236].
- $Ti_{1-x}O_2:Zn_x$ showed greater carrier concentration and Hall mobility with conduction through greater hole addition [248].
- $Ti_{1-x}O_2:W_x$ [389] showed less promising results as compared to $Ti_{1-x}O_2:Nb_x$ films.

Other TCO's synthesized from doped cadmium [390-392], indium oxides [393, 394] or pure nickel [395] have also been studied for potential TCO utilization.

Overall, commercial issues associated with ITO films has generated research into disparately doped SnO_2, ZnO and TiO_2 for improvement of 2 x 10^{-4} Ω.cm resistivity and 90 % visible spectrum transparency gained from ITO films as TCO's. Unfortunately FTO and Doped ZnO (AZO/GZO) fall slightly short. FTO reported 5 x 10^{-4} Ω.cm resistivity and 87 % transparency. Whilst doped ZnO reported 2.6 x 10^{-4} Ω.cm resistivity and > 80 % transparency, but is chemically unstable in non-neutral environments. However, TNO films provide a reasonable TCO alternative with 2.3 x 10^{-4} Ω.cm resistivity and 97 % transmittance detected.

1.7 Outline of thesis research

In this thesis the following research topics are described:

- Hospital cleaning agent (Actichlor Plus™, Chloraprep™, Stericlean™ and Virusolve+™) exposure effects on photocatalytic activity of Pilkington Activ™ TiO_2 films with respect to basic blue 66 and resazurin ink photodegradation and water contact angle variation on UV light irradiation.
- The ALD synthesis and characterization of the as-grown and annealed nanolaminate doped $Ti_{1-x}O_2:Ag_x$, $Ti_{1-x}O_2:Al_x$, $Ti_{1-x}O_2:Hf_x$, $Ti_{1-x}O_2:Sn_x$ and $Ti_{1-x}O_2:V_x$ (99:1 and 19:1) (Ti:M) films with dopant role highlighted in determining the electrical, morphological and optical properties. Furthermore, photocatalytic properties were determined with respect to

basic blue 66 ink photodegradation and water contact angle variation on UV light irradiation.

- The extended analysis of the photocatalytic $Ti_{1-x}O_2:Sn_x$ (19:1) film properties with respect to basic blue 66 and resazurin ink photodegradation and water contact angle variation on UV light irradiation, subsequent to cleaning agent (Virusolve^{+TM} and Actichlor Plus^{TM}) exposure. Additionally, the photo-killing nature of $Ti_{1-x}O_2:Sn_x$ (19:1) is examined in accordance with *E.coli* colony attachment and colony counting studies.
- The ALD synthesis and subsequent analysis of nanolaminate doped $Ti_{1-x}O_2:Ga_x$ (99:1) and (19:1) films, including further synthesis and analysis of nanolaminate doped Ga-capped $Ti_{1-x}O_2:Ga_x$ (99:1), (74:1), (49:1), (39:1), (32:1), (19:1) and (9:1) films.

Chapter 2: Synthetic and analytical techniques

2.1 Synthetic techniques

Physical and chemical properties of TiO_2 (specifically photocatalytic and conductive) are greatly dependent on synthesis method, with crystallinity and dopant diffusion variation generating activation differences. A range of deposition methods have been used to grow TiO_2 films, with some of the more frequently utilized processes discussed below:

2.1.1 Sol-gel processing

Sol-gel processing is the most frequently reported technique for growing doped/undoped TiO_2 films in the literature [396]. Typically this process involves colloidal solution (sol) generation from converted monomers creating a precursor solution (sol) for an integrated polymer or detached particle network (gel). TiO_2 deposition is then achieved through initial aqueous or alcohol based mixture precursor decomposition, generating a biphasic gel (consisting of solid and liquid phases) across the substrate surface. Drying follows to remove liquid components and a high temperature sintering process favouring polycondensation finishes the synthesis. Both of these processes increase overall processing time.

The resulting TiO_2 layer possesses good conformality, but film thicknesses are only controllable to approximately 1 nm [397], resulting in low or uneven coverage for thinner TiO_2 films. Film shrinkage can occur during drying and sintering (usually 450-500 ^oC for a TiO_2 film of quality comparable to a sample grown by vapour deposition) indicating incompatibility with low temperature fabrication techniques [398]. Low temperature sintering processes have been attempted [396], but again lower quality film synthesis is produced as compared to vapour deposition grown TiO_2 [398].

2.1.2 CVD and related methods

CVD [399-401] is a chemical deposition process incorporating precursor vaporization and transportation to a reaction chamber. Precursor vapours subsequently diffuse across substrate surfaces and can undergo gas phase reactions followed by chemisorption, chemisorption with subsequent reaction, or

decomposition. All reactions generate volatile by-products, subsequently removed through reaction via the flow of gas through the chamber. CVD film synthesis advantageously results in greater conformity and uniformity across uneven substrate surfaces, but pales in comparison to ALD. Many variant CVD processes exist, with some of the more notable processes mentioned below:

- Plasma Enhanced Chemical Vapour Deposition (PECVD) [399] utilizes an identical chemical process to CVD, but increases precursor reactivity towards substrate surfaces by introducing a plasma to the reacting precursor vapour phases.
- Atmospheric Pressure Chemical Vapour Deposition (APCVD) [399, 402] utilizes an identical chemical process as conventional CVD, but at atmospheric pressure.
- Aerosol Assisted Chemical Vapour Deposition (AACVD) [402] utilizes a nebulizer to create an aerosol from solvent dissolved non-volatile precursors with subsequent transport to substrates.
- Direct Liquid Injection Chemical Vapour Deposition (DLICVD) [403] (also known as Atomic Vapour Deposition (AVD)) similarly utilizes non-volatile liquid and solid precursors dissolved into solvent, however, is followed by direct chamber injection above substrates. Non-volatile precursor utilization at high temperatures enhances processing, however, also generates increased impurity concentrations from the solvents usage.
- Combustion Chemical Vapour Deposition (CCVD) [404] (also known as flame pyrolysis) is an open atmosphere, flame based deposition process. Precursor addition to a burning gas near a substrate surface creates highly reactive intermediates, which synthesize a strongly adhered film through efficient substrate reactions. Advantages include process cost effectiveness, controllable thickness through varying process parameters and open atmosphere deposition. However, disadvantages include the incorporation of film impurities and the limitation to predominately oxide deposition.

- Metal-Organic Chemical Vapour Deposition or Metal-Organic Vapour Phase Epitaxy (MOCVD/MOVPE) [405] are similar growth processes that utilize metallorganic precursor chemical reactions in contrast to physical deposition for multilayer growth. Initially, vaporized precursors are combined at elevated temperatures in the reaction chamber. Heated precursors then undergo pyrolysis (decomposition in absence of oxygen), creating a layer of atoms on the substrate surface. Subsequent layer growth progresses through second precursor reaction with the initial layer, and generated by-products undergo gas flow removal. In MOVPE, crystalline films are produced through initial epitaxial growth at the substrate surface. Additionally, MOCVD advantageously provides straightforward multi-layer structure growth.

The final method within the general category of a CVD process is ALD. Since this deposition method is utilized within this research, current ALD technology and possible improvements are discussed in greater detail beneath.

2.1.3 ALD

ALD is a self-limiting deposition method (figure 2.1) [406]. In a typical ALD process, vaporized precursors are sequentially pulsed into the reaction chamber and chemisorb onto substrates or previously chemisorbed surfaces. Additionally, purging of any unreacted precursor or reacted by-products occurs between sequential precursor pulsing, through utilizing an inert gas flow and a vacuum pump. Furthermore, precursor diffusion can occur across substrate surfaces, providing alternative saturation surface reactions that proceed in a step-wise manner to ensure a self-limiting growth process (figure 2.1).

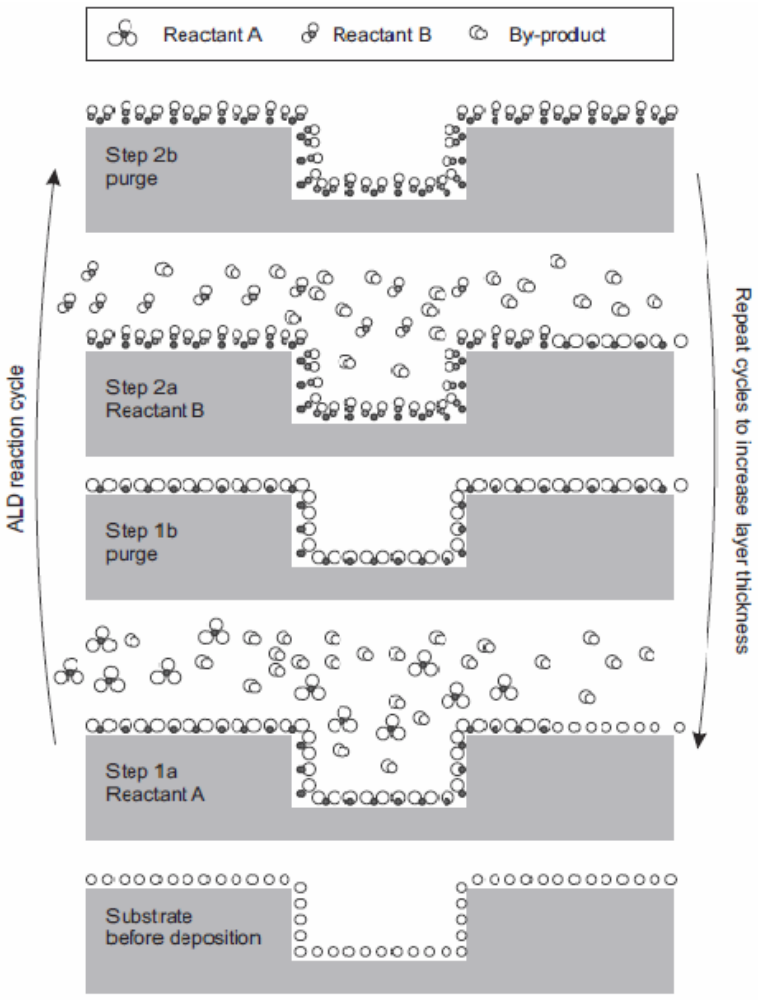

Figure 2.1: ALD process [406]

ALD requires precursors with; sufficient volatility (below decomposition temperatures), no self-reaction or self-decomposition during self-terminating reactions and highly volatile by-product generation for efficient purging [407]. All precursors possess individual substrate temperature ranges for potentially achieving saturated self-limited growth during the ALD temperature window (figure 2.2). Comparatively, temperatures greater than the ALD window can provide either re-evaporation after physisorption or CVD island growth from precursor decomposition. In comparison, decreased temperatures result in either negligible film growth or precursor condensation. Therefore new precursors typically undergo initial deposition experiments, highlighting precursor-specific temperature windows and determining ideal growth rates necessary to result in maximum growth rate per cycle with negligible impurities.

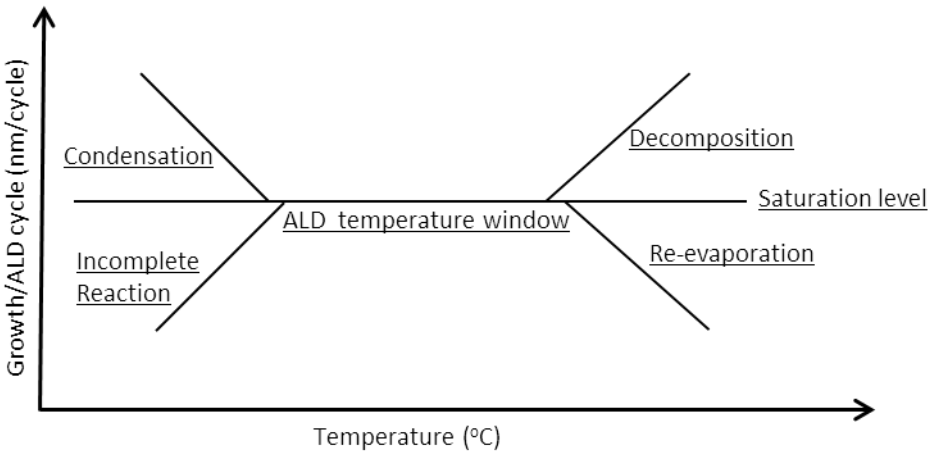

Figure 2.2: ALD temperature window [407]

To summarize, ALD provides highly uniform, low pinhole density and conformal film growth across substrate surfaces. ALD is advantageous with; film thickness control, good reproducibility, relatively low substrate temperature utilization and good lamination on previously generated multilayer structures [406].

However, ALD growth rates are often too slow for high throughput industrial processing, indicating the need for scale up [408]. Furthermore, complications in reactant handling and injection, and problems with uniformity over greater surface areas, arise from scaling up processing in the literature [408]. Several possibilities for the scale up of ALD processes have been identified (figure 2.3):

- Batch ALD – using a single reaction chamber to process multiple substrates with both increased reactant exposure and purging time required.
- Large area ALD – film deposition on a large substrate or a batch of substrates with identical disadvantages as batch ALD.
- In-line and spatial ALD – typically involve back and forth or circular substrate movement through disparate precursor pulsing and purging areas, to ensure full exposure, high film quality and deposition rates. However, throughput is limited and high pressure operation is required for purging.

- Roll to Roll ALD – flexible substrates pass through confined precursor gases, achieving good film uniformity by varying the precursor gas pressures and substrate temperature.

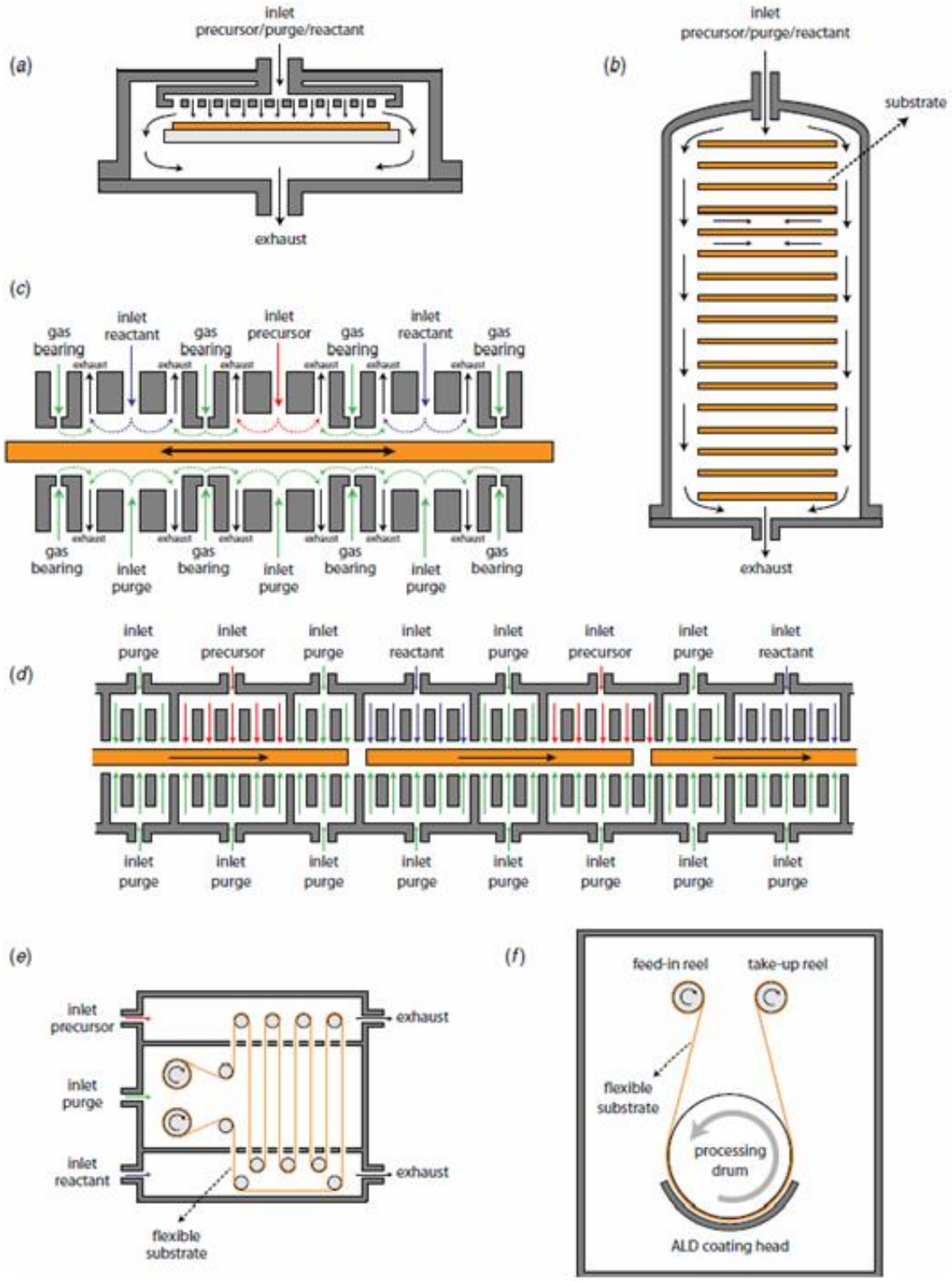

Figure 2.3: Different ways of scaling up ALD for industrial processes: a) Batch ALD, b) Large area ALD, c) spatial ALD, d) in-line ALD, e and f) roll-to-roll ALD [408].

Through utilizing the above mentioned ALD processing variables for scaled up manufacture, large substrates and flexible substrates can both undergo ALD film growth. Doped film growth, however, provides a greater challenge with dopant precursors substituting for bulk film precursors between purges without mixing, extending ALD cycle time and hence generating increased deposition times.

2.1.4 ALD doping cycles

As previously outlined, the ALD process utilizes doping cycles to grow layered materials, for example; metal oxides are typically grown through sequential pulsing of metal and oxidative precursors. However, doped materials can be synthesized though utilizing either a dopant/non-dopant precursor mix or nanolaminate dopant layer substitution.

A heterogeneous dopant/non-dopant precursor possessing the required dopant concentration could potentially either be mixed in the bubbler or from separate bubblers (using a precursor pulsing ratio) prior to transport to the ALD chamber. This doping process provides potential to generate a homogeneously doped film through ALD [409, 410]. However, both dopant and non-dopant precursors would require similar ALD temperature window properties and to also not undergo vapour phase reactions with each other.

In contrast, nanolaminate dopant layer substitution occurs through either cationic or anionic (figure 2.5) dopant precursor cycle substitution of a regular ALD pulse (figure 2.4). These dopant precursor pulses are substituted at set ratios (dopant cycles per ALD cycle), dependent on eventual doping concentration required [163]. Therefore a near-complete nanolaminate dopant monolayer can be generated, dependent on a sufficient dopant precursor residence time (ALD pulse time before chamber purging). However, on annealing, smaller dopant ions can diffuse throughout lattices to occupy interstitial sites, resulting in greater dopant ion distribution [411].

Within this research, cationic dopant growth cycles have been periodically utilized to substitute titanium growth cycles (figure 2.5). Additionally, a subsequent oxygenating precursor pulse is utilized to supposedly create a nanolaminate dopant

oxide layer specifically incorporated into $Ti_{1-x}O_2:M_x$ lattices and thus induce the correct surface conditions for further titanium precursor chemisorption. However, subsequent $Ti_{1-x}O_2:M_x$ film annealing would potentially vary expected dopant location.

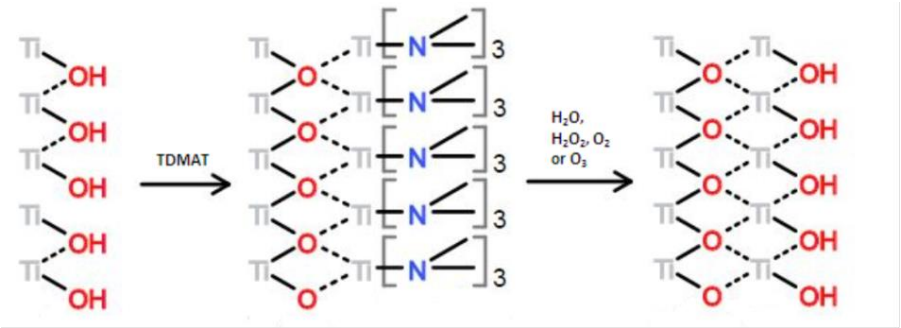

Figure 2.4: Regular ALD cycles for a metal oxide synthesis (namely TiO_2 using TDMAT (tetrakis(dimethylamino)titaniumIV) and an oxidative precursor) [412]

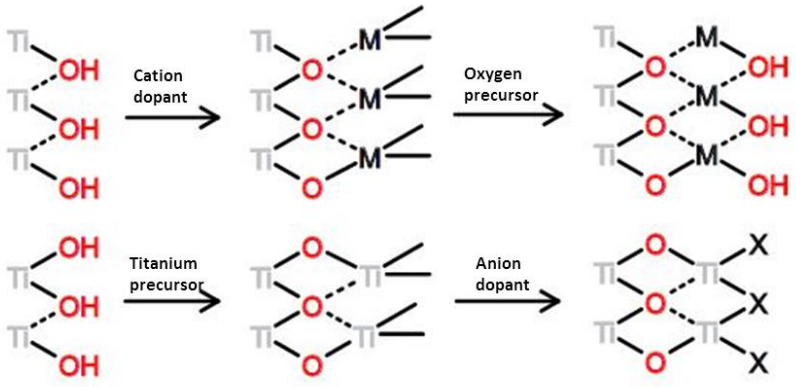

Figure 2.5: Nanolaminate substitutional cation and anion doping cycles for synthesizing a doped TiO_2 film [205, 413]

By varying the precursors, temperatures and residence times, it is possible to change the doped film constitution. Insufficient residence time, sterically hindering "bulky" precursors and low temperatures would not generate full dopant monolayer growth. Therefore more dopant pulses are required to ensure correct ratio percentages, which would also provide increased dopant distribution. In contrast, longer residence times and the use of less sterically hindering precursors can ensure complete monolayer coverage and therefore the required nanolaminate dopant layer. Subsequent amorphous film annealing at elevated

temperatures provides the required energy to increase dopant diffusion throughout the film matrix, as discussed later.

In contrast, doped film synthesis in sol-gel or CVD processes typically occurs by previously mixing required precursor (dopant and non-dopant) concentrations, prior to film growth. CVD or sol-gel processes subsequently provide greater dopant distribution throughout the films. In addition, CVD processes suggest increased dopant surface concentrations [414].

Therefore, ALD has been utilized in this research as the deposition method of choice with TiO_2 cationic nanolaminate doping provided through substitutional deposition. ALD was chosen predominately due to its potential batch processing capabilities, conformality [415], controllability [166] and repeatability towards film growth across varied, high aspect ratio substrates [416] in contrast to alternative deposition and doping techniques.

2.1.5 Annealing

In general, annealing is utilized to modify the physical and/or chemical material properties through elevated heat treatment. This typically results in the onset of crystallinity [417] and encouraging dopant or impurity diffusion [418, 419] or impurity removal [420].

In this work annealing of TiO_2 is utilized to induce anatase formation (≤550 ^oC) within previously deposited TiO_2 films [162]. Therefore, heating and maintaining amorphous TiO_2 above the recrystallization temperature (≤220 ^oC), provides sufficient energy for Ti-O bond cleavage and subsequent atomic migration, eradicating defects. In addition, slow heating is beneficial in terms of homogeneous nucleation and crystallite generation, reducing grain boundary concentrations and promoting preferable single crystal nucleation [162, 421].

Annealing also generates thermally stable crystalline structures (rutile) at higher temperatures (≥550 ^oC) [422], reduces disorder [106], and removes film impurities [106]. However, smaller dopant ions (as purposely incorporated impurities) can diffuse throughout the TiO_2 film via substitutional or interstitial sites to create an

increasingly homogeneous film. Additionally, smaller dopant ions can also undergo surface or grain boundary aggregation [423] developing large dopant oxide areas in the bulk TiO_2, blocking charge carrier diffusion. Furthermore, utilizing oxidizing or reducing atmospheres during annealing can alter the bulk to surface oxygen diffusion gradients, providing variations in film defect concentrations [114].

In this research, annealing of TiO_2 and doped TiO_2 films at 400 ^oC in air was attempted to provide both anatase crystallite growth and high bulk oxygen defect concentrations ($V_{O^{\cdot\cdot}}/Ti^{3+}$), designed to influence photocatalytic activity. For this procedure a Thermolyne^{TM} Benchtop 1100 ^oC Muffle Furnace was used, set typically to 400 ^oC, for up to two hours in air. A closed system was used at atmospheric pressure.

2.2 Analytical techniques

The specific analytical techniques undergoing utilization here are summarized in the following chapters. Each summary is not meant to be comprehensive and therefore only provides limited information on technique; theory, methodology, specifications utilized and specific measurements made. Comparisons between differing techniques are also discussed relating to subsequent research chapters.

2.2.1 Grazing Incidence X-Ray Diffraction (GIXRD)

GIXRD determines the crystalline or amorphous structure possessed by a film and specific crystalline structure/s present [424]. This is accomplished through mounting and subsequent alignment on a goniometer with further X-ray bombardment across a broad 2ϑ range identifying specific crystalline structures through detected reflections.

Crystals are defined as “regular atomic arrays” and generate seven unique single unit structures, stacked indefinitely along three principal directions (x, y and z) creating fourteen possible bravais lattices [425]. X-rays (electromagnetic radiation waves) strike atomic electrons in crystal structures producing secondary spherical waves (elastic scattering). A regular spherical wave array is fabricated by regular symmetrical crystal atomic arrays possessing specific d-separations between diffracting miller planes. Additionally, waves undergo both destructive interference

and constructive addition, as determined by Bragg's Law (equation 2.1) [425] with d corresponding to spacing between miller planes, ϑ = beam incident angle and λ = incident beam wavelength.

$$2d\sin\theta = n\lambda \qquad \text{Equation 2.1}$$

Constructive inference occurs in directions with length difference (2dsinϑ) equal to a beam wavelength multiple. Subsequently, the 2ϑ angle deflects incoming beams with crystalline material producing a reflection spot on detection. Crystalline material further provides a regularly spaced spot (reflections) diffraction pattern, observed at different sample rotations through 2ϑ, as determined by material electron density [425]. Furthermore, graphed data peaks therefore correspond to certain crystalline Miller planes within films.

In the presented research, GIXRD is utilized to determine specific crystalline phases (anatase, rutile or brookite) of undoped and doped TiO_2 films. Typically, TiO_2 anatase indicates greatest photocatalytic activity potential with a predominant 101 miller plane peak occurring at 25 ^{o} 2ϑ [424]. Additionally, peak broadening or relocation on annealing or within doped TiO_2 films would suggest alternative film structures and could be indicative of increasing photocatalytic activity, relating to the ART [37, 426, 427].

In this research GIXRD was performed using a XpertPRO PANalytical XRD machine, with scans typically between 20-60 ^{o} 2ϑ and utilizing; rocking curve, 30 beam intensity for alignment, 45 beam intensity for measurement and a Cu/Ni 0.2/0.02 nm manual attenuator. Furthermore, Si<100> substrate samples were aligned to unit cell (100) Si 004 peak.

2.2.2 Scanning Electron Microscopy (SEM)

SEM measurements were utilized to determine surface morphology, estimate film thickness and highlight surface features or structure (smooth/granular). SEM is achieved via the use of focused electron beam, which performs a raster pattern scan of films, exciting atoms to emit electrons, with higher tilt (angle between electron beam and film surface) resulting in increased emitted electrons.

Subsequently, the emission intensity from the scanned areas is used to create an image. After image generation, the line measurement function can estimate film thickness with tilt and cross section corrections.

In the research performed here, glass based substrate insulating properties can affect the images, resulting in surface charging and other image faults [428]. However, negating charging effects through gold or gold/palladium alloy sputter coating is possible [429]. Furthermore, TiO_2 film thickness estimates, morphology and unusual surface structure variances between disparate samples characterise possible favourable growing conditions and film crystallinity [19].

In this research, the following conditions were utilized on a Quanta 650 SEM, which are identical for EDX. Images were produced at 1.5 nm resolution, with a 30 kV beam power and 2.5 a.u spot size for SEM, and a 20 kV beam power and 5 a.u spot size for EDX. For compositional data from EDX, INCA software was utilized with peaks compared against a cobalt standard.

2.2.3 Energy Dispersive X-ray spectroscopy (EDX)

EDX occurs through stimulating X-ray emission by electron beam excitation of an inner-shell electron, creating a hole which is subsequently filled by a higher energy outer-shell electron. The energy disparity between both levels involved generates emission of X-rays with emitted X-ray energy and intensity providing elemental characterisation. Subsequently, X-rays produce a signal at the detector, undergoing conversion into a voltage, conveyed to a pulse processor for measurement and subsequently sent to an analyser. The analyser then displays voltages in graphical format with manually assignable peaks, previously standardized with certified cobalt [430].

However, analysis of small sample volumes containing an even smaller volume of active film under examination typically results in signals being dominated by substrate features [431]. This is particularly applicable for the work described here, where the presence of species at dopant concentration levels in films of thickness between 10 and 40 nm has been investigated. Therefore an alternative method was required for the present research as described in the following section.

Additionally, using EDX on the TEM would be particularly unsatisfactory for the study of Ga^{3+} doping (see chapter 6), since a Ga^{3+} FIB beam is used to prepare the TEM sample, generating a significant concentration inaccuracy [432]. Therefore depth profiling XPS (as described in the following section) was solely utilized here in order to provide more reliable estimates of dopant concentration and location.

2.2.4 Transmission Electron Microscopy (TEM)

TEM involves the transmission of an electron beam through a sample thinned by using a focused ion beam system (FIB) with the resulting diffracted transmitted electron beams producing images [433]. Typically, diffractive electrons are focused using an objective lens and recombined to generate an image, namely the electron diffraction pattern. The deployed electron beam also results in ionisation of the target atoms, giving rise to so-called secondary electron emission and also X-ray emission. The analysed emitted X-ray energies can further reveal sample composition [434], known as energy dispersive analysis of X-rays or EDX.

TEM advantageously provides greater resolution (≈1 Å) compared to SEM (≈10 nm), with TEM typically distinguishing internal crystalline atomic columns and SEM utilized more frequently for the analysis of sample surface composition and morphology. Furthermore, HRTEM (high resolution transmission electron microscopy) can be performed under conditions to provide individual atomic resolution. Therefore HRTEM is particularly advantageous for defect or disordered structure determination [433]. However, TEM possesses significant limitations:

- An assumption of similarity throughout the films studied, based on minimal observational area utilization and relying on prior poorer resolution technique examination across greater areas.
- Difficult interpretation of a 2D transmission image formed from a 3D structure [434], however, electron tomography may be used to create a 3D image through utilization of an image sequence at different tilts.
- Damage from ionizing electron beam radiation may occur, with damaged regions appearing as brighter regions following bombardment. Such effects are exacerbated on utilization of greater voltages and exposure times.

However, this type of damage can be sometimes offset using computational image enhancement methods and by utilization of alterative electron sources and detectors.

- Observe different atoms with similar atomic size can be difficult in a typical TEM system. An example of this applies to present work with vanadium doping of TiO_2, see chapter 4.

Despite these limitations, TEM was utilized in the research described here to provide an accurate estimate of TiO_2 film thickness, and to gauge film morphology (polycrystalline anatase or amorphous).

In the work described here, a FEI Quanta 3D 200i Dual Beam Focused Ion Beam (FIB) microscope was utilized. Protective layers of TEOS (tetraethyl orthosilicate) and $W(CO)_6$ (tungsten) deposited using electron beam-induced decomposition. Platinum was deposited from methylcyclopentadienyl(trimethyl)platinumIV by using electron beam induced deposition. Electron beam induced deposition was performed at 5 kV 5.5 nA for both TEOS and $W(CO)_6$, whilst ion beam induced deposition of platinum occurred at 5 kV 1.4 nA. The electron source was a tungsten filament emitting electrons via thermionic emission. The ion beam source was gallium (Ga^{3+}) and was initially used to polish surfaces at 30 kV 100 picoamps on both sides of the lamella. Further polishing at 5 kV 48 picoamps until the lamella were under 100 nm thick, which is the typical requirement for TEM imaging.

The TEM system used in these experiments was a JEOL 2100 TEM system, equipped with a LaB6 filament electron source, operated at 200 kV. A Gatan double tilt sample holder imager was used giving a max resolution of: 0.21 nm. The system calibration was achieved using the MAGICAL TEM standard, performed by Dr Patrick Carolan and Dr Micheal Schmidt.

2.2.5 Raman Spectroscopy

Raman spectroscopy typically provides information on the nature of the vibrations that occur within a sample from a change in polarizability. Subject to TiO_2-based materials here, Raman spectroscopy reveals phonon spectrum nature of the

material, which can undergo variation with crystalline type and degree of crystallinity [435].

Typically, visible/near IR wavelength high intensity monochromatic light radiation passing through a TiO_2 film induces an oscillating polarization in the electron cloud. This is sequentially modified by the vibration in question to create an excited "virtual" electronic state. Subsequent virtual state "emission" involves the system relaxing to either a higher excited vibration state than the initial (ground) state (Stokes) or a lower vibrational state (anti-Stokes) [436]. Although adequately explained by the virtual state description, in reality Raman is a scattering phenomenon without direct light absorption.

Furthermore, Raman-scattered photons emerge at either higher (anti-Stokes) or lower (Stokes) energies, as compared to the energy of the exciting radiation, which itself appears in the form of Rayleigh (elastically scattered) radiation. A monochromator subsequently collects the Raman-scattered electromagnetic radiation, filtering out the Rayleigh scattering and dispersing either Stokes or anti-Stokes emitted photons onto a detector.

In the research described here, Raman spectroscopy was utilized in to study both undoped and doped TiO_2 films, typically focusing on the phonon spectrum as a measure of type and extent of crystallinity. This was feasible as both anatase and rutile are known to exhibit six or four Raman active modes, respectively [1]. Anatase modes are labelled as: $A_{1g} + 2B_{1g} + 3E_g$ and rutile modes as: $A_{1g} + B_{1g} + B_{2g} + E_g$ with labels referring to symmetry of modes in question.

The experiments described here utilized an Invia Reflex Micro Raman Renishaw in backscattering mode with a 514 nm argon ion laser, focused to 1 μm spot size and possessing 1.5 mW in terms of power. Raman measurements were performed by Dr. Mircea Modreanu.

2.2.6 X-ray Photoelectron Spectroscopy (XPS)

In this work, TiO_2 film elemental compositions, empirical formulas and chemical and electronic states to a depth determined by photoelectron escape depth and inelastic mean free paths, were typically measured by XPS [437].

XPS operates via irradiation of a sample with an X-ray beam of known wavelength, producing photoelectrons through the ionisation of electrons in core levels. These photoelectrons may be subsequently emitted from the sample and analysed with respect to possessed energy.

As the X-ray wavelength is known (E_{photon}) and emitted electron kinetic energies are recorded ($E_{kinetic}$), electron binding energies ($E_{binding}$) are generated (Equation 2.2).

$$E_{binding} = E_{photon} - (E_{kinetic} + \phi) \qquad \text{Equation 2.2}$$

In equation 2.2, work function (Φ) depends on the spectrometer and is a known parameter. Therefore by electrostatically measuring the kinetic energy of the electron, the exact binding energy can be calculated, assuming that the incident X-ray photon energy is known.

Individual elements possess specific binding energies associated with electrons in various energy levels, generating characteristic peak spectra on collection. Binding energies directly correspond to atomic electron configurations (1s, 2s, 2p, etc.) and peak intensities correlate to detected elemental concentration, which may be further converted into atomic percentages [438]. However, hydrogen and helium are not detected through XPS analysis [439].

Typically, generated XPS spectra possess variation in peak positions arising from the following phenomena:

- Peak energy variations or shifts are often detected from identical core levels but where a chemically disparate environment exists for the target atom. For instance, XPS energy peak energy will shift by approximately 1 eV per unit change in oxidation state. Peak position is also influenced by the hybridization nature of the orbital in question. For example, the increase in

binding energy detected between carbon-carbon: 284.8 eV, carbon-oxygen: 286 eV and oxygen=carbon-oxygen: 288 eV bond electrons, correlates to increasingly higher energy required to eject a 1s electron from the carbon atom in disparate environments [440, 441].

- Peak positions may also be influenced by spin-orbital coupling with doublet and triplet peaks, particularly for photoelectrons originating from p, d and f orbitals. For example: Ti_{2p} presents two spin coupling modes $2p^{1/2}$ and $2p^{3/2}$ creating a doublet of doublet in a 2:1 size ratio [418].
- Auger peaks also complicate XPS spectra, originating from secondary electron emission on some core hole-filling internal relaxation events [437].

Differing XPS parameters are utilized for either bulk or surface analysis. Bulk depth profiling occurs via utilization of an argon ion beam (2-4 keV) or an argon plasma cluster (5-10 keV) [442, 443] to etch surfaces and expose bulk material for analysis. This generates elemental identification and relative atomic concentrations as a function of increasing sample depth. However, interactions with positively charged argon ion beam or cluster etching can alter the chemical and electronic states [444, 445]. Contrastingly, surface angled XPS operates through reducing the X-ray beam surface irradiation angle to simultaneously decrease escape depth and increase the sampled surface area. This creates an analysis limited to surface and near surface regions only [437].

In the research presented here XPS spectra were measured by Dr.Fathima Laffir at MSSI Limerick. The instrument used was a Kratos Ultra DLD spectrometer, operating at a sample temperature of 20-30 ^{o}C. The X-ray gun was a monochromated Al Kα, operating at; 1486.58 eV 150 W (10 mA, 15 kV). The pass energy was 160 eV for survey spectra and 20 eV for narrower, higher resolution scans. The step size employed was; 1 eV for survey scans and 0.05 eV for all other regions. The dwell times used were 50 ms for the survey scans and 100 ms for all other regions. Typically, 12 sweeps were recorded for every survey scan and 5-40 sweeps for high resolutions. Calibration of the system was achieved by charge referencing to the C 1s line at 284.8 eV. Other spectra were collected in the direction normal to the surface. XPS detection limits were estimated at 0.1 atm%. A

quantitative analysis mode was used for both survey and high resolution spectra undergoing Ar^+ sputtering. The analysis areas were: 1 mm^2 with 10 nm depth penetration. During data processing, synthetic peak construction (mixed Gaussian-Lorenzian type) and peak fitting in narrow region spectra were utilized, alongside a Shirley type background. Relative sensitivity factors (RSF) values were used for individual peaks from CasaXPSlibrary containing Scofield cross sections.

2.2.7 Secondary Ion Mass Spectroscopy (SIMS)

SIMS is a sensitive, high vacuum ($<10^{-4}$ Pa), but destructive analysis technique to measure the chemical composition of a surface or bulk sample of material [446]. A signal is generated through firing a focused primary ion beam (usually electron ionized noble gases: Ar^+, Xe^+, oxygen; $^{16}O_2^+$) [446] towards a surface at an energy of several keV, which sputters the target region. A representative fraction of sputtered species (ejected secondary ions) undergoes mass spectrometric detection to generate chemical profiles versus average depth, incorporating sample surface removal with ion beam exposure. SIMS typically possesses detection limits of ca. 10^{12}-10^{16} atoms cm^{-3} for most elements, but the sensitivity is process dependent, requiring the use of calibration standards for reliable measurements [447].

Furthermore, SIMS processing can either be dynamic or static [446]:

- Dynamic SIMS utilizes a raster scan pattern, where the surface ion beam sputtering removes several layers to provide fragmented species, including secondary ions which are detected using mass spectrometry. However, the process involves considerable disruption of sputtered surface layers and so reliable compositional estimates of nanostructured layers are difficult to achieve.
- Static SIMS utilizes a slow removal of surface layers under less damaging conditions providing suitability for surface or near surface analysis.

For the research detailed here, dynamic SIMS was utilised to provide depth profile information regarding a range of doped and undoped TiO_2 samples.

All SIMS spectra presented in this thesis were measured by Dr.Alison Chew at Loughborough Surface Analysis Ltd, using a DektakXT Stylus Profiler. O^- and Cs^+ were the primary ion species used with 10 keV energy. For O^- utilization; a 10 nA current, 125 µm raster size, positive secondary ions, a 10 µm analysed area and No 2 contrast aperture were all used. For Cs^+ utilization, a 20 nA current, 100µm raster size, negative secondary ions, 30 µm analysed area and No 3 contrast aperture were all used. A 150 µm transfer lens and 250 mass resolution were also utilized.

2.2.8 UV/Visible light spectrophotometry and Tauc plot

Typically, light incident on a sample can provide absorption (A), reflectance (R) and transmittance (T) processes, which are equatable to both emitted light intensity (I) and light intensity irradiation (I_o). Most films also produce scattering, but to a first approximation this can be often neglected for samples appearing highly transparent. Furthermore, as indicated in equation 2.3, the percent absorbance can be determined from a rearrangement of the Beer-Lambert law. The Beer-Lambert law reveals an exponential relationship between light intensity before (I_o) and after (I_t) passing through the sample, in relation to the molar absorptivity (ε), concentration (c) and pathway length (l).

$$100\% = R + T + A$$

$$I_t/I_0 \times 100 = \%T$$

$$A = \log(\%T/100) = \varepsilon cl \qquad \text{Equation 2.3}$$

As previously discussed, pure undoped TiO_2 is a transparent wide band gap semiconductor (3-3.3 eV), only capable of absorbing UV light. In the research presented, accurate determination of band gap for various undoped and doped TiO_2 samples was achieved by utilizing the Tauc plot approach. Tauc plots have been utilized to estimate band gap size to an accuracy of 0.001 eV [448]. To generate a Tauc plot, it is necessary to calculate the absorption coefficient (α) as shown in equation 2.4. Equation 2.4 [448] is reliant on the bandgap energy (Eg), the transition nature (n), the light wavelength (hv) and the individual film thickness (x).

$$(\alpha h\nu)^{1/n} = C(h\nu - Eg)$$

$$I_t = I_0 e^{\alpha x},\ I_t/I_0 = T$$

$$T = (1-R)^2 e^{\alpha x}$$

$$Ln(T/(1-R)^2 = \alpha x$$

$$(Ln(T/(1-R)^2)/x = \alpha \qquad \text{Equation 2.4}$$

Once the values for the expression $(\alpha h\nu)^{1/n}$ have been calculated, further analysis subsequently depends on the nature of the material in question in terms of correct choice of n. For a direct band gap material n = ½, whilst for an indirect band gap material n = 2.

In relation to the work presented here, UV/visible spectroscopy was utilized to measure film transmittance. Additionally, reference background measurements were recorded from bare substrates (Vitreosil®077 optical fused quartz (chapters 4 and 6) or coring micro slide plain glass (chapter 6)) for subtraction from spectra generated for various substrate/film combinations.

Furthermore, anatase TiO_2 possesses both indirect and direct band gap contributions [35]. So appropriate fitting usually corresponds with values closest to typical 3-3.2 eV range, especially for low values of film thickness (<40 nm). However, indirect TiO_2 contributions are unfavourable, occurring at higher band gap [1] and also requiring additional phonon momentum.

In this work an UV-2401PC Shimadzu spectrometer was utilized. Wavelength range of 190-900 nm, resolution of 0.1 nm, spectral bandwidth of 2 nm, wavelength repeatability ±0.1 nm and wavelength accuracy of ±0.3 nm with a medium wavelength scan speed. A 50 W halogen lamp (2,000 hours life) and a D2 lamp (500 hours life) were utilized with a light source lamp switching between 282 nm and 393 nm and having less than 0.015 % stray light at 220 nm and 340 nm. A photometric double-beam, direct ratio system with dynode feedback was used, capable of measuring the absorbance, reflectance, transmittance and energy of

samples across a photometric ranges for absorbance: 4-5 %, transmittance: 0-99.9 % and reflectance: 0-99.9 %. Photometric accuracy of: ±0.002 for absorbance values of 0-0.5, ±0.004 for absorbance values of 0.5-1 and ±0.3 % for transmittance values of 0-100 % with a NIST 930D filter. Photometric repeatability of: ±0.001 for absorbance values of 0-1 and ±0.1 % for transmittance. Baseline correction is selectable with storage in firmware, including a baseline flatness within absorbance values of ± 0.001, excluding noise with a 2 nm silt width and SLOW wavelength scan speed. Less than 0.0004 absorbance drift per hour.

2.2.9 Water Contact Angle Measurements

Water contact angle measurements are used to probe the "wettability" of a solid surface by a liquid according to Young's equation in equation 2.5 [449].

$$\gamma_{SG} - \gamma_{LS} - \gamma_{LG}\cos\theta_c = 0 \qquad \text{Equation 2.5}$$

In Young's equation, (equation 2.5 and figure 2.6) (γ_{SG}), (γ_{LS}) and (γ_{LG}) correspond to the solid-gas, solid-liquid and liquid-gas interface energies respectively with (θ_c) generated from the angle between a surface (γ_{LS}) and a water droplet tangent (γ_{LG}).

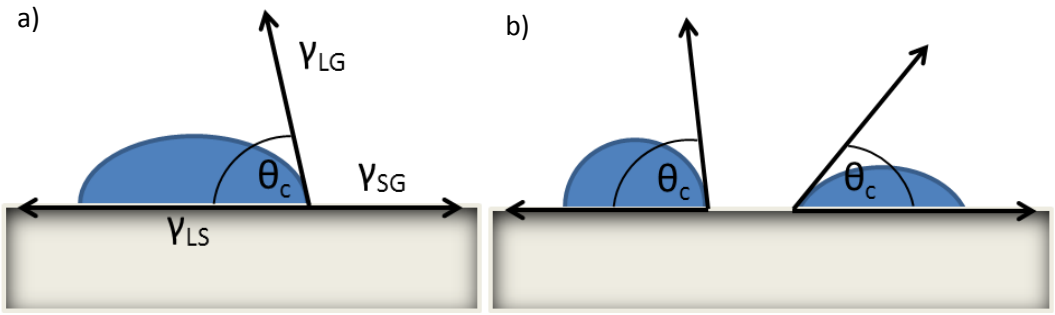

Figure 2.6 a and b) Young equation diagram and hydrophobic/hydrophilic contact angles

Surface wettability corresponds to water droplet spreadability across film surfaces with increased or decreased spreading indicating greater hydrophilicity (≤90 °) or hydrophobicity (>90 °), respectively. In particular, complete surface wetting (<15 °) is known as superhydrophilicity, with superhydrophobicity (>150 °) corresponding to near complete surface un-wetting. Superhydrophilicity typically corresponds

with increased run-off capability [292, 450] a feature which is used to enhance the rinsing away of degraded pollutant residues from self-cleaning TiO_2 surfaces.

Typically hydrophilicity (similar to photodegradation) corresponds to significantly high surface ROS concentrations [451]. TiO_2 surfaces irradiated with UV light commonly exhibit hydrophilicity [452], which is created through either:

- Surface lattice oxygen trapping of photogenerated holes diffusing from bulk TiO_2, weakening bridging Ti-O binding energies, dissociating surface water molecules and generating surface hydrogen bonding.
- Electron surface diffusion creating double $V_{O^{\cdot\cdot}}$ at oxygen bridging sites, increasing surface affinities towards surface water molecule dissociation, further generating both hydroxyl groups and hydrogen bonding.

Therefore, significant surface ROS generation induces hydrophilicity and also indicates possible photocatalytic activity [453]. Additionally, in the context of this present research both hydrophilicity and photocatalytic activity may be increased by the inclusion of specific dopants into TiO_2. Furthermore, after submersion in darkness for a significant period, the UV light-activated surface wettability typically reverts to the pre-irradiated state [454]. This indicates repeatable ROS generation and therefore also potentially continued activity towards photomineralization.

A standard measurement method (ISO/WD 27448-1) for water contact angle measurements utilizes a goniometer. In this method, water droplet application to the sample surface occurs through a perpendicular syringe. The droplet shape on the surface is examined utilizing droplet image processing software, which also utilizes Young's equation (equation 2.5), to derive angles between the both tangents to the surface and water droplet, respectively. Average surface contact angles are formulated through either;

- Proportionally increasing the droplet size with resulting contact angle measurement (maintaining identical surface contact area and minimizing hysteresis) [455].

- Or (as in this research) measuring multiple contact angle droplets, indicating film surface growth homogeneity across surfaces.

However, water contact angle measurements are significantly affected by both; relative humidity [456] and surface roughness [457]. Relative humidity can alter initial water droplet spread and increase evaporation e.g. low relative humidity. Therefore, it is essential to operate under reproducible conditions of relative humidity, with conditions typical of a normal room environment. Additionally, film surface roughness also modifies surface area wetting characteristics. Dependency on this roughness factor, suggests that smoother or rougher films typically generate increased hydrophilic or hydrophobic natures, respectively.

In the present research the SCA20 software system was utilized for contact angle measurements. Both 1.0 µL water droplet sizes and 1.0 medium droplet speed were utilized with seven contact angles measured. Two outlying contact angles were removed to result in an average of five measurements. Typically, contact angle measurements were performed on samples before and throughout UV light irradiation (at 30 and 60 minutes irradiation). Samples were then situated in darkness for a week (10800 minutes) to evaluate Pilkington Activ^{TM} hydrophobicity rejuvenation after UV light irradiation.

2.2.10 Organic Photocatalytic Degradation Techniques

The use of various methods of surface organic degradation to determine the degree of photoactivity in the material is diverse and reported extensively in the literature. Unfortunately, most studies occur without consideration of appropriate standardization [286, 458-460]. Stearic acid decomposition, ink/dye photodegradation and microbiological sanitization undergo frequent utilization. However, these studies typically present disparate light irradiation, degradation material and photocatalyst or degradation material concentrations. Photodegradation techniques usually specify a particular material degradation process, but have generated a number of comparability issues.

However, the following sections attempt to summarize, compare and contrast the range of TiO_2 photocatalytic surface degradation techniques, highlighting specific advantages and disadvantages, as well as present standardization.

2.2.10.1 Stearic acid decomposition and Fourier Transform Infra-Red spectroscopy (FTIR)

Stearic acid ($C_{18}H_{36}O_2$) is an elongated carbon chain molecule with carboxyl group termination, which undergoes mineralisation into CO_2 and H_2O on UV/visible light activated TiO_2 [267, 461, 462]. The basic mineralisation procedure initially involves stearic acid dissolution in methanol, spin-coating for uniform coverage and drying across a TiO_2 film surface. Subsequently FTIR analysis is used to monitor photocatalytic degradation on UV/visible light exposure.

FTIR spectroscopy monitors the stearic acid degradation by following the rate of disappearance of the IR bands corresponding to the CH_3 asymmetric stretching mode (2958 cm^{-1}) and the CH_2 asymmetric and symmetric (2923 and 2853 cm^{-1}) C-H stretching modes during irradiation. This quantifies the photodegradation process and provides data suitable for reliable degradation rate calculations. Stearic acid photomineralization proceeds through photogenerated TiO_2 surface ROS, initially degrading stearic acid molecules into smaller carbon chains and further into CO_2 and H_2O with complete photomineralization.

However, to date, only very minimal attempts to standardize this technique are found in the literature. Examples of parameters that widely vary between analyses include; sample size, spin coater rotational frequency and stearic acid concentration [16, 463]. As a consequence, samples studied often consist of films of widely varying thicknesses, providing difficulties on comparing experiments performed in disparate laboratories. Another rarely mentioned disadvantage influencing a range of studies performed in the manner described is the “coffee-mug” effect [464] resulting from drying after spin coating deposition. The “coffee-mug” effect easily results in non-uniform deposition thicknesses with stearic acid accumulation into ridges across TiO_2 surfaces generating differing

photodegradation rates. However, the “coffee-mug” effect could be negated through utilizing different spreading/drying techniques, such as dip coating [460].

2.2.10.2 Photocatalytic dye/ink degradation

Photocatalytic dyes are organic coloured compounds indicating oxidative or reductive degradation on photo-irradiation with UV light in the presence of an activated photocatalyst (e.g. UV light irradiated TiO_2). Typically, photocatalytic dyes undergo three degradation mechanisms; through direct (exciton-based) hole oxidation, direct (exciton-based) electron reduction or exciton synthesized hydroxyl group attack. These degradation mechanisms result in disparate photocatalytic degradation rates amongst differing dye family functional groups, for example; azo-dyes [465, 466], triphenylmethane and anthraquinone [467, 468].

However, photocatalytic degradation is also dependent on a number of other factors such as surface TiO_2 adsorption characteristics [469], the light source deployed [468] and the presence of any contaminants such as inorganic salts [470]. Photocatalytic degradation typically occurs through either colour bleaching (dyes such as; methylene blue (figure 2.7), methyl orange (figure 2.7), rhodamine B (figure 2.7), basic blue 66 (figure 2.10) and acid violet 7 (figure 2.10)) or colour switching (dyes such as resazurin (figure 2.9)). Both types of dyes provide a quantifiable estimate of the rate of photocatalytic degradation through deterioration in colour intensity with light source exposure time.

Methylene blue bleaching has been frequently deployed in studies of photocatalytic degradation by UV or visible light irradiated TiO_2 in the literature [89, 337, 453, 471-475]. However, methylene blue bleaching has not undergone proper standardization and as such reported studies often utilize disparate methylene blue dilutions, photocatalyst quantities and light intensities. Therefore to provide sensible comparisons between contrasting studies is difficult.

Also suffering from a lack of standardization in various reported studies, the bleaching of photo-oxidative dyes such as methyl orange [476] and rhodamine B [134, 177, 187, 477] has been reported under widely varying conditions of; dye concentration, irradiation intensity and reactor design.

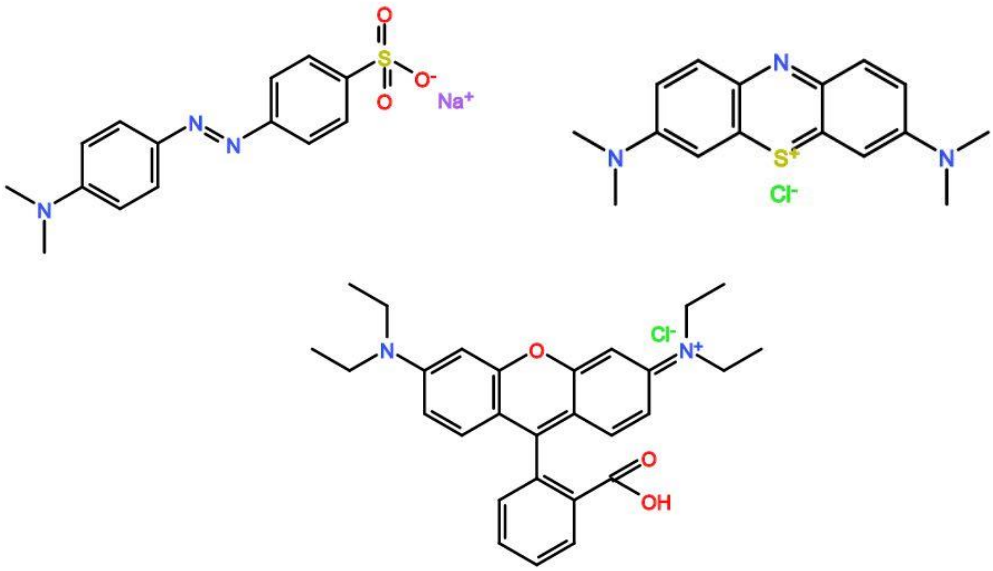

Figure 2.7: The dyes often utilized to measure photocatalytic activity of UV-activated TiO_2 surfaces. Top left; methyl orange, right; methylene blue and bottom; rhodamine B.

However, Bae [478] highlighted limitations of dye degradation standardization, suggesting efficiency of dye decolourization is poorly correlated with dye mineralization under visible light irradiation. Furthermore indicating high method specificity towards both dye and photocatalyst with certain combinations providing disparate photodegradation rates. In particular:

- Both dye sensitization and bandgap excited photocatalysis can contribute to the dye decolourisation,
- The dye decolourisation indicates chromophore group deterioration, but not full photodegradation,
- The dye degradation depends on respective concentration,
- Absorption monitoring at a specific wavelength cannot provide accurate data about the dye degradation kinetics.

In contrast, a range of photocatalytic inks consisting of; stabilizing polymers, sacrificial electron donors (SED) and photocatalytic dyes, were developed by Evans and Mills [458, 462, 479, 480] and are sold by Inkintelligent® [481]. Photocatalytic inks utilize a reductive degradation mechanism (figure 2.8) to provide increased

degradation rates. From a reductive degradation mechanism, results are typically available in minutes compared to hours [479], generating quantifiable and comparable data with possibilities for future standardization. Both basic blue 66 (figure 2.10) and resazurin (figure 2.9) photocatalytic inks (developed by Ink Intelligent ^{TM}) [481] were utilized in the studies reported in this thesis.

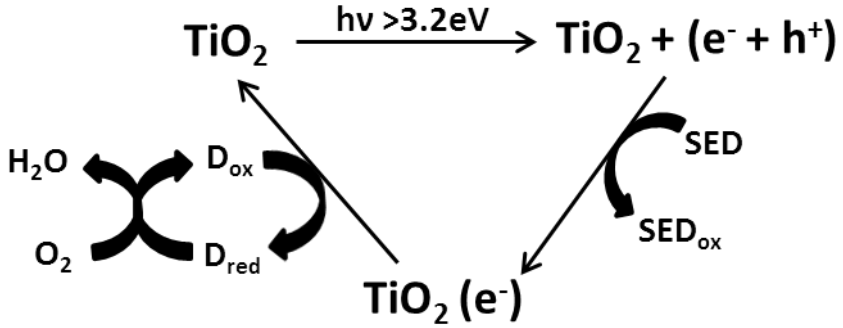

Figure 2.8: The proposed mechanism for reductive TiO_2 photocatalytic ink degradation [73].

Photocatalytic inks alter the typical photodegradation mechanism as mentioned in chapter 1. Photocatalytic inks contain glycerol as an SED, which prevents dye oxidative degradation by recombining excition holes prior to direct hole oxidation processes. Therefore excited excition TiO_2 electrons reductively decompose dye molecules providing a controlled, quicker photocatalytic ink colour change and/or bleaching on comparison to other photo-oxidation processes. In this research, measurement of either basic blue 66 or resazurin ink photodegradation were typically performed until complete ink deterioration, as determined by colour bleaching on visual inspection.

Specifically, the reductive degradation of resazurin initially generates a blue to pink (resourfin) reductive colour change (figure 2.9) under UV light irradiation with further irradiation leading to photo-bleaching. Resazurin ink degradations correlate with contact angle analysis [458] and stearic acid degradation measurements [458]. Determining facile comparisons between colour variation measurements with traditional stearic acid benchmarks.

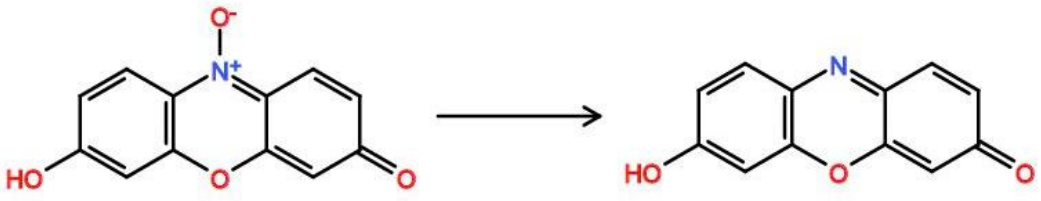

Figure 2.9: Photocatalytic ink resazurin reduction to resourfin (blue to pink colour change).

However, the initial development of a reliable and reproducible resazurin ink-based photodegradation test by Mills took considerable time. Both the uniformity of the resazurin ink layer and subsequent methods of detecting colour change were found to be highly problematic. In particular, problems were encountered in relation to coverslip usage and the reliability of spectrophotometric colour detection correlating to variation in peak intensities at 610 nm and 580 nm. Further process development thus resulted in deployment of a K hand coater™ designed to provide uniform resazurin ink surface layers, and digital scanner (Skypix handscanner™) utilization to further analyse pixel colour variance. Both the K hand coater™ and the digital scanner were used to provide easily quantifiable and comparable results [482].

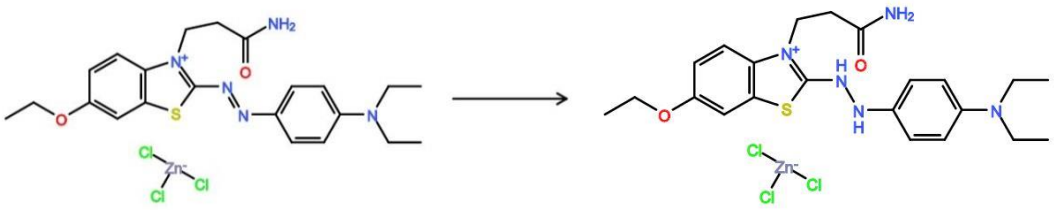

Figure 2.10: Basic blue 66 ink degradation [483]

Furthermore, development of dye-based photocatalytic inks also occurred during research by Mills, particularly in relation to the selection of inks appropriate for the photocatalytic activity level of the surfaces in question. Namely, basic blue 66 (figure 2.10) (purple to colourless) and acid violet 7 (figure 2.11) (pink to colourless), created for lower and higher reactivity surfaces respectively, were produced during ink development studies.

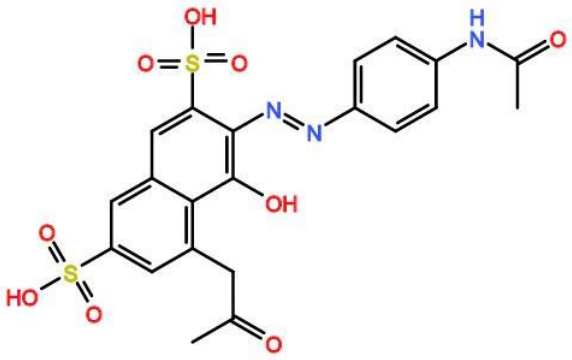

Figure 2.11: Acid violet 7 structure.

With the aforementioned advances in development of properly standardized testing, at the time of writing, INTEC [481] are currently attempting ink degradation process standardization. INTEC are attempted standardisation in order to provide methodologies comparable to those developed for both NO_x degradation (ISO/DIS22197-1) and water droplet contact angle (ISO/WD 27448-1) tests.

Currently, INTEC's standard technique involves the application of a felt tip basic blue 66 ink pen test for initial photocatalytic activity detection. Together with either a basic-blue 66-based or a resazurin-based test applied by a 0.3 mm K-bar in order to provide accurate time to bleach (ttb) average values. Typically, ttb averages are determined through resazurin ink application across nine samples with scanned digital images subsequently generated at set times (basic blue 66 initial ink degradation determined), before and during UV light irradiation. Digital image collection occurs until consistent pink resourfin is indicated with subsequent pixel analysis from changing red, green and blue visible light absorption. A subsequent ttb average of five samples is generated from a comparison between graphed exponential and stationary gradients, corresponding with during and after photocatalytic reduction of resazurin ink.

In this present research, the standardized INTEC approach has been used to generate quantifiable ttb averages comparisons between compositionally similar doped/undoped TiO_2 films.

2.2.10.3 Anti-microbiological testing

The antimicrobial properties of the samples generated here are examined as part of this presented research. Initially, TiO_2 samples were sterilized prior to bacterial culture growth studies through a 20 minute UV light exposure, killing any previously physisorbed microbes. Subsequently, samples were studied though utilizing spectrophotometry, viable colony counts and fluorescence microscopy.

In a typical experiment, three 5ml volumes of Lysogenic Broth (LB) medium underwent inoculation with *Escherichia coli* (*E.coli*) MG1665 and were incubated for 24 hours at 35 ^{o}C, whilst shaking. After growth, each culture underwent both optical density (OD) measurements at 600 nm and subsequent centrifugation at 16,000 g for 2 minutes. Furthermore, the resulting cell pellets were re-suspended in phosphate buffered saline (PBS) equating to 1 OD.

Further experimentation focused on the related processes of attachment or alternatively photodegradation, since the inhibition of attachment or the destruction of attached microbes both equate to antimicrobial activity.

In order to investigate if *E.coli* moieties underwent surface attachment, the surfaces in question were placed into diluted solutions containing *E.coli* (equation 2.6; V: volume, C: concentration).

$$V1*C1 = V2*C2 \qquad \text{Equation 2.6}$$

The samples were half-submerged in solution and colony growth was examined, leaving samples for 24 hours at 37 ^{o}C. Subsequently, surfaces were washed with distilled water, tapped dry and stained using purple violet dye over a 15 minute period. Excess purple violet was removed by using PBS and water washing. Subsequent washing with ethanol removed the *E.coli* absorbed stain. Stain mixtures were analysed through spectrophotometry OD measurements at 600 nm, to obtain the percentage of *E.coli* attachment.

Attachment studies are typically advantageous in terms of generating quantifiable data to indicate the presence of naturally antimicrobial surfaces that operate

through decreased colony attachment and biofilm generation [484]. However, photosterilization from activated surfaces requires initial microorganism surface attachment and biofilm formation, suggesting non-attachment is not the only antimicrobial effect.

Contrastingly, in order to examine if *E.coli* moieties attached to a TiO_2 surface could be "killed" by TiO_2 photodegradation, the following procedures were used: a solution containing *E.coli* was diluted to 400 µL (equation 2.6), applied to TiO_2 surfaces and suspended in water-filled petri dishes. Samples subsequently underwent UV light exposure with continuous PBS addition in order to prevent drying out. A control TiO_2 samples were also treated with *E.coli* solution and kept in darkness for identical time periods.

Furthermore, samples were evaluated to determine the extent (if any) of colony growth as a function of time either situated in the dark (control samples) or under UV irradiation. This evaluation was performed in two different ways; firstly viability counting was employed. Here cultures were removed initially, throughout and subsequent to UV irradiation, 10-fold PBS 10^9 serially-diluted and spot plated onto LB agar plates. LB agar plates were further incubated for 24 hours at 37 ^oC and subsequent colony forming units (cfu) calculated through visible counting of obtained colonies (equation 2.7; CC: colony count, D: dilution, V: volume plated).

$$cfu/ml = (CC*D)/V \qquad \text{Equation 2.7}$$

Secondly, live/dead staining methods were employed. After various times of exposure to UV irradiation, TiO_2 surfaces were washed with distilled water and tapped dry to remove excess *E.coli* and medium. TiO_2 surfaces were then rinsed with $MgCl_2$ solution and staining with 0.5 ml of live/dead staining solution (5 µM SYTO9 dye, 30 µM Propidium iodide and 0.1 % saponin in $MgCl_2$) for 15 minutes. The excess staining solution was removed samples were sealed using a cover slip.

Both the SYTO9 and Propidium iodide are DNA specific resulting in identification of the total viable bacterium population. This occurs through the use of the membrane permeable green SYTO9 and the detection of the non-viable

compromised membrane bacterium population through red Propidium iodide. The samples were further analysed by utilizing fluorescence microscopy in order to calculate the percentage differences of live and dead bacteria [485].

Typically utilization of both viability counting and live/dead staining indicates bacterium photodegradation through UV light activated TiO_2, however, disadvantages arise from both techniques. Viability counting incorporates dilution, assuming similar *E.coli* colony losses from differing samples, and is dependent on live/dead bacteria ratio variability; only measuring cell growth from viable colonies. In contrast, Live/Dead staining is comparatively inaccurate with assumed average percentages between viable and unviable vitality bacterium cell counts and significant utilization of disparate stains [486].

Furthermore, as with the photocatalytic ink degradation studies, negligible microbiological photodegradation standardization exists in the literature. Varying experimental properties (microorganism concentration [77] and irradiation intensity/time [63, 89], etc.) all influence detected microorganism resilience. Whilst a number of studies towards addressing specific microorganism related industrial problems [28, 487] have been performed, effective comparisons are difficult due to the nature of these studies.

The literature has typically focused on utilizing both *E.coli* [69, 76, 77, 86, 89, 321, 323, 487] and *staphylococcus aureus (S.aureus)* [69, 77, 86, 89]. However, *Pseudomonas aeruginosa (P.aeruginosa)* [89, 137], *Bacilius subtils (B.subtils)* [89], *Deinococcus geothermalis* (*D.geothemalis*) [28] and *Micrococcus lylae* (*M.lylae*) [488] have also been utilized to a limited extent.

2.2.10.4 Alternative chemical degradation

UV light activated titanium dioxide also indicates photodegradation of numerous alternative chemicals, namely:

- Alcohols/Carboxylic acids [55, 489, 490],
- Hydrocarbons [491-493],
- Nitrogen containing compounds [494-499],

- Organochlorides [307, 500-504],
- Phenol derivatives [66, 505-508],
- Surfactants [509],

Typically possessing negligible standardization within water pollutant removal and specifically corresponding with by-products resulting from industrial processes. UV light activated TiO_2 also undergoes utilization in air pollutant removal and contrastingly to water pollutant removal, possesses standardization for NO_x surface photocatalytic oxidation into nitrate species (ISO/DIS22197-1) [510, 511].

2.2.11 Electrical conductivity

Technically unrelated to photocatalytic degradation, but interesting in terms of potential photovoltaic applications of TiO_2 (e.g. for some transparent conducting oxides), the four point probe method measures film conductivity or resistivity. The experiment involves utilization of a four point collinear probe arrangement with equal spacing according to ASTM F390-11 [512]. ASTM F390-11 details simultaneous measuring of both the voltage difference and the current flow between two separate sets of sample surface contacts and therefore overcomes the limitations associated with two point systems. Subsequently, Ohm's law (equation 2.8) describes the relationship between voltage (V), current (I) and the uniform material electrical resistance (R).

$$I = V/R \qquad \text{Equation 2.8}$$

Generating an I-R curve from plotted data, therefore indicating either; a conducting Ohmic (equations below) or Schottky contact. Film resistivity (ρ)/conductivity (σ) is further devised from electrical resistance through rearranging Pouillet's Law (equation 2.9) and based on the material thickness (t) and cross sectional film surface (A). The inverse of these resistivity measurements provides the conductivity (equation 2.10).

$$R = \rho \times (t/A), \text{ rearranged: } \rho = R \times (t/A) \qquad \text{Equation 2.9}$$

$$\sigma = 1/\rho \qquad \text{Equation 2.10}$$

Resistivity and conductivity are independent material properties from film surface area and therefore can accurately correlate to changes in the film electronic structure, induced by variation in doping or morphology. As such this approach was utilized extensively during research on TiO_2 films described in this thesis. However, the four point probe method is not without disadvantages, including the following:

- Probe tip contacts can cause film compression damage [513], subsequently increasing with repeat measurements and altering the measured electrical conductivity through lowering film thickness. However, compression damage can be alleviated to a degree by utilizing polyimide cushions [513].
- Probe tips may form improper contact or puncture very thin films, resulting in conductivity measurements of the substrate, however, utilizing thicker films can alleviate such effects.

In this research, the system was used to make electrical measurements (chapter 6) was a Cascade Manual Prober combined with a HP4156 Parameter Analyser. Four probes were placed 1 cm^2 apart in box shape. A classic test I/V sweep with a channel setup of: SMU1, VI, I1, V, variable, SMU2, V2, I2, V, constant was utilized.

Other measurements (chapters 4 and 6) were performed using a 302 resistivity stand (Lucas labs) four point probe connected to a Keithley 2602 A power source. Standards of ruthenium, copper and gold metals grown on Si<100> substrate were used, with copper and gold indicating a linear amps vs. voltage relationship. Furthermore, SP4 osmium probe heads were used with radii of 0.005 inches, spring pressure of 85 g and tip spacing of 0.0625 inches.

2.3 Summary

Methods utilized throughout the experiments described in this thesis are outlined in this chapter and advantages and disadvantages of each are highlighted where possible. Necessarily, emphasis occurs on both TiO_2 film synthesis and methods for photocatalytic activity determination. Where feasible, the use of standardized testing methods is described and any lack of standardization is highlighted.

With the previous discussion in mind, the reader should now be able to appreciate why particular techniques, namely; photocatalytic degradation of INTEC® inks (basic blue 66 and resazurin), microbiological *E.coli* testing and contact angle analysis were selected as the primary methods for the study of photocatalytic activity for the research presented here.

Chapter 3: Cleaning agent exposure effects on photocatalytic activity of Pilkington Activ™ TiO_2 films

3.1 Introduction

Photocatalytic titanium dioxide (TiO_2) films are frequently utilized for self-cleaning [514, 515] surface applications in outdoor environments, but interest in anti-microbial applications for sterile indoor environments (hospitals) is also increasing [5, 30, 516]. However, indoor environments provide two major challenges towards TiO_2 film utilization;

- Visible light photocatalytic activation
- Photocatalysis retention following necessary sterilization procedures

Typically, commercial TiO_2 films (e.g. Pilkington Activ™/St Gobain Bioclean™) are significantly composed of polycrystalline anatase [16, 517, 518]. As previously discussed, anatase morphology generally generates the greatest photocatalytic activity of all TiO_2 polymorphs, incorporating a 3.2 eV band gap [519] and increased surface hydroxyl group density [64]. However, the greatest photocatalytic activity related to morphology is indicated with polycrystalline TiO_2 anatase containing minimal rutile crystallites [20, 520]. Which produces charge trapping in morphologically separate conduction and valence bands to improve exciton pair (e^- + h^+) lifetimes and surface ROS creation [64].

The photocatalytic activation of anatase TiO_2 is well documented [30, 39, 99, 424, 477, 521] and occurs under electromagnetic wavelengths possessing energy greater or equal to band gap size (UV light) [18]. However, indoor environments lack significant UV light irradiation for photocatalytic activation requiring either: transition metal doping (as described in chapters 4, 5 and 6) [21, 423, 471, 500, 522], non-metal doping [94, 414, 523-525], composite semiconductor utilization [526-528] or noble metal loading [529-532], to effectively decrease the TiO_2 band gap and generate visible light photocatalytic activity. Additionally, visible light photoactive TiO_2 is only now (as of writing) undergoing commercial production in significant quantities [533]. Traditionally, visible light photoactive TiO_2 has possessed low synthesis consistency [19] and visible light photoactivity

deterioration over time [534], hindering potential utilization. Therefore, pathogenic degradation in sterile indoor environments could also be achieved with handheld UV light generators supplying activation to commercial TiO_2 films.

Commercial TiO_2 films typically ensure routine photocatalytic activity with reconstitution under non-contaminated environments as a necessary industrial standard. TiO_2 film placement in sterile indoor environments increases pathogenic growth resistance and pathogen destruction on surfaces and instruments, therefore requiring ambient conditions to rejuvenate photocatalytic activity. However, indoor sterile environments (hospitals) require regular exposure to various cleaning agents in order to sterilise surfaces. Commercial TiO_2 films are therefore subjected to contamination and abrasion throughout these necessary cleaning procedures, potentially deteriorating the photocatalytic activity. Continued cleaning agent exposure possibly generates contaminant accumulation, reducing or removing TiO_2 photocatalytic activity and preventing pathogenic destruction. Typically, cleaning agents contain both organic and inorganic species; however, only organic surface contaminants (inks, pollutants or microbes) frequently undergo photocatalytic decomposition on TiO_2 films [267, 472, 475, 477, 535]. To date, research into the effects of cleaning agent exposure has generally focused on surfactant (a common cleaning agent component) degradation by photocatalytically active TiO_2 surfaces [473, 477, 500, 536]. However, negligible research into surfactant exposure effects on TiO_2 photocatalytic activity has occurred, despite surface surfactant exposure affecting TiO_2 film photoelectrical performance [537] or improving corrosion resistance [538].

From an industrial perspective, standard **ISO 10545-13:2016** establishes a chemical resistance determination methodology at ambient temperatures for ceramic tiles on subjection to test solutions (containing: carbon, chlorine, nitrogen and sodium contaminants) and visually evaluates any degradation subsequent to a set time period [539]. Although physical-chemical degradation of TiO_2 films also degrades photocatalytic activity, specific photocatalytic activity deterioration through cleaning agent ion accumulation or possible steric hindrance by surfactant molecules, remains essentially unexamined.

Furthermore, analyses detailing common cleaning agent exposure have previously been implemented on Pilkington Activ™ and St Gobain Bioclean™. Additionally, specific non-photocatalytically destructive cleaning agents are listed on the respective company websites [517, 518]. However, detailed experimental information is not provided, but approved cleaning agents are known to frequently incorporate alkali metal salts and long carbon backbone molecules including chlorine, nitrogen, phosphorus and sulphur-containing functional groups, as potential contamination sources.

Hence, only the exposure effects to commonly utilized window cleaning agents have been previously studied to date, relative to two main commercial TiO_2 coated glass products. Furthermore, prior to presented research, no systematic studies have been reported on the influence of commonly utilized hospital agents on commercial TiO_2 coated glass product stability and photocatalytic activity.

Consequently, this chapter describes the first systematic study of Pilkington Activ™ sample behaviour [16] following exposure to disparate commonly utilized Irish hospital cleaning agents. Photocatalytic activity analysis was performed with respect to possible resulting abrasion and contamination of Pilkington Activ™ samples, thereby generating insight into potential mechanisms underpinning TiO_2 photocatalytic activity deterioration in sterile indoor environments.

3.2 Specific methodology

Irish hospital cleaning agents (Actichlor Plus™, ChloraPrep™, Virusolve+™ and SteriClean™) were donated by Dr Deidre O'Brien, Head of Infection Control at the Mercy University Hospital, Cork. Each consists of the following active components:

- Virusolve+™: Didecyldimethylammonium Chloride and Bis(3-aminopropyl) dodecylamine.
- Actichlor Plus™: 1.7 g Sodium dichloroisocyanurate in an inert effervescent base combined with a compatible detergent.
- ChloraPrep™: Chlorhexidine gluconate (2 %w/v) and isopropyl alcohol (70 %w/v) with a sunset yellow tint (E110).
- SteriClean™: Standard sterile 70 % isopropyl alcohol wipe.

Pilkington Activ™ samples (2.5 cm^2) underwent cleaning agent washing through following described cleaning instructions per product below:

- Virusolve+™: 5 ml per 100 ml (5 %) aqueous solution, spray on necessary surface, allow one minute contact time minimum and wipe off with a cloth. Rinse if required.
- Actichlor Plus™: 1 tablet in 100 ml aqueous solution for 10,000 ppm available chlorine, wipe onto surface required, leave to soak and subsequently wipe off.
- ChloraPrep™: press sponge applicator against surface and break seal to release liquid. Subsequently rub against surfaces for 30 seconds and leave to dry afterwards.
- SteriClean™: wipe affected surface.

A procedure for standardizing a single cleaning agent exposure per Pilkington Activ™ sample was developed, incorporating: constant surface agitation over one minute cleaning agent coverage and ten second water rinsing, to mimic stubborn stain cleaning from both ChloraPrep™ and SteriClean™ applicators.

Typically, all other experimentation followed the methodology as described in chapter 2, with any specific variation for this chapter, stated here:

- For preliminary results:
    - Water contact angle experiments utilized only one (2.5 cm^2) Pilkington Activ™ sample per individual cleaning agent, with one cleaning agent exposure occurring prior to UV light irradiation and following contact angle measurements. Water contact angles were measured at: 5, 10, 20, 30 and 60 minutes of UV light irradiation with an average intensity of: 2.34 mW/cm^2.
    - Photodegradation of basic blue 66 ink (inkintelligent®) was performed on three (2.5 cm^2) Pilkington Activ™ samples per individual cleaning agent. Each ttb result is therefore a three sample average. Basic blue 66 ink was spread across each sample by a 0.3µm K hand coater™. An average UV light intensity of: 2.34 mW/cm^2 was utilized for sample irradiation. A Skypix Handyscan™

handheld camera-scanner scanned images of samples before, and every 20 s during, UV light irradiation.

- After preliminary results:
    - All cleaning agent treatments were repeated thrice (for an average) with water rinsing and nitrogen gas drying following cleaning agent (or non-cleaning agent) exposure.
    - Water contact angles utilized three Pilkington Activ™ samples per individual cleaning agent, ensuring material surface equality through generating average water contact angles. Water contact angles were measured at: 0, 30 and 60 minutes UV light irradiation.
    - Photodegradation of resazurin ink (inkintelligent®) was performed across nine Pilkington Activ™ samples. Subsequent samples (specified) were also irradiated with UV light of an average intensity of: 3.42 mW/cm^2.

Prior to XPS analysis, one of the nine Pilkington Activ™ samples utilized for resazurin ink photodegradation above underwent cleaving to produce ca.1cm^2 pieces. This was followed by cleaning agent re-exposure, water rinsing and nitrogen gas drying.

3.3 Preliminary Results

Preliminary results derived photocatalytic activity experimental standards with water contact angle and photocatalytic ink degradation experimentation both subsequently altered to increase reproducibility and comparability in later results.

Water contact angle measurements were initially implemented without distilled water rinsing following cleaner agent exposure (figure 3.1). As expected, Pilkington Activ™ samples unexposed to any cleaning agent present greater hydrophilicity (approximately 49-23 ^{o}) after 60 minutes UV irradiation, demonstrating greatest surface hydrophilicity. Furthermore, this observed trend towards greater hydrophilicity during UV light irradiation, suggests surface ROS ($OH^{\cdot}/O_2^{\cdot-}$) creation from combination of UV light activated TiO_2 electrons with hydroxyl groups.

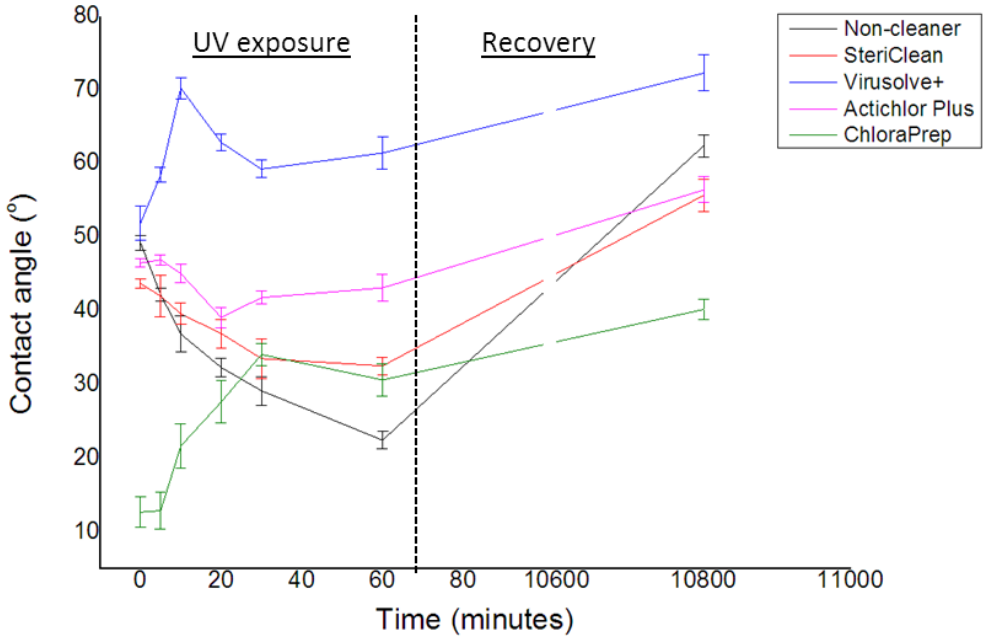

Figure 3.1: Water contact angles from cleaning agent exposed Pilkington Activ™ (0 minutes), during UV irradiation (5, 10, 20, 30 and 60 minutes) and after a week of darkness (10800 minutes).

From figure 3.1, the trend in contact angles recorded for both Pilkington Activ™ samples treated with SteriClean™ or Actichlor Plus™, corresponds to the trend in data recorded for the Pilkington Activ™ sample unexposed to any cleaning agent. Initial contact angles between 40-50 ° appear for samples treated with SteriClean™ or Actichlor Plus™ become increasingly hydrophilic throughout UV irradiation. Unexpectedly, Pilkington Activ™ samples exposed to the non-chlorinated SteriClean™ did not achieve as high hydrophilicity (44-33 °) with UV irradiation, as unexposed Pilkington Activ™ samples. This possibly relates to physical abrasion of the Pilkington Activ™ film during cleaning agent exposure.

Additionally, the unexposed Pilkington Activ™ sample, as well as samples exposed to SteriClean™ and Actichlor Plus™ show recovery after being left in darkness to a more hydrophobic surface as compared to the starting pre-irradiated surface. This hydrophobic enhancement following UV exposure originates from exciton pair recombination after electron relaxation to the TiO_2 valence band and release of surface adsorbed water molecules from metastable hydrophilic states on reaction

with atmospheric oxygen [451]. Therefore, UV exposure results in a compositional change at the surface in comparison to the starting Pilkington Activ™ surface.

Interestingly, figure 3.1 also indicates contact angles recorded for Pilkington Activ™ samples exposed to Virusolve+™ or ChloraPrep™ during UV irradiation initially results in disparate behaviour, as compared to other samples with increasing hydrophobicity detected. This hydrophobic increase does not continue throughout UV irradiation, suggesting surface chemical variations are occurring during exposure. Both samples again indicate hydrophobic recovery after being left in darkness and similarly to other samples, provides a more hydrophobic surface as compared to the starting Pilkington Activ™ surface. This again suggests cleaning reagent exposure results in either a chemical or structural surface variation.

Furthermore, the most striking feature emerging from figure 3.1 concerns the behaviour of a Pilkington Activ™ surface treated with ChloraPrep™. It is apparent ChloraPrep™ treatment produces an orange coloured surface film which is superhydrophilic in nature, even before UV irradiation. Subsequent UV exposure further results in an increase in contact angle, suggesting the surface becomes more hydrophobic. However, the increasing hydrophobicity results from contact angle water droplets removing the orange coloured film from the TiO_2 surface. This steadily produced a contact angle closer to that of the TiO_2 surface with this small scale water rinsing over time.

As previously noted, Pilkington Activ™ samples were initially examined subsequent to cleaning agent treatment, without the utilization of any rinsing step. For this reason, experiments described in figure 3.1 were repeated, with each Pilkington Activ™ sample undergoing distilled water rinsing prior to UV light irradiation (figure 3.2).

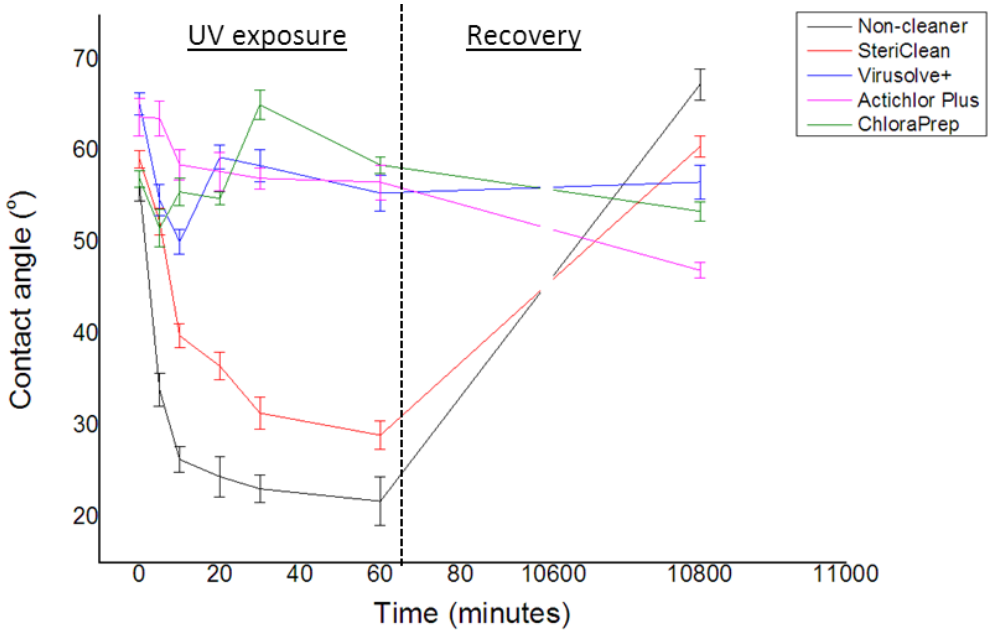

Figure 3.2: Water contact angles from cleaning agent exposed Pilkington Activ™ with water rinsing prior to UV irradiation (0 minutes), during UV irradiation (5, 10, 20, 30 and 60 minutes) and after a week of darkness (10800 minutes).

Figure 3.2 reveals markedly different data for cleaning agent exposed Pilkington Activ™ after water rinsing as compared to figure 3.1. Subsequent to rinsing, the initial state of all Pilkington Activ™ surfaces is effectively equivalent with average contact angles between 55-65 °. Therefore, the rinsing step successfully removes the orange coloured surface film resulting on ChloraPrep™ exposure.

Interestingly, Pilkington Activ™ surfaces exposed to the three chlorinated cleaning agents all now exhibit a similar trend of no appreciable variation upon UV exposure. This suggests surface metastable oxygen deficient state stabilization [452] potentially resulting from cleaning agent recombination centre accumulation on TiO_2 surfaces.

Contrastingly, utilization of the non-chlorinated SteriClean™ (essentially just isopropyl alcohol) again provides a trend in increasing hydrophilicity with UV irradiation, mimicking the untreated Pilkington Activ™ surface. Thus it is suggested that chlorinated cleaner utilization results in a permanent chemical change to the Pilkington Activ™ surface. This change is essentially very detrimental regarding photocatalytic activity, but with the caveat that this comparison is based only on

contact angle measurements thus far. In contrast, utilization of isopropyl alcohol or no cleaner produces a Pilkington Activ™ surface with the expected photocatalytic response regarding increasing hydrophilicity on UV irradiation, followed by hydrophobic recovery in darkness.

Overall, these preliminary results suggest exposure to most chlorinated cleaning agents (other than ChloraPrep™) retains consistently high water contact angles with minimal variation on UV light irradiation. Contrastingly, ChloraPrep™ exposure produces a hydrophilic film across Pilkington Activ™ surfaces, but undergoes removal on water rinsing. Additionally, water rinsing affected all treated surfaces, as might be expected, to remove excess cleaning agent residue.

Contact angles only indicate potential photoactivity and cannot generate quantifiable or reliable photocatalytic active data because of influence by specific factors, namely;

- Light intensity,
- Room humidity,
- Room temperature,
- Sample temperature
- Time between droplet placement and recording.

Therefore photocatalytic ink degradation was utilized as a direct measure of Pilkington Activ™ photoactivity under UV light irradiation. After preliminary water contact angle measurements suggested a reduction in photocatalytic activity. Repeat photocatalytic basic blue 66 ink degradations were performed on Pilkington Activ™ samples exposed to various cleaning agents, prior to each degradation (figure 3.3).

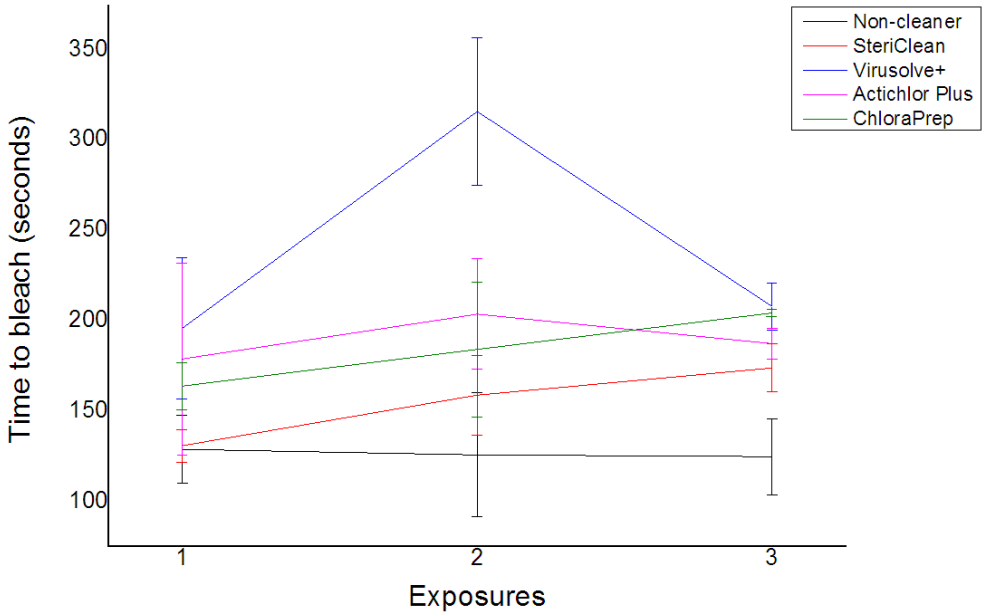

Figure 3.3: Repeat photocatalytic basic blue 66 ink degradation on Pilkington Activ™ undergoing cleaning agent exposure and water rinsing prior to each degradation.

Figure 3.3 indicates the Pilkington Activ™ sample not exposed to any cleaning agent consistently possesses the shortest ttb across multiple basic blue 66 ink photodegradations. Interestingly, Pilkington Activ™ samples treated with SteriClean™ suggest deterioration in photodegradation capabilities towards basic blue 66 ink, alongside other Pilkington Activ™ samples exposed to chlorinated cleaning agents. Furthermore, all cleaning agents seem to produce a less active surface (a longer ttb) as compared to the unexposed Pilkington Activ™ surface, with little variation detected across further cleaning treatments, implying the alteration occurs during the first cleaning agent exposure. This is consistent with previous observations of chlorinated cleaning agents affecting surface wetting, increasing difficulties associated with dirt removal without a water "sheeting" effect [53]. However, the error bars on data points shown on figure 3.3 are large due to a small sampling set (three Pilkington Activ™ samples), and so these observations cannot be thought of as conclusive.

To summarise, these preliminary results are somewhat inconclusive. Contact angle measurements suggest only Pilkington Activ™ exposed to SteriClean™ results in a surface comparable to the control Pilkington Activ™. In comparison, chlorinated

cleaning agents appear to result in an immediate degradation in photocatalytic activity after one application. Additionally, basic blue 66 ink photodegradation experiments further suggest “damaged” surfaces remain so after subsequent exposures. However, issues with the reliability of these latter measurements are apparent from the large error bars presented in figure 3.3.

With this in mind, a further set of measurements were performed utilizing identical cleaning agents. Whilst contact angle measurements were again recorded to compare results directly with previous sets, for this second set of Pilkington Activ™ samples, resazurin ink degradation and a larger sample set were employed as an alternative.

3.4 Results and Discussion

In further water contact angle experiments, three Pilkington Activ™ samples per cleaning agent exposure underwent water contact angle measurement after: 0, 30 and 60 minutes UV irradiation (figure 3.4).

From figure 3.4, both control Pilkington Activ™ samples (not exposed to a cleaning agent) and Pilkington Activ™ samples exposed to SteriClean™ possess similar trends in contact angle. These trends show greater hydrophilicity for increasing UV irradiation time (69-26-16 ^{o} and 53-34-22 ^{o} respectively) and subsequent recovery in more hydrophobic values in darkness (64 and 63 ^{o} respectively). As observed previously, the Pilkington Activ™ exposed to SteriClean™ retains slightly greater hydrophobicity throughout UV irradiation.

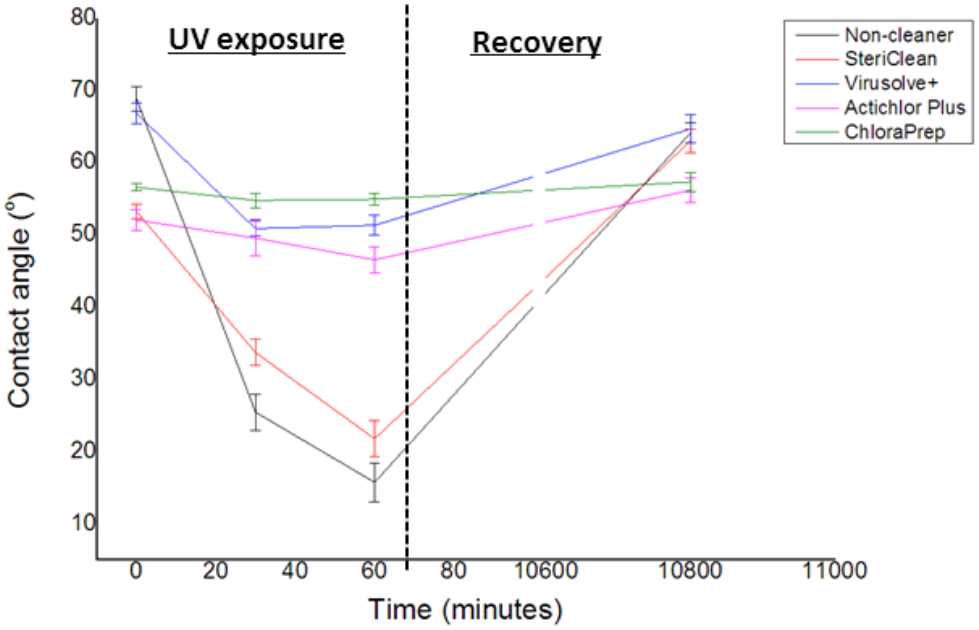

Figure 3.4: Water contact angles subsequent to cleaning agent exposure after; 0, 30 and 60 minutes UV irradiation and 10800 minutes in darkness.

From figure 3.4, the contact angle measurement trends attained for chlorinated cleaning agents (Virusolve^{+TM}: 67-51-51 °, Actichlor Plus^{TM}: 52-50-47 ° and ChloraPrep^{TM}: 57-55-55 °) throughout UV irradiation are similar to those obtained in preliminary experimentation involving the application of a cleaning agent to Pilkington Activ^{TM} surfaces, prior to water rinsing (figure 3.2). Consistent water contact angles during UV irradiation could suggest surface cleaning agent ion ($Na^+/S^{6+}/Cl^-$) poisoning. Surface poisoning could potentially provide excess exciton pair recombination centres [452] to prevent hydrophilic contact angles.

With the confirmation of this previous result in mind, further experimentation utilizing the photocatalytic degradation of resazurin ink was performed on a larger Pilkington Activ^{TM} set of nine samples. Less run-to-run variation in the data was subsequently observed in figure 3.5, as compared to the results in figure 3.3.

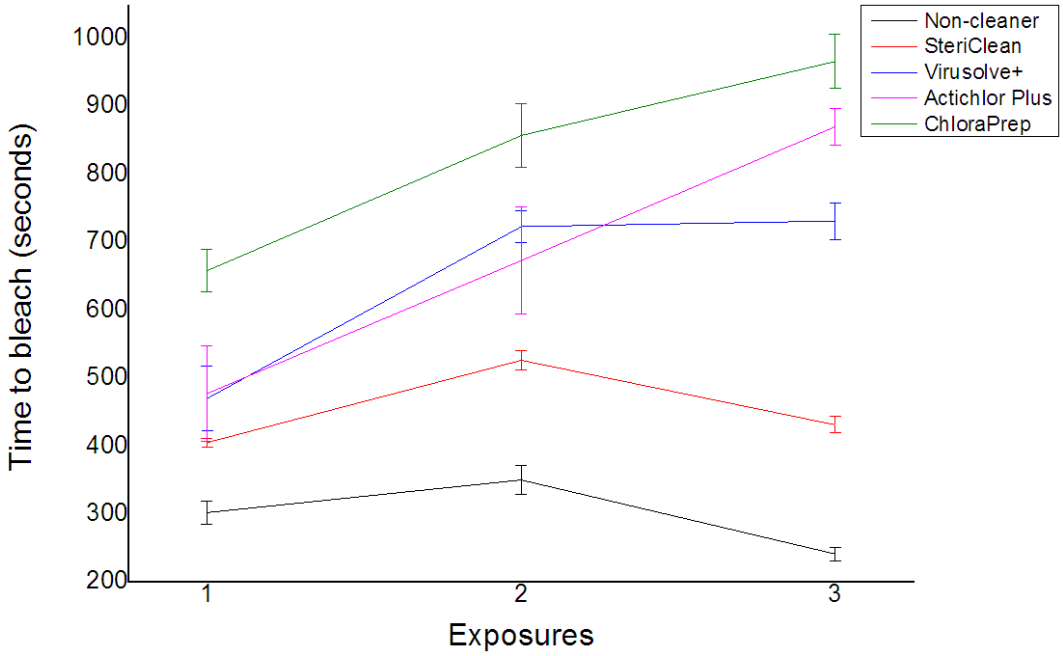

Figure 3.5: Repeat photocatalytic resazurin ink ttb subsequent to repeat cleaning agent exposure with rinsing on Pilkington Activ™.

From figure 3.5, through utilizing resazurin ink photodegradation on a larger Pilkington Activ™ sample set, the behaviour of disparate cleaning agent exposed Pilkington Activ™ samples can be distinguished. Within this data, lowest resazurin ink ttb values are consistently indicated for the Pilkington Activ™ control sample not pre-exposed to any cleaning agent (between 241-351 seconds). However, since this trend is not simply a "horizontal line" across multiple exposures, a clear run-to run variation exists from the nature of this test.

Additionally, all Pilkington Activ™ samples treated with any cleaning agent indicate greater ttb values as compared to the control sample. Pilkington Activ™ surface treated with SteriClean™ emerge with consistently lower resazurin ttb values (406-530 seconds) subsequent to repeat SteriClean™ exposure and water rinsing. Furthermore, chlorinated cleaning agent exposure appears to consistently deteriorate the Pilkington Activ™ surface photocatalytic activity, in the order; ChloraPrep™ > Actichlor Plus™ > Virusolve+™.

Figure 3.5 also suggests continuing deterioration in the photocatalytic degradation of resazurin for Pilkington Activ™ samples exposed to chlorinated cleaning agents with longer ttb values detected subsequent to initial and second exposures.

However, it is unclear whether this trend continues, with third cleaning agent exposures only showing a significant ttb value increase for Pilkington Activ™ samples exposed to Actichlor Plus™. Conclusively, with the possible exception of Pilkington Activ™ exposed to SteriClean™, all other cleaning agents degrade the photocatalytic activity of Pilkington Activ™ samples surfaces, towards resazurin ink reduction.

Interestingly, both ChloraPrep™ (providing significant photocatalytic activity degradation) and SteriClean™ (producing minor, recoverable photocatalytic activity degradation) involve utilization of a constant surface rubbing motion during cleaning agent application. Obviously, mechanical damage could result to the Pilkington Activ™ sample surface, but given the disparate nature of cleaning agents in question, it is proposed mechanical damage alone is unlikely to be responsible for a loss in photocatalytic activity.

The photocatalytic resazurin ink degradation experiments on Pilkington Activ™ samples subject to periodic disparate cleaning agent exposures and water rinsing were repeated using higher UV light exposure levels. Greater UV light intensity was used in order to try and enhance any variability between Pilkington Activ™ samples treated with different cleaning agents (figure 3.6).

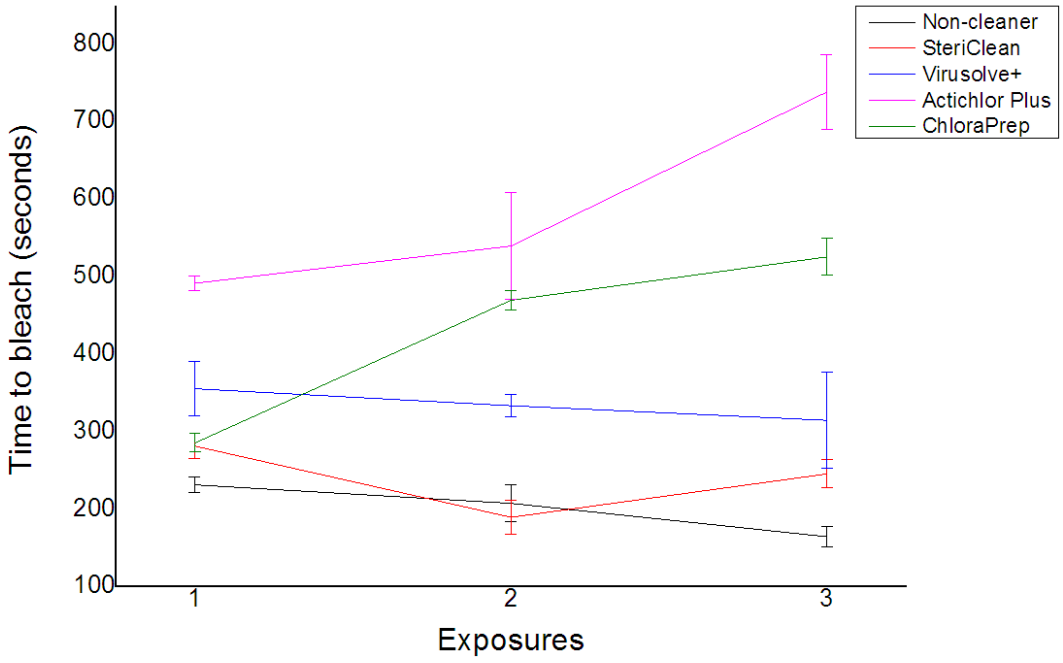

Figure 3.6: Repeated resazurin ink ttb following repeat cleaning agent exposure on Pilkington Activ (under greater UV light exposure: 3.42 mW/cm^2)

From figure 3.6, Pilkington Activ™ samples treated with SteriClean™ are observed to behave most similarly to the untreated Pilkington Activ™ sample with minimal disparity in ttb values across all three photocatalytic resazurin ink degradations. This strengthens the previous proposal, suggesting the utilization of isopropyl alcohol causes no permanent photocatalytic activity degradation of Pilkington Activ™ surfaces.

Chlorinated cleaning agent exposed Pilkington Activ™ samples again indicate greater ttb values throughout multiple resazurin photocatalytic degradations, suggesting deterioration of photocatalytic activity. For this set of experiments, Pilkington Activ™ samples exposed to Actichlor Plus™ consistently result in greatest ttb values. Contrastingly, Pilkington Activ™ samples exposed to ChloraPrep™ provided the longest ttb values for measurements recorded with lower light intensities (figure 3.5).

However, since considerable run-to-run variation still exists, it would be unwise to focus on anything other than obvious trends within these measurements. Figures 3.5 and 3.6 reveal two essential features, namely; Pilkington Activ™ photocatalytic activity is degraded by chlorinated cleaners with Pilkington Activ™ samples exposed to ChloraPrep™ or Actichlor Plus™ suggesting progressive deterioration. However, non-chlorinated cleaners do not degrade Pilkington Activ™ photocatalytic activity. Furthermore, several possibilities should be considered for regarding exactly how the chlorinate cleaners apparently inhibit the photocatalytic activity of TiO_2 films, namely:

- Chlorinated cleaners could provide surface recombination centres for UV light excited exciton pairs, preventing reactions with adsorbed hydroxyl groups or oxygen required to generate surface ROS [540].
- Alternatively, chlorinated cleaners could provide sterically hindering surfaces, blocking active sites and preventing interaction with surface adsorbed oxygen and water molecules required to constitute surface ROS [541].

Following photocatalytic analysis, XPS analysis was performed on Pilkington Activ™ prior and subsequent to variable cleaning agent exposure and resazurin

photocatalytic ink degradation tests under UV light. Six Pilkington Activ™ samples underwent subsequent XPS analysis; one reference, one exposed to triplicate resazurin ink photodegradation tests and four individually exposed to cleaning agents (Virusolve+™, Actichlor Plus™, ChloraPrep™ or SteriClean™) prior and subsequent to triplicate resazurin photodegradation tests.

On degradation, aqueous resazurin ink and various cleaning agents can potentially impart: carbon, chlorine, nitrogen, potassium, sodium and sulphur contaminants across Pilkington Activ™ surfaces at significant concentrations for XPS detection.

A Pilkington Activ™ sample not exposed to a cleaning reagent or resazurin ink was initially analysed as a reference. This sample confirmed a TiO_2 film through a 1:2 Ti:O ratio with titanium (18.1 %) and oxygen (48 %) constituting approximately 54 % of surface elements as TiO_2 (table 3.1). Carbon contamination constituted 30.9 % of surfaces and originated from adsorbed organics (C-C/C=C) or chemisorbed surface carbonates (O-C=O or C-O). The remaining surface composition consisted of ca. 0.6 % nitrogen (399.4 eV) from atmospheric sources, 0.4 % phosphorus (132.7 eV), 0.3 % chlorine (199.6 eV) and 1.8 % silicon (101.8 eV).

Peak	Position (eV)	Concentration (%)
O 1s	529.3	48
Ti 2p	458.1	18.1
C 1s	284.4	30.9
N 1s	399.4	0.6
Si 2p	101.8	1.8
Cl 2p	199.6	0.3
P 2p	132.7	0.4

Table 3.1: Low resolution XPS results for an untreated Pilkington Activ™ surface.

XPS was then performed on a Pilkington Activ™ sample that had previously undergone triplicate resazurin ink photo-degradation under UV irradiation. Resazurin ink photo-degradation typically requires TiO_2 film activation, affecting

surface ion and ROS concentration. Therefore XPS was performed on this particular sample to eliminate ion variables, prior to comparison with cleaning agent exposed Pilkington Activ™ samples. The various resazurin ink components together with associated XPS detectable elements are listed in table 3.2.

Component	Elements	Structure
Hydroxyethyl cellulose	C, O	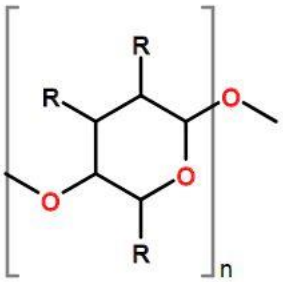 R = H or (CH2)nOH
Glycerol	C, O	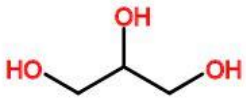
Polysorbate 20 surfactant	C, O	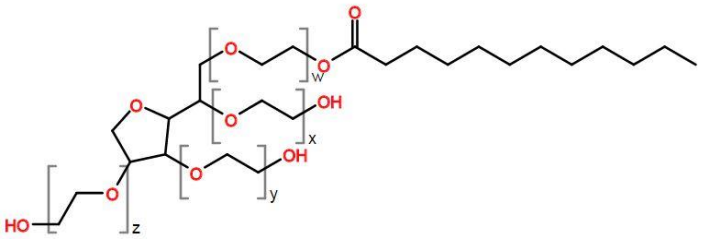
Resazurin sodium salt	C, O, N, Na	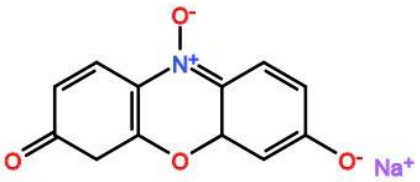

Table 3.2: Resazurin ink components and constituent XPS detectable elements

This Pilkington Activ™ sample also confirmed a 1:2 Ti:O ratio, incorporating 15.8 % titanium and 49.7 % oxygen to constitute approximately 48 % of surface elements as TiO_2 (table 4.3). Additionally, table 3.3 indicates similar carbon surface contamination (29.2 %) compared to Pilkington Activ™ control samples, showing a

natural variation between Pilkington Activ™ surfaces. Furthermore, table 3.4 suggests greater surface carbonate (289-289.5 eV) [542] concentrations (11 % high resolution) suggesting increased carbon oxidation for the Pilkington Activ™ sample previously undergoing resazurin ink degradations.

Peak	Position (eV)	Concentration (%)
O 1s	529.3	49.7
Ti 2p	458.1	15.8
C 1s	284.6	29.2
N 1s	399.3	1.5
Si 2p	102.1	2.9
Cl 2p	200.0	0.4
Zn 2p	1021.0	0.1
Ca 2p	347.0	0.2

Table 3.3: Low resolution XPS for a Pilkington Activ™ sample surface after triplet resazurin ink degradations.

Peak	Position (eV)	Concentration (%)
O 1s_1 (metal oxide)	529.7	35.2
O 1s_2 (organics, OH)	531.0	6.7
O 1s_3 (organics, SiO_x)	532.5	9.3
Ti 2p_1 (Ti^{4+} $2p_{3/2}$)	485.5	11.4
Ti 2p (Ti^{4+} $2p_{1/2}$)	464.2	5.7
C 1s_1 (C=C/C-C)	284.8	17.8
C 1s_2 (C-O)	286.3	10.5
C 1s_3 (O-C=O)	288.2 (288.6)	3.4

Table 3.4: High resolution XPS (focused on titanium, carbon and oxygen peaks) for a Pilkington Activ™ sample surface after triplet resazurin ink degradations with differing untreated sample peak positions.

Correspondingly, carbon (288.2 eV) peak shifts towards lower binding energies (figure 3.7) reflect electron enrichment within surface environments.

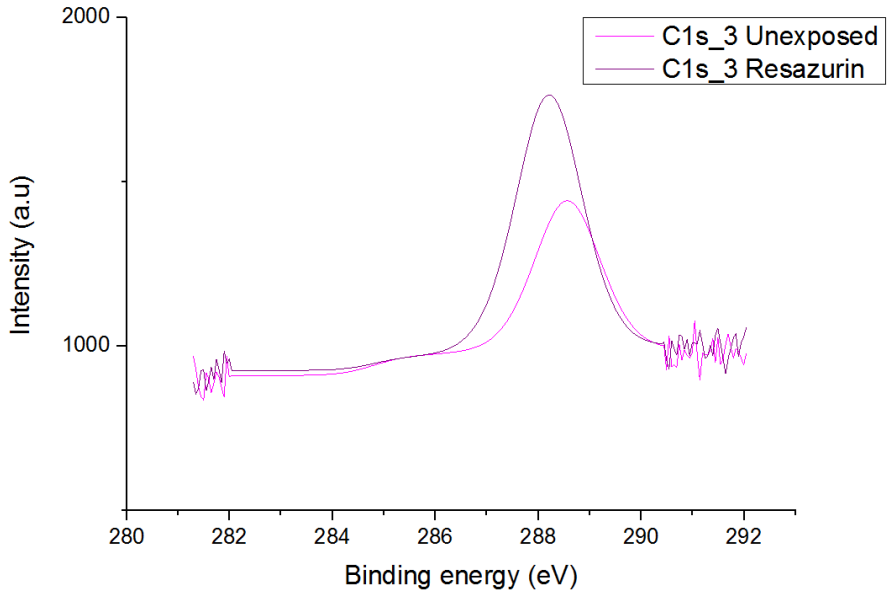

Figure 3.7: Carbon peak shifting between untreated Pilkington Activ™ and Pilkington Activ™ after triplicate resazurin ink photodegradations.

Other detected contaminants include; 2.9 % silicon, 1.5 % nitrogen (from adsorbed atmospheric nitrogen, as C-N bonding is undetected) and minimal; 0.4 % chlorine, 0.2 % calcium and 0.1 % zinc concentrations (potential glass substrate ion diffusion).

Furthermore XPS was performed on the Pilkington Activ™ sample previously treated with SteriClean™ prior to and after repeat resazurin ink photodegradation. Therefore, the various SteriClean™ components together with constituent elements detectable using XPS are listed in table 3.5.

Component	**Elements**	**Structure**
Isopropyl alcohol	C, O	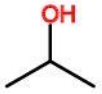

Table 3.5: SteriClean™ components and constituent elements detectable using XPS.

XPS data indicated in table 3.6, suggests SteriClean™ utilization between resazurin ink photo-degradations provided no appreciable surface contamination, probably corresponding to reagent evaporation from high isopropyl alcohol volatility.

Peak	Position (eV)	Concentration (%)
O 1s	529.4	50.9
Ti 2p	458.0	15.6
C 1s	284.4	28.5
N 1s	400.3	0.9
Si 2p	102.3	3.2
P 2p	132.9	0.6
Zn 2p	1021.1	0.3

Table 3.6: Low resolution XPS for a Pilkington Activ™ sample after SteriClean™ exposure prior to each and after triplicate resazurin ink photodegradations.

Furthermore, table 3.6 shows SteriClean™ exposure resulted in a Pilkington Activ™ surface of essentially similar composition to a Pilkington Activ™ sample previously undergoing triplicate resazurin photodegradation tests. Typically adventitious surface carbon contamination was observed (28.5 %), alongside additional surface species including; 0.9 % nitrogen, 0.6 % phosphorus and 0.3 % zinc.
Some 3.2 % silicon is also detected on this sample, with low silicon "contamination" naturally occurring across all other analysed Pilkington Activ™ surfaces (1.8-3.7 %). This silicon contamination originates either from; cleaving to create physically smaller XPS samples, or physical TiO_2 abrasion during cleaning agent exposure, both revealing underlying substrate material (as also indicated in subsequent chapters).

XPS was further performed on the Pilkington Activ™ sample previously treated with Virusolve+™ surrounding repeat resazurin ink photodegradation. Therefore,

the various Virusolve^{+TM} components with associated constituent elements detectable using XPS are listed in table 3.7.

Component	Elements	Structure
Potassium Carbonate	C, O, K	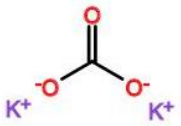
2-Aminoethanol	C, N, O	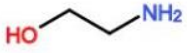
Alkyl Triamine	C, N	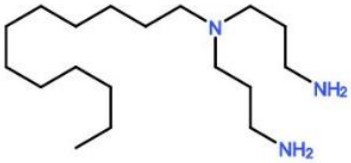
Cationic Surfactant	C, N, Cl	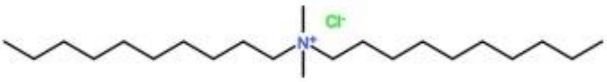
Non-ionic surfactant	C, O	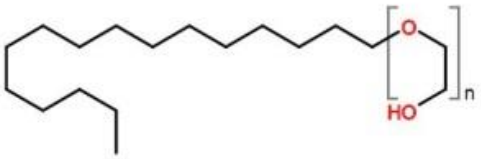

Table 3.7: Virusolve^{+TM} components, XPS detectable elements and structures

XPS data collected from a Virusolve^{+TM} treated Pilkington Activ^{TM} sample is indicated in Table 3.8. The Virusolve^{+TM} exposed Pilkington Activ^{TM} surface suggests a nearly identical composition from both samples undergoing triplicate resazurin photodegradation and either: no other treatment or SteriClean^{TM} exposure. A majority 1:2 Ti:O TiO_2 film is confirmed, consisting of approximately 52 % (titanium: 17.4 % and oxygen: 49.3 %) of surface detected elements as TiO_2. Similar carbon concentrations (28.3 %) are again observed.

Peak	Position (eV)	Concentration (%)
O 1s	529.0	49.3
Ti 2p	457.6	17.4
C 1s	284.4	28.3
N 1s	400.0	1.3
Si 2p	102.1	3.7

Table 3.8: Low resolution XPS for a Pilkington Activ™ sample after Virusolve+™ exposure prior to each and after triplicate resazurin ink photodegradations.

Overall, surface XPS data somewhat surprisingly suggests various Virusolve+™ components (table 3.7) are simply removed by washing. However, residual silicon is again detected (3.7 %) and whilst very low, (1.3 %) nitrogen is also indicated, suggesting known present amino compounds are unlikely to produce any surface contamination. Also surprisingly, other potentially expected specific elemental impurities, namely potassium and chlorine (table 3.7) remain undetected by XPS.

XPS was also performed on the Actichlor Plus™ treated Pilkington Activ™ sample, where Actichlor Plus™ application occurred around repeat resazurin ink photodegradation. Therefore, the various components of Actichlor Plus™ together with constituent XPS detectable elements are listed in table 3.9.

Components	Elements	Structures
Troclosene sodium	C, N, O, Na, Cl	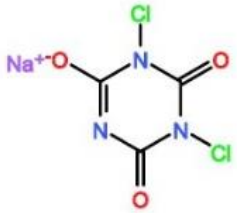
Adipic acid	C, O	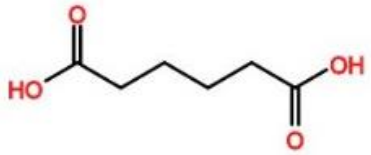
Aryl sulfonate	C, O, S	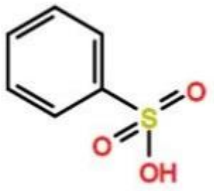
Sodium fatty acid sarcosides	C, N, O, Na	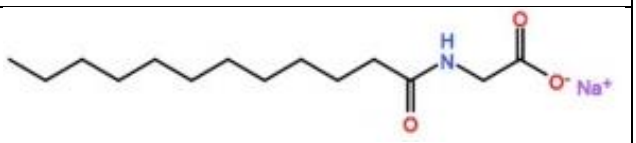

Table 3.9: Actichlor Plus™ components, XPS detectable elements and structures

XPS data collected from an Actichlor Plus™ treated Pilkington Activ™ sample is indicated in table 3.10. The Actichlor Plus™ exposed Pilkington Activ™ sample essentially consists of stoichiometric TiO_2 with approximately 49 % (titanium: 16 % and oxygen: 52 %) of detected surface elements as TiO_2.

Significant surface impurity concentrations are indicated, namely: 2.3 % sodium (1070.8 eV) from either; Troclosene sodium or Sodium fatty acid sarcoside residue and 1.2 % phosphorus (132.9 eV) within P-O bonding [543]. The sodium binding energy (1070.8 eV) [544] could suggest $Na^{+-}O$-Ti bridging bond formation from surface Na_2O [545] or even minimal sodium titanate creation [546]. Additionally, surface sodium ionic presence has previously indicated up to 70 % photocatalytic activity deterioration [547], with sodium titanate also generating catalytically inactive centres [514]. Therefore, low Pilkington Activ™ photocatalytic activity after exposure to Actichlor Plus™ could potentially result from surface sodium ion

presence. However, this is merely speculation without possessing a greater knowledge of the chemical nature of impurities present.

Peak	Position (eV)	Concentration (%)
O 1s	529.3	51.8
Ti 2p	457.9	16.4
C 1s	284.3	23.5
N 1s	399.8	0.8
Si 2p	102.4	3.4
Cl 2p	199.7	0.2
P 2p	132.9	1.2
Ca 2p	346.8	0.5
Na 1s	1070.8	2.3

Table 3.10: Low resolution XPS for a Pilkington Activ™ sample after Actichlor Plus™ exposure prior to each and after triplicate resazurin ink photodegradations.

Interestingly, carbon contamination is reduced (24 %) compared to non-exposed Pilkington Activ™ (29 %). These similar surface adsorbed organics (C-C/C=C) and lower carbonate (C-O/O-C=O) concentrations suggests Actichlor Plus™ exposure does not generate an additional organic layer on the Pilkington Activ™ sample. Other impurities also include: 3 % silicon (102.4 eV) from cleaving or physical abrasion, 0.8 % nitrogen (399.8 eV) from atmospheric sources, 0.5 % calcium (346.8 eV) and 0.2 % chloride (199.7 eV), both potentially from the substrate.

Furthermore XPS was performed on the Pilkington Activ™ sample previously treated with ChloraPrep™ before and after repeat resazurin ink photodegradation. Therefore, the various ChloraPrep™ components with associated constituted elements detectable utilizing XPS are listed in table 3.11.

Components	Elements	Structures
Chlorhexidine gluconate	C, N, O, Cl	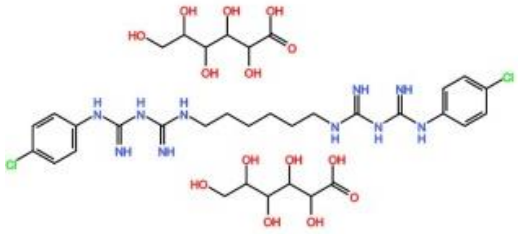
Sunset Yellow Tint	C, N, O, S, Na	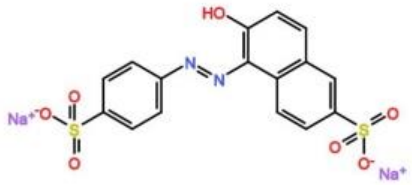
Isopropyl alcohol	C, O	

Table 3.11: ChloraPrep™ components, detectable elements and structures

XPS data recorded from a Pilkington Activ™ surface exposed to ChloraPrep™ is indicated in table 3.12.

Peak	Position (eV)	Concentration (%)
O 1s	530.5	17.6
Ti 2p	458.0	2.5
C 1s	284.4	59.3
N 1s	399.2	13.8
Si 2p	101.9	0.5
Cl 2p	200.3	3.1
S 2p	167.6	3.2

Table 3.12: Low resolution XPS for a Pilkington Activ™ sample after ChloraPrep™ exposure prior to each and after triplicate resazurin ink photodegradations.

From table 3.12, ChloraPrep™ exposure to a Pilkington Activ™ surface indicated significant impurity coverage, unlike similar treatment with alternative cleaning agents also examined. Additionally, low (2.5 %) titanium surface XPS detection probably corresponds to a substantial carbon based residue after ChloraPrep™ exposure, masking XPS signals from the underlying TiO_2. Despite this, crude photocatalytic activity experiments still revealed photoactivation after UV light exposure with resulting resazurin ink photodegradations.

This substantial carbon based residue resulting from previous ChloraPrep™ exposures was detected as orange coloured impurities (figure 3.8) and are possibly related to Sunset Yellow Tint. Furthermore, this carbon based residue correlated with the greatest reduction in surface activity as determined by both contact angle and ink photodegradation measurements.

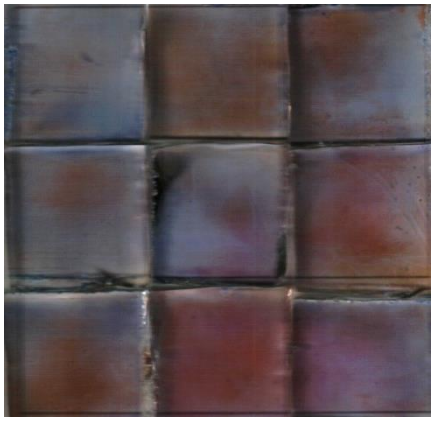

Figure 3.8: Orange coloured impurities across Pilkington Activ™ surfaces after ChloraPrep™ exposure, water rinsing and resazurin ink application (blue colour), and prior to third UV light irradiation, during photocatalytic ink degradations.

Therefore, some 59 % carbon (284.8, 285.8 and 288.6 eV) and 14 % nitrogen (398.6 and 400 eV) results, presumably derived from chlorhexidine gluconate remnants within the considerable surface residue. Specifically, utilizing a higher resolution as in table 3.13, indicated 38 % C-C/C=C bonding (284.8 eV) originating from chlorhexidine gluconate and sunset yellow tint. Additionally, 20 % C-O (285.8 eV), 5 % O-C=O (288.6 eV), 13 % C-NH_2 (400.0 eV) and 3 % C=NH (398.6 eV) bonding were

also detected, relating to chlorhexidine gluconate functional groups chemisorbed onto ChloraPrep™ exposed Pilkington Activ™ sample.

Peak	Position (eV)	Concentration (%)
O 1s_1	529.8	5.3
O 1s_2	531.4 (531.0)	9.9
O 1s_3	532.9 (532.5)	2.8
Ti 2p_1	458.6	1.9
Ti 2p	464.4	0.9
C 1s_1	284.8	37.9
C 1s_2	285.8 (286.3)	20.4
C 1s_3	288.6 (288.2)	5.2
N 1s_1	398.6	2.5
N 1s_2	400.0	13.3

Table 3.13: High resolution XPS (focused on oxygen, titanium, carbon and nitrogen peaks) for a Pilkington Activ™ sample after ChloraPrep™ exposure prior to each and following triplicate resazurin ink photodegradation, with peak shifts highlighted.

Furthermore, table 3.13 suggested variation in binding energy shifts for carbon (figure 3.9) and oxygen (figure 3.10) peaks, compared to a Pilkington Activ™ sample only exposed to resazurin ink. Correspondingly, surface environmental variation of C-O, O-C=O and O-H bonds, reflects electron density alteration in relation to considerable surface residue.

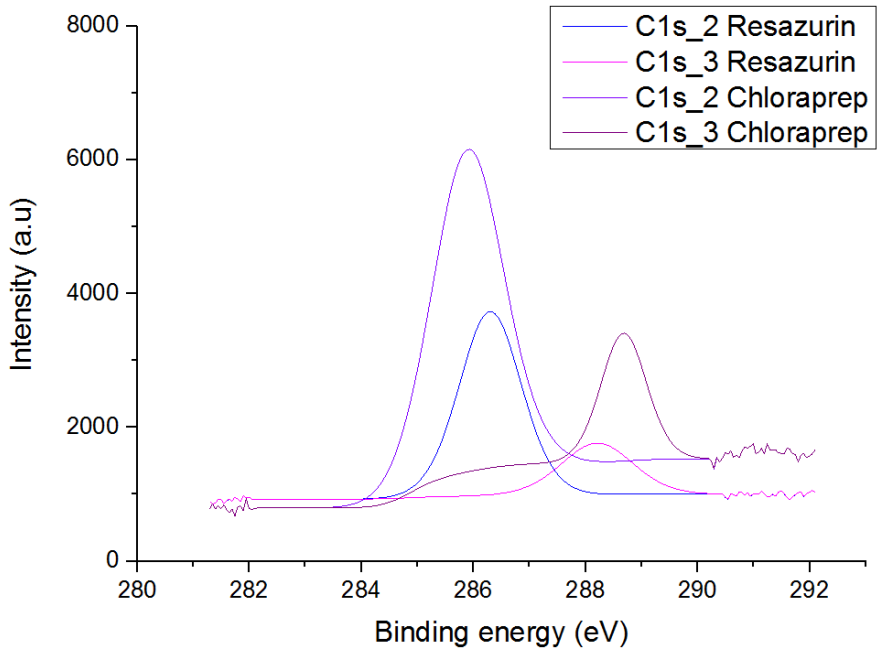

Figure 3.9: Carbon (C1s) peak shifts between a Pilkington Activ™ sample exposed to ChloraPrep™ during resazurin photodegradation and a Pilkington Activ™ sample only exposed to resazurin photodegradation.

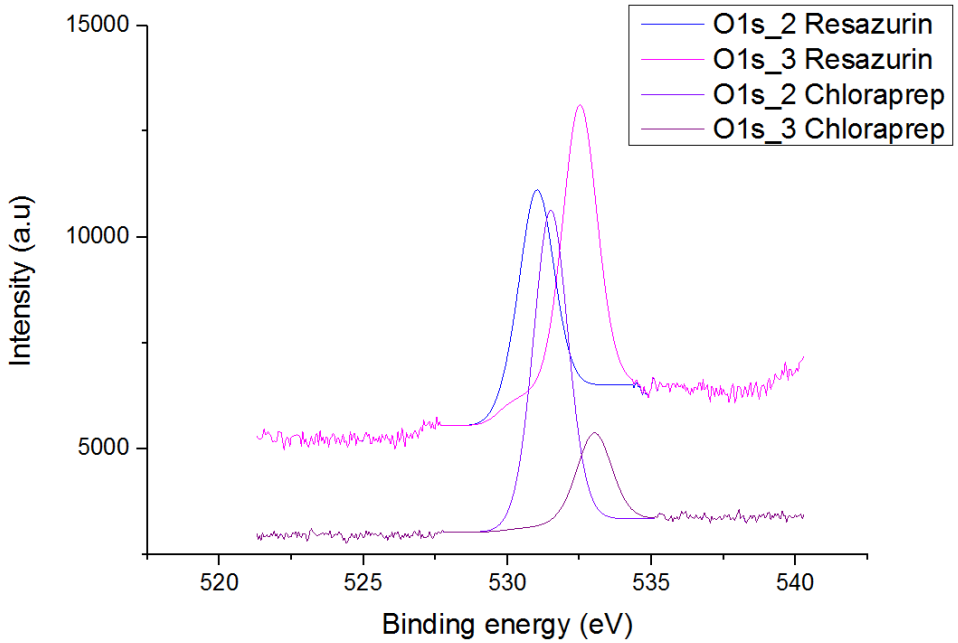

Figure 3.10: Oxygen (O1s_2 and 1s_3) peak shifts between a Pilkington Activ™ sample exposed to ChloraPrep™ during resazurin photodegradation and a Pilkington Activ™ sample only exposed to resazurin photodegradation.

In contrast with other exposed Pilkington Activ™ samples, considerable inorganic contamination was detected after ChloraPrep™ exposure in the form of 3 % sulphur (167.6 eV) and 3 % chlorine (200.3 eV). Sulphur probably originates from the sunset yellow tint present in the ChloraPrep™, with the S_{2p} XPS peak possibly correlating to either a sulphone (C-SO_2-C) [548] or a type of sulphite (SO_3^{2-}) [549]. Additionally, sulphate accumulation has also been indicated to block active surface sites [550], and hence deactivate TiO_2 [521, 551, 552].

Furthermore, chlorine most likely originates from chlorhexidine gluconate present in ChloraPrep™. The Cl_{2p} and C_{1s} XPS peak shifts would be consistent with C-Cl bonding of sp^2 or sp^3 carbon atoms [553]. Surface chlorine could also contribute to the deactivation of TiO_2 [541, 554], potentially through decreasing O_2 and CO-O_2 adsorption intermediate generation [540].

Overall, the XPS analysis is consistent with the assumptions previously made in terms of a correlation between levels of surface contamination and the detected degradation in photocatalytic activity deterioration (ttb increase).

Pilkington Activ™ samples exposed to Actichlor Plus™ showed evidence of sodium ion accumulation (2 %). However, Pilkington Activ™ samples exposed to ChloraPrep™ indicated high carbon (59 %) and nitrogen (14 %) contaminations, together with chlorine (3 %) and sulphur (3 %).

In contrast, Pilkington Activ™ samples exposed to Virusolve+™ indicated negligible evidence of additional surface contamination, whilst for reported resazurin ink degradation experiments, an increase in ttb values was nevertheless observed. Furthermore, Pilkington Activ™ samples exposed to SteriClean™ again indicated negligible evidence of additional surface contamination, correlating in this case with little or no increase in ttb being detected during ink degradation experiments.

Both X-ray diffraction (XRD) and Raman spectroscopy were applied to the Pilkington Activ™ samples to study the possible role of cleaning agents in altering crystallinity of Pilkington Activ™ films. Initial XRD studies of film crystallinity proved to be ineffectual, predominately resulting from very thin natures of analysed films combined with a general lack of XRD sensitivity as an analysis method. Therefore,

Raman spectroscopy was utilized as an alternative technique. Figures 3.11 and 3.12 indicate Raman spectra recorded from a reference Pilkington Activ™ sample and furthermore Pilkington Activ™ samples after repeat resazurin photocatalytic degradation and exposure to individual cleaning agents.

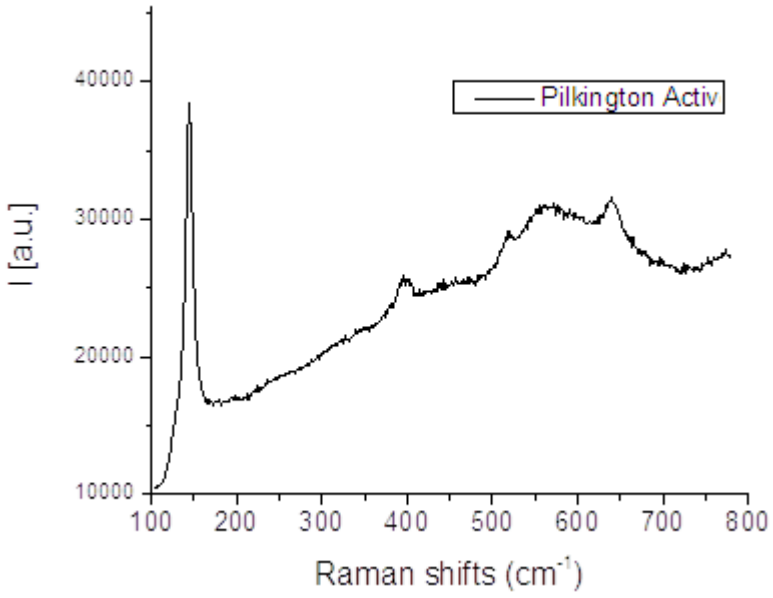

Figure 3.11: Raman spectroscopy data for a reference Pilkington Activ™ sample

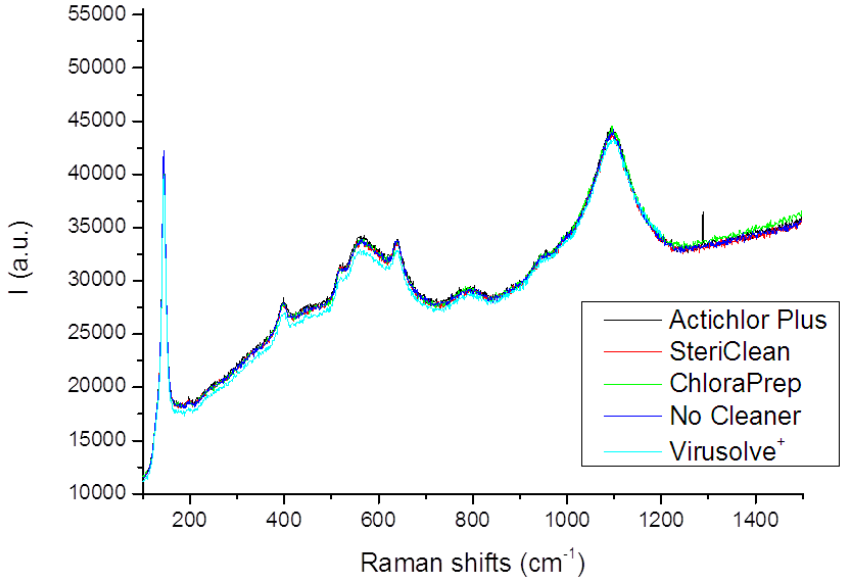

Figure 3.12: Raman spectroscopy data for Pilkington Activ™ samples after repeat resazurin photocatalytic degradation and exposure to individual cleaning agents.

Raman spectra are essentially identical from all studied samples in figures 3.11 and 3.12, displaying modes at: 144 cm^{-1}, 399 cm^{-1}, 517 cm^{-1} and 636 cm^{-1}, correlating to E_g, E_g, A_{1g} + B_{1g} and E_g vibration modes of crystalline anatase TiO_2 [555]. Additionally, a broad band at 560 cm^{-1} can be attributed to the Pilkington Activ™ SiO_2 coated glass substrate.

Furthermore, figure 3.13 focuses on the 144 cm^{-1} E_g mode to highlight any disparities in peak intensity or width. This potentially results from variable amounts of surface roughening [556, 557] corresponding to differing cleaning agent exposures during repeat resazurin photocatalytic degradation.

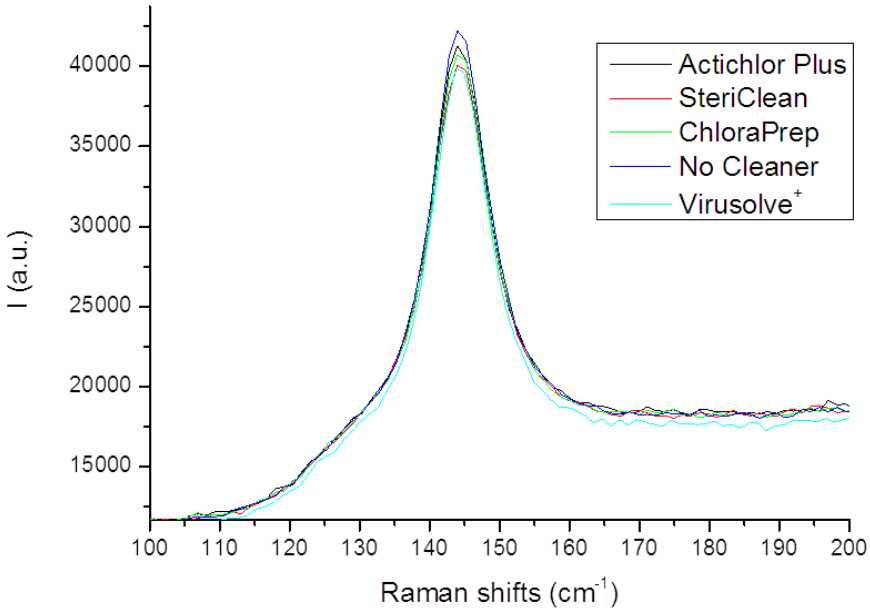

Figure 3.13: Differing 144 cm^{-1} E_g peak intensity for Pilkington Activ™ samples individually exposed to disparate cleaning agents during resazurin ink degradation.

As indicated in figure 3.13 spectra for all treated and untreated Pilkington Activ™ samples are essentially identical within analytical process variation. Therefore, within the parameters of Raman spectroscopy analysis, cleaning agent application did not induce any particular surface damage or variation in crystallinity.

Furthermore, to highlight possible chemical or mechanical influences of cleaning agent application on Pilkington Activ™ surface morphology after repeat resazurin

ink photocatalytic degradations, surface SEM was performed on all samples (figure 3.14).

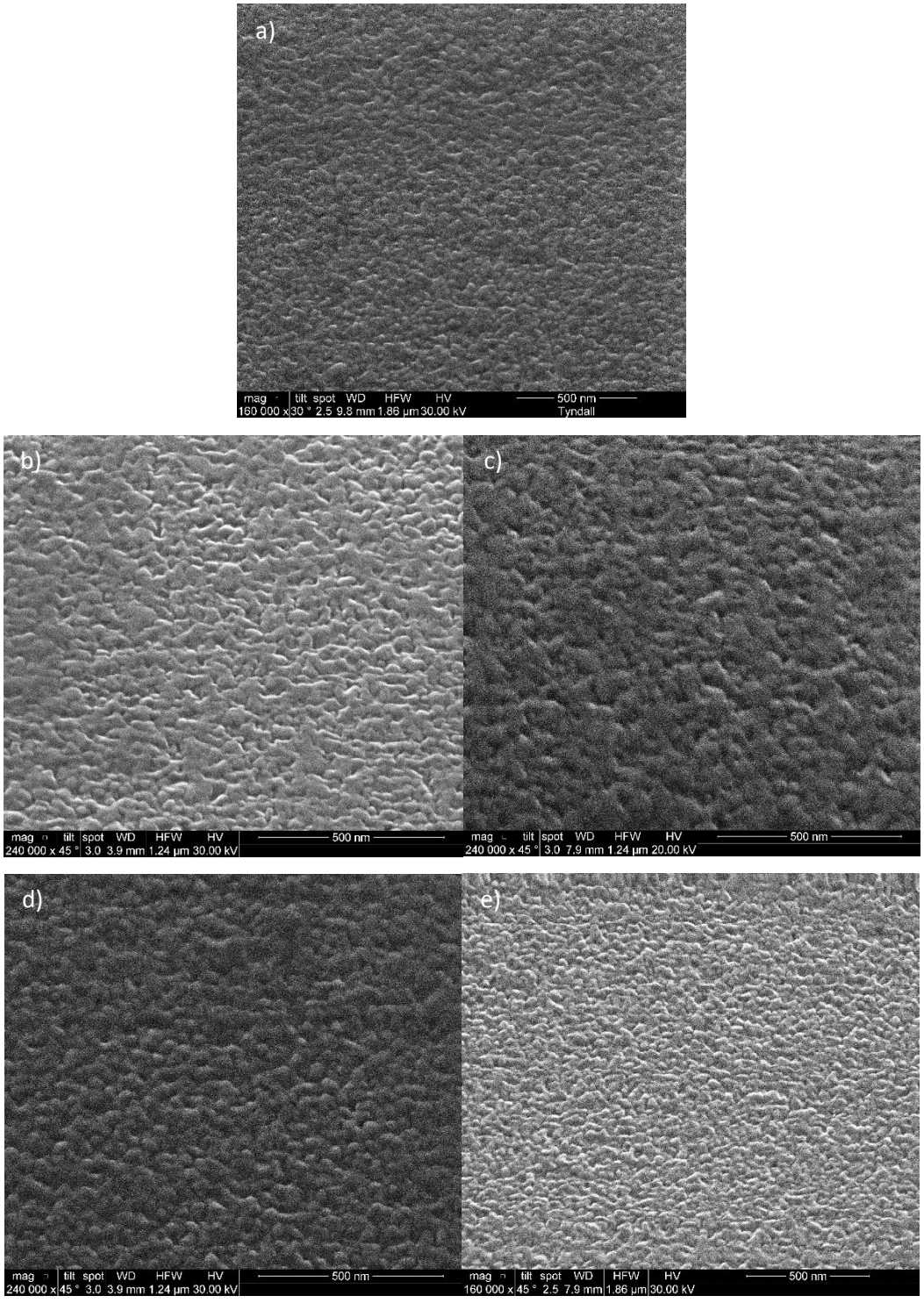

Figure 3.14 a-e): indicate surface SEM images of; a) untreated Pilkington Activ™ surface and Pilkington Activ™ surfaces treated with b) SteriClean™, c) Virusolve+™, d) Actichlor Plus™ and e) ChloraPrep™.

As suggested from figure 3.14, apart from variation in instrumental contrast, Pilkington Activ™ surfaces all appear similar, incorporating a high density globular anatase crystallite surface structure and correspond with Raman spectroscopic data. Correspondingly, it is not possible to cite utilization of cleaning agents in terms of possible surface roughening or smoothening, elsewhere indicated to alter surface area and photocatalytic activity [558].

3.5 Conclusions

This study has revealed the following:

- The expected increase in hydrophilic water contact angle under UV light exposure for the Pilkington Activ™ films, is not observed on treatment with Actichlor Plus™, Chloraprep™ or Virusolve+™ cleaning agents.
- The photocatalytic activity of Pilkington Activ™ surfaces is decreased with respect to the photo-reduction of resazurin ink on hospital cleaning agent exposure.
- In particular, the photocatalytic activity of Pilkington Activ™ surfaces can be drastically reduced by residue presence after treatment with Actichlor Plus™ or Chloraprep™.
- Multiple treatments provide variable effect on the photocatalytic activity of the Pilkington Activ™ film. Largest reductions in photocatalytic activity was observed typically after one exposure for Virusolve+™ and Stericlean™ treatments and after two exposures for the Chloraprep™ treatment. Additionally, the treatment with Actichlor Plus shows continued photocatalytic activity degradation across all three exposures.
- Treating Pilkington Activ™ surfaces with Stericlean™ or Virusolve+™ did not provide any significant residue or variation in surface environment. Whereas treatment of Pilkington Activ™ films with Actichlor Plus™ or Chloraprep™ created sodium, chlorine and sulphurous residues equatable to cleaning agent constituents and provided variation in surface environments.

- None of the cleaning agents cause any noticeable structural or morphological alterations to the Pilkington Activ™ films.

Henceforth, this research suggests if regular treatment of an antimicrobial TiO_2 film with an antibacterial agent is required throughout the working day in a clinical environment, then Stericlean™ would be the cleaning agent of choice. However, despite Stericlean™ treatment showing the lowest effect on the photocatalytic activity of Pilkington Activ™ films. Stericlean™ may not be as effective towards microbes as other cleaning agents, in this case, Virusolve+™ could be a good compromise. Additionally, the other cleaning reagents (Actichlor Plus™ and Chloraprep™) examined here may cause permanent loss of photocatalytic activity across repeat cleaning treatments.

Chapter 4: ALD growth and characterization of a range of nanolaminate doped TiO_2 films: The role of the dopant in determining electrical, morphological, optical and photocatalytic properties.

4.1 Introduction

As discussed in chapter 1, typical TiO_2 film properties vary on doping with specific dopants, based on: radius, charge, oxide band gap, incorporation type and concentration. In particular, doping concentration varies photoactivity depending on the dopant metal or metal oxide properties with an optimal dopant concentration of around 0.01-1 % in TiO_2 reportedly providing an increase in photocatalytic activity, irrespective of dopant [155]. This research also notes going beyond the optimal 0.01-1 % concentrations range for advantageous dopants may provide mid-band gap energy state generation to decrease overall band gap size and thus facilitate greater light absorption. However, other work cites an optimal dopant concentration range 3-5 % [30]. Further dopant incorporation beyond the optimal is said to increase the number of recombination centres [171, 187, 396], as well as induce metal dopant oxide insolubility [559], both serving to degrade photocatalytic ability.

Furthermore, dopants (M) typically undergo either substitutional (M_{Ti}) or interstitial (M_i) incorporation into TiO_2, dependent on the dopant ionic size and charge with lattice distortion [198] and defects resulting. Photocatalytic activities are subsequently influenced by higher defect concentrations [153, 560, 561] and/or disruption to crystallinity [562, 563].

Dopants located at bulk or surface sites also vary the photocatalytic properties, with surface dopants providing recombination sites and bulk dopants adversely acting as deep charge carrier trapping sites, increasing recombination [30]. However, smaller dopants as compared to Ti^{4+} (74.5 pm), can provide interstitial and substitutional incorporation, varying TiO_2 defect concentrations by inducing lattice strain (M_i) and charge compensation (M_i and M_{Ti}) [285, 296].

The necessary charge compensation for overall lattice cell neutrality originates from interactions on aliovalent/isovalent doping, varying the naturally occurring $Ti^{3+}/V_O^{\cdot\cdot}$ and $V_{Ti}^{''''}$ defect concentrations through oxygen TiO_2 film diffusion [2, 18, 150, 154]. Substitutional aliovalent dopants are either:

- n-type, providing; states beneath TiO_2 conduction band minimum and $V_{Ti}^{''''}$ species necessary for charge compensation [205].
- p-type, providing both states above the TiO_2 valence band maximum and $Ti^{3+}/V_O^{\cdot\cdot}$ to compensate charge [19, 150, 564].

Additionally, interstitial doping generates excess electron donation into the TiO_2 lattice [418, 565], creating $V_{Ti}^{''''}$ necessary for charge compensation. Predominately, charged defect creation produces greater exciton trap density and mid-band gap energy levels, further decreasing the effective band gap. As a result, lower optimal dopant concentrations are thought to be required in order to increase both excition lifetimes and surface ROS generation [566]. However, dopants possessing similar properties to Ti^{4+} usually undergo successful substitution with lower defect concentration and film strain resulting.

In the research detailed here, a range of aliovalent/isovalent dopants possessing disparate ionic sizes: Ag^{+}, Al^{3+}, Hf^{4+}, $Sn^{2+/4+}$ and $V^{5+/4+/3+}$ have undergone incorporation into TiO_2, through nanolaminate ALD cycle growth. The subsequent section describes the potential photocatalytic properties resulting from these doped TiO_2 films with a brief description of previous literature included here, so as to provide a context for the description of the following experimental systems.

Aluminium ions (Al^{3+}: 67.5 pm) either occupy interstitial lattice (Al_i) or substitute into Ti^{4+} ($Al_{Ti'}$) sites [163-166] with associated $V_O^{\cdot\cdot}$ generation. $Ti_{1-x}O_2{:}Al_x$ films show inconsistent photocatalytic activity with both increasing [167-170] and decreasing [45, 171-173] activity on aluminium incorporation reported in contrast to nominally undoped TiO_2. This suggests outcomes are highly dependent on the film synthesis procedure, the doping method and the dopant concentration utilized.

However, optimal dopant concentrations (0.5-1.1 %) for $Ti_{1-x}O_2:Al_x$ films correlate to an increase in photocatalytic activity [167-170], resulting from secondary charge compensation and $V_{O^{\cdot\cdot}}$ generation to create mid band gap states. Further increase in aluminium concentration [171-173] provides a suppression of photocatalytic activity resulting from Al^{3+} dopant ions acting as deep traps [45], capturing charge carriers prior to surface migration.

Hafnium ions (Hf^{4+}: 85 pm) possess an identical oxidation state, but an increased size as compared to Ti^{4+}, probably resulting in lattice stain on substitutional doping. Hf^{4+} substitution typically provides a decrease in photocatalytic activity through inducing strain in $Ti_{1-x}O_2:Hf_x$ films to produce anatase/amorphous morphologies [182]. Since the $V_{O^{\cdot\cdot}}$ concentration variation is not expected to alter upon Hf^{4+} doping, any appreciable increase in the density of mid-band gap states is unlikely. This essentially provides immobile conduction and valence band states and constant band gap, with strain decreasing the degree of crystallinity resulting in decreasing photocatalytic activity on hafnium doping [183, 184]. However, the mixed oxide $TiHfO_2$ has been shown to exhibit visible light photocatalysis associated with a red shift in band gap as compared to TiO_2, and has consequently been utilized in water splitting applications [185].

Silver ions (Ag^{+}: 129 pm) present a lower oxidation state and an ionic radius of almost double size as compared to Ti^{4+}, suggesting the creation of significant charge compensation defects and strain on substitutional doping. However, Ag_2O possesses a 1.46 eV band gap, suggesting the possibility of visible light wavelength absorption through mid-band gap state creation on formation within TiO_2, but complexities could arise here due to transitions to and mixing with filled 4d orbitals.

Silver ions have been shown to trap electrons [186], decreasing recombination rates [186, 188] through interfacial charge transfer to provide increased surface ROS concentrations [187]. Silver ions may also contribute towards weakening of surface bridging complex bonds, promoting ART [189] and extending the material

absorption properties and therefore photocatalytic activity into the visible spectrum [186, 190, 191].

Tin ions exist in two stable oxidation states, Sn^{2+}: 136 pm and Sn^{4+}: 83 pm and both could substitute Ti^{4+} sites (typically Sn^{4+} [196]) in TiO_2. This substitution would induce lattice distortion and increase surface defect concentrations [145, 197], influencing the subsequent photocatalytic activity.

SnO_2 also possesses a lower energy conduction band as compared to TiO_2 [200], further facilitating excited electron charge transfer between TiO_2 and SnO_2 conduction bands to increase charge carrier trapping and excited state lifetimes. As a consequence, if Sn^{4+} is incorporated into TiO_2 in the form of SnO_2 or a very similar sub oxide, a reduction in band gap is likely [197], improving photocatalytic activity. Additionally, SnO_2 conduction band electrons could capture oxygen molecules to generate superoxide radicals [197], increasing the photocatalytic activity. Furthermore, strong Sn 5s hybridization with O 2p and Sn 5s/5p lone pair states near valence bands could also induce visible light activity [198, 201].

Three vanadium ions (V^{3+}: 78 pm, V^{4+}: 72 pm and V^{5+}: 68 pm) could undergo substitution into Ti^{4+} sites with each generating negligible strain as a result of similar ionic sizes as compared to Ti^{4+}. On substitution, mid-band gap states could be provided should the corresponding oxides (V_2O_3, VO_2, V_2O_5) form as a result of lower band gaps possessed (0.6, 0.6/2.4 and 2.3 eV, respectively). $Ti_{1-x}O_2:V_x$ has previously been found to possess increased photocatalytic activity [45] with a red shift towards visible light absorption [205] and a 400-500 % increase in methylene blue degradation rate, as compared to undoped TiO_2. Also, V^{4+} substitutional doping (V_{Ti}) is shown to generate a band gap decrease through V^{4+} 3d and Ti^{4+} orbital overlap, with V^{4+} favouring exciton generation.

In the following sections, doped TiO_2 films synthesized with the dopants previously described are examined for possessed photocatalytic properties relating to film structure and composition.

4.2 Methodology

4.2.1 ALD film synthesis

Nominally undoped and doped TiO_2 films were grown by thermal atomic layer deposition (Cambridge Nano Tech Fiji 200 system) at 180 ^oC under argon gas onto pre-cleaned (5 minutes oxygen plasma) fused quartz substrates (Vitreosil® 077 optical fused quartz). TDMAT (tetrakis(dimethylamino)titanium(IV)) and H_2O were utilized as TiO_2 precursors and were kept at 80 ^oC and 25 ^oC respectively. Nanolaminate dopant precursor (as listed in table 4.1) cycle addition replaced titanium precursor cycles in order to generate two separate dopant film concentrations with 19:1 and 99:1 (titanium:dopant) cycle ratios, across 400 cycles overall.

Dopants	Precursors	Bubbler Temperatures (^oC)
Aluminium	TMA (trimethylaluminium)	25
Hafnium	TEMAH (tetrakis(ethylmethylamino)hafnium(IV))	95
Silver	TMHDAg (2,2,6,6-tetramethyl-3,5-heptanedionatosilver(I))	100
Tin	TDMASn (tetrakis(dimethylamino)tin(IV)	60
Vanadium	TDMAV (tetrakis(dimethylamino)vanadium(IV))	70

Table 4.1: Dopants and associated precursors

All samples underwent annealing at 400 ^oC in an air furnace (Thermolyne™ Benchtop 1100 ^oC Muffle Furnace) for two hours.

4.2.2 TiO_2 and $Ti_{1-x}O_2:M_x$ sample analysis

All films were analysed utilizing previously described methodology within Chapter 2. Specific technique variation or films analysed to this chapter are listed here:

- SEM image scales: 5 μm for $Ti_{1-x}O_2:Ag_x$ (19:1) and 50 μm for $Ti_{1-x}O_2:Hf_x$ (99:1).
- TEM on nominally undoped TiO_2 and $Ti_{1-x}O_2:Ag_x$ (19:1) films (both annealed) with images scaled at 50, 20 and 5 nm.
- XPS was performed on nominally undoped annealed TiO_2 and all (19:1) doped TiO_2 films after 3 seconds sputtering. Depth profiling was performed on $Ti_{1-x}O_2:Ag_x$ (19:1), $Ti_{1-x}O_2:Sn_x$ (19:1) and $Ti_{1-x}O_2:Hf_x$ (19:1) films with continued argon beam sputtering until silicon concentration increase from film-substrate interfaces.
- Initial photocatalytic ink degradation was applied by felt tip, followed by 150 minutes under 3.31 mW/cm^2 UV light intensity, with images scanned at: 0, 5, 10, 15, 20, 30, 45, 60 75, 90, 120 and 150 minutes. Further analysis was performed utilizing a 3 mm K-bar for application of basic blue 66 or resazurin ink for two separate scans under 3.24 mW/cm^2 UV light intensity. Nominally undoped TiO_2, $Ti_{1-x}O_2:Ag_x$ (19:1) and $Ti_{1-x}O_2:Sn_x$ (19:1) samples were irradiated for 22 minutes with images recorded at 2 minute intervals. $Ti_{1-x}O_2:Hf_x$ (19:1), $Ti_{1-x}O_2:Hf_x$ (99:1) and $Ti_{1-x}O_2:Sn_x$ (99:1) samples were irradiated for 120 minutes with images recorded at 10 minute intervals.
- Initial water contact angle measurements under a UV light irradiation of 3.19 mW/cm^2. Further water contact angles were measured after: 30, 60, 90 and 120 minutes exposure to a UV light irradiation of 3.53 mW/cm^2, for samples showing a previous degree of photocatalytic ink degradation or water contact angle variation.

4.3 Results

Prior to annealing, all doped films were amorphous in nature as determined by XRD and Raman measurements. As might be expected, films indicated no evidence of photocatalytic activity regarding bleaching of basic blue 66 ink or a reduction in water contact angle. Therefore, it is concluded for the amorphous films, dopant addition did not induce any appreciable photocatalytic activity. (Data included in appendix A).

After annealing, XRD and RAMAN measurements were repeated on all nominally undoped and nanolaminate doped TiO_2 films. In the XRD experiments, reflections at 25.3° 2ϑ, indicative of anatase (101) planes were generated from the nominally undoped TiO_2 film, as well as the $Ti_{1-x}O_2:Ag_x$, $Ti_{1-x}O_2:Hf_x$ and $Ti_{1-x}O_2:V_x$ films doped at 99:1 cycle ratios (figure 4.1). In contrast, the doped samples prepared utilizing the 19:1 nanolaminate cycle ratio as well as the $Ti_{1-x}O_2:Sn_x$ and $Ti_{1-x}O_2:Al_x$ (99:1) films indicate no evidence of anatase generation, suggesting that these samples are essentially amorphous (figure 4.2).

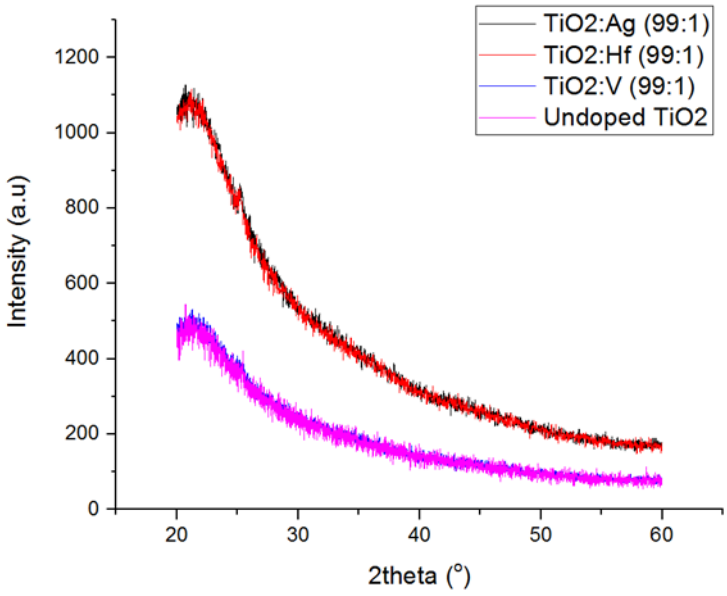

Figure 4.1: XRD of the annealed undoped TiO_2 film, the $Ti_{1-x}O_2:Ag_x$ (99:1) film, the $Ti_{1-x}O_2:Hf_x$ (99:1) film and the $Ti_{1-x}O_2:V_x$ (99:1) film indicating very weak 25.3 ° (101) anatase reflections.

Not surprisingly, minimal doping (99:1) has a negligible effect on the crystallinity with a majority of films possessing some evidence of anatase crystallinity. However, where detected the (101) anatase peak reflection intensities are barely distinguishable from high background noise that is typically observed from an amorphous material, figure 4.2. Limited peak reflection intensities originate from either the presence of only a minimal amount of anatase TiO_2 in the sample or the lack of technique sensitivity, as the samples produced were approximately 20 nm thick. Therefore, Raman spectroscopy was further utilized to study the samples indicated.

Raman spectroscopy revealed anatase presence in the undoped sample in figure 4.3, though appearance of peaks at; 144 cm^{-1} (E_g), 199 cm^{-1} (E_g), 399 cm^{-1} (B_{1g}), 517 cm^{-1} (A_{1g}+B_{1g}) and 636 cm^{-1} (E_g). Additionally, Raman peaks were detected in the spectra corresponding to doped samples. The spectrum for $Ti_{1-x}O_2$:Al_x (99:1) contained a peak at; 144 cm^{-1}. The spectrum for $Ti_{1-x}O_2$:Sn_x (19:1) showed peaks at; 142 cm^{-1}, 197 cm^{-1}, 395 cm^{-1} and 636 cm^{-1}. The spectrum for $Ti_{1-x}O_2$:V_x (19:1) indicated peaks at; 144 cm^{-1}, 201 cm^{-1}, 395 cm^{-1}, 513 cm^{-1} and 639 cm^{-1}, whilst the $Ti_{1-x}O_2$:V_x (99:1) spectrum showed peaks at 146 cm^{-1}, 202 cm^{-1} and 640 cm^{-1} (figure 4.3).

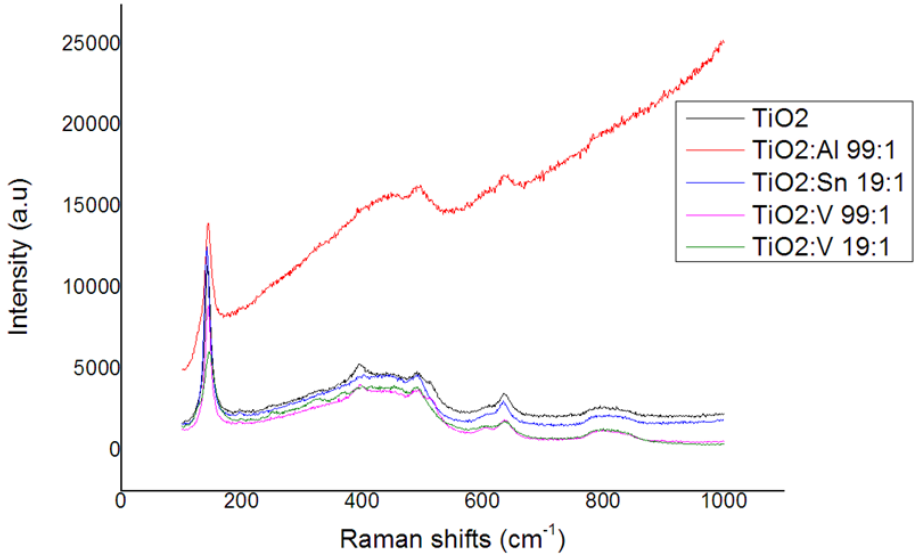

Figure 4.3: Raman spectra recorded from nominally undoped TiO_2, $Ti_{1-x}O_2$:Al_x (99:1), $Ti_{1-x}O_2$:Sn_x (19:1) and $Ti_{1-x}O_2$:V_x (19:1) and (99:1) films on quartz substrates (rest in appendix A).

The other spectra peaks present arise either from the quartz substrate [567-569] or from the dopant oxides, e.g. the peak for the $Ti_{1-x}O_2$:Al_x (99:1) sample at 645 cm^{-1} and the peaks for the $Ti_{1-x}O_2$:V_x (19:1) sample at 257 cm^{-1} and 332 cm^{-1}. Therefore indicating dopant oxide may form via the nanolaminate growth approach. Al_2O_3 and VO_2 appear to form resulting from possible ionic diffusion at elevated temperatures utilized for annealing. Typically dopant ions may accumulate at crystalline film defects (grain boundaries) and coalesce into dopant oxides, creating

mixed-oxide films. $Ti_{1-x}O_2:V_x$ and $Ti_{1-x}O_2:Al_x$ both involve dopant ions possessing smaller ionic radii (Al^{3+}: 67.5 pm and V^{4+}: 72 pm) in contrast to Ti^{4+} (74.5 pm). This potentially allows greater ionic diffusion through TiO_2 lattices as compared to $Ti_{1-x}O_2:Sn_x$ (Sn^{4+}: 83 pm), $Ti_{1-x}O_2:Hf_x$ (Hf^{4+}: 85 pm) and $Ti_{1-x}O_2:Ag_x$ (Ag^{+}: 129 pm) films. Furthermore, the other $Ti_{1-x}O_2:M_x$ (99:1 and 19:1) films indicated essentially featureless spectra, suggesting an amorphous nature to these samples.

Overall, the appearance of anatase crystallinity correlates loosely with dopant concentration for the limited number of samples studied. The $Ti_{1-x}O_2:Ag_x$ and $Ti_{1-x}O_2:Hf_x$ (99:1) films exhibit some degree of anatase crystallinity. However, increasing dopant incorporation in films by increasing the ALD ratio to (19:1) for the $Ti_{1-x}O_2:Al_x$, $Ti_{1-x}O_2:Ag_x$ and $Ti_{1-x}O_2:Hf_x$ films provides essentially amorphous materials, as observed in XRD and Raman spectroscopy.

Increasing the nanolaminate concentrations, for example for the $Ti_{1-x}O_2:Hf_x$ and $Ti_{1-x}O_2:Al_x$ (19:1) samples, appears to physically disrupt the otherwise minimal anatase formation process. This disruption presumably results from the increased ionic radius of Hf^{4+}, which can inhibit atomic reorganisation processes or the smaller ion radius of Al^{3+} allowing effective diffusion and inhibition of anatase formation. Furthermore, as noted earlier, increased aluminium concentration also appears to facilitate Al_2O_3 generation (Raman feature at 645 cm^{-1}) through diffusion.

As expected the $Ti_{1-x}O_2:V_x$ (99:1) film retains some degree of anatase crystallinity. However, here interestingly the anatase crystallinity persists even when the vanadium content is increased as in the $Ti_{1-x}O_2:V_x$ (19:1) film. This suggests that V^{4+} induces minimal disruption to the host lattice as a result of V^{4+} possessing an ionic radius similar to the host Ti^{4+} ion. Furthermore, as previously noted, increased vanadium concentration also appears to facilitate VO_2 formation (Raman features at 257 cm^{-1} and 332 cm^{-1}) through diffusion.

In stark contrast to the above results, the $Ti_{1-x}O_2:Sn_x$ (99:1) sample appears to be amorphous, whilst $Ti_{1-x}O_2:Sn_x$ (19:1) containing greater tin concentrations, appears to indicate evidence of anatase generation. Literary reports cite the ability of tin to induce anatase stabilization via a catalytic nucleation effect [204, 570]. Therefore, it

is possible, dissimilar to other systems studied here, that increased tin concentrations may lead to an enhancement in terms of anatase creation.

SEM and HRTEM were utilized to study the surface topography of the samples produced here, as well as to search for evidence of crystallinity in cross sectional samples. Figure 4.4 shows SEM images of the as-grown and annealed nominally undoped samples. The unannealed surface possesses a smooth surface morphology (figure 4.4 a). In comparison, the SEM image for the annealed nominally undoped TiO_2 sample (figure 4.4 b) shows a more mixed surface morphology, which is possibly indicative of the some crystallinity presence together with amorphous morphology.

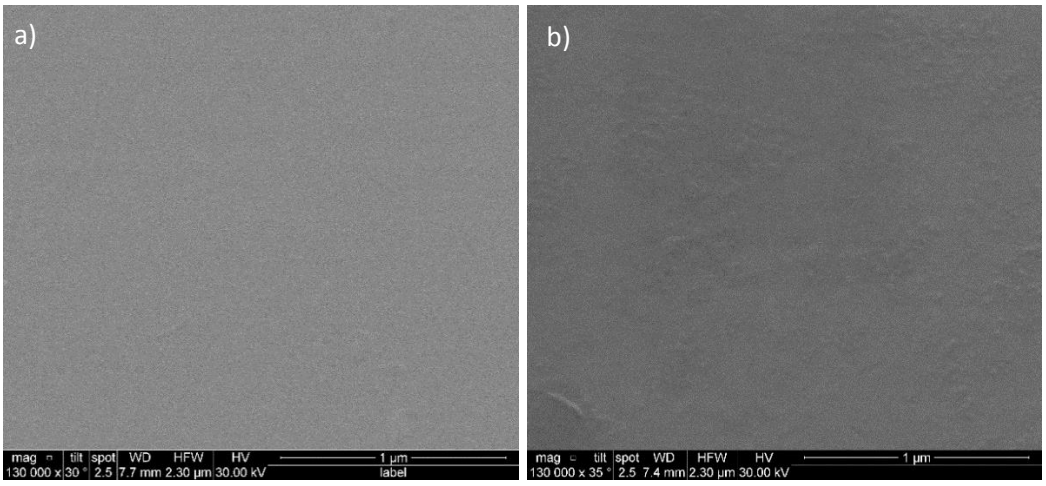

Figures 4.4: a) As-grown and b) annealed nominally undoped TiO_2 surfaces.

SEM images of the annealed $Ti_{1-x}O_2:Ag_x$ (19:1) sample are presented in figure 4.5. From this figure, the presence of some structure in the form of granular regions within an otherwise smooth morphology is suggested (figure 4.5 a)). Figure 4.5 b) also appears to show evidence of scattered surface pinhole formation, even though it is difficult to tell directly. Furthermore, the other as-grown TiO_2 films suggested smooth surface morphologies with corresponding SEM images in appendix A.

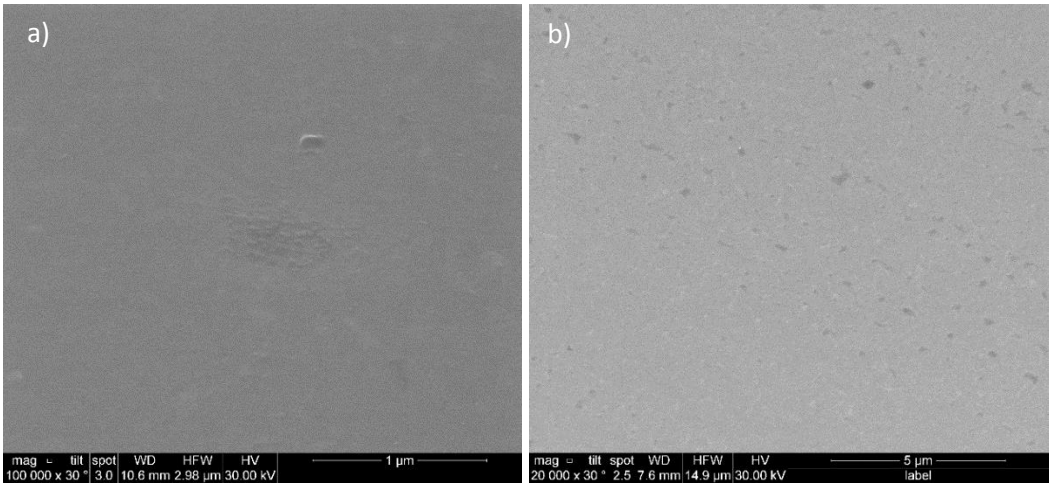

Figures 4.5: Surface SEM of the a) as-grown and b) annealed $Ti_{1-x}O_2:Ag_x$ (19:1) films.

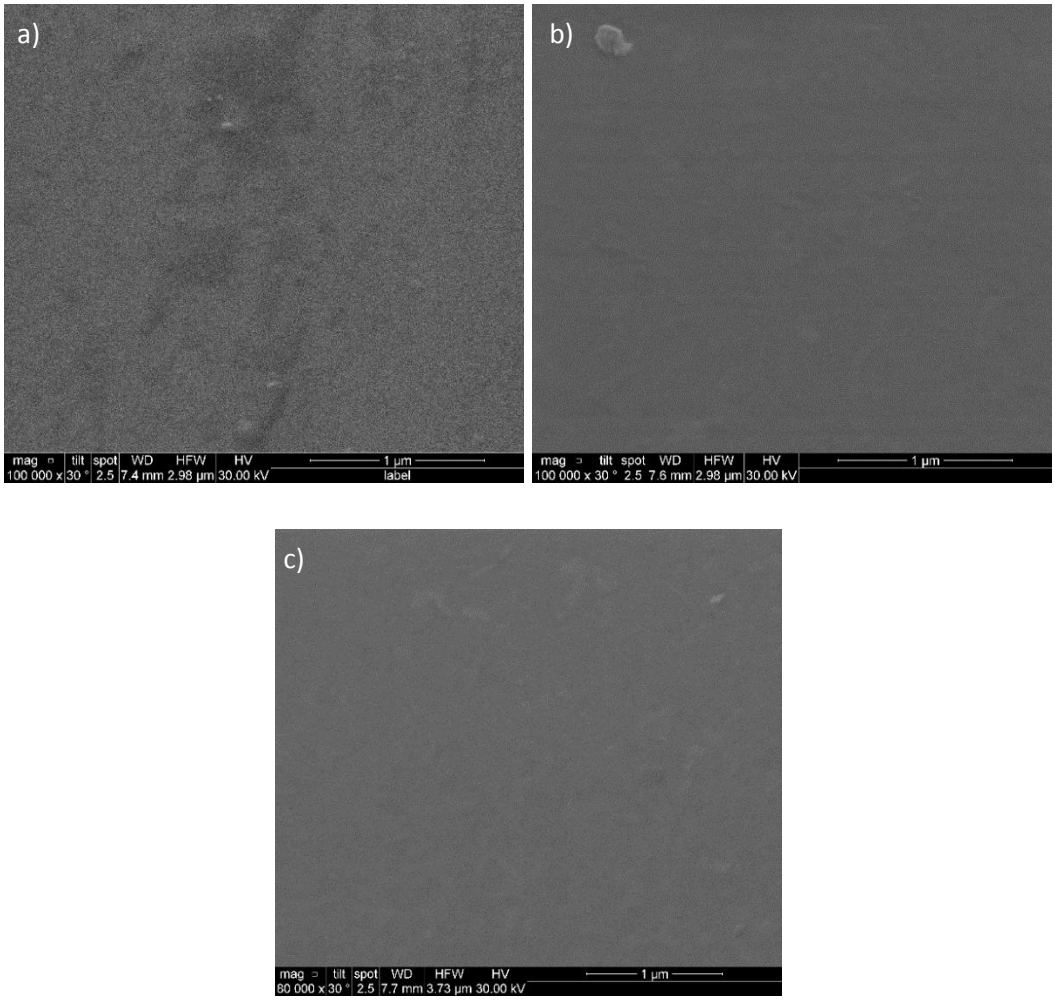

Figure 4.6: Surface SEM of a) the annealed $Ti_{1-x}O_2:Ag_x$ (99:1), b) the annealed $Ti_{1-x}O_2:Al_x$ (99:1) film and c) the annealed $Ti_{1-x}O_2:Al_x$ (19:1) film.

In comparison, the SEM images of $Ti_{1-x}O_2:Ag_x$ (99:1), as well as $Ti_{1-x}O_2:Al_x$ (99:1 and 19:1) samples show evidence of scattered lamellae structures surrounded by otherwise smooth regions (figures 4.6 a) and b)).

As might be expected, SEM images of the $Ti_{1-x}O_2:Hf_x$ and $Ti_{1-x}O_2:Sn_x$ samples show rather more structure, (figures 4.7 a), b), c) and d)). In particular the $Ti_{1-x}O_2:Hf_x$ (99:1) sample appears to possess greater granular density and pin hole size (<2 μm) as compared to the $Ti_{1-x}O_2:Hf_x$ (19:1) sample. This suggests that the detected trend of reducing crystallinity with increasing dopant inclusion carries over to these samples.

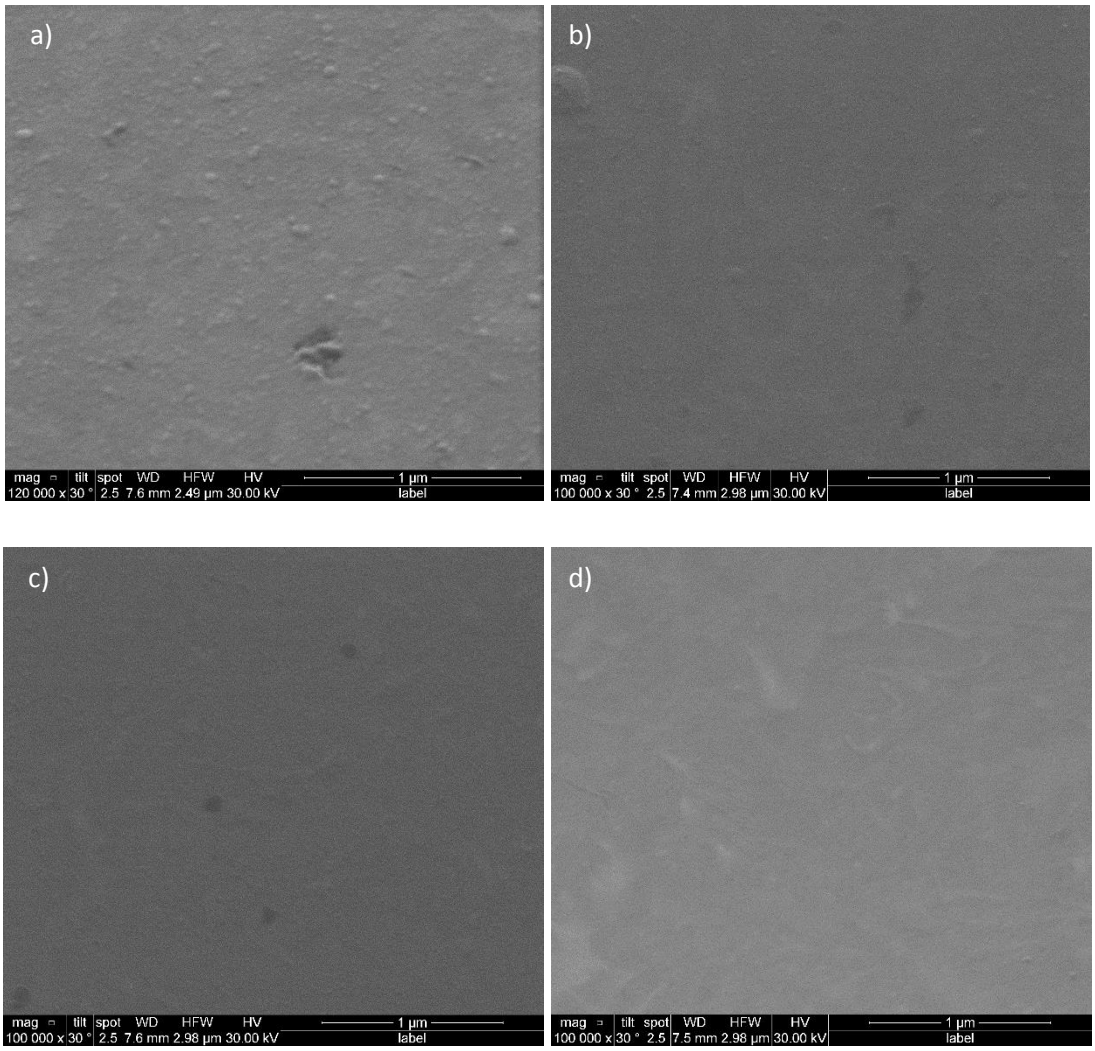

Figure 4.7: Surface SEM of a) the annealed $Ti_{1-x}O_2:Hf_x$ (99:1) film, b) the annealed $Ti_{1-x}O_2:Hf_x$ (19:1) film, c) the annealed $Ti_{1-x}O_2:Sn_x$ (99:1) film and d) the annealed $Ti_{1-x}O_2:Sn_x$ (19:1) film.

However, the $Ti_{1-x}O_2:Sn_x$ (99:1) sample appears to present a similar granular density as compared to $Ti_{1-x}O_2:Hf_x$ (19:1). The $Ti_{1-x}O_2:Sn_x$ (19:1) sample also shows evidence of a lamella morphology, indicating tin inclusion appears to favour crystallinity against the observed trend, as compared to undoped TiO_2.

SEM images recorded from the $Ti_{1-x}O_2:V_x$ (99:1 and 19:1) samples show the presence of a structure similar to that observed for the $Ti_{1-x}O_2:Sn_x$ samples, figures 4.8 a) and b). The lamella-like morphology observed in figure 4.8 a) is suggestive of some crystallinity presence. To discern any major disparities between the 99:1 and 19:1 samples is difficult, arguably the $Ti_{1-x}O_2:V_x$ sample with higher vanadium concentration shows more structure, perhaps resulting from a higher degree of crystallinity.

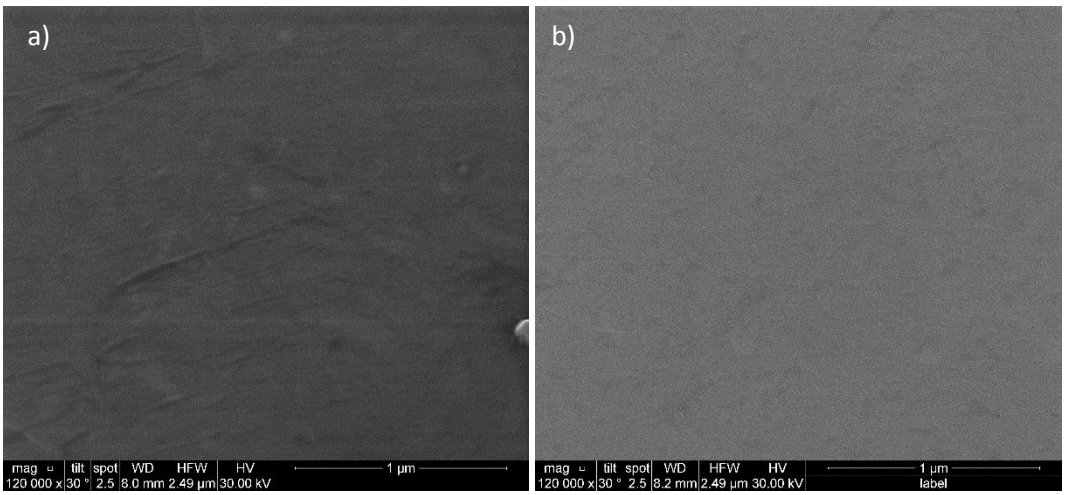

Figure: 4.8 Surface SEM of a) the annealed $Ti_{1-x}O_2:V_x$ (99:1) film and b) the annealed $Ti_{1-x}O_2:V_x$ (19:1) film.

To summarize, all as-grown TiO_2 and $Ti_{1-x}O_2:M_x$ films are essentially amorphous in nature. In contrast, annealed nominally undoped TiO_2 and some $Ti_{1-x}O_2:M_x$ films suggest anatase crystallite formation, specifically; the $Ti_{1-x}O_2:Ag_x$ (99:1), $Ti_{1-x}O_2:Hf_x$ (99:1) and $Ti_{1-x}O_2:V_x$ (99:1) films through XRD, and the $Ti_{1-x}O_2:Al_x$ (99:1), $Ti_{1-x}O_2$:Sn (19:1) and $Ti_{1-x}O_2:V_x$ (99:1 and 19:1) films through Raman spectroscopy. Additionally Surface SEM suggests some crystalline presence throughout all annealed $Ti_{1-x}O_2:M_x$ films with scattered granular or lamella morphologies.

Transmission electron microscopy (TEM) was performed on both the annealed nominally undoped TiO_2 sample and the noticeably thinner, annealed $Ti_{1-x}O_2$:Ag (19:1) sample (figure 4.9 a), b), c) and d)). The images presented for the nominally undoped TiO_2 indicates the presence of some anatase polycrystalline morphology with grain boundaries and an average film thickness of 18.5 nm. The $Ti_{1-x}O_2$:Ag_x (19:1) sample also possesses some polycrystalline morphology and grain boundaries separating both amorphous and anatase regions may be seen.

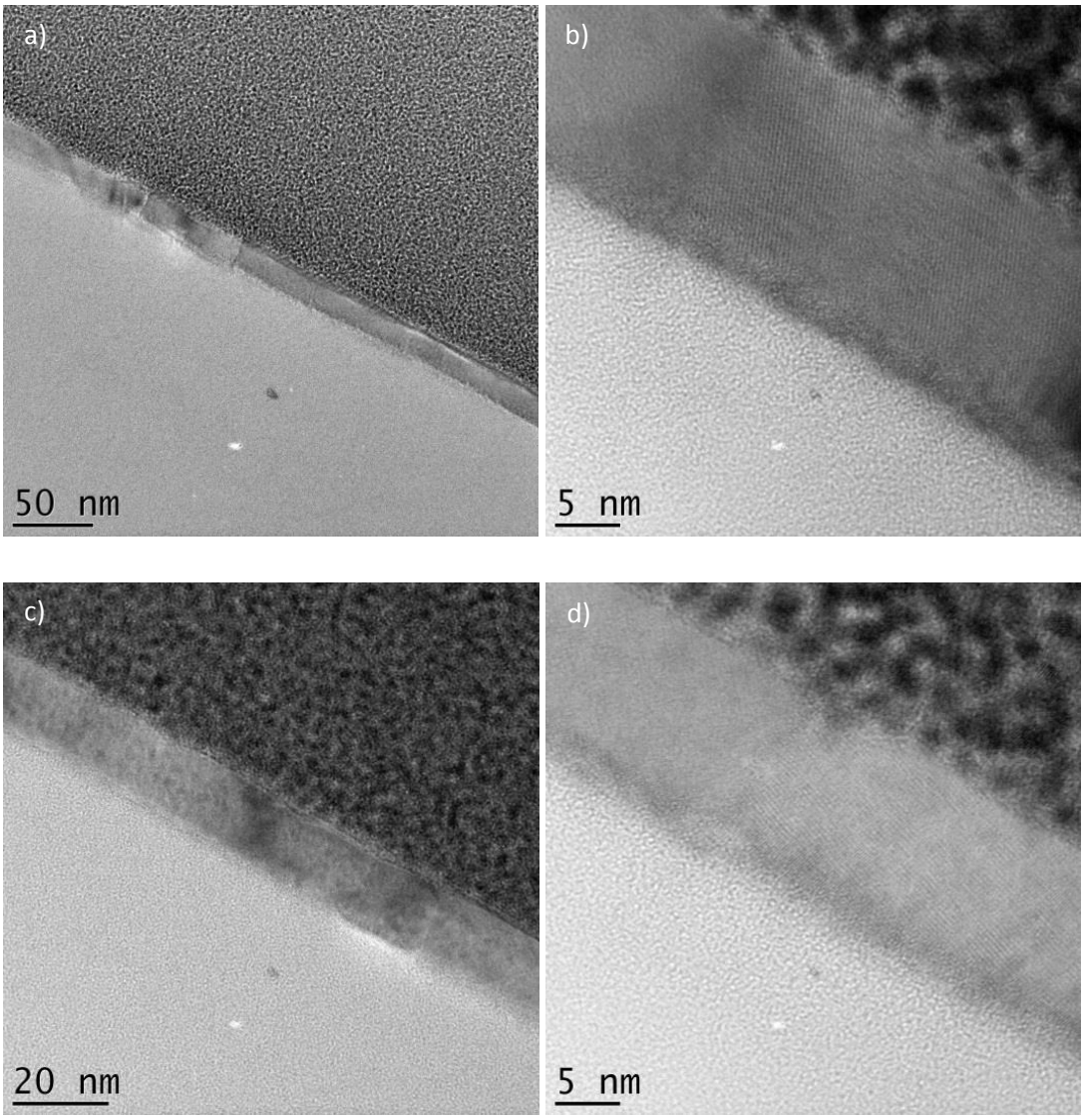

Figure 4.9: TEM on a) and b) the nominally undoped TiO_2 film, as well as on c) and d) the $Ti_{1-x}O_2$:Ag_x (19:1) film, suggesting: film thicknesses, grain boundaries and crystalline planes.

Interestingly, conclusive evidence for some crystallinity in $Ti_{1-x}O_2:Ag_x$ was not forthcoming from the XRD, Raman or SEM analysis. Also of interest is the noticeably lower average 13.6 nm thickness of the $Ti_{1-x}O_2:Ag_x$ (19:1) sample, as compared to the undoped TiO_2 sample, implying either the silver or silver precursor is somehow inhibits the growth of TiO_2.

Both the nominally undoped TiO_2 and $Ti_{1-x}O_2:Ag_x$ (19:1) samples possess distinct crystalline planes with an identical average interplanar spacing of 0.37 nm, comparable to the 0.35nm found in (101) anatase TiO_2 [571, 572]. Notably, TEM is capable of directly detecting crystallite presence, similar to those previously indicated above, in contrast to the other analytical methods utilized here, namely; XRD, Raman and SEM. Therefore, to rely solely on Raman, XRD and SEM to obtain evidence of crystallinity within the particularly thin films mentioned here would be erroneous.

XPS analysis was performed on the nominally undoped TiO_2 (Table 4.2 and 4.3) and doped TiO_2 films prepared here to determine the film composition and stoichiometry. XPS was also utilized to determine any evidence for Ti^{3+} formation, since Ti^{3+} is known to influence photocatalytic activity. Table 4.2 and 4.3 show the presence of some 5.6 % Ti^{3+} ($2p_{3/2}/2p_{1/2}$, 457.7/462.2 eV) equating to 18.5 % of the total detected titanium signal with the remaining 24.6 % (81 % total) titanium present as Ti^{4+} ($2p_{3/2}/2p_{1/2}$, 459.3/464.9 eV) [150, 573]. On comparison with the signals for lattice incorporated oxygen (O 1s, 530.6 eV) at 58.8 %, a very slight bulk oxygen deficiency is indicated if one assumes an ideal 1:2 (Ti:O). This suggests that Ti^{3+} formation may arise through $V_{O^{\cdot\cdot}}$ defect creation from oxygen diffusion [574].

Low resolution	TiO_2	TiO_2
Peak	Position (eV)	Concentration (%)
O 1s	529.9	66.9
Ti 2p	458.9	30.1
C 1s	284.9	3.0

Table 4.2: Low resolution XPS results for the annealed nominally undoped TiO_2 film.

High resolution	TiO_2	TiO_2
Peak	Position (eV)	Concentration (%)
O 1s_1	530.6	58.8
O 1s_2	531.7	8.7
Ti^{3+} 2p_1	457.7	3.7
Ti^{3+} 2p	462.6	1.9
Ti^{4+} 2p_1	459.3	16.4
Ti^{4+} 2p	464.9	8.2
C 1s_1	284.7	1.6
C 1s_2	286.6	0.4
C 1s_3	289.4	0.3

Table 4.3: High resolution XPS results for the annealed nominally undoped TiO_2 film.

After three seconds sputtering, it was found that signals due to surface nitrogen, carbon and silicon contamination were removed. Detection of these elements subsequent to sputtering may be attributed as arising directly from the growth process. For the nominally undoped TiO_2 film, minimal bulk carbon (1.6 % C-C/C=C bonding) and remnant surface (0.7 % C-O/O-C=O) contamination result from absorbed atmospheric CO_2 generating surface carbonates on reaction with hydroxyl groups [575].

For doped TiO_2 samples, Ti^{3+} concentrations were indicated to vary as a function of both annealing and the dopant nature. Table 4.4 compares Ti^{3+} percentages in doped TiO_2 films with remaining titanium ions present as Ti^{4+} in sufficiently oxygen saturated environments (a 1:2 (Ti 2p : O 1s) ratio).

	Total Ti^{3+} % as-grown films	Total Ti^{3+} % annealed films	Total Ti^{3+} % after sputtering
TiO_2	n/a	19	n/a
$Ti_{1-x}O_2:Ag_x$ (19:1)	17	16	52
$Ti_{1-x}O_2:Al_x$ (19:1)	20	12	n/a
$Ti_{1-x}O_2:Hf_x$ (19:1)	16	16	18
$Ti_{1-x}O_2:Sn_x$ (19:1)	13	11	31
$Ti_{1-x}O_2:V_x$ (19:1)	15	8	n/a

Table 4.4: Ti^{3+} percentages in as-grown and annealed (surface and depth profile) for the nominally undoped and doped TiO_2 films

As observed, annealing decreases Ti^{3+} concentrations (table 4.4) for all doped TiO_2 films, suggesting efficient Ti^{3+} to Ti^{4+} oxidization from excess heat energy provision in an oxygen rich environment. However, increasing film depth on sputtering reveals significantly greater bulk Ti^{3+} concentrations for the annealed $Ti_{1-x}O_2:Ag_x$ and $Ti_{1-x}O_2:Sn_x$ (19:1) films, as compared to surface regions. As well as minimal bulk Ti^{3+} concentration increase for the annealed $Ti_{1-x}O_2:Hf_x$ (19:1) film, as compared to surface regions. This variation between bulk and surface regions, could either be from direct atmospheric oxidation or could correlate with bulk oxygen leaching during annealing, providing greater bulk Ti^{3+} concentrations through reduction of Ti^{4+}.

Additionally, no obvious correlation is detected between the nature of the dopant and Ti^{3+} concentration variation with film annealing. However, the as-grown $Ti_{1-x}O_2:Al_x$ (19:1) film shows the greatest Ti^{3+} concentration as compared to all other doped films studied. Although a correlation cannot be proven from the presented data, the as-grown $Ti_{1-x}O_2:Al_x$ (19:1) possessing highest Ti^{3+} concentration could originate via charge compensation mechanisms. These mechanisms lead to greater $V_O^{\cdot\cdot}/Ti^{3+}$ concentrations, through aliovalent (Al^{3+}) dopant ion "substitution" for Ti^{4+} ions.

Furthermore, the annealed $Ti_{1-x}O_2:Al_x$ (19:1) samples indicates a significant decrease in Ti^{3+} concentration. As previously noted, this presumably arises from annealing in an oxygen rich atmosphere. Under such conditions, electrical factors similar to charge compensation are presumably negated by alternative chemical variations related to dopant oxide formation, as suggested from the Raman spectroscopy data presented on page 129.

Tables 4.5, 4.6 and 4.7 show the XPS analysis of the as-grown and annealed $Ti_{1-x}O_2:Ag_x$ (19:1) films with table 4.6 comparing $Ti_{1-x}O_2:Ag_x$ (19:1) film peak positions with the annealed nominally undoped TiO_2 film (table 4.2 and 4.3). Additionally, table 4.7 shows XPS analysis of the annealed $Ti_{1-x}O_2:Ag_x$ (19:1) film subsequent to 40 seconds sputtering with peak position comparison to the un-sputtered annealed $Ti_{1-x}O_2:Ag_x$ (19:1) film.

	$Ti_{1-x}O_2:Ag_x$ (19:1)	$Ti_{1-x}O_2:Ag_x$ (19:1)	Annealed $Ti_{1-x}O_2:Ag_x$ (19:1)	Annealed $Ti_{1-x}O_2:Ag_x$ (19:1)
Peak	Position (eV)	Concentration (%)	Position (eV)	Concentration (%)
O 1s	530.5	63.7	531.9	58.2
Ti 2p	458.5	27.0	457.9	8.6
C 1s	285.5	8.2	284.9	4.4
N 1s	n/a	n/a	399.9	0.3
Si 2p	102.5	1.0	102.7	27.6
Fe 2p	n/a	n/a	710.9	0.6
Ca 2p	n/a	n/a	346.9	0.3

Table 4.5: Low resolution XPS results for both the as-grown and annealed $Ti_{1-x}O_2:Ag_x$ (19:1) films.

	$Ti_{1-x}O_2:Ag_x$ (19:1)	$Ti_{1-x}O_2:Ag_x$ (19:1)	Annealed $Ti_{1-x}O_2:Ag_x$ (19:1)	Annealed $Ti_{1-x}O_2:Ag_x$ (19:1)
Peak	Position (eV)	Concentration (%)	Position (eV)	Concentration (%)
O 1s_1 (metal oxide)	530.6	54.2	530.5	25.0
O 1s_2 (organics, hydroxide)	531.8	10.1	532.6 (531.7)	57.3
Ti 2p_1 (Ti^{3+} $2p_{3/2}$)	457.5	3.3	457.1 (457.7)	1.2
Ti 2p (Ti^{3+} $2p_{1/2}$)	462.8	1.6	462.2 (462.6)	0.6
Ti 2p_1 (Ti^{4+} $2p_{3/2}$)	459.1	15.8	458.9 (459.3)	6.2
Ti 2p (Ti^{4+} $2p_{1/2}$)	464.8	7.9	464.5 (464.9)	3.1
C 1s_1 (C=C/C-C)	284.7	3.9	284.8	4.7
C 1s_2 (C-O)	286.3 (286.6)	2.4	286.0 (286.6)	1.6
C 1s_3 (O-C=O)	289.2	0.9	288.8 (289.4)	0.4

Table 4.6 High resolution XPS results for both the as-grown and annealed $Ti_{1-x}O_2:Ag_x$ (19:1) films with the peak shifts from the annealed nominally undoped TiO_2 film positions highlighted in brackets.

	Annealed $Ti_{1-x}O_2:Ag_x$ (19:1) 40 seconds sputtering	Annealed $Ti_{1-x}O_2:Ag_x$ (19:1) 40 seconds sputtering
Peak	Position (eV)	Concentration (%)
O 1s_1	531.9 (530.5)	25.6
O 1s_2	533.4 (532.6)	65.9
Ti^{3+} 2p_1	458.7 (457.1)	2.7
Ti^{3+} 2p	464.3 (462.2)	1.3
Ti^{4+} 2p_1	460.1 (458.9)	2.5
Ti^{4+} 2p	465.8 (464.5)	1.2
C 1s_1	285.4 (284.8)	0.7

Table 4.7: High Resolution XPS results for the annealed $Ti_{1-x}O_2:Ag_x$ (19:1) films after 40 seconds sputtering, with comparison to peak positions for the annealed $Ti_{1-x}O_2:Ag_x$ (19:1) after 3 seconds sputtering highlighted in brackets.

Most strikingly, tables 4.5 and 4.6 shows that silver (Ag^+ $3d_{5/2}$: 367.5 or 367.7 eV) [573, 576] is absent from both as-grown and annealed $Ti_{1-x}O_2:Ag_x$ (19:1) film surface regions. Additionally, table 4.7 indicates silver is also absent from bulk $Ti_{1-x}O_2:Ag_x$ (19:1) films, either suggesting; an unsuccessful doping during ALD synthesis or negligible silver concentrations below XPS detectable limits.

Table 4.5 also indicates small amounts (0.3 %) of adventitious nitrogen as well as 0.3% Ca^{2+} 2p (346.9-347.9 eV) [577] and 0.6% Fe^{2+} $2p_{(3/2 \text{ and } 1/2)}$ (709.9-710.9 and 724.9 eV) [545] contamination. Ca^{2+} and Fe^{2+} possibly result from quartz substrate ion diffusion on annealing with quartz substrates containing 0.5ppm calcium and 0.1ppm iron concentrations [578].

Additionally, table 4.5 also suggests a large disparity between the as-grown and annealed $Ti_{1-x}O_2:Ag_x$ (19:1) films with a greater (20.9 %) silicon signal detected in annealed films. This possibly results from either a lower $Ti_{1-x}O_2:Ag_x$ (19:1) film thickness observed from TEM, or less likely a silicon ion diffusion from substrates. In comparison, 1 % silicon is detected in as-grown surfaces.

Somewhat unsurprisingly, table 4.7 shows an even greater bulk silicon concentration (27.6 %) in or under the annealed $Ti_{1-x}O_2:Ag_x$ (19:1) film, after 40 seconds sputtering. Table 4.7 also indicates significant 2p Ti and O 1s peak shifts (+1.5/2.1/1.2/1.3 eV) and (+1.4/0.8 eV) respectively, between surface and 40 seconds sputtered $Ti_{1-x}O_2:Ag_x$ (19:1) regions. Therefore suggesting a change in titanium and oxygen chemical environments, potentially influenced by greater silicon concentrations (figures 4.10 and 4.11).

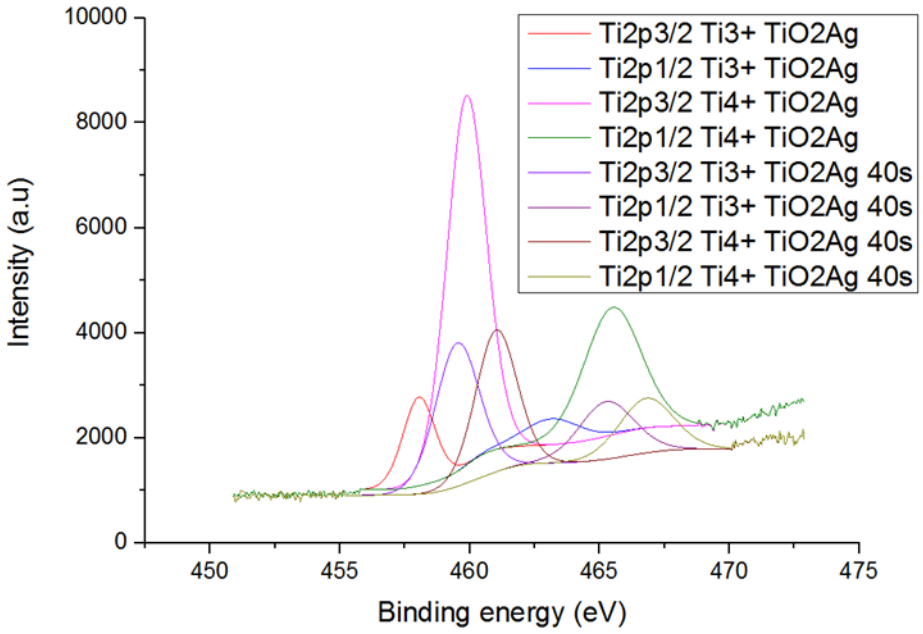

Figure 4.10: Ti 2p peak shifts between surface (after 3 seconds sputtering) and bulk (after 40 seconds sputtering) for annealed $Ti_{1-x}O_2:Ag_x$ (19:1) film environments.

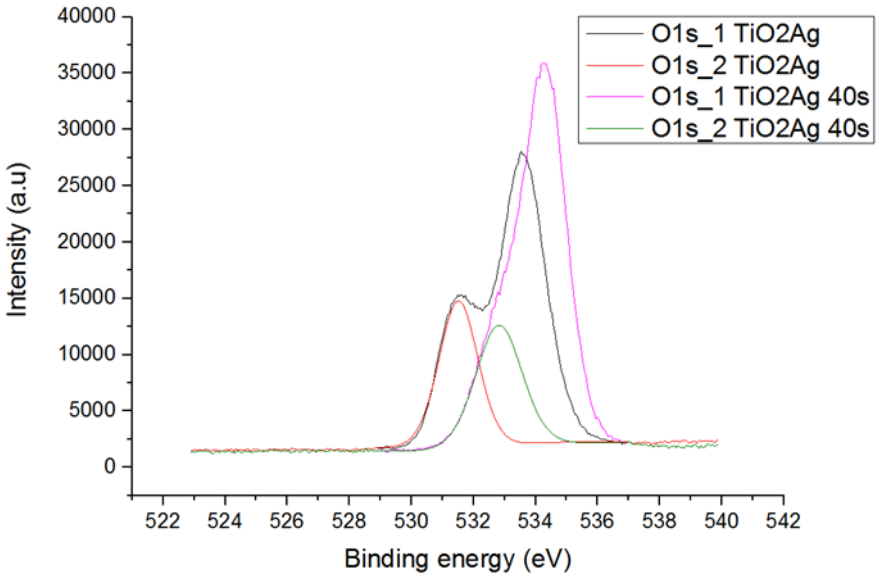

Figure 4.11: O 1s_1 and O 1s_2 peak shifts between surface (after 3 seconds sputtering) and bulk (after 40 seconds sputtering) for annealed $Ti_{1-x}O_2:Ag_x$ (19:1) film environments

Greater silicon concentrations could also provide the variation in titanium and oxygen chemical environments. As suggested by the O 1s_2 (0.9 eV) and Ti 2p (0.4-0.6 eV) peak shifts between the nominally undoped TiO_2 and $Ti_{1-x}O_2:Ag_x$ (19:1) films, shown in figures 4.12 and 4.13.

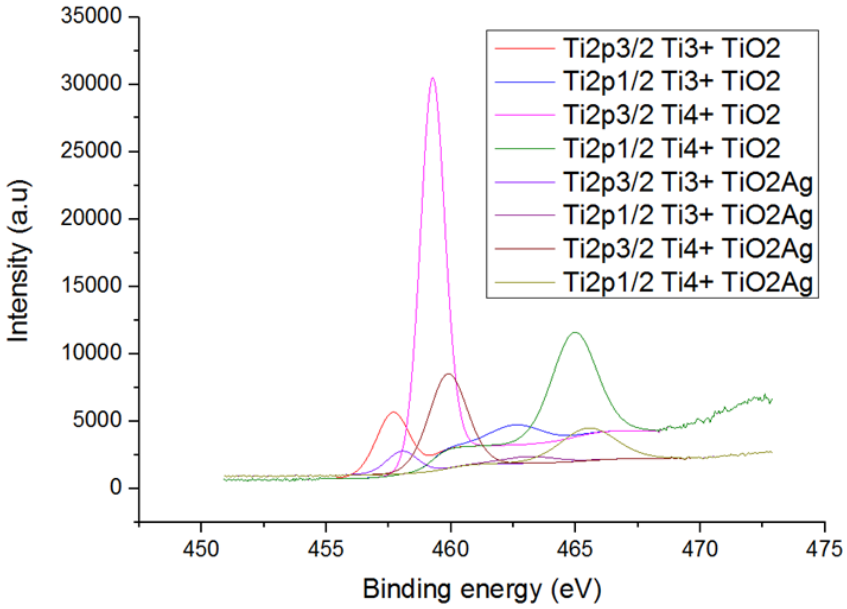

Figure 4.12: Ti 2p peak shifts between the annealed nominally undoped TiO_2 film and the annealed $Ti_{1-x}O_2:Ag_x$ (19:1) film.

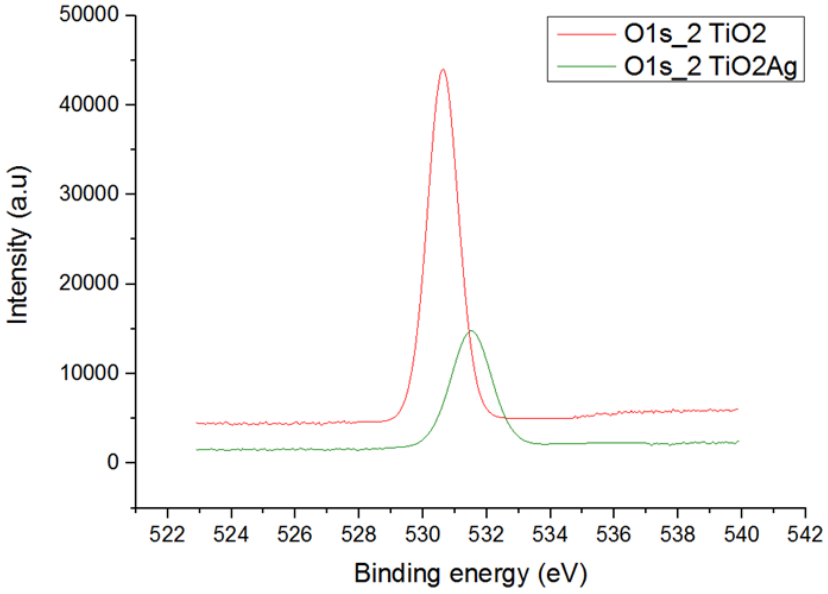

Figure 4.13: O 1s_2 peak shifts between the annealed nominally undoped TiO_2 film and the annealed $Ti_{1-x}O_2:Ag_x$ (19:1) film.

Furthermore, relatively large adventitious carbon concentrations occur subsequent to sputter cleaning (7.2/6.7 %, as-grown/annealed $Ti_{1-x}O_2:Ag_x$ (19:1)), suggesting incomplete surface contamination removal. Additionally, C 1s_2 and C 1s_3 peak shifts are detected between the nominally undoped TiO_2 and $Ti_{1-x}O_2:Ag_x$ (19:1) films (figure 4.14). As well as C 1s_1 peak shifts between the surface (3 second sputtering) and bulk (40 seconds sputtering) $Ti_{1-x}O_2:Ag_x$ (19:1) film regions (figure 4.15). These peak shifts suggesting an alteration in carbon chemical environments, possibly related to the high silicon concentrations observed.

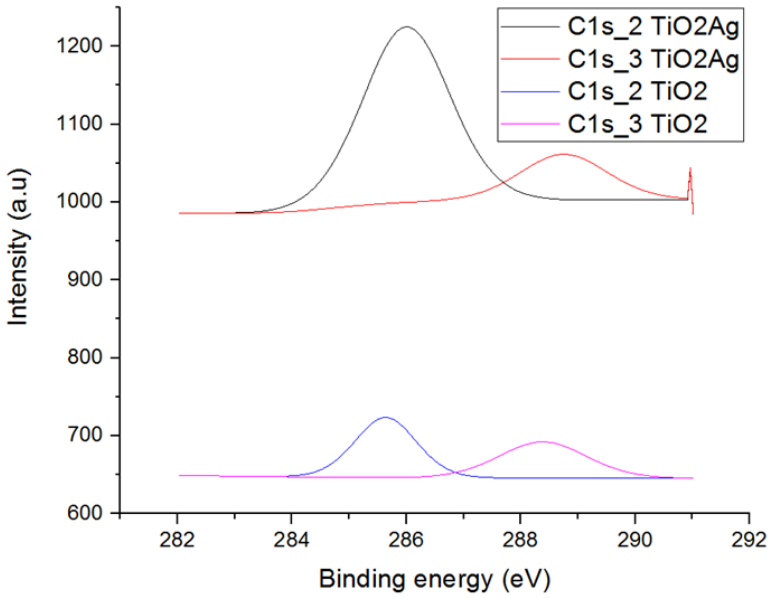

Figure 4.14: C 1s_2 and C 1s_3 peak shifts between the nominally undoped TiO_2 film and the $Ti_{1-x}O_2$:Ag_x (19:1) film.

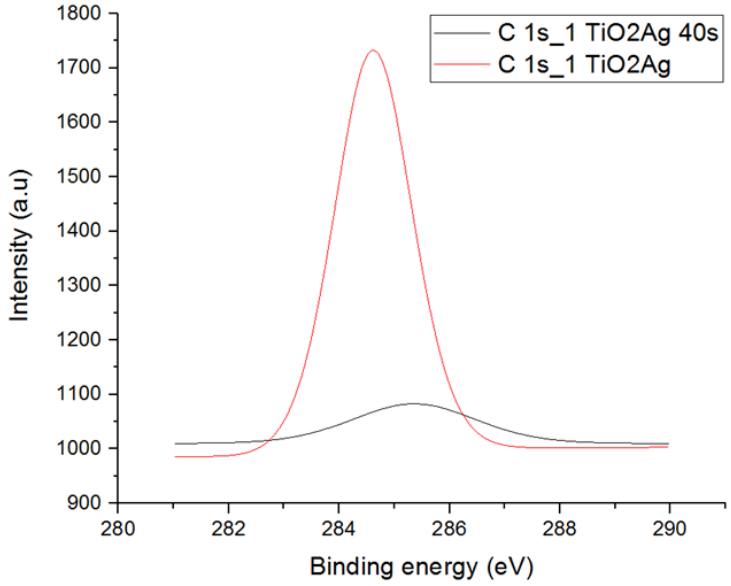

Figure 4.15: C 1s_1 peak shifts between surface (after 3 seconds sputtering) and bulk (after 40 seconds sputtering) for annealed $Ti_{1-x}O_2$:Ag_x (19:1) film environments.

And furthermore, depth profiling indicates a significantly lower thickness to the annealed $Ti_{1-x}O_2$:Ag_x (19:1) film with a 100 second sputtering maximum, as compared to 700 and 1500 second sputtering maximums for the annealed $Ti_{1-x}O_2$:Sn_x and $Ti_{1-x}O_2$:Hf_x (19:1) films respectively, shown below.

	$Ti_{1-x}O_2:Al_x$ (19:1)	$Ti_{1-x}O_2:Al_x$ (19:1)	Annealed $Ti_{1-x}O_2:Al_x$ (19:1)	Annealed $Ti_{1-x}O_2:Al_x$ (19:1)
Peak	Position (eV)	Concentration (%)	Position (eV)	Concentration (%)
O 1s	529.7	62.9	529.5	61.3
Ti 2p	458.7	25.0	485.5	24.2
Al 2p	73.7	6.2	73.5	6.1
C 1s	284.7	5.8	284.5	8.5

Table 4.8: Low resolution XPS results for both the as-grown and annealed $Ti_{1-x}O_2:Al_x$ (19:1) films.

	$Ti_{1-x}O_2:Al_x$ (19:1)	$Ti_{1-x}O_2:Al_x$ (19:1)	Annealed $Ti_{1-x}O_2:Al_x$ (19:1)	Annealed $Ti_{1-x}O_2:Al_x$ (19:1)
Peak	Position (eV)	Concentration (%)	Position (eV)	Concentration (%)
O 1s_1	530.5	54.7	530.4	55.4
O 1s_2	531.7	8.2	531.7	6.9
Ti^{3+} $2p_{3/2}$	457.4 (457.7)	3.4	457.3 (457.7)	2.0
Ti^{3+} $2p_{1/2}$	462.8	1.7	462.9 (462.6)	1.0
Ti^{4+} $2p_{3/2}$	459.0 (459.3)	13.6	458.9 (459.3)	14.6
Ti^{4+} $2p_{1/2}$	464.7	6.8	464.6 (464.9)	7.3
C 1s_1	284.7	3.7	284.8	5.0
C 1s_2	286.5	1.7	286.6	1.7
C 1s_3	289.3	0.5	289.1 (289.4)	0.7
Al 2p_1	74.3	5.0	74.2	4.8
Al 2p	76.1	0.6	76.0	0.5

Table 4.9: High resolution XPS results for both the as-grown and annealed $Ti_{1-x}O_2:Al_x$ (19:1) films with the peak shifts from the annealed nominally undoped TiO_2 film positions highlighted in brackets.

Tables 4.8 and 4.9 show the XPS analysis of the as-grown and annealed $Ti_{1-x}O_2:Al_x$ (19:1) films and table 4.9 compares $Ti_{1-x}O_2:Al_x$ peak positions with the annealed nominally undoped TiO_2 film (tables 4.2 and 4.3). Both films indicate high Al^{3+} concentrations; 5.6/5.3 % (unannealed/annealed), predominately accumulated (5/4.8 %) assumedly as nanolaminate AlO_x (2p: 74.3/74.2 eV) [579]. This generated $Ti_{0.82}Al_{0.18}O_2/Ti_{0.83}Al_{0.17}O_2$ film compositions on comparison of titanium and aluminium concentrations. Subsequent Al-O-Ti bond formation provides 0.4/0.3 eV peak shifts for Ti 2p (457.3, 462.9, 458.9 and 464.6eV) (figures 4.16 and 4.17).

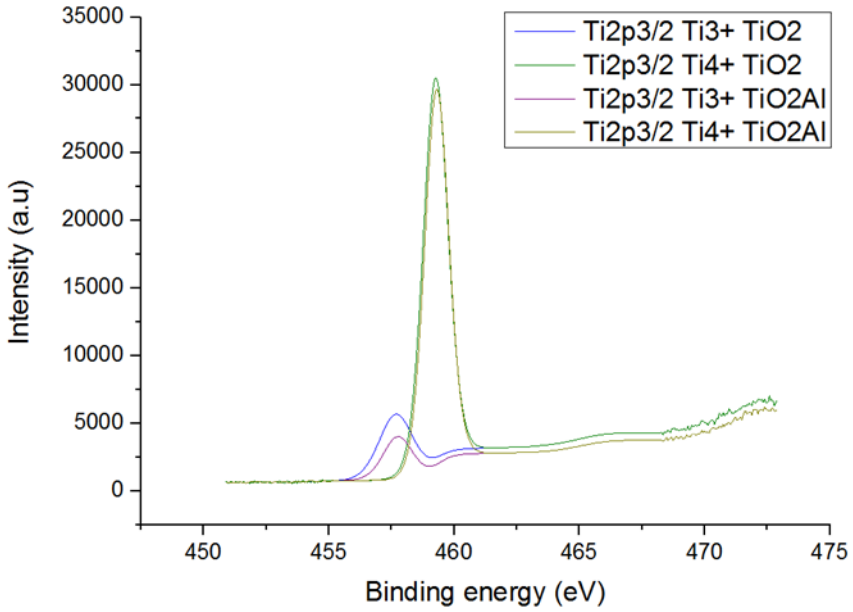

Figure 4.16: Ti 2p peak shifts between the annealed nominally undoped TiO_2 film and the as grown $Ti_{1-x}O_2:Al_x$ (19:1) film.

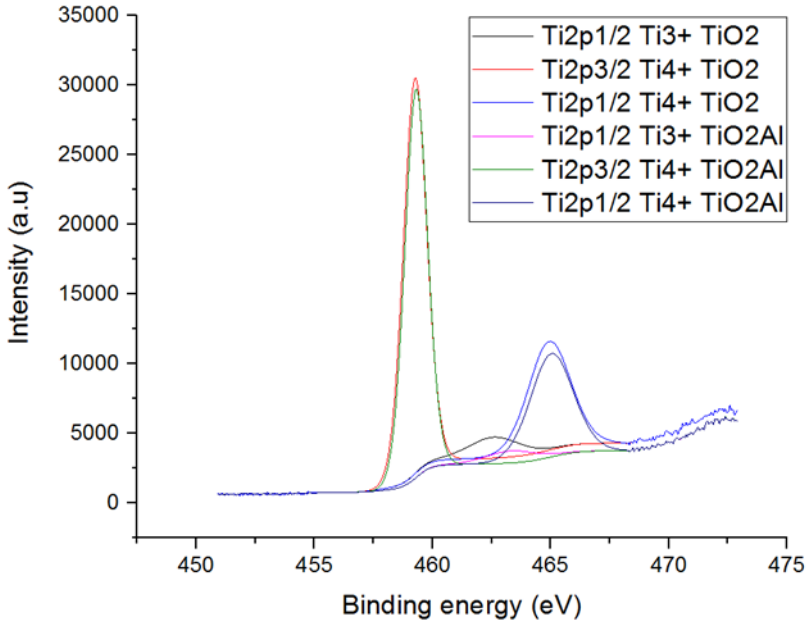

Figure 4.17: Ti 2p peak shifts between the annealed nominally undoped TiO_2 film and the annealed TiO_2:Al (19:1) film.

Remaining Al^{3+} (0.6/0.5 %) are present within Al-O-C bonding (2p: 76.1/76.0 eV) [580], generating a 0.3 eV C 1s (289.1 eV) peak shift with relatively high surface adsorbed carbon contamination after sputter cleaning (5.8/8.5 % total). Thus suggesting incomplete surface contamination removal (figure 4.18).

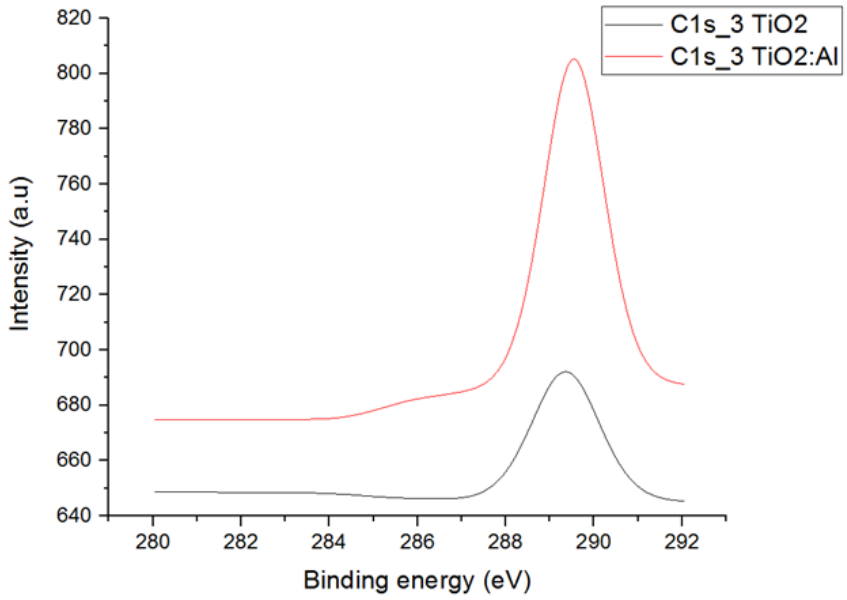

Figure 4.18: C 1s_3 peak shifts between the annealed nominally undoped TiO_2 film and the annealed $Ti_{1-x}O_2$:Al_x (19:1) film.

Tables 4.10, 4.11 and 4.12 show the results of XPS analysis on the as-grown and annealed $Ti_{1-x}O_2:Hf_x$ (19:1) films with comparison to the annealed nominally undoped TiO_2 film (tables 4.2 and 4.3).

	$Ti_{1-x}O_2:Hf_x$ (19:1)	$Ti_{1-x}O_2:Hf_x$ (19:1)	Annealed $Ti_{1-x}O_2:Hf_x$ (19:1)	Annealed $Ti_{1-x}O_2:Hf_x$ (19:1)
Peak	Position (eV)	Concentration (%)	Position (eV)	Concentration (%)
O 1s	529.5	63.8	529.9	64.7
Ti 2p	458.5	26.5	458.9	28.7
Hf 4d	212.5	1.7	212.9	0.5
C 1s	284.5	7.3	284.9	6.1
N 1s	400.5	0.7	-	-

Table 4.10: Low resolution XPS results for both the as-grown and annealed $Ti_{1-x}O_2:Hf_x$ (19:1) films.

	Annealed $Ti_{1-x}O_2:Hf_x$ (19:1)	Annealed $Ti_{1-x}O_2:Hf_x$ (19:1)
Peak	Position (eV)	Concentration (%)
O 1s	530.7	67.9
Ti 2p	459.3	29.9
C 1s	284.9	1.6
Hf 4d	213.7	0.6

Table 4.11 High resolution XPS results for the annealed $Ti_{1-x}O_2:Hf_x$ (19:1) film after 100 seconds sputtering.

	$Ti_{1-x}O_2:Hf_x$ (19:1)	$Ti_{1-x}O_2:Hf_x$ (19:1)	Annealed $Ti_{1-x}O_2:Hf_x$ (19:1)	Annealed $Ti_{1-x}O_2:Hf_x$ (19:1)
Peak	Position (eV)	Concentration (%)	Position (eV)	Concentration (%)
O 1s_1	530.4	54.4	530.4	57.6
O 1s_2	531.7	7.0	531.6	7.8
Ti^{3+} $2p_{3/2}$	457.4 (457.7)	2.7	457.5	3.0
Ti^{3+} $2p_{1/2}$	462.4	1.3	462.4	1.5
Ti^{4+} $2p_{3/2}$	458.9 (459.3)	14.7	459.1	16.1
Ti^{4+} $2p_{1/2}$	464.6 (464.9)	7.3	464.7	8.1
C 1s_1	284.7	6.6	284.7	3.2
C 1s_2	286.5	3.0	286.5	1.2
C 1s_3	289.2	0.9	289.4	0.7
N 1s	399.8	0.4	400.4	0.4
N 1s	401.2	0.2	-	-
Hf 4d_1	213.5	0.9	213.4	0.2
Hf 4d	224.2	0.7	224.0	0.2

Table 4.12: High resolution XPS results for both the as-grown and annealed $Ti_{1-x}O_2:Hf_x$ (19:1) films with the peak shifts from the annealed nominally undoped TiO_2 film positions highlighted in brackets.

Both films contain low Hf^{4+} concentrations: 1.6/0.4 % corresponding to $Ti_{0.96}Hf_{0.04}O_2$/$Ti_{0.99}Hf_{0.01}O_2$ film composition (as-grown/annealed). Additionally, table 4.11, the $Ti_{1-x}O_2:Hf_x$ (19:1) film after 100 seconds sputtering indicates 0.6 % Hf^{4+}, predominately accumulating assumedly as nanolaminate HfO_2 (Hf 4d: 213.5/213.4 and 224.2/224 eV) [581] to generate a $Ti_{0.97}Hf_{0.03}O_2$ bulk composition. Figure 4.19 shows 0.3-0.6 eV peak shifts across a majority of Ti 2p peaks (457.4, 458.9 and 464.6eV) potentially resulting from lower electronegativity of hafnium (1.3) compared to titanium (1.5), subsequently varying titanium atomic electron density on Ti-O-Hf bonding [582].

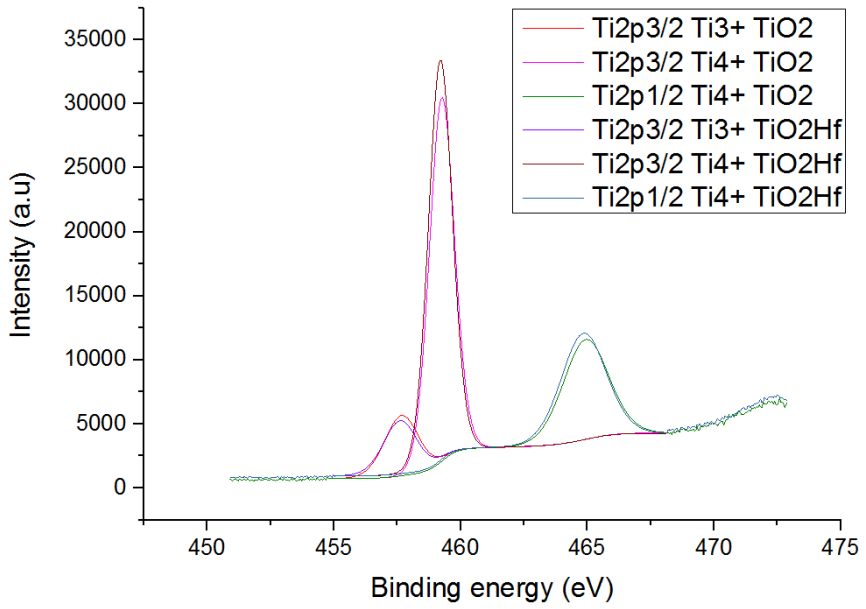

Figure 4.19: Ti 2p peak shifts between the annealed nominally undoped TiO_2 film and the as-grown $Ti_{1-x}O_2:Hf_x$ (19:1) film.

From Table 4.12, the $Ti_{1-x}O_2:Hf_x$ (19:1) films both suggest adventitious carbon (7.3 and 5.1 %) and nitrogen (0.6 and 0.4 %) contamination probably resulting from atmospheric sources. Furthermore, from table 4.11, lower (1.6 %) carbon contamination exists after 100 seconds sputtering, suggesting minimal precursor residue throughout the annealed $Ti_{1-x}O_2:Hf_x$ (19:1) film.

	$Ti_{1-x}O_2:Sn_x$ (19:1)	$Ti_{1-x}O_2:Sn_x$ (19:1)	Annealed $Ti_{1-x}O_2:Sn_x$ (19:1)	Annealed $Ti_{1-x}O_2:Sn_x$ (19:1)
Peak	Position (eV)	Concentration (%)	Position (eV)	Concentration (%)
O 1s	529.7	64.4	529.7	63.5
Ti 2p	458.7	27.8	458.7	26.8
Sn 3d	486.7	3.0	485.7	3.1
C 1s	285.7	4.8	284.7	4.9
N 1s	-	-	401.7	0.3
Si 2p	-	-	100.7	1.4

Table 4.13: Low resolution XPS results for both the as-grown and annealed $Ti_{1-x}O_2:Sn_x$ (19:1) films.

	$Ti_{1-x}O_2:Sn_x$ (19:1)	$Ti_{1-x}O_2:Sn_x$ (19:1)	Annealed $Ti_{1-x}O_2:Sn_x$ (19:1)	Annealed $Ti_{1-x}O_2:Sn_x$ (19:1)
Peak	Position (eV)	Concentration (%)	Position (eV)	Concentration (%)
O 1s_1	530.5	56.8	530.3 (530.6)	61.4
O 1s_2	531.6	6.9	531.8	3.1
Ti^{3+} $2p_{3/2}$	457.4 (457.7)	2.5	457.5	2.1
Ti^{3+} $2p_{1/2}$	462.6	1.3	462.2 (462.2)	1.0
Ti^{4+} $2p_{3/2}$	459.0 (459.3)	16.5	458.9 (459.3)	16.2
Ti^{4+} $2p_{1/2}$	464.6 (464.9)	8.3	464.6 (464.9)	8.1
C 1s_1	284.7	2.7	284.7	3.5
C 1s_2	286.4	1.6	286.5	1.1
C 1s_3	289.1 (289.4)	0.6	289.2	0.6
Sn 3d	486.9	2.9	486.7	3.0

Table 4.14: High resolution XPS results for both the as-grown and annealed $Ti_{1-x}O_2:Sn_x$ (19:1) films with the peak shifts from the annealed nominally undoped TiO_2 film positions highlighted in brackets.

	Annealed $Ti_{1-x}O_2:Hf_x$ (19:1)	Annealed $Ti_{1-x}O_2:Hf_x$ (19:1)
Peak	Position (eV)	Concentration (%)
O 1s	530.5	67.6
Ti 2p	459.1	29.5
C 1s	285.0	0.7
Sn 3d	486.9	2.2

Table 4.15 High resolution XPS results for the annealed $Ti_{1-x}O_2:Sn_x$ (19:1) film after 60 seconds sputtering.

Tables 4.13, 4.14 and 4.15 show the results of XPS analysis on the as-grown and annealed $Ti_{1-x}O_2:Sn_x$ (19:1) films with comparison to the annealed nominally undoped TiO_2 film (table 4.2 and 4.3). Both the as-grown and annealed $Ti_{1-x}O_2:Sn_x$ films indicate approximately 3.0 % Sn^{4+}, predominately accumulated as SnO_2 [549] and producing $Ti_{0.9}Sn_{0.1}O_2$ film compositions on comparison between titanium and tin concentrations. Continued sputtering of the annealed $Ti_{1-x}O_2:Sn_x$ (19:1) film subsequently indicates lower bulk tin concentrations (2.2 % at 60 seconds) resulting in a bulk $Ti_{0.98}Sn_{0.02}O_2$ film composition. Additionally, the annealed $Ti_{1-x}O_2:Sn_x$ (19:1) film shows O 1s_1 (530.3 eV) and Ti 2p (462.2, 458.9 and 464.6 eV) peak shifts (0.3-0.4 eV) with tin doping (figures 4.20 – 4.23), suggesting a variation in oxygen and titanium chemical environments [582].

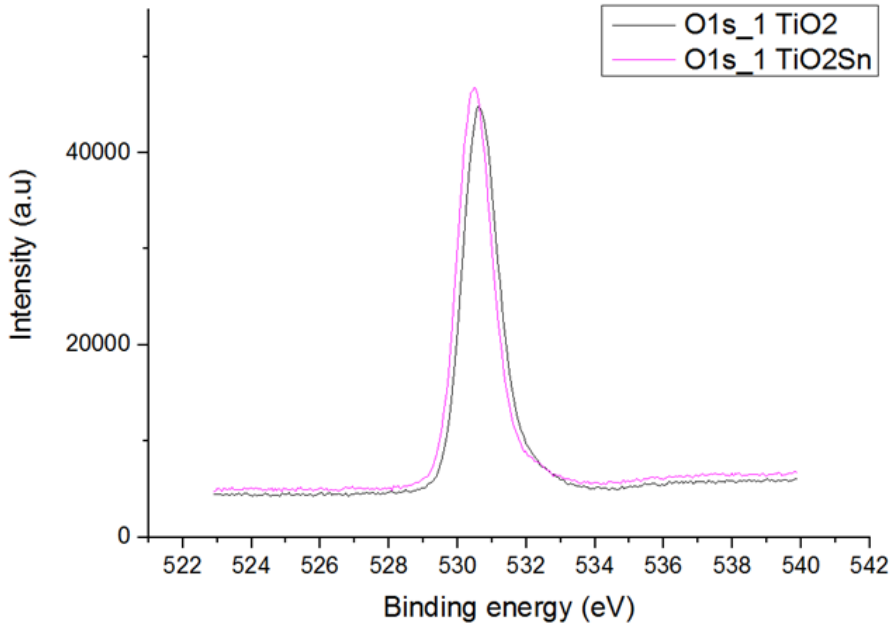

Figure 4.20: O 1s_1 peak shifts between the annealed nominally undoped TiO_2 film and the annealed $Ti_{1-x}O_2:Sn_x$ (19:1) film.

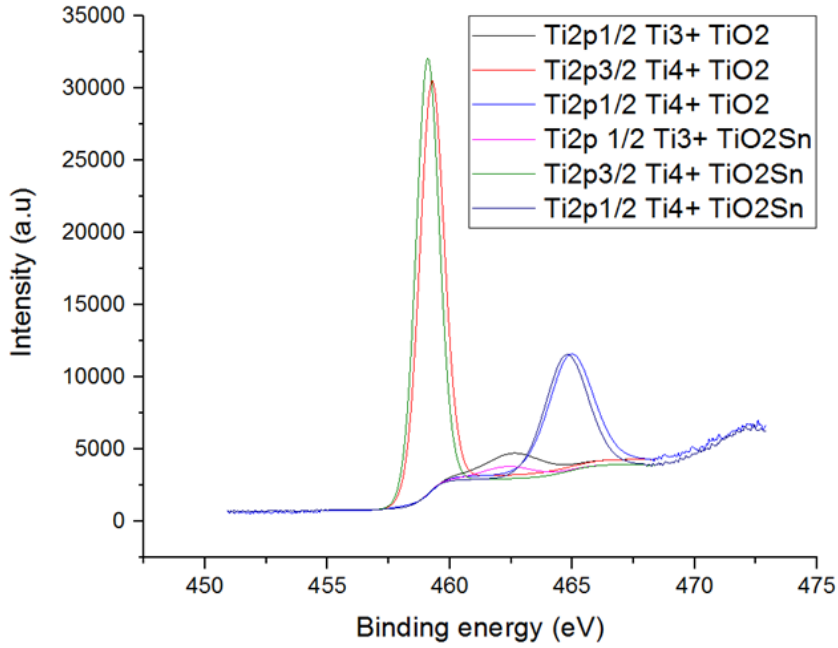

Figure 4.21: Ti 2p peak shifts between the annealed nominally undoped TiO_2 film and the annealed $Ti_{1-x}O_2:Sn_x$ (19:1) film.

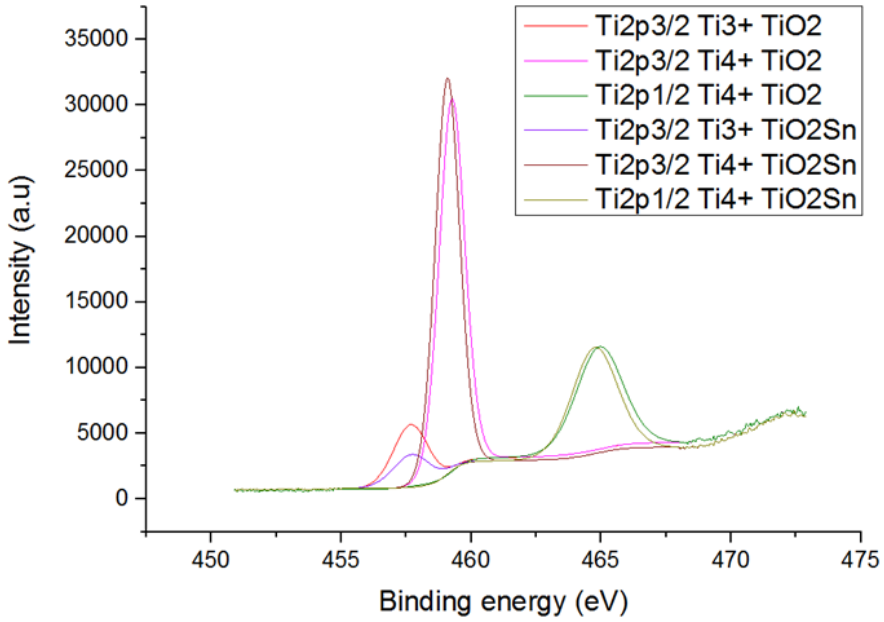

Figure 4.22: Ti 2p peak shifts between the annealed nominally undoped TiO_2 film and the as-grown $Ti_{1-x}O_2:Sn_x$ (19:1) film.

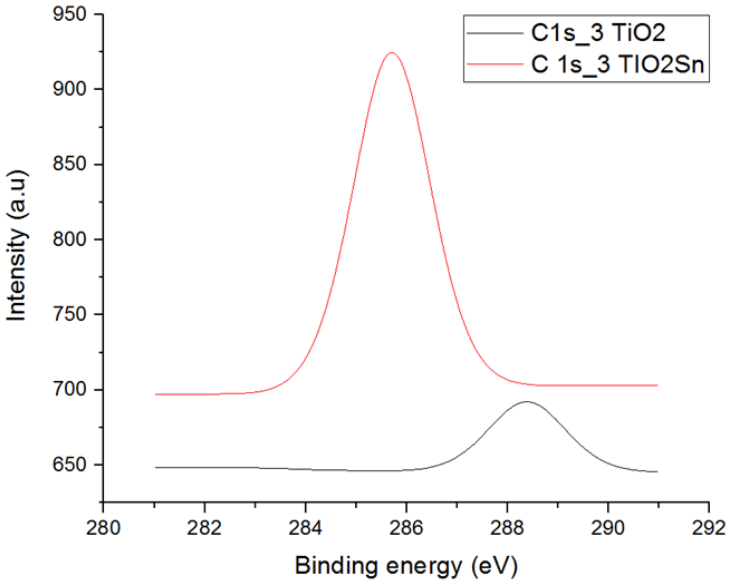

Figure 4.23: C 1s_3 peak shifts between the annealed nominally undoped TiO_2 film and the as-grown $Ti_{1-x}O_2:Sn_x$ (19:1) film.

Table 4.13 also shows approximately 4.9 % adventitious surface carbon contamination from atmospheric sources. Furthermore, table 4.15 shows minimal carbon contamination detection (0.7 %) throughout the $Ti_{1-x}O_2:Sn_x$ (19:1) film, suggesting the presence of minimal precursor residues.

	$Ti_{1-x}O_2:V_x$ (19:1)	$Ti_{1-x}O_2:V_x$ (19:1)	Annealed $Ti_{1-x}O_2:V_x$ (19:1)	Annealed $Ti_{1-x}O_2:V_x$ (19:1)
Peak	Position (eV)	Concentration (%)	Position (eV)	Concentration (%)
O 1s	530.3	63.1	529.9	64.3
Ti 2p	458.3	23.9	457.9	22.9
V 2p	515.3	1.2	514.9	0.7
C 1s	285.3	5.3	284.9	4.0
N 1s	399.3	0.5	-	-
Si 2p	102.3	0.9	101.9	3.1
Al 2p	74.3	5.2	74.9	5.0

Table 4.16: Low resolution XPS results for both the as-grown and annealed $Ti_{1-x}O_2:V_x$ (19:1) films.

	$Ti_{1-x}O_2:V_x$ (19:1)	$Ti_{1-x}O_2:V_x$ (19:1)	Annealed $Ti_{1-x}O_2:V_x$ (19:1)	Annealed $Ti_{1-x}O_2:V_x$ (19:1)
Peak	Position (eV)	Concentration (%)	Position (eV)	Concentration (%)
O 1s_1	530.5	58.8	530.6	59.2
O 1s_2	532.0 (531.7)	8.7	532.2 (531.7)	9.2
Ti^{3+} $2p_{3/2}$	457.4 (457.7)	2.5	457.5	1.3
Ti^{3+} $2p_{1/2}$	462.6	1.2	462.8	0.7
Ti^{4+} $2p_{3/2}$	459.0 (459.3)	14.4	459.1	15.2
Ti^{4+} $2p_{1/2}$	464.6 (464.9)	7.2	464.8	7.6
C 1s_1	284.7	3.8	284.8	3.9
C 1s_2	286.5	1.4	286.6	1.1
C 1s_3	289.4	0.5	289.7 (289.4)	0.6
N 1s	400.1	0.5	400.0	0.3
V 2p	515.7	1.0	515.8	0.9

Table 4.17: High resolution XPS results for both the as-grown and annealed $Ti_{1-x}O_2:V_x$ (19:1) films with the peak shifts from the annealed nominally undoped TiO_2 film positions highlighted in brackets.

Tables 4.16 and 4.17 show XPS analysis results of the as-grown and annealed $Ti_{1-x}O_2:V_x$ (19:1) films with table 4.16 highlighting peak shifting compared to the annealed nominally undoped TiO_2 film (tables 4.2 and 4.3). Additionally, table 4.16, a high aluminium contamination of approximately 5 % is present within the as-grown and annealed $Ti_{1-x}O_2:V_x$ films, equating to Ti-O-Al bond creation [579]. The source of aluminium contamination is unknown, with aluminium ion diffusion from substrate sources unlikely due to both a low substrate concentration (15 ppm) [578] and a lack of continuity across the other doped TiO_2 films. Therefore the $Ti_{1-x}O_2:V_x$ (19:1) and (99:1) films underwent energy dispersive X-ray spectroscopy (EDX) analysis for aluminium containing particulates (figure 4.24 a) and b).

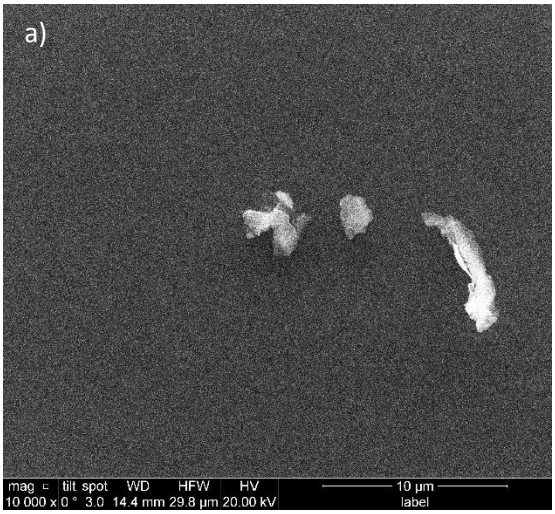

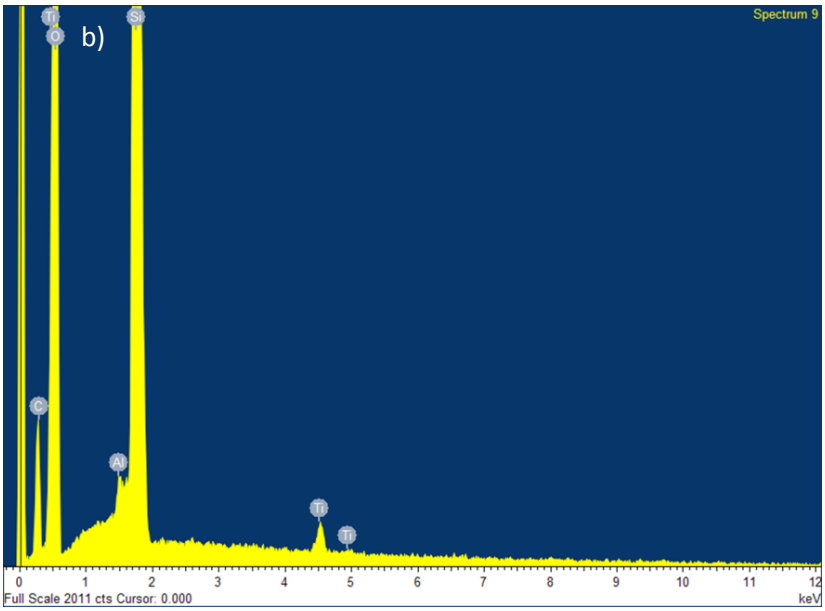

Figure 4.24: a) showing surface SEM of the $Ti_{1-x}O_2:V_x$ (19:1) film indicating particulate contamination and b) showing the corresponding EDX of the respective SEM image.

From figure 4.24 a) particulates are observed at surface regions of the annealed $Ti_{1-x}O_2:V_x$ (19:1) film and on comparison with figure 4.24 b) showing that detected particulates could correspond to aluminium contamination. Speculatively, this aluminium oxide particulate contamination could possibly result from synthesis in the Cambridge Nano Tech Fiji 200 ALD machine reaction chamber. So, for any comparable properties with other doped films, the as-grown and annealed $Ti_{1-x}O_2:V_x$ (19:1) films require repeat synthesis.

From table 4.17, vanadium concentrations within the as-grown and annealed $Ti_{1-x}O_2:V_x$ (19:1) films are slightly lower than expected from the 19:1 cycle ratio utilized. This resulted in V^{4+} concentrations of approximately 1 % to produce a film composition of $Ti_{0.96}V_{0.04}O_2$ on comparison of titanium and vanadium concentrations.

Additionally, figure 4.25 shows Ti 2p shifts for as-grown $Ti_{1-x}O_2:V_x$ (19:1) film corresponding to change in titanium chemical environment, potentially explainable by surface Ti-O-V-O-H bonding [583]. Additionally, figure 4.26 shows peak position shifting for O 1s_2, suggesting a variation in surface oxygen chemical environments.

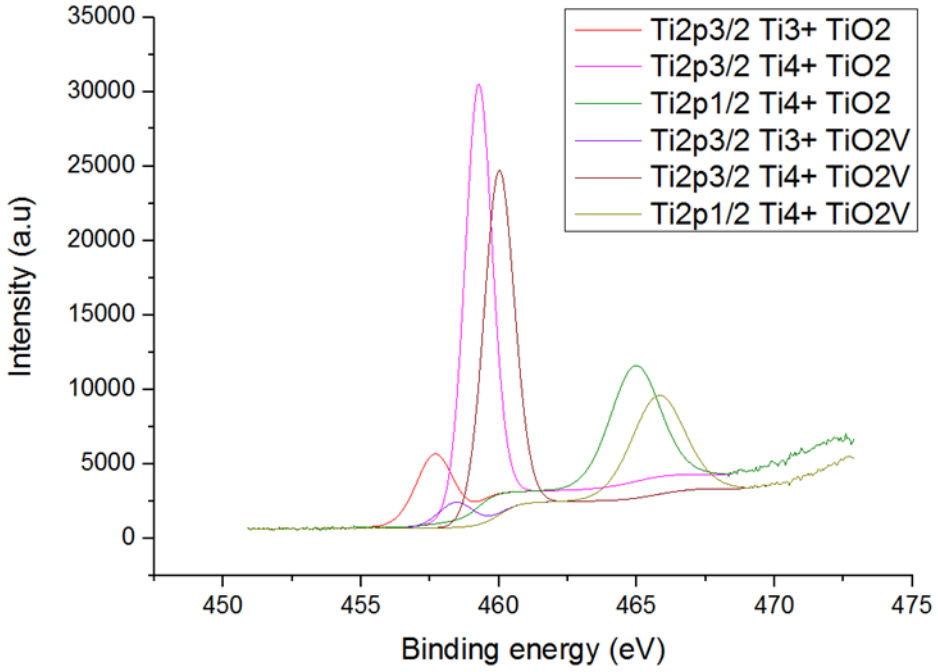

Figure 4.25: Ti 2p peak shifts between the annealed nominally undoped TiO_2 film and the as-grown $Ti_{1-x}O_2:V_x$ (19:1) film.

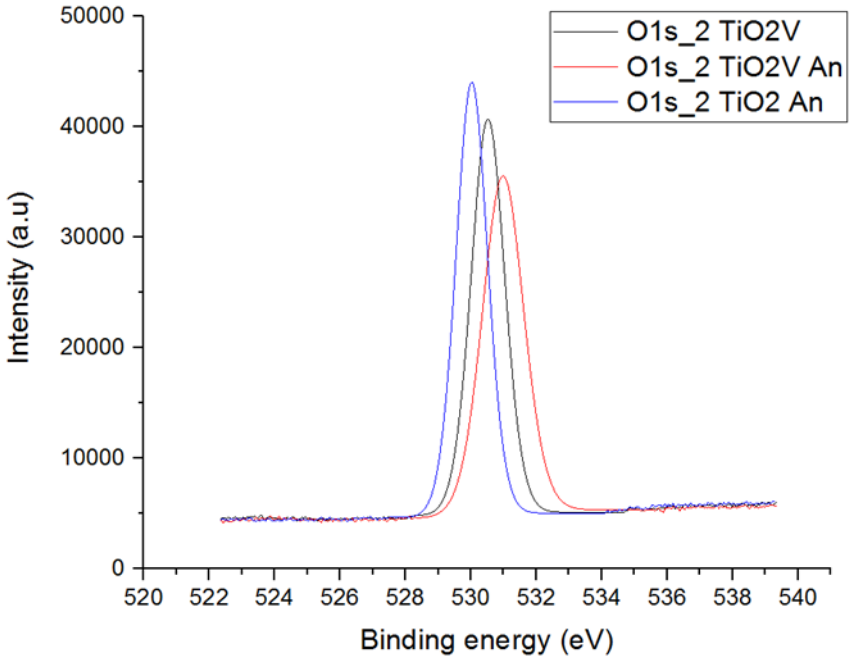

Figure 4.26: O 1s_2 peak shifts between the annealed nominally undoped TiO_2 film, the as-grown $Ti_{1-x}O_2:V_x$ (19:1) film and the annealed $Ti_{1-x}O_2:V_x$ (19:1) film.

Furthermore, tables 4.16 and 4.17 show adventitious surface carbon (3.9 %) and nitrogen (0.5 %) contamination, on both the as-grown and annealed $Ti_{1-x}O_2:V_x$ (19:1) films. Figure 4.27 also suggests a 0.3 eV C 1s_3 peak shift equatable to variation in surface carbon chemical environments.

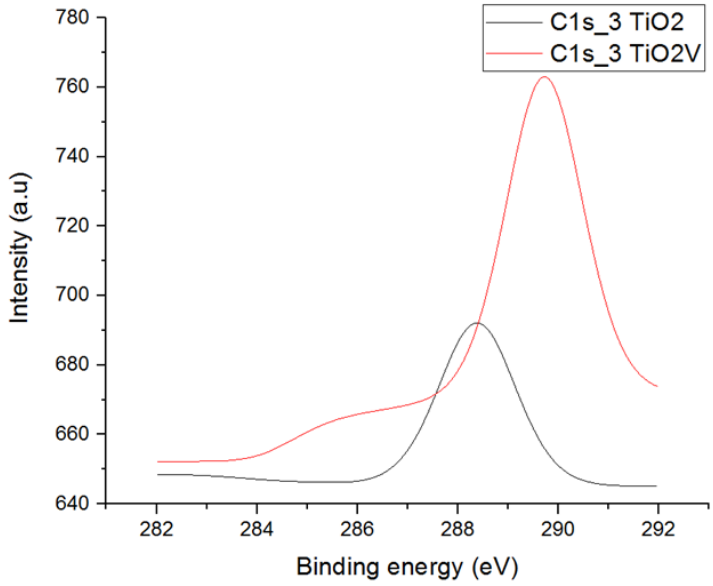

Figures 4.27: C 1s_3 peak shifts between the annealed nominally undoped TiO_2 film and the annealed $Ti_{1-x}O_2:V_x$ (19:1) film.

Annealing of the $Ti_{1-x}O_2:M_x$ (19:1) films typically induces minimal anatase crystallinity with most Ti 2p and O 1s peak shifts between the as-grown and annealed $Ti_{1-x}O_2:M_x$ (99:1 and 19:1) films, occurring within error (≤0.02 eV). However, a Ti^{3+} $2p_{(1/2)}$ peak shift of 0.4 eV is observed between the as-grown and annealed $Ti_{1-x}O_2:Sn_x$ (19:1) film, indicating Ti-O environmental variation.

In summary, XPS analysis suggested dopant incorporation variability with lower than expected concentrations of hafnium in $Ti_{1-x}O_2:Hf_x$ (19:1) films (1.6-0.4 %), vanadium in $Ti_{1-x}O_2:V_x$ (19:1) films (1 %). Unexpectedly, no silver concentration was detected in $Ti_{1-x}O_2:Ag_x$ (19:1) films. Additionally, Ti^{3+} were shown to exist throughout all $Ti_{1-x}O_2:M_x$ (19:1) films, resulting in 8-16 % surface Ti^{3+} and greater 18-52 % Ti^{3+} bulk concentrations for the $Ti_{1-x}O_2:Hf_x$, $Ti_{1-x}O_2:Sn_x$ and $Ti_{1-x}O_2:Ag_x$ (19:1) films. Both adventitious surface carbon and nitrogen were observed across all $Ti_{1-x}O_2:M_x$ (19:1) films. Only $Ti_{1-x}O_2:V_x$ (19:1) films showed other significant contamination regarding aluminium particulates possibly resulting from ALD synthesis chamber conditions. Furthermore, doping was shown to induce significant (>0.2 eV) variation in titanium, oxygen and carbon environments as compared to the nominally undoped TiO_2 film. The effect of doping on photocatalysis of $Ti_{1-x}O_2:M_x$ films is discussed in the section below.

4.3.1 Optical and Photocatalytic activity

The photocatalytic activity of the doped and un-doped samples prepared here was examined utilizing the basic blue 66 ink degradation test under UV light, as outlined in Chapter 2. Initial results obtained via the utilization of felt-tip applicators suggested the nominally undoped TiO_2, the $Ti_{1-x}O_2:Ag_x$ (19:1), the $Ti_{1-x}O_2:Sn_x$ (99:1 and 19:1) and the $Ti_{1-x}O_2:Hf_x$ (19:1 and 99:1) samples all photo-bleached basic blue 66 ink under 3 hours irradiation. Additionally, minimal degradation was also observed on the $Ti_{1-x}O_2:Al_x$ (99:1) film (figure 4.28).

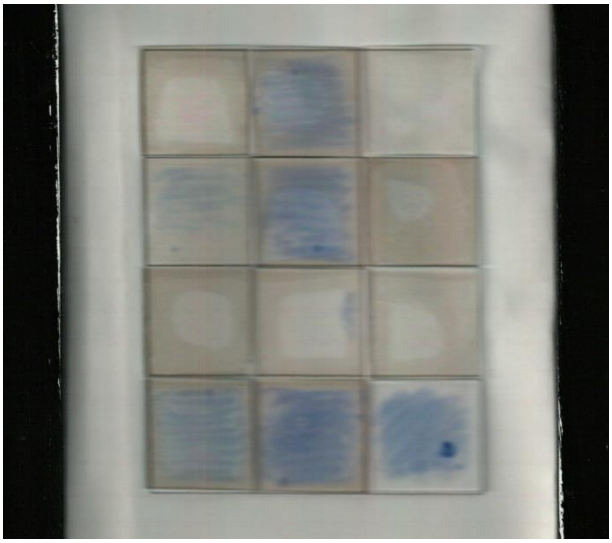

Figure 4.28: Basic blue 66 ink degradation subsequent to three hours UV irradiation on; a) nominally undoped TiO_2, b) $Ti_{1-x}O_2:Ag_x$ (99:1), c) $Ti_{1-x}O_2:Ag_x$ (19:1), d) $Ti_{1-x}O_2:Al_x$ (99:1), e) $Ti_{1-x}O_2:Al_x$ (19:1), f) $Ti_{1-x}O_2:Hf_x$ (99:1), g) $Ti_{1-x}O_2:Hf_x$ (19:1), h) $Ti_{1-x}O_2:Sn_x$ (99:1), i) $Ti_{1-x}O_2:Sn_x$ (19:1), j) $Ti_{1-x}O_2:V_x$ (99:1), k) $Ti_{1-x}O_2:V_x$ (19:1) and l) a blank quartz substrate.

Further analysis of photocatalytically active samples utilizing a 3mm K-Bar for basic blue 66 ink application and increased chronological measurement accuracy was performed (scanning every two (TiO_2, $Ti_{1-x}O_2:Ag_x$ (19:1) and $Ti_{1-x}O_2:Sn_x$ (19:1)) and ten ($Ti_{1-x}O_2:Hf_x$ (19:1 and 99:1) and $Ti_{1-x}O_2:Sn_x$ (99:1)) minutes), to obtain increasingly accurate ttb values (table 4.18).

TiO_2 films	**ttb (minutes. seconds)**
TiO_2	11.04
$Ti_{1-x}O_2:Ag_x$ (19:1)	6.04
$Ti_{1-x}O_2:Sn_x$ (19:1)	6.42
$Ti_{1-x}O_2:Sn_x$ (99:1)	42.27
$Ti_{1-x}O_2:Hf_x$ (19:1)	44.46
$Ti_{1-x}O_2:Hf_x$ (99:1)	57.07

Table 4.18: ttb values calculated for photocatalytically active nominally undoped and doped TiO_2 films.

From table 4.18, it is apparent the $Ti_{1-x}O_2:Ag_x$ and $Ti_{1-x}O_2:Sn_x$ (19:1) films are most photoactive towards basic blue 66 ink bleaching of all the samples prepared. This is true even of the undoped sample, which possesses a ttb approaching two times of both the $Ti_{1-x}O_2:Ag_x$ and $Ti_{1-x}O_2:Sn_x$ (19:1) films. It is possible to speculate as to why the $Ti_{1-x}O_2:Ag_x$ (19:1) and $Ti_{1-x}O_2:Sn_x$ (19:1) samples exhibit the highest levels of photocatalytic activity on basic blue 66 ink degradation. Firstly the XPS data indicates significant Ti^{3+} concentration possessed for both films (table 4.2). Additionally, through Raman analysis, some evidence of anatase crystallite formation occurs for the $Ti_{1-x}O_2:Sn_x$ (19:1) film, with TEM providing minimal evidence of anatase crystallinity in the $Ti_{1-x}O_2:Ag_x$ (19:1) film.

Whilst this reasoning is also true to a degree for the photocatalytically inactive $Ti_{1-x}O_2:V_x$ and $Ti_{1-x}O_2:Al_x$ films with respect to basic blue 66 ink degradation. Both the $Ti_{1-x}O_2:V_x$ and $Ti_{1-x}O_2:Al_x$ films indicate considerably lower levels of Ti^{3+} in bulk regions (from depth profiling results) and also show some evidence of dopant oxide formation (from Raman spectroscopy). Furthermore, dopant oxide formation may assist in the chemical relaxation method (recombination), prior to exciton charge pair combination with surface oxygen-based groups to generate ROS species [171, 584].

In contrast to the $Ti_{1-x}O_2:Ag_x$ (19:1) and $Ti_{1-x}O_2:Sn_x$ (19:1) films, the other doped TiO_2 films synthesized all show higher ttb values as compared to the nominally undoped TiO_2 film. Considering both the $Ti_{1-x}O_2:Hf_x$ (19:1) and $Ti_{1-x}O_2:Sn_x$ (99:1) films, Raman and XRD indicate that these samples are amorphous, showing very little evidence of any crystallisation. However, if this was the only explanation, lower levels of photocatalytic activity would correlate with the lack of anatase in undoped and doped TiO_2 films. Nevertheless, the ttb is longer for the $Ti_{1-x}O_2:Hf_x$ (99:1) film containing a lower hafnium concentration, suggesting crystallisation could be inhibited by the strain imparted on Hf^{4+} addition to the TiO_2 film. The above observations further imply that percentage or sub-percentage levels of dopants within 10 nm from film surfaces, have a marked effect on the detected surface chemical properties.

In order to further assess the photocatalytic activity of grown samples, water contact angle measurements were performed as described in Chapter 2 (Figure 4.29). From figure 4.29, both $Ti_{1-x}O_2:Sn_x$ and $Ti_{1-x}O_2:Ag_x$ (19:1) films showed a transition towards superhydrophilicity (<15 ^{o}) after 30 and 60 minutes UV exposure respectively. This might be expected resulting from the basic blue 66 ink bleaching experiments described in the previous experiments.

Other samples, namely the nominally undoped TiO_2, $Ti_{1-x}O_2:Al_x$ (99:1) and $Ti_{1-x}O_2:Sn_x$ (99:1), all indicated some discernible reduction in contact angle to average around 40 ^{o} after 60 minutes of exposure to the UV light source (figure 4.29).

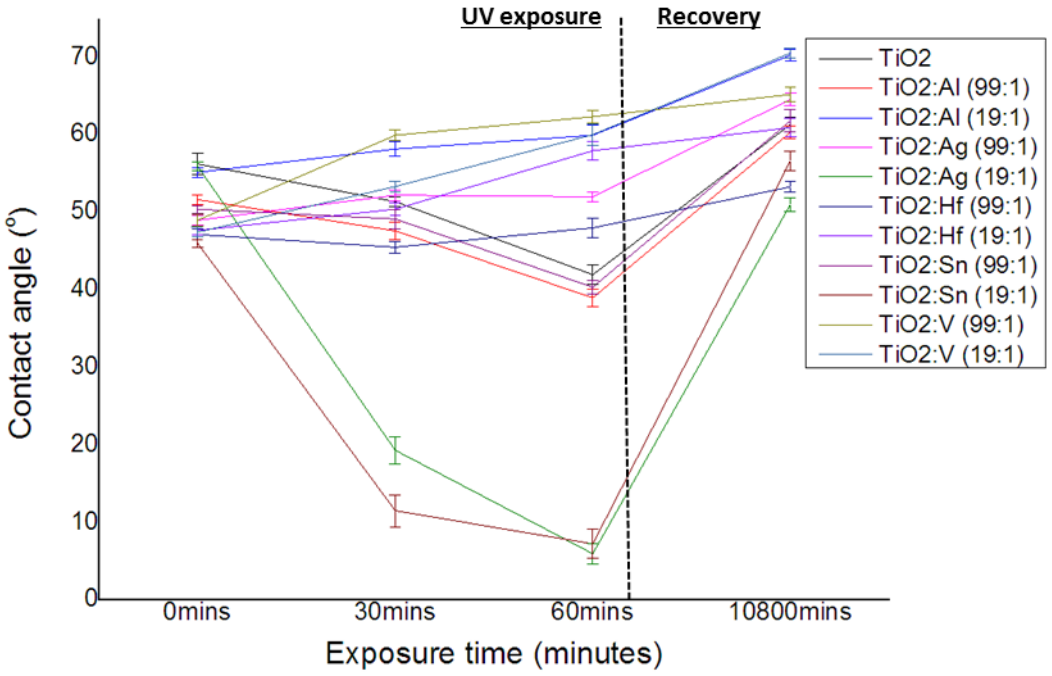

Figure 4.29: Water contact angle analysis prior to, subsequent to 30 and 60minutes UV irradiation and after a week of darkness for the nominally undoped TiO_2 film, the $Ti_{1-x}O_2$:Al (99:1 and 19:1) films, the $Ti_{1-x}O_2:Ag_x$ (99:1 and 19:1) films, the $Ti_{1-x}O_2:Hf_x$ (99:1 and 19:1) films, the $Ti_{1-x}O_2:Sn_x$ (99:1 and 19:1) films and the $Ti_{1-x}O_2:V_x$ (99:1 and 19:1) films.

Correlating these results with the ink photodegradation results presented in the previous section. It is noted the $Ti_{1-x}O_2:V_x$ (99:1 and 19:1), $Ti_{1-x}O_2:Al_x$ (19:1) and Ti_{1-}

$_xO_2$:Ag_x (99:1) samples, all appear to exhibit increasing hydrophobicity upon UV irradiation, suggesting a progressively diminished capacity for ROS generation.

Unexpectedly, $Ti_{1-x}O_2$:Hf_x (99:1) and (19:1) indicate no variation in contact angle upon UV irradiation despite showing evidence of ink photodegradation, as discussed earlier. Additionally figure 4.30, reveals all TiO_2 films undergo some degree of hydrophobic "recovery" with surface site deactivation resulting from being left in darkness, further indicative of a repeatable reaction.

While a majority of the contact angle results agree qualitatively with those presented for the ink degradation experiments. The contradicting results serve to illustrate the requirement to perform disparate examinations into order to properly ascertain the material response towards UV light. In other words, the results illustrate simply becoming hydrophilic is not necessarily a true indication of the surface ability to perform the photocatalytic ink reduction and vice versa.

Further water contact angle experimentation were performed on films previously expressing either photocatalytic basic blue 66 ink degradation in figure 4.30 or slight hydrophilic increase in figure 4.30. However, UV light irradiation was extended to two hours to provide greater time for potential hydrophilic development.

Figure 4.30 reveals after two hours UV light irradiation, the nominally undoped TiO_2 sample generates near superhydrophilic contact angles (18.4 ^{o}), indicating the presence of surface ROS. The $Ti_{1-x}O_2$:Sn_x (99:1) sample indicates very little variation over the two hour period while the $Ti_{1-x}O_2$:Al_x (99:1) sample and the $Ti_{1-x}O_2$:Hf_x (99:1) sample both appear to show an increase in hydrophobicity, if anything. Whilst this is unusual and is perhaps unexpected, increasing hydrophobicity for the $Ti_{1-x}O_2$:Al_x (99:1) and $Ti_{1-x}O_2$:Hf_x (99:1) films is consistent with the results shown in figure 4.29 above. Another feature of note from figure 4.30, is after two hours UV irradiation the $Ti_{1-x}O_2$:Hf_x (19:1) sample shows a significant reduction in contact angle to an average of 37.4 ^{o}. This reduction was not previously noted in measurements only using one hour of UV light exposure (figure 4.29).

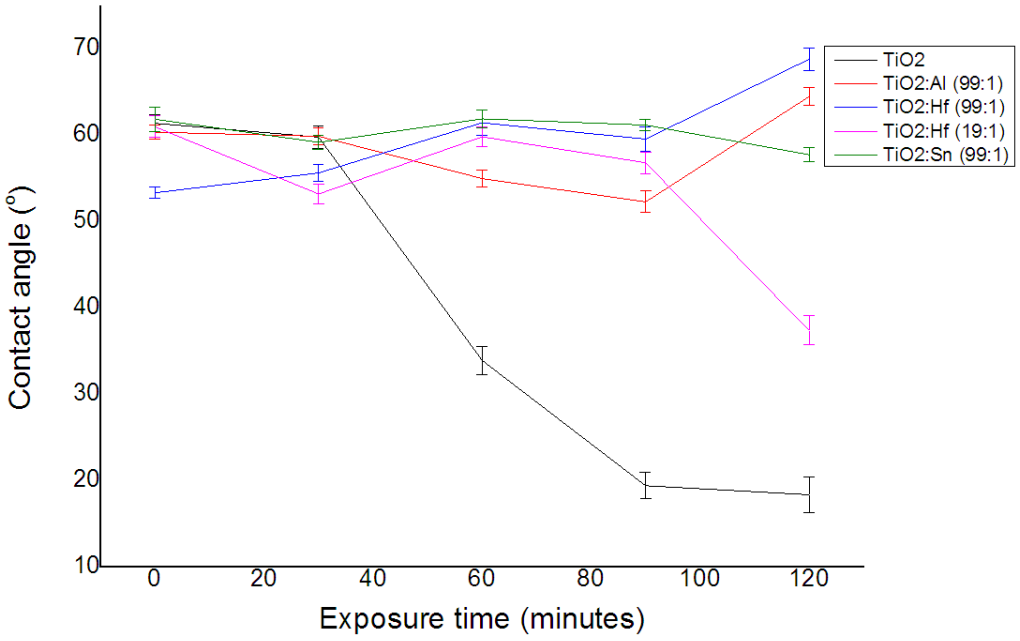

Figure 4.30: water contact angles of the nominally undoped TiO_2 film, the $Ti_{1-x}O_2:Al_x$ (99:1) film, the $Ti_{1-x}O_2:Hf_x$ (99:1 and 19:1) films and the $Ti_{1-x}O_2:Sn_x$ (99:1) film under two hours UV irradiation.

The explanation for this discrepancy is unclear, but concerning possible mechanisms underpinning these observations, it is noted that doubling the total time for UV light surface exposure may have both thermal and chemical consequences to consider. Regarding thermal consequences, the light source utilized results in some discernible heating of the samples. Additionally, UV light can cause surface bond disintegration and contamination destruction without the need to invoke the special photocatalytic process in question.

UV/Visible light transmission experiments were performed on all samples grown (figure 4.31). Furthermore from figure 4.31, it is apparent regarding transmission and absorption characteristics, that all samples are very similar, as might be expected.

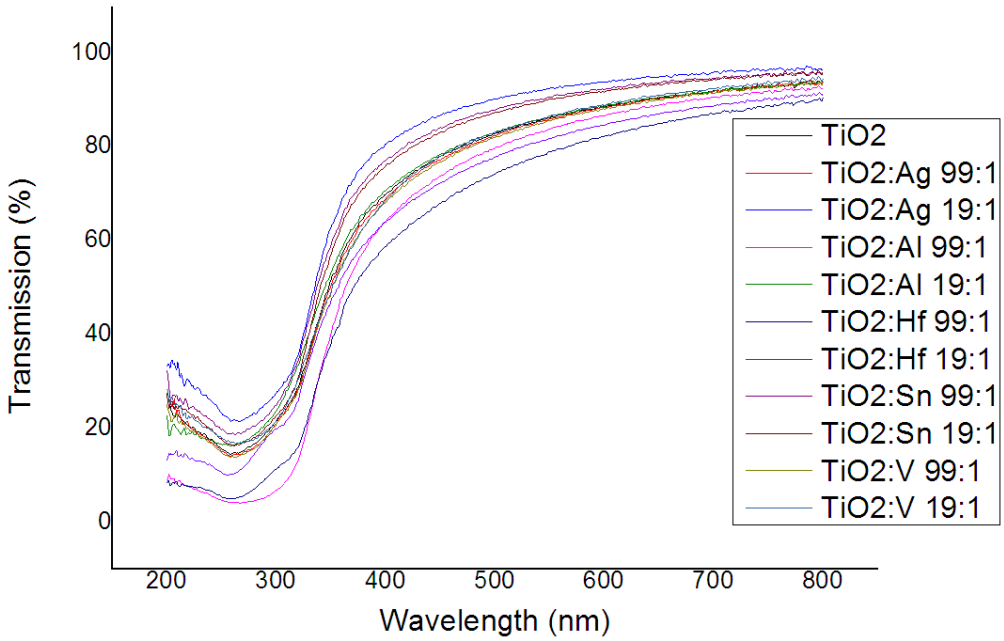

Figure 4.31: Spectrophotometry across near UV/visible light range (200-800nm)

The data shown in figure 4.31 was combined with reflectivity measurements (not shown) to provide Tauc plots (figure 4.32) which were utilized to estimate band gap, table 4.19.

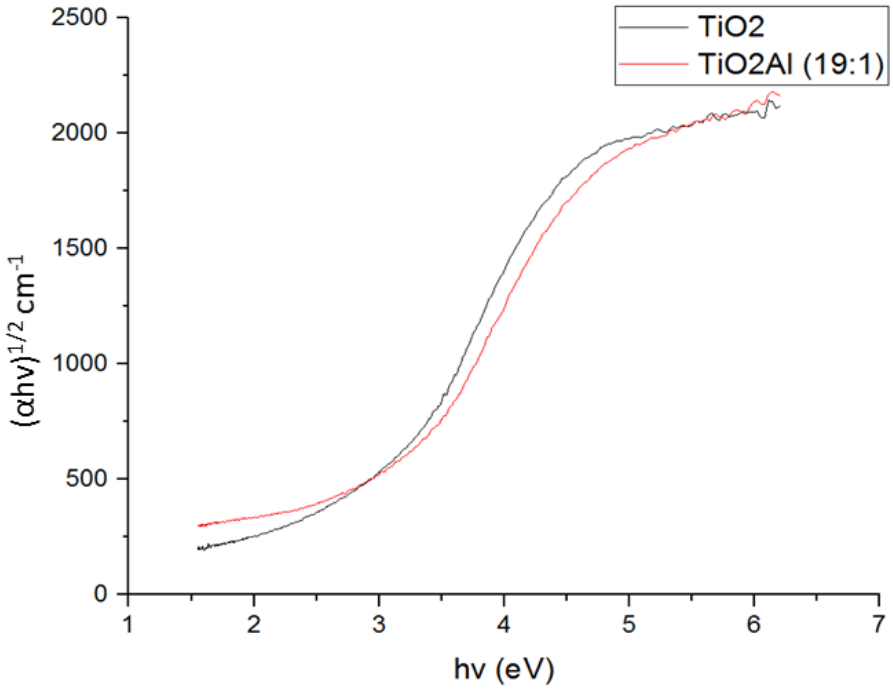

Figure 4.32: An example of calculated Tauc plots for the annealed nominally undoped TiO_2 and annealed $Ti_{1-x}O_2:Al_x$ (19:1).

	As-grown (eV)	Annealed (eV)
TiO_2	2.80	2.83
$Ti_{1-x}O_2:Ag_x$ (19:1)	2.96	3.05
$Ti_{1-x}O_2:Ag_x$ (99:1)	2.77	2.87
$Ti_{1-x}O_2:Al_x$ (19:1)	2.74	3.08
$Ti_{1-x}O_2:Al_x$ (99:1)	2.82	2.75
$Ti_{1-x}O_2:Hf_x$ (19:1)	2.61	2.86
$Ti_{1-x}O_2:Hf_x$ (99:1)	2.68	2.91
$Ti_{1-x}O_2:Sn_x$ (19:1)	2.80	3.01
$Ti_{1-x}O_2:Sn_x$ (99:1)	2.84	2.92
$Ti_{1-x}O_2:V_x$ (19:1)	2.88	2.70
$Ti_{1-x}O_2:V_x$ (99:1)	2.85	2.87

Table 4.19: Tauc-plot calculated direct band gap sizes for the as-grown and annealed nominally undoped and doped TiO_2 films

From table 4.19, the nominally undoped TiO_2 film grown here shows a reduction in band gap, as compared to the equivalent literature band gap size [440, 572, 585]. This reduction in band gap possibly relates to the greater Ti^{3+} concentrations possessed by the undoped TiO_2 film. As is also apparent from table 4.19, the doped samples possess variable band gaps which do not correlate in terms of either an increase or decrease on annealing. However, all doped TiO_2 films attain band gap sizes beneath the expected from the equivalent mix of amorphous and anatase crystalline morphologies already observed. This is suggestive of mid TiO_2 band gap state generation either directly from dopant addition or indirectly though $Ti^{3+}/V_O^{\cdot\cdot}$ formation as a part of charge compensating effects [44, 150].

From both the Raman and XPS data corresponding to the $Ti_{1-x}O_2:Al_x$ (99:1 and 19:1) and $Ti_{1-x}O_2:V_x$ (19:1) films, it can be suggested that compared to the other materials studied, these samples may contain appreciable amounts of Al_2O_3 and VO_2. Therefore under such conditions dependent on band alignment, it might be expected that some increase in band gap due to Burstein-Moss effects may arise. However, table 4.19 reveals that apart from the $Ti_{1-x}O_2:Al_x$ (19:1) film, the band gap shows no appreciable increase for any other $Ti_{1-x}O_2:Al_x$ and $Ti_{1-x}O_2:V_x$ samples. Additionally, the band gap increase observed for the $Ti_{1-x}O_2:Al_x$ (19:1) film on annealing (2.74-3.08 eV) could also correlate to Ti^{3+} surface concentration decrease from 20 to 12 % [150].

Furthermore, the band gaps for both the $Ti_{1-x}O_2:Ag_x$ (99:1 and 19:1) and the $Ti_{1-x}O_2:Sn_x$ (99:1 and 19:1) film increase on annealing. Band gap increase for the $Ti_{1-x}O_2:Sn_x$ films could result from greater excited electron concentrations or conduction band energetic increase on TiO_2 and SnO_2 mixing [198, 201]. However, band gap increase for the $Ti_{1-x}O_2:Ag_x$ (19:1) film could potentially result from the high silicon concentration detected in XPS, further providing Burstein-Moss effects through Si 2p electron addition to the TiO_2 conduction band.

4.3.2 Electrical conduction

Electrical properties of the deposited TiO_2 were studied through four point probe measurements. As for the other films presented in this research, all films were essentially resistive.

4.4 Discussion

The nominally undoped TiO_2 film presents a largely amorphous film with the presence of anatase crystallites with an average thickness of 18.6 nm. The nominally undoped TiO_2 film also shows photocatalytic activity with a ttb of 11 minutes 4 seconds ±35 seconds with respect to basic blue 66 ink photodegradation under UV irradiation and near-superhydrophilic (18 ^{o}) water contact angles after 90 minutes UV light exposure.

The photocatalytic activity observed for the nominally undoped TiO_2 would result from the polycrystalline anatase structure, providing superior exciton charge pair

mobility (reducing radiative recombination) and increased surface hydroxyl density [91-93]. The surface Ti^{3+} concentration of 19 % would also assist with increasing photocatalytic activity by providing a photogenerated hole trap. This hole trap increases excited electron lifetimes near surface oxide species and provides a greater chance of surface ROS generation. High Ti^{3+} concentrations would also insert mid-band gap states below the conduction band, corresponding to the overall lower 2.80/2.83 eV band gap size observed here, in comparison to the 3-3.2 eV seen in the literature [1].

Interestingly the $Ti_{1-x}O_2$:Ag_x (19:1) film possesses significantly higher photocatalytic activity as compared to the nominally undoped TiO_2 film with respect to a basic blue 66 ink ttb of 6 minutes and 4 seconds and superhydrophilic water contact angles after 60 minutes UV light irradiation. This larger photocatalytic activity is despite the $Ti_{1-x}O_2$:Ag_x film possessing lower polycrystalline anatase morphology, as compared to the nominally undoped TiO_2 film and is only detected through TEM imaging. Therefore, the larger photocatalytic activity of the $Ti_{1-x}O_2$:Ag_x film probably results from the extraordinary 52 % bulk Ti^{3+} concentration observed [574, 586], resulting in high surface ROS concentrations on UV irradiation.

Therefore, silver ion incorporation is unlikely to be the source of high photocatalytic activity, with silver ions either present in concentrations below XPS detection limits [447, 587] or not present at all. This very low silver ion incorporation (if any), possibly results from low solid solubility of such a large Ag^+ ion (129 pm) [61] on substitution into a Ti^{4+} site (74.5 pm) (Ag_{Ti}''') according to Hume-Rothery rules [144]. However, negligible amounts of silver incorporation could have occurred with charge compensation from Ag_{Ti}''' formation. This results in the production of three $V_O^{\cdot\cdot}$ defects, creating an extremely oxygen deficient film Ti_2O_3/TiO_2 environment [118, 588], as observed here. The bulk oxygen deficient Ti_2O_3/TiO_2 film environment correlates with the XPS peak shifts observed for titanium and oxygen bonding environments in the bulk $Ti_{1-x}O_2$:Ag_x (19:1) film.

Furthermore, another potential reason for negligible silver precursor addition could be related to the lower thickness (14.5 nm) of the $Ti_{1-x}O_2$:Ag_x film. Ag(THMD)

addition is therefore suggested to suppresses TiO_2 growth, instead of depositing silver, possibly through ligand steric hindrance towards TDMAT surface attachment [589].

The $Ti_{1-x}O_2:Ag_x$ (99:1) film in comparison provides no measureable photocatalytic activity relating to surface ROS production with respect to both basic blue 66 ink photodegradation and hydrophilic increase under UV light irradiation. This lack of photocatalytic activity is unusual given the 25.3 ^{o} 2ϑ reflection corresponding to the (101) anatase miller plane

Despite the $Ti_{1-x}O_2:Al_x$ (99:1) film possessing a largely amorphous film with the presence of anatase crystallites similar to, but less than compared to that observed for the nominally undoped TiO_2 film. No photocatalytic properties are observed for either of the $Ti_{1-x}O_2:Al_x$ (99:1 and 19:1) films with respect to photocatalytic degradation of basic blue 66 ink and hydrophobic contact angle retention under UV light irradiation. This suggests a significant photocatalytic activity decrease on aluminium doping, potentially resulting from uniformly distributed Al^{3+} dopant ions acting as deep traps and increasing recombination prior to surface migration [45]. Additionally, both decreased Ti^{3+} concentrations (12 %), as compared to the nominally undoped TiO_2 film, and the amorphous nature of $Ti_{0.82}Al_{0.18}O_2$ (19:1) could also lower photocatalytic activity generation.

Furthermore, greater aluminium concentrations (5.3 %) possibly form Al_2O_3, as shown by a 645 cm^{-1} peak in Raman spectroscopy. This implies Al^{3+} concentrations above solid solubility limits [559] with Al_2O_3 previously showing crystalline growth restriction on annealing [164, 166]. Greater Al_2O_3 concentrations also increase band gap size (3.08 eV) as compared to $Ti_{1-x}O_2:Al_x$ (99:1) through Burstein-Moss effects [151], again decreasing potential photocatalytic activity.

Both the annealed $Ti_{1-x}O_2:Hf_x$ (99:1 and 19:1) films show disparate crystalline morphologies correlating to differences in Hf^{4+} concentrations, possibly relating to strain from larger Hf^{4+} (85 pm) substitution into a Ti^{4+} (74.5 pm) site (Hf_{Ti}). As a consequence, the $Ti_{1-x}O_2:Hf_x$ (99:1) film possesses poorly polycrystalline anatase with a 25.3 ^{o} 2ϑ peak detected relating to an anatase (101) miller plane and the Ti_{1-}

$_xO_2$:Hf_x (19:1) film is shown as amorphous. Despite the different structures detected, both the $Ti_{1-x}O_2$:Hf_x (99:1 and 19:1) films show photodegradation of basic blue 66 ink under UV light irradiation. This shows a ttb of 44 minutes 46 seconds for the $Ti_{1-x}O_2$:Hf_x (19:1) film and 57 minutes 7 seconds for the $Ti_{1-x}O_2$:Hf_x (99:1) film. The lower photocatalytic activity, as compared to the nominally undoped TiO_2 film, could result from a combination of the 16 % surface and 18 % bulk Ti^{3+} increasing ROS generation, alongside 0.5 % Hf^{4+} acting as shallow electron traps [155] to increase recombination rates. Additionally, lower Hf^{4+} concentrations (0.5 %) than expected (5 %) are observed within the $Ti_{1-x}O_2$:Hf_x (19:1) film, possibly suggesting solid solubility limits were reached.

Furthermore, both annealed $Ti_{1-x}O_2$:Hf_x films (99:1 and 19:1) indicate band gap increase: 2.86 and 2.91 eV, assumed to be a result of Burstein-moss effects [151] on potential HfO_2 band gap (5.3-5.7 eV) inclusion.

Interestingly, the $Ti_{1-x}O_2$:Sn_x (19:1) film possesses a similar poorly polycrystalline anatase morphology (Raman peaks: 142 cm^{-1}, 197 cm^{-1}, 295 cm^{-1}, 513 cm^{-1} and 636 cm^{-1}) to the nominally undoped TiO_2 film. However, the $Ti_{1-x}O_2$:Sn_x (19:1) film shows a higher photocatalytic activity with respect to a greater basic blue 66 ink ttb of 6 minutes 42 seconds and superhydrophilic water contact angles after 30 minutes of UV light irradiation. This larger photocatalytic activity could result from both greater bulk Ti^{3+} concentrations (31 %) providing an electron sink alongside Sn^{4+} to trap photogenerated holes, so as to provide greater ROS formation from extending excited electron lifetimes [199, 200]. Additionally, greater photocatalytic properties for the $Ti_{0.9}Sn_{0.1}O_2$ (19:1) film could also originate from SnO_2 possessing a slightly lower energy conduction band [200]. This could lead to excited electron trapping on transfer from the TiO_2 conduction band, again extending charge carrier lifetimes and producing increased surface ROS concentrations [197]. Furthermore, SnO_2 conduction band excited electrons have been shown to capture O_2 molecules, increasing superoxide radical generation [152, 590].

In comparison, the $Ti_{1-x}O_2$:Sn_x (99:1) film possesses a more amorphous nature, resulting in a lower photocatalytic activity with respect to basic blue 66 ink

degradation under UV light irradiation and a ttb of 42 minutes and 27 seconds. The lower polycrystalline morphology possessed by the $Ti_{1-x}O_2:Sn_x$ (99:1) film possibly originates from lower Sn^{4+} concentrations which have been shown to prevent anatase crystallization [198], decreasing photocatalytic activity.

Furthermore, both $Ti_{1-x}O_2:Sn_x$ films suggest an increase in band gap (2.92 eV (99:1) and 3.01 eV (19:1)), as compared to nominally undoped TiO_2 (2.83 eV), possibly resulting from SnO_2 and TiO_2 valence band state mixing [198, 201].

Despite the $Ti_{1-x}O_2:V_x$ (99:1 and 19:1) films possessing a largely amorphous film with the presence of anatase crystallites, similar to undoped TiO_2, no photocatalytic properties are observed for either film with respect to basic blue 66 ink degradation and hydrophobicity retention under UV light irradiation. Destruction of photocatalytic capabilities could potentially result from vanadium doping. Low percentages of V^{4+} are observed (1 %) with V^{4+} presence also providing a minimal band gap decrease for the $Ti_{0.96}V_{0.04}O_2$ (19:1) film, suggestive of V^{4+} and Ti^{4+} 3d orbital overlap [205]. Additionally, the $Ti_{0.96}V_{0.04}O_2$ film contains the lowest Ti^{3+} concentrations (8 %) of all doped TiO_2 films, potentially suggesting decreased free electron concentrations available for surface ROS generation. Moreover, significant aluminium particulate contamination (5.2 %) exists, further reducing potential photocatalytic properties, with Al^{3+} acting as a charge carrier trap [45], increasing recombination rates prior to surface migration. Furthermore, Raman spectroscopy shows two peaks (257 and 332 cm^{-1}) corresponding to either Al_2O_3 from aluminium particulate presence, or VO_2 creation from dopant diffusion and agglomeration [418]. However, providing conclusions for variation in TiO_2 film photocatalytic properties on vanadium doping is merely speculative given the high aluminium particulate contamination present.

4.5 Conclusions

In conclusion, as-grown and annealed nominally undoped TiO_2 films and a range of as-grown and annealed $Ti_{1-x}O_2:M_x$ (99:1 and 19:1) films where M = Al, Hf, Sn and V, were successfully grown onto quartz substrates by thermal ALD. Additionally, as-grown and annealed $Ti_{1-x}O_2:Ag_x$ (99:1 and 19:1) film growth was attempted onto

quartz substrates by thermal ALD, however, lack of silver doping was observed. The influence of disparate dopants and dopant concentrations on the variation of the photocatalytic, structural, optical and electrical characteristics on TiO_2 films was investigated.

Photocatalytic activity with respect to basic blue 66 ink photodegradation was observed for the annealed $Ti_{1-x}O_2:Ag_x$ (19:1), $Ti_{1-x}O_2:Hf_x$ (99:1 and 19:1) and $Ti_{1-x}O_2:Sn_x$ (99:1 and 19:1) films. Interestingly, both the annealed $Ti_{1-x}O_2:Ag_x$ (19:1) and $Ti_{1-x}O_2:Sn_x$ (19:1) films showed faster ttb values of; 6 minutes 4 seconds and 6 minutes 42 seconds respectively, as compared to a ttb value of 11 minutes 4 seconds ±35 seconds for the nominally undoped TiO_2 film. Furthermore, water contact angle analysis also showed superhydrophilicity for the $Ti_{1-x}O_2:Ag_x$ (19:1) film and the $Ti_{1-x}O_2:Sn_x$ (19:1) film after 30 minutes to an hour of UV irradiation. However, superhydrophilicity was detected for the nominally undoped TiO_2 film after 90 minutes of UV irradiation. The increased photocatalytic activity for both the annealed $Ti_{1-x}O_2:Ag_x$ (19:1) and $Ti_{1-x}O_2:Sn_x$ (19:1) films, as compared to the nominally undoped TiO_2 film, potentially results from large bulk Ti^{3+} concentrations (52 and 31 %) providing excess electrons for surface ROS creation. Additionally, Sn^{4+} could also provide an excited electron sink to increase surface ROS concentrations. Overall, the $Ti_{1-x}O_2:Sn_x$ (19:1) film suggests optimal dopant concentration for both photocatalytic activity, whilst providing reasonable crystallinity formation.

The lower photocatalytic activities observed for the $Ti_{1-x}O_2:Hf_x$ (99:1 and 19:1) and $Ti_{1-x}O_2:Sn_x$ (99:1) films as compared to the nominally undoped TiO_2, have been correlated to lower bulk Ti^{3+} concentrations and Hf^{4+} centres acting as an electron traps. However, structurally both the $Ti_{1-x}O_2:Hf_x$ (99:1 and 19:1) films show minimal anatase crystallite formation, as compared to the more photocatalytically active $Ti_{1-x}O_2:Ag_x$ (19:1) and $Ti_{1-x}O_2:Sn_x$ (19:1) films. This relates to strain on incorporation of Hf^{4+} and Sn^{4+} centres, confirming photocatalytic activity is initially based on film morphology, but dopant solid solubility can provide significant variation.

Furthermore, it was found that all the annealed $Ti_{1-x}O_2:Al_x$ (99:1 and 19:1) and $Ti_{1-x}O_2:V_x$ (19:1) films that contain aluminium show no photocatalytic activity, possibly resulting from Al^{3+} acting as deep charge carrier traps to increase recombination. However, photocatalytic quantification for $Ti_{1-x}O_2:V_x$ (19:1) was difficult with such a large aluminium (5 %) particulate concentration, requiring repeat $Ti_{1-x}O_2:V_x$ (19:1) synthesis.

Chapter 5: Further analysis of $Ti_{1-x}O_2:Sn_x$ (19:1) with respect to cleaning agent and microbial exposure.

5.1 Introduction

As discussed extensively elsewhere in this thesis for TiO_2 the photocatalytic degradation of surface pollutants is well-documented [18, 591-593]. Furthermore, incorporation of dopants into TiO_2 has been shown to provide increased activation under ultraviolet (UV) light irradiation [199] or even visible light activation [19, 23]. Typically, TiO_2 surface irradiation results in exciton generation [92] with subsequent surface diffusion and surface site trapping, providing excited charge carriers for reaction with adsorbed water or oxygen molecules to generate reactive oxide species ($O_2^{\cdot -}$ or $OH^{\cdot}$) [32, 33].

At optimal concentrations, certain types of extrinsic doping are known to improve both exciton generation [23] and surface site trapping, increasing photocatalytic activity. However, as discussed in previous chapters, substitutional metal doping introduces strain which may generate lattice deformation and distortion [146], reducing photocatalytic activity through hindering anatase phase generation.

As previously shown in Chapter 4, tin doping in the $Ti_{1-x}O_2:Sn_x$ (19:1) film was suggested to induce strain and reduce the level of anatase formation as compared to a nominally undoped TiO_2 film. However, the $Ti_{1-x}O_2:Sn_x$ (19:1) film also indicated a shorter ttb value with basic blue 66 ink degradation. Correspondingly, the literature suggests this increased level of photocatalytic activity may be further linked to greater surface defect concentrations [145, 197].

In particular, tin doping is believed to provide excited electron charge transfers between TiO_2 and slightly lower energy SnO_2 conduction bands (0.07 and -0.34 eV respectively, versus a normal hydrogen electrode) [200], increasing exciton lifetimes, trapping and decreasing effective band gap size [197]. Tin doping can also results in;

- Strong $Sn^{(2/4+)}$ 5s hybridization with O 2p and $Sn^{(2/4+)}$ 5s/5p lone states near the valence bands, reducing effective band gap size [198, 201].

- Enhanced capture of oxygen molecules by SnO_2 conduction band electrons to generate superoxide radicals [197].

The above described factors contribute to the apparent enhanced photocatalytic activity of the $Ti_{1-x}O_2:Sn_x$ (19:1) film as compared to the nominally undoped TiO_2 film. However, for antimicrobial applications where surfaces of this type would be deployed in a hospital or similar medical environment, effective TiO_2 photocatalytic activity is necessary in indoor environments, away from any UV light sources. Furthermore, effective TiO_2 photocatalytic activity must persist after the surface has been exposed to regular cleaning with a variety of cleaning agents.

Consequently, this chapter examines the photocatalytic performance of the $Ti_{1-x}O_2:Sn_x$ (19:1) film in relation to being treated with various cleaning agents, previously studied in chapter 3. In particular, $Ti_{1-x}O_2:Sn_x$ (19:1) suggested greatest reliable levels of photocatalytic activity out of the films previously grown in chapter 4 and therefore was selected for comparison against a standard of Pilkington Activ™.

5.2 Methodology

$Ti_{1-x}O_2:Sn_x$ (19:1) films are synthesized through ALD and annealed as outlined in Chapter 4. The $Ti_{1-x}O_2:Sn_x$ (19:1) films were analysed utilizing previously described methodology within Chapters 2 and 3. However, specific technique variation or films analysed to this chapter are listed here:

- Water contact angles were generated across three $Ti_{1-x}O_2:Sn_x$ (19:1) films at 3.32 mW/cm^2 UV light irradiation, with average water contact angles provided by these three values.
- Photocatalytic activity was initially measured through felt tip basic blue 66 ink application and subsequent degradation under 3.37 mW/cm^2 UV light irradiation for an indication of photocatalytic activity. Nine $Ti_{1-x}O_2:Sn_x$ (19:1) film surfaces were covered in basic blue 66 ink test by a 3 mm K-bar application under 3.30 mW/cm^2 UV light irradiation for 20 minutes, with an image being created every minute. Further experimentation was subsequently performed on nine $Ti_{1-x}O_2:Sn_x$ (19:1) film surfaces undergoing

3 mm K-bar resazurin ink application under 3.25-3.41 mW/cm^2 UV light irradiation for 50 minutes (with or without either Actichlor Plus^{TM} or Virusolve^{+TM} cleaning agent exposure). Again, images were initially generated every minute, but latterly the interval between image collection was extended to every 2-3 minutes.

- X-ray photospectroscopy was performed without initial surface sputtering on the $Ti_{1-x}O_2$:Sn_x (19:1) films exposed either to Virusolve^{+TM} or Actichlor Plus^{TM}.

5.2.1 Microbiological exposure

Initial *E.coli* culture synthesis and the subsequent colony counting and dead or alive experimentation methods used were identical to those previously described in chapter 2. Following the initial experimentation, there was some variation in methodology used with the following approaches utilized:

- Initial exposures; 100 µl of re-suspended *E.coli* culture underwent addition to plain quartz, Pilkington Activ™ and $Ti_{1-x}O_2$:Sn_x (19:1) on quartz (all 1 cm^2) sample surfaces in petri dishes (4 identical samples per petri dish). Half of the samples were exposed to 3.30m W/cm^2 UV light irradiation and half to darkness (except during measurement). Exposures were at room temperature until significant dryness (50 minutes) was noted, with cultures being removed after 0, 10, 20, 30, 40 and 50 minutes UV light irradiation.
- Further exposures: Quartz, Pilkington Activ™ and $Ti_{1-x}O_2$:Sn_x (19:1) on quartz (all 2.5 cm^2) samples were suspended over petri dishes (4 identical samples per petri dish) filled with distilled water. 400 µl of re-suspended *E.coli* culture was added and the samples were exposed to 3.30 mW/cm^2 UV light intensity for six hours at room temperature. Cultures were removed before (t=0) and after (t=6) periods of UV light irradiation. Drying was also prevented by the hourly addition of fresh phosphate buffered saline (PBS) solution.

5.3 Results and Discussion

Water contact angle measurements were initially performed on three untreated $Ti_{1-x}O_2:Sn_x$ (19:1) films after 0, 30 and 60 minutes UV irradiation and after a week in darkness (10800 minutes) (figure 5.1). From figure 5.1, it may be seen that water contact angles for untreated samples are shown to generate a hydrophilic response to UV light irradiation, reaching near superhydrophilicity (18 ^{o}). Thereby the hydrophilic response indicates ROS presence and greater water run-off [451], subsequent to one hour of UV light irradiation. Hydrophobic recovery after a week in darkness is also detected with all results correlating well with the $Ti_{1-x}O_2:Sn_x$ (19:1) contact angle measurements depicted in chapter 4.

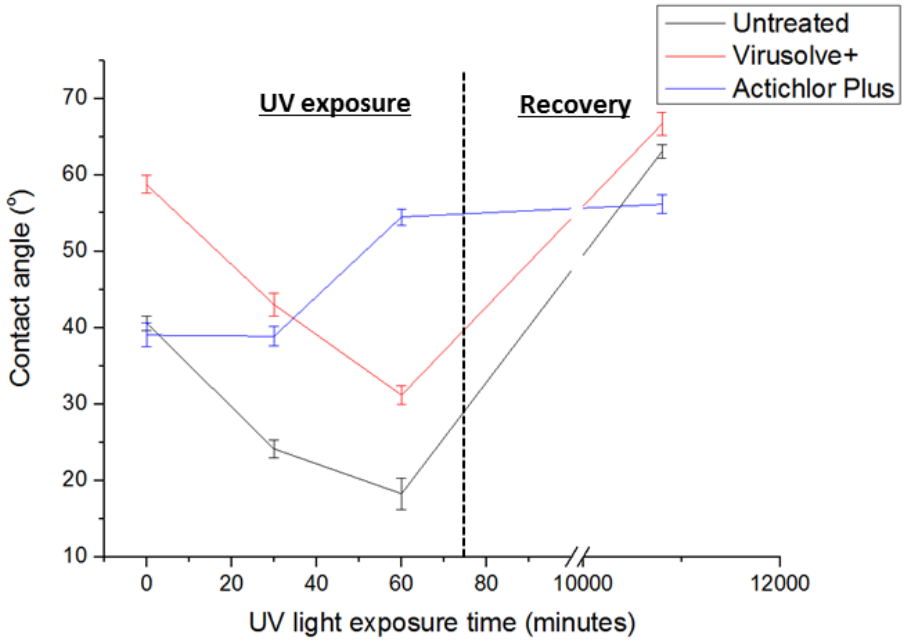

Figure 5.1: Water contact angles of unexposed, Virusolve^{+TM} exposed and Actichlor Plus^{TM} exposed $Ti_{1-x}O_2:Sn_x$ (19:1).

Correspondingly, the $Ti_{1-x}O_2:Sn_x$ (19:1) sample exposed to Virusolve^{+TM} also shows a hydrophilic trend, with average contact angles decreasing from 59 ^{o} to 31 ^{o} on 60 minutes UV irradiation. The higher initial contact angle noted for this sample suggests Virusolve^{+TM} exposure increases the initial $Ti_{1-x}O_2:Sn_x$ (19:1) hydrophobicity, but the sample still facilitates ROS generation during UV light irradiation. In contrast, the $Ti_{1-x}O_2:Sn_x$ (19:1) sample exposed to Actichlor Plus^{TM} shows no initial variation in contact angle between 0 and 30 minutes, as compared

to the untreated sample. However, the Actichlor Plus™ exposed $Ti_{1-x}O_2:Sn_x$ (19:1) sample exhibits a modest increase in hydrophobicity (39 ^{o} to 55 ^{o}) upon additional UV light irradiation. This is suggestive of a subtle variation in surface chemistry, providing a reduction in ROS formation.

Additionally, the sample exposed to Virusolve^{+TM} in figure 6.1, exhibits hydrophobic state recovery, subsequent to a week in darkness (10800 minutes). In contrast, the $Ti_{1-x}O_2:Sn_x$ (19:1) sample exposed to Actichlor Plus™ shows no appreciable variation. This implies treatment with this particular cleaning agent results in a permanent inhibition of photoactivity, possibly resulting from surface contamination.

The initial basic blue 66 ink test was applied to a larger sample set compared to that utilized in Chapter 4, decreasing associated error. It was found that the average ttb for the $Ti_{1-x}O_2:Sn_x$ (19:1) films was ca. 5 minutes and 12 seconds ± 1 minute 13 seconds error.

In contrast, the undoped TiO_2 sample exhibited a ttb of 11 minutes and 4 seconds ± 35 seconds error. Thus this experiment confirms the result present in Chapter 4, which indicated enhanced photocatalytic activity of the $Ti_{1-x}O_2:Sn_x$ (19:1) film, as compared to the nominally undoped TiO_2 sample grown under (nearly) identical conditions, table 5.1.

	TiO_2:Sn (19:1) ttb (minutes:seconds)	Pilkington Activ™ ttb (minutes:seconds)
Basic blue 66 ink	5:12 ±1:13	2:07 ±0:19
Resazurin ink	31:12 ±4:21	3:22 ±0:16

Table 5.1: ttb variation of basic blue 66 and resazurin inks between photo-activated $Ti_{1-x}O_2:Sn_x$ (19:1) and Pilkington Activ™.

The photocatalytic resazurin ink degradation test was subsequently applied to the $Ti_{1-x}O_2:Sn_x$ film (19:1), figure 5.2.

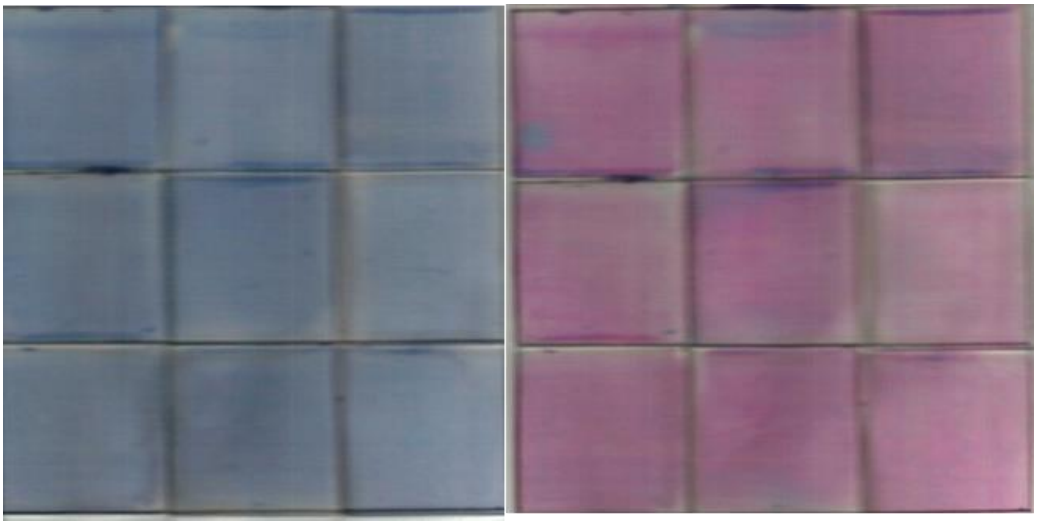

Figure 5.2: Resazurin ink degradation (before and after UV light irradiation) on $Ti_{1-x}O_2:Sn_x$ (19:1).

From figure 5.2, the $Ti_{1-x}O_2:Sn_x$ (19:1) film also showed photocatalytic activity according to resazurin ink degradation, as expected from the results presented in chapter 4. The $Ti_{1-x}O_2:Sn_x$ (19:1) film changed the resazurin ink colour from blue (resazurin) to pink (resourfin) in approximately 30 minutes. These results illustrate that although not as photocatalytically active as the Pilkington Activ™ standard, the $Ti_{1-x}O_2:Sn_x$ (19:1) film still nevertheless was demonstrably photoactive according to the two ink degradation tests employed.

Interestingly, resazurin ink takes "longer" to be reduced than basic blue 66 ink on Pilkington Activ™, indicating that particular ink degradations must only be compared with the same ink reaction on other substrates [478, 594]. In other words, providing direct comparisons between disparate ink degradation tests is fraught with difficulty [478]. This was readily illustrated by considering for basic blue 66 ink, both the $Ti_{1-x}O_2:Sn_x$ (19:1) and Pilkington Activ™ films studied here give roughly comparable ttb values of approximately 5 minutes and 2 minutes respectively. In contrast, the corresponding ttb values for the resazurin ink degradation are approximately 31 minutes and 3 minutes respectively. Therefore, the $Ti_{1-x}O_2:Sn_x$ (19:1) film require some 10 times the exposure as compared to the Pilkington Activ™ sample [595]. Furthermore, since resazurin ink degradation

indicated the greatest differential between samples, this test was subsequently utilized.

In order to examine the effects of repeated exposure to the hospital cleaning agents on the $Ti_{1-x}O_2:Sn_x$ (19:1) films. $Ti_{1-x}O_2:Sn_x$ (19:1) films were subjected to the resazurin ink degradation test after exposure to either Virusolve^{+TM} or Actichlor Plus^{TM}, with a control $Ti_{1-x}O_2:Sn_x$ (19:1) film set left untreated prior to resazurin ink application. Cleaning agent treatment (or not in the case of the control) and subsequent resazurin ink degradation was also performed three times in succession, figure 5.3.

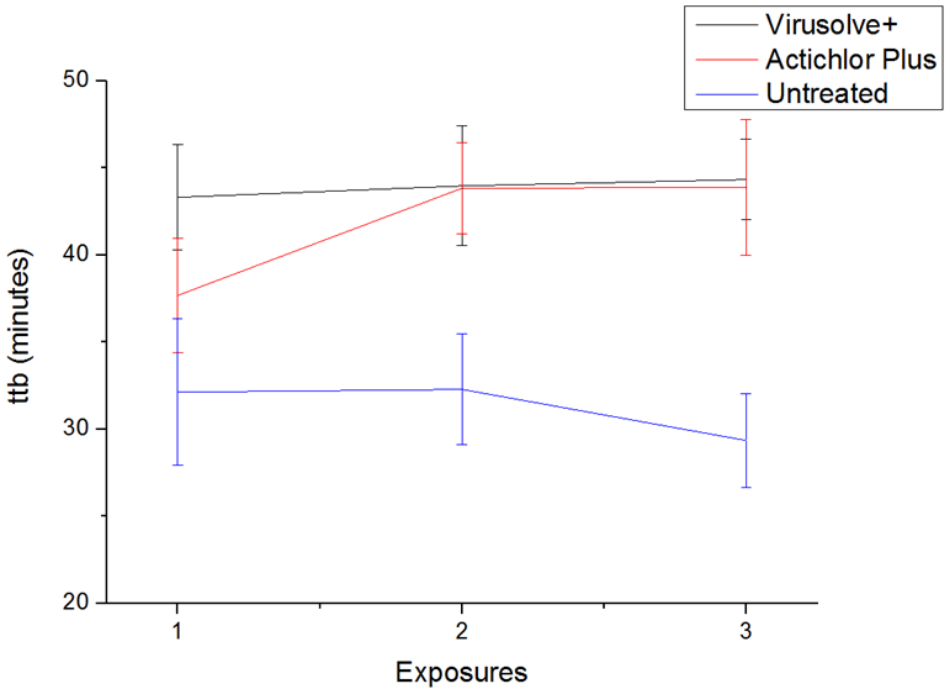

Figure 5.3: ttb results generated from triplicate resazurin ink degradation on $Ti_{1-x}O_2:Sn_x$ (19:1) films with prior exposure each time to either Virusolve^{+TM} or Actichlor Plus^{TM}, or left untreated.

From figure 5.3, the Virusolve^{+TM} or Actichlor Plus^{TM} treated $Ti_{1-x}O_2:Sn_x$ (19:1) films clearly indicate a consistently longer ttb after multiple exposures, as compared to the untreated $Ti_{1-x}O_2:Sn_x$ (19:1) film. This suggests cleaning agent exposure decreases the photocatalytic degradation of resazurin ink, as previously observed in chapter 3. Furthermore, figure 5.3 shows that within the limits of experimental error, repeated exposures to either Virusolve^{+TM} or Actichlor Plus^{TM} has no

appreciable influence on the resazurin ttb values recorded. The error bars here were measured from each real experimental variation indicating potential discrepancies of 5 minutes or more. Therefore subtle disparities arising from real chemical alterations may not be easily detected utilizing this type of methodology.

XPS was performed on the $Ti_{1-x}O_2:Sn_x$ (19:1) films prior and subsequent to either Virusolve^{+TM} or Actichlor Plus^{TM} exposure (tables 5.2 and 5.3). This was to determine if a chemically altered surface or possible surface contamination resulted, that could sequentially influence the photocatalytic activity.

	Actichlor Plus^{TM} exposed $Ti_{1-x}O_2:Sn_x$ (19:1)	Actichlor Plus^{TM} exposed $Ti_{1-x}O_2:Sn_x$ (19:1)	Virusolve^{+TM} exposed $Ti_{1-x}O_2:Sn_x$ (19:1)	Virusolve^{+TM} exposed $Ti_{1-x}O_2:Sn_x$ (19:1)
Peak	Position (eV)	Concentration (%)	Position (eV)	Concentration (%)
O 1s	529.2	52.5	529.3	47.8
Ti 2p	458.2	19.5	457.3	17.8
Sn 3d	485.2	2.9	485.3	2.9
C 1s	284.2	21.3	284.3	28.7
N 1s	400.3	1.3	399.3	1.7
Si 2p	102.2	0.8	100.3	1.1
Cl 2p	200.2	0.4	-	-
P 2p	190.2	1.3	-	-

Table 5.2: Low resolution XPS results for the Actichlor Plus^{TM} exposed $Ti_{1-x}O_2:Sn_x$ (19:1) film and the Virusolve^{+TM} exposed $Ti_{1-x}O_2:Sn_x$ (19:1) film.

From table 5.2, both $Ti_{1-x}O_2:Sn_x$ (19:1) films suggest a material very close to stoichiometric TiO_2. A majority 1:2 Ti:O ratio provided approximately 53.2 % (17.8 % titanium and 35.4 % oxygen) for Virusolve^{+TM} exposed $Ti_{1-x}O_2:Sn_x$ and 59.4 % (19.5 % titanium and 38.9 % oxygen) for Actichlor Plus^{TM} exposed $Ti_{1-x}O_2:Sn_x$ of surface detected elements as TiO_2. Furthermore, dissimilar to the data presented in Chapter 4, no evidence of any Ti^{3+} species is detected. This observation may actually be due to previous Ti^{3+} detection resulted in samples subsequent to XPS

sputter cleaning. Since the experiments described in this chapter, did not involve surface sputter cleaning prior to XPS analysis, detected signals could arise solely from fully oxidized surface species [150].

Additionally, lower tin concentrations than expected (2.9 %) are incorporated. These lower concentrations potentially result from decreased titanium and tin precursor growths on disparate equivalent oxides [164, 166], and further correlate with the $Ti_{1-x}O_2:Sn_x$ (19:1) film synthesis in chapter 4.

Table 5.2 also indicates both the non-sputtered $Ti_{1-x}O_2:Sn_x$ (19:1) films exposed to Virusolve^{+TM} and Actichlor Plus^{TM} show clear evidence of expected adventitious surface carbon and nitrogen. Despite this, obvious disparities in carbon concentration exist between the $Ti_{1-x}O_2:Sn_x$ (19:1) films exposed to either Virusolve^{+TM} or Actichlor Plus^{TM}, possibly related to different cleaning agent exposures. Minimal silicon concentrations are also indicated, potentially originating from sample cleaving.

No other impurities are detected for the $Ti_{1-x}O_2:Sn_x$ (19:1) film exposed to Virusolve^{+TM}. However, as in chapter 3, small concentrations of both chlorine (0.4 %) and phosphorus (1.3 %) are present on the $Ti_{1-x}O_2:Sn_x$ (19:1) film exposed to Actichlor Plus^{TM}.

From Table 5.3, high resolution XPS indicates significant oxygen, titanium, carbon and tin XPS peak shifts for the $Ti_{1-x}O_2:Sn_x$ films exposed to either Virusolve^{+TM} or Actichlor Plus^{TM}, as compared to an untreated $Ti_{1-x}O_2:Sn_x$ (19:1) sample. These peak shifts are highlighted throughout figures 5.4-5.7. However, peak shifts could also result from differences in surface environments corresponding to variation in surface preparation. This surface preparation includes sputtering to remove adventitious carbon for the untreated $Ti_{1-x}O_2:Sn_x$ (19:1) film and no sputtering for the Virusolve^{+TM} and Actichlor Plus^{TM} exposed $Ti_{-x}O_2:Sn_x$ (19:1) films.

	Actichlor Plus™ exposed $Ti_{1-x}O_2:Sn_x$ (19:1)	Actichlor Plus™ exposed $Ti_{1-x}O_2:Sn_x$ (19:1)	Virusolve+™ exposed $Ti_{1-x}O_2:Sn_x$ (19:1)	Virusolve+™ exposed $Ti_{1-x}O_2:Sn_x$ (19:1)
Peak	Position (eV)	Concentration (%)	Position (eV)	Concentration (%)
O 1s_1 (metal oxide)	529.7 (530.3)	43.2	529.2 (530.3)	40.7
O 1s_2 (organics, OH)	531.0 (531.8)	14.3	530.6 (531.8)	12.1
Ti 2p_1 (Ti^{4+} $2p_{3/2}$)	458.5 (458.9)	13.6	458.0 (458.9)	12.5
Ti 2p (Ti^{4+} $2p_{1/2}$)	464.2 (464.6)	6.8	463.7 (464.6)	6.2
C 1s_1 (C=C/C-C)	284.8	13.1	284.8	18.8
C 1s_2 (C-O)	286.1 (286.5)	4.1	286.0 (286.5)	4.8
C 1s_3 (O-C=O)	287.9 (289.2)	1.1	287.7 (289.2)	1.6
C 1s_4 (CO_3)	288.9	0.5	-	-
Sn 3d	486.2 (486.7)	3.4	485.7 (486.7)	3.4

Table 5.3: High resolution XPS results for both the Actichlor Plus™ exposed $Ti_{1-x}O_2:Sn_x$ (19:1) and the Virusolve+™ $Ti_{1-x}O_2:Sn_x$ (19:1) films with significant peak shifts from the unexposed $Ti_{1-x}O_2:Sn_x$ (19:1) film highlighted in brackets.

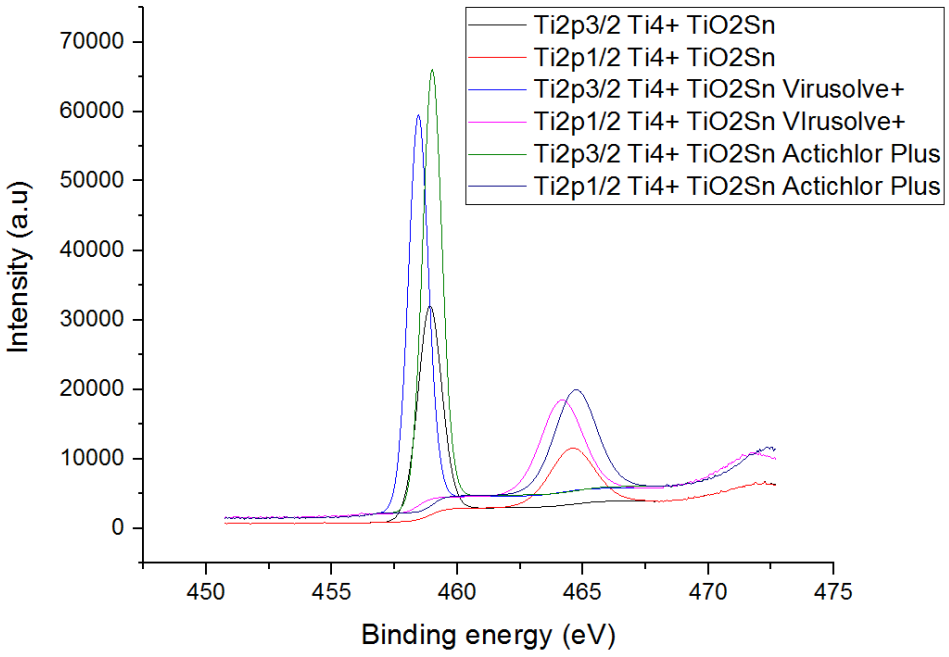

Figure 5.4: Ti^{4+} $2p_{3/2}$ and $_{1/2}$ peak shifts for the unexposed $Ti_{1-x}O_2:Sn_x$ (19:1) film, the $Ti_{1-x}O_2:Sn_x$ (19:1) film exposed to Actichlor Plus™ and the $Ti_{1-x}O_2:Sn_x$ (19:1) film exposed to Virusolve^{+}™.

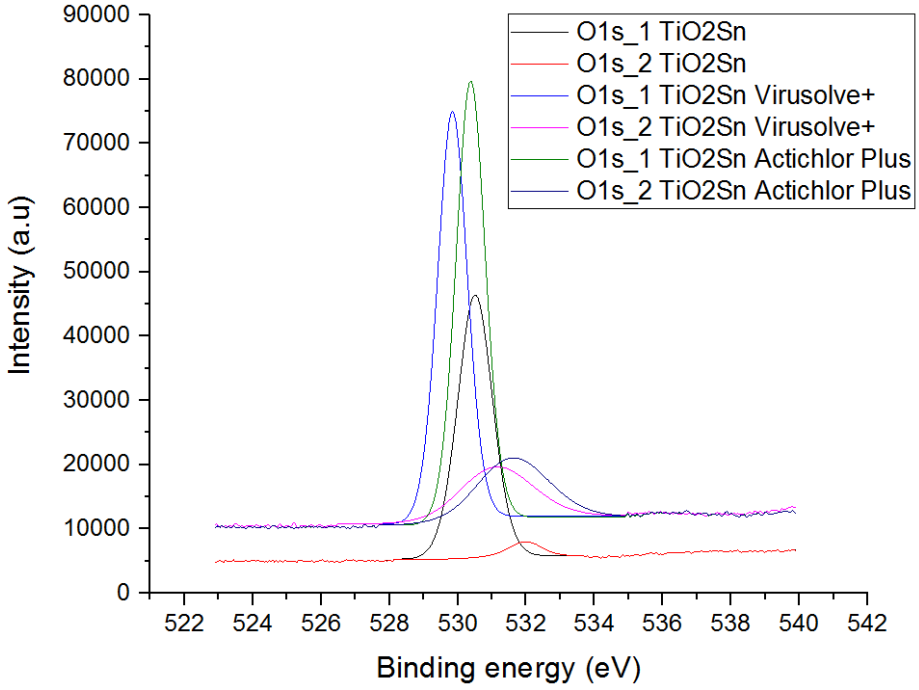

Figure 5.5: O 1s_1 and 1s_2 peak shifts for the unexposed $Ti_{1-x}O_2:Sn_x$ (19:1) film, the $Ti_{1-x}O_2:Sn_x$ (19:1) film exposed to Virusolve^{+}™ and the $Ti_{1-x}O_2:Sn_x$ (19:1) film exposed to Actichlor Plus™.

Figures 5.4 and 5.5 show decreased binding energy $Ti_{2p3/2}$, $Ti_{2p1/2}$, O_{1s_1} and O_{1s_2} peak shifts for both the Actichlor Plus™ and the Virusolve+™ exposed $Ti_{1-x}O_2:Sn_x$ films, as compared to the untreated $Ti_{1-x}O_2:Sn_x$ (19:1) film. This suggests a change in titanium and oxygen chemical environments in both Ti-O and Ti-O-H bonding in relation to the cleaning agent exposure.

Additionally, figure 5.6, also shows a decrease in binding energy corresponding to Sn_{3d} peaks for both the Virusolve+™ and the Actichlor Plus™ exposed $Ti_{1-x}O_2:Sn_x$ (19:1) films, as compared to the untreated $Ti_{1-x}O_2:Sn_x$ (19:1) film. Again, this suggests a variation in Sn-O and Ti-O-Sn chemical environments in relation to the cleaning agent exposure.

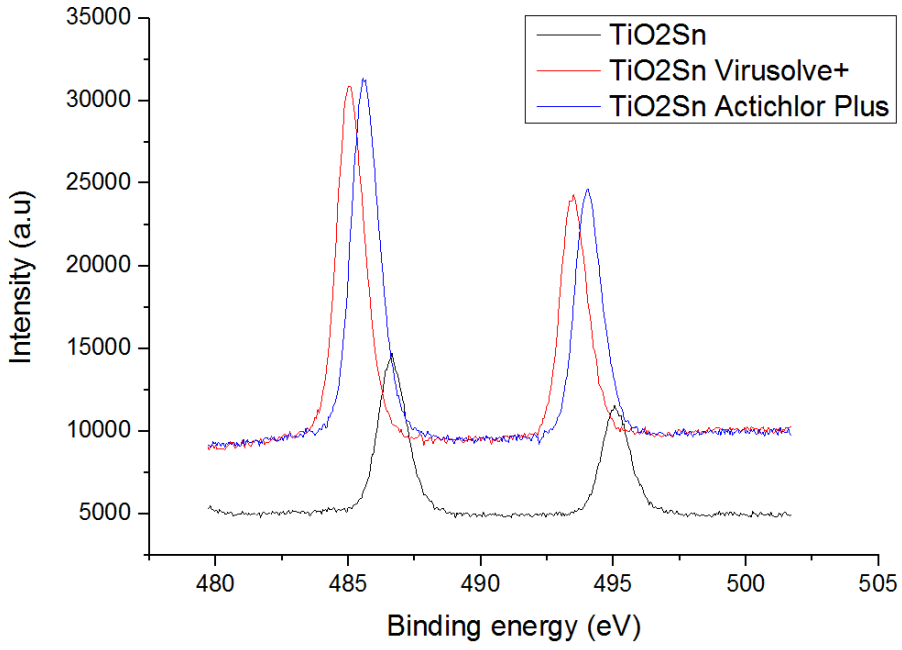

Figure 5.6: Sn 3d peak shifts for the unexposed $Ti_{1-x}O_2:Sn_x$ (19:1) film, the $Ti_{1-x}O_2:Sn_x$ (19:1) film exposed to Virusolve+™ and the $Ti_{1-x}O_2:Sn_x$ (19:1) film exposed to Actichlor Plus™.

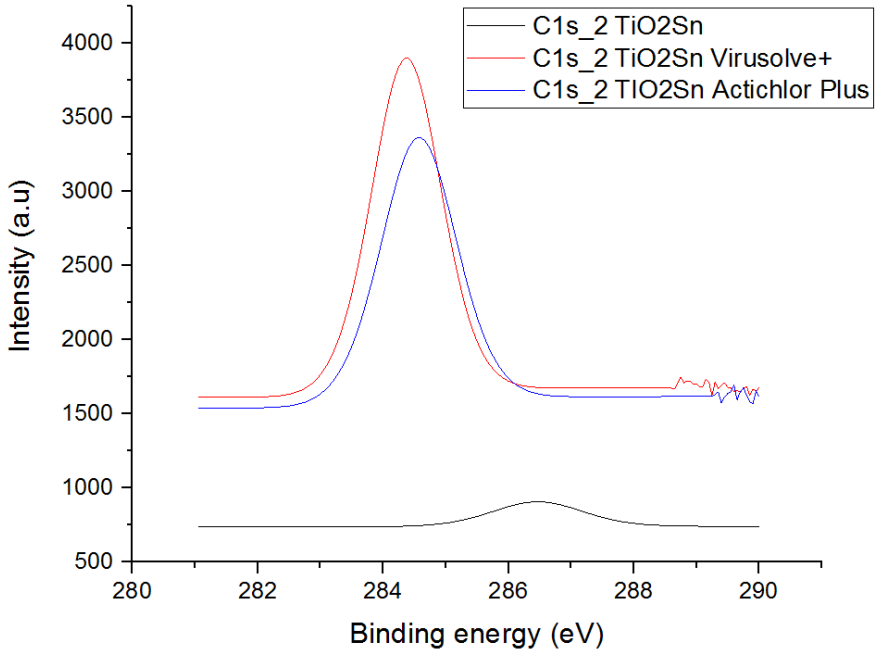

Figure 5.7: C 1s_2 peak shifts for the unexposed $Ti_{1-x}O_2:Sn_x$ (19:1) film, the Virusolve^{+TM} exposed $Ti_{1-x}O_2:Sn_x$ and Actichlor Plus^{TM} exposed $Ti_{1-x}O_2:Sn_x$.

Furthermore, figure 5.7 shows an altered chemical environment for surface carbon present in surface carbonate groups with decreased binding energy C_{1s_2} peak shifts for Virusolve^{+TM} and Actichlor Plus^{TM} exposed $Ti_{1-x}O_2:Sn_x$ (19:1) films.

Overall, Actichlor Plus^{TM} exposure provides specific surface ion contamination of either Pilkington Activ^{TM} or $Ti_{1-x}O_2:Sn_x$ (19:1) surfaces, which could lead to reduced photocatalytic activity and increased water contact angle hydrophobicity [596, 597]. It was found that both the Pilkington Activ^{TM} and $Ti_{1-x}O_2:Sn_x$ (19:1) films were contaminated with 1.2-1.3 % phosphorus, as well as 0.4 % chlorine. This presumably arises from exposure to the troclosene sodium component in the Actichlor Plus^{TM} (see table 5.2 here and chapter 3). In contrast, $Ti_{1-x}O_2:Sn_x$ (19:1) exposure to Virusolve^{+TM} did not result in residual ion presence.

$Ti_{1-x}O_2:Sn_x$ (19:1) samples exposed to Actichlor Plus^{TM} showed the most evidence of reduction in photocatalytic activity. The photocatalytic activity reduction potentially arose from chlorine residues after the cleaning process, with Cl^- previously shown to prevent O_2 adsorption and CO-O_2 intermediate creation [598]. However, such residues were not detected on the $Ti_{1-x}O_2:Sn_x$ (19:1) films treated

with Virusolve^{+TM}, which showed an initial decrease to a persistent lower level of photocatalytic activity.

Since chemical or mechanical damage may have also resulted to the films in question during the cleaning process, $Ti_{1-x}O_2:Sn_x$ (19:1) sample surfaces were examined using SEM. SEM was performed prior to, (figure 5.8) and after disparate cleaning agent treatment (figure 5. a) and b)), following on from the procedures established for Pilkington Activ^{TM} in chapter 3.

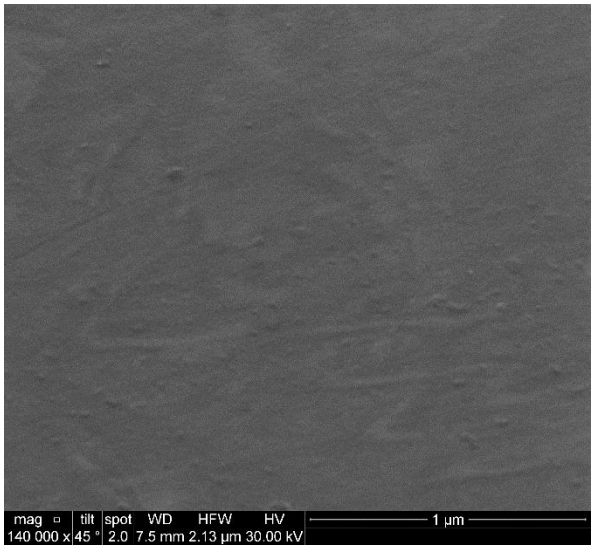

Figure 5.8: Surface SEM of untreated $Ti_{1-x}O_2:Sn_x$ (19:1)

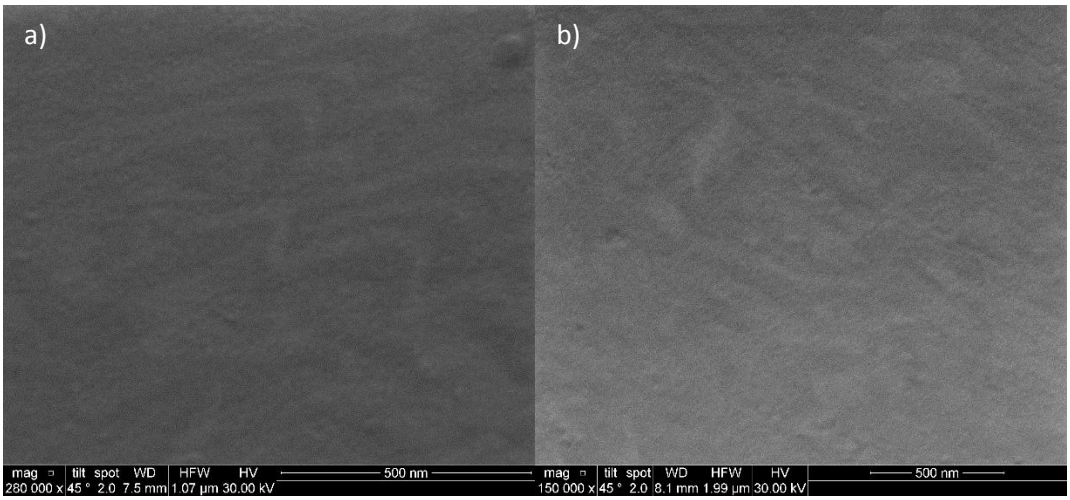

Figures 5.9: Surface SEM of the $Ti_{1-x}O_2:Sn_x$ (19:1) film following exposure to a) Virusolve^{+TM} and b) Actichlor Plus^{TM} treatments

From figure 5.8, the untreated $Ti_{1-x}O_2:Sn_x$ (19:1) film appears to consist of smaller "crystalline" regions and scattered larger grains, somewhat consistent with previous studies on this material in chapter 4. Figure 5.9 indicates negligible variation in terms of general surface appearance results subsequent to exposure of the $Ti_{1-x}O_2:Sn_x$ (19:1) sample to either Virusolve^{+TM} (figure 5.9a)) or Actichlor Plus^{TM} (figure 5.9b)). In both cases, $Ti_{1-x}O_2:Sn_x$ (19:1) surfaces remain composed of small crystalline regions, suggesting no overall variation resulting from chemical or mechanical damage.

5.3.1 Microbiological exposure

Initially microbiological surface attachment with *E.coli* was performed (table 5.4), utilizing the optical density method previously described in Chapter 2. This was applied to the detection of purple violet stain corresponding to attached *E.coli* concentrations. It was found that the lowest levels of attachment were present on the Pilkington Activ^{TM} sample, which showed an average optical density of 0.11 (at 600 nm, 1 optical density = $8x10^8$ bacteria ml^{-1}). The largest levels of attachment were indicated on the $Ti_{1-x}O_2:Sn_x$ (19:1) sample, which showed an average optical density of 0.38.

	Average OD_{595nm}	**Replicate 1 OD_{595nm}**	**Replicate 2 OD_{595nm}**	**Replicate 3 OD_{595nm}**
Pilkington Activ™	0.11	0.09	0.16	0.09
$Ti_{1-x}O_2:Sn_x$ (19:1)	0.38	0.37	0.41	0.36
Quartz	0.31	0.32	0.38	0.21

Table 5.4: *E.coli* attachment (CV staining) on various film surfaces; Plain Glass, Pilkington Activ^{TM} and $Ti_{1-x}O_2:Sn_x$ (19:1)

As may be observed from table 5.4, average *E.coli* surface attachment was greater on the $Ti_{1-x}O_2:Sn_x$ (19:1) sample and lower on both the Pilkington Activ^{TM} and plain fused quartz samples. However, the antimicrobial activity of similar surfaces may be viewed from two distinct perspectives;

- Lower attachment levels are beneficial and will necessarily limit biofilm formation.
- Attachment may also be regarded as favourable, but only if the surface is subsequently capable of antimicrobial activity via a photocatalytic reaction.

To assist in solving this conundrum, photocatalytic degradation of surface grown *E.coli* was performed, incorporating colony counting and viable cell counts (dead or alive experimentation).

The initial *E.coli* colony counting results obtained from all three samples were inconclusive with TNTC (too numerous to count) frequencies generated across all agar-grown *E.coli* cultures. Furthermore, the dead or alive experiments performed using 50 minutes of UV light exposure indicated minimal *E.coli* cell death (95-99 % alive). The initial results therefore suggest none of the samples were capable of performing *E.coli* colony photosterilization. As might be expected, TNTC was also reported for all corresponding samples left in darkness.

Furthermore, no E.coli colony growth distortion or aggregation [63, 599] was detected as may be expected to result from colony damage only induced by UV light. Which suggested the utilization of insufficient irradiation time/intensity to significantly attack the *E.coli* colonies [63] during this experiment.

Considering this, the experiments were subsequently repeated utilizing pre-activation of samples by UV light, prior to addition of *E.coli*. Samples were irradiated by UV light for 1 hour and 30 minutes, followed by *E.coli* inoculation and semi-immersed in water with hourly PBS addition to prevent drying out. Larger samples (2.5 cm^2) were also utilized in order to improve subsequent observations. The results of these experiments are indicated in table 5.5, with the data labelled as “initial” corresponding to an agar filled petri dish inoculated with a sample of *E.coli*, prior to pre-activated sample surface application.

	(1.00E+09) cfu/ml average	Replicate 1 (cfu/ml)	Replicate 2 (cfu/ml)	Replicate 3 (cfu/ml)
Initial	2.88E+12	TNTC	2.75E+12	3.01E+12
Pilkington Activ™	2.71E+12	2.68E+12	TNTC	2.75E+12
$Ti_{1-x}O_2:Sn_x$ (19:1)	1.94E+12	1.88E+12	2.36E+12	1.59E+12
Quartz	1.84E+12	TNTC	1.42E+12	2.25E+12

Table 5.5: E.coli colony counts corresponding to initial (t=0) and after 6 hours (t=6) UV light irradiation for; plain quartz, Pilkington Activ™ and $Ti_{1-x}O_2:Sn_x$ (19:1) films

From table 5.5, plain quartz is observed to possess the lowest average levels of colony formation, followed by the $Ti_{1-x}O_2:Sn_x$ (19:1) film and then by the Pilkington Activ™ film. These results are not as expected and only correlate with previous attachment studies for the Pilkington Activ™ and $Ti_{1-x}O_2:Sn_x$ (19:1) samples. Therefore greater attachment equates to lower colony formation after six hours of UV light irradiation.

From the presented results, it can be speculated that a high *E.coli* colony degradation rate could initially occur on the pre-irradiated Pilkington Activ™ and $Ti_{1-x}O_2:Sn_x$ (19:1) films, resulting in debris from damaged/dead *E.coli* bacteria. Without the subsequent removal of this debris and reconstitution of ROS sites, further photocatalytic degradation reactions are sterically and chemically hindered with the debris providing suitable attachment sites for *E.coli* bacteria. From this point onwards any *E-coli* colony death and growth distortion [599] would probably result from direct UV light exposure, hence the low colony counts from a plain quartz sample.

5.4 Conclusions

In conclusion, the $Ti_{1-x}O_2:Sn_x$ (19:1) film indicates greater photocatalytic activity than initially observed in chapter 4. This is determined from both water contact angle measurements and photocatalytic degradation with respect to basic blue 66 and resazurin inks under UV light irradiation. When treated once with either Virusolve+™ or Actichlor Plus™ cleaning agents, the photocatalytic activity of Ti_{1-}

$_xO_2$:Sn_x (19:1) films was generally impaired with respect to resazurin ink degradation. Additionally, repeated cleaning agent exposure provided negligible variation in photocatalytic activity, similar to results from Chapter 3. Again suggesting a significant amount of research is necessary prior to any TiO_2-based photocatalytically active coating deployment in any environment undergoing regular cleaning agent exposure.

Concerning antimicrobial activity, it appears that attachment factors dictate antimicrobial ability for the Pilkington Activ^{TM} and $Ti_{1-x}O_2$:Sn_x (19:1) films, with attachment required for photocatalytic degradation of *E.coli* cultures. Furthermore, the enhanced photocatalytic activity of the $Ti_{1-x}O_2$:Sn_x (19:1) films in relation to the nominally undoped TiO_2, presumably arises from inducing subtle modification in local environments surrounding the Sn^{4+}, although the exact reasoning to support these observations is not clear.

Chapter 6: Synthesis and subsequent analysis of $Ti_{1-x}O_2:Ga_x$ films.

6.1 Introduction

As previously outlined in chapter 1, both the photocatalytic and conductive properties of TiO_2 films undergo alteration on dopant incorporation. Specifically, $Ti_{1-x}O_2:Ga_x$ ($x \leq 0.05$) structures typically show a slight improvement in photocatalytic properties as compared to undoped TiO_2. This photocatalytic improvement correlates with indirect charge compensation introduction on Ga^{3+} substitution into Ti^{4+} sites ($Ga_{Ti'}$) and resulting $V_{O}^{\cdot\cdot}/Ti^{3+}$ creation [600]. Additionally, the $V_{O}^{\cdot\cdot}$ generated possess electron trapping capabilities [178] to enhance hole lifetimes and hence assist in surface hydroxyl radical creation, improving the photocatalytic activity. Ga^{3+} sites have also been proposed as electron trapping centres, further increasing potential photocatalytic activity [180].

Both Ga^{3+} (76 pm) and Ti^{4+} (74.5 pm) possess similar ionic radii, but $Ga_{Ti'}$ site substitution induces morphological strain. This strain hinders grain growth and assists in excess GaO_x agglomeration [339] leading to increased recombination on $Ti_{1-x}O_2:Ga_x$ surfaces [180]. Additionally, $Ga_{Ti'}$ substitution promoted the extension of the ART to higher temperatures [600]. This provided both an increased thermodynamic stability of the anatase morphology and greater surface concentrations of titanol groups [177]. Additional promotion of surface adsorbed O_2 conversion to O_2^- was also detected [178].

Furthermore, $Ti_{1-x}O_2:Ga_x$ structures typically display a red-shift in band gap towards visible light wavelengths [178, 180, 339, 600, 601], probably corresponding to generated $Ti^{3+}/V_{O}^{\cdot\cdot}$ mid-band gap states upon $Ga_{Ti'}$ site substitution. Comparatively, GaO_x and TiO_2 band mixing is unlikely to directly affect the overall band gap size with a large 4.9 eV indirect Ga_2O_3 band gap presumably providing Burstein-Moss effects.

In metal oxides, enhanced semiconductivity induced though gallium doping is typically dominated by $Zn_{1-x}O:Ga_x$ films [371, 372, 374] with reported resistivities equivalent to ITO magnitudes, e.g: 1.2×10^{-4} Ω.cm [372], 2.6×10^{-4} Ω.cm [373],

$3.18x10^{-4}$ Ω.cm [362] and $6.3x10^{-4}$ Ω.cm [14]. In contrast, reports of resistivity measurements for $Ti_{1-x}O_2:Ga_x$ are minimal. However, an ALD grown nanolaminate $Ti_{0.95}O_2:Ga_{0.05}$ film was synthesized recently [603] which indicated evidence of hole repulsion and electron trap hopping through $V_O^{\cdot\cdot}$ defect generation upon $Ga_{Ti'}$ site substitution.

Therefore, although $Ti_{1-x}O_2:Ga_x$ particulates and films have been studied previously, an understanding of the optimal gallium concentrations remains elusive. At the time of writing ALD grown $Ti_{1-x}O_2:Ga_x$ has not been subjected to photocatalytic studies. Consequently, the remainder of this chapter discusses $Ti_{1-x}O_2:Ga_x$ film synthesis and associated analysis for potential photocatalytic and conductivity improvement over similarly ALD grown undoped TiO_2 films.

Furthermore, as the photocatalytic activity of nominally undoped TiO_2 typically results from the effect UV light irradiation possesses on the bulk electronic structure and how this further effects the TiO_2 surface chemistry. To examine the relationship between the bulk electronic structure and surface chemistry possessed by the $Ti_{1-x}O_2:Ga_x$ film, the surface of $Ti_{1-x}O_2:Ga_x$ was deliberately altered in further experiments. This alteration was performed by creating surface GaO_x was through using a final pulse of TEGa (figure 6.1). Additionally, this process was also applied to a range of $Ti_{1-x}O_2:Ga_x$ films incorporating disparate gallium concentrations (based on different ALD precursor cycle ratios).

Figure 6.1: The theoretical structure of Ga-capped $Ti_{1-x}O_2:Ga_x$ films (Not to scale).

6.2 Methodology

6.2.1 ALD synthesis of nanolaminate $Ti_{1-x}O_2:Ga_x$ films

Through utilizing an identical nanolaminate thermal ALD process to chapter 4 [604]. $Ti_{1-x}O_2:Ga_x$ films were grown on quartz substrates (Vitreosil® 077 optical fused quartz) at 180 ^oC under argon gas. Triethylgallium (TEGa) was utilized as the gallium precursor and was kept at 25 ^oC. Half of all synthesized samples underwent annealing, as previously described.

6.2.2 ALD synthesis of Ga-capped $Ti_{1-x}O_2:Ga_x$ films

A Cambridge Nanotech ALD system was utilized for film growth onto approximately 10nm ALD-grown Al_2O_3 (utilizing TMA (trimethylaluminium) at 26 ^oC in the bubbler and water as precursors) on silicon wafer (<100>, p-type, boron doped) and corning micro slide plain glass substrates, under argon gas. Ga-capped nanolaminate $Ti_{1-x}O_2:Ga_x$ film growth proceeded at 325 ^oC with TDMAT and O_2 plasma (20cm^3 oxygen in 140cm^3 argon gas at 300W) as precursors. The undoped TiO_2 was also grown utilizing the identical conditions described above.

Gallium substituted titanium growth cycles were designed by considering nominal gallium oxide ($GaOx/Ga_2O_3$) growth within films. Ratio utilization was performed as GaO_x and TiO_2 growth rates were initially assumed to equate for monolayer growth (nominal 5 % bulk Ga_2O_3 relating to a 19:1 titanium: gallium (Ti:Ga) cycle ratio). Cycle ratios were repeated for 550 cycles on average, synthesizing films with a thickness dependent on the specific number of cycles or cycle ratio employed. Furthermore, a final single TEGa ALD pulse was used to cap the $Ti_{1-x}O_2:Ga_x$ film.

6.2.3 Analysis of nanolaminate $Ti_{1-x}O_2:Ga_x$ films

$Ti_{1-x}O_2:Ga_x$ (99:1) and (19:1) underwent analysis subject to previously described methodology within chapter 2. Specific technique variations are listed here:

- A second Raman spectroscopy scan was performed on the UCC system. This system utilized a standard 532 nm optical microscope, Raman probe head and Ocean Optics QE PRO Raman spectrometer with variable slit widths,

typically an 8 cm^{-1} tuneable resolution. 532 nm wavelength, 0.1-0.2 laser spot size, and 30 mW laser power were also used.

- Separate aluminium contamination study was performed through XPS analysis, involving compositional scans at seven randomly located points across $Ti_{1-x}O_2:Ga_x$ (19:1) surface.
- Photocatalytic ink degradation was performed by initial dispersion of basic blue 66 ink across $Ti_{1-x}O_2:Ga_x$ surfaces by a 3 mm K hand coater™. Samples were exposed to two and a further six ($Ti_{1-x}O_2:Ga_x$ (99:1) only) hours (after initial deactivation) UV light irradiation.
- Average contact angle measurement at 30, 60, 90 and 120 minute intervals during UV light irradiation.

6.2.4 Analysis of Ga-capped nanolaminate $Ti_{1-x}O_2:Ga_x$ films

All nominally undoped TiO_2 and Ga-capped $Ti_{1-x}O_2:Ga_x$ films were analysed according to the previously described methodology (chapter 2). Specific technique variations or films analysed to this chapter are listed here:

- X-ray photoelectron spectroscopy was performed without adventitious carbon removal prior to analysis.
- All films (Ga-capped $Ti_{1-x}O_2:Ga_x$, nominally undoped TiO_2, Pilkington Activ™ and glass substrates) underwent photocatalytic activation from four hours of UV light irradiation prior to basic blue 66 ink application with a 3 mm K hand coater™. Subsequent 10 minutes UV light irradiation with scanning every 10 seconds throughout for image generation was performed.
- Average water contact angles were determined at 240 minutes during UV irradiation.

6.3 Results from nanolaminate $Ti_{1-x}O_2:Ga_x$ film analysis.

XRD was performed on the as-grown and annealed $Ti_{1-x}O_2:Ga_x$ (99:1) and (19:1) films (figure 6.2) with no significant crystalline reflections being detected, suggesting the material was essentially amorphous.

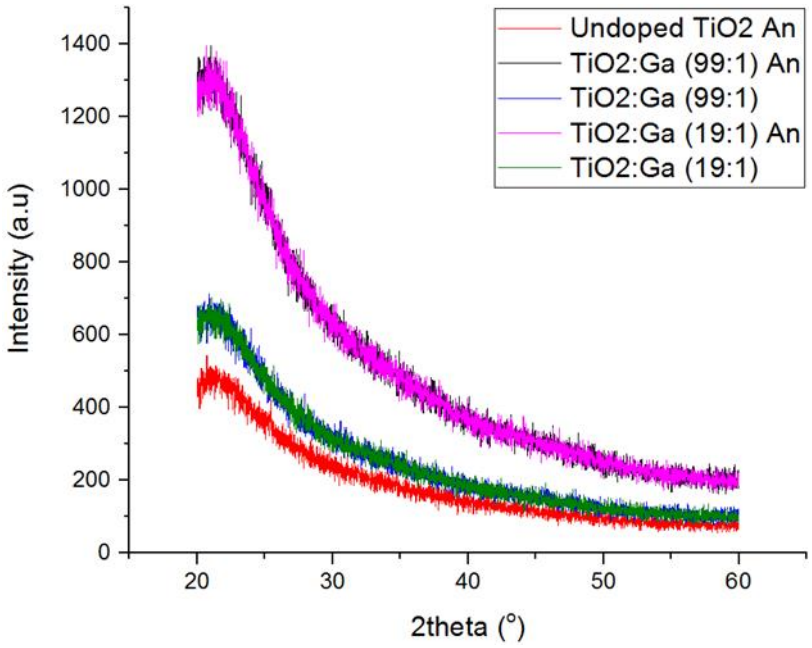

Figure 6.1: XRD spectra of the as-grown $Ti_{1-x}O_2:Ga_x$ (99:1) and (19:1) films and the annealed (An) nominally undoped TiO_2, $Ti_{1-x}O_2:Ga_x$ (99:1) and (19:1) films.

Raman spectroscopy generally confirms this (figures 6.3 and 6.4) for the as-grown $Ti_{1-x}O_2:Ga_x$ (99:1) and (19:1) sample and the annealed $Ti_{1-x}O_2:Ga_x$ (19:1). However, single 144cm^{-1} peak detection for annealed $Ti_{1-x}O_2:Ga_x$ (99:1) (figure 6.3) is indicative of anatase morphology, possibly resulting from lower GaOx nanolaminate concentrations. Additionally, on comparison to a Raman spectra for an annealed nominally undoped TiO_2 (figure 6.5), where peaks corresponding to anatase crystallinity appear at 144 cm^{-1} (E_g), 199 cm^{-1} (E_g), 399 cm^{-1} (B_{1g}), 517 cm^{-1} ($A_{1g}+B_{1g}$) and 636 cm^{-1} (E_g). It could be suggested gallium dopant addition decreases potential anatase generation after annealing.

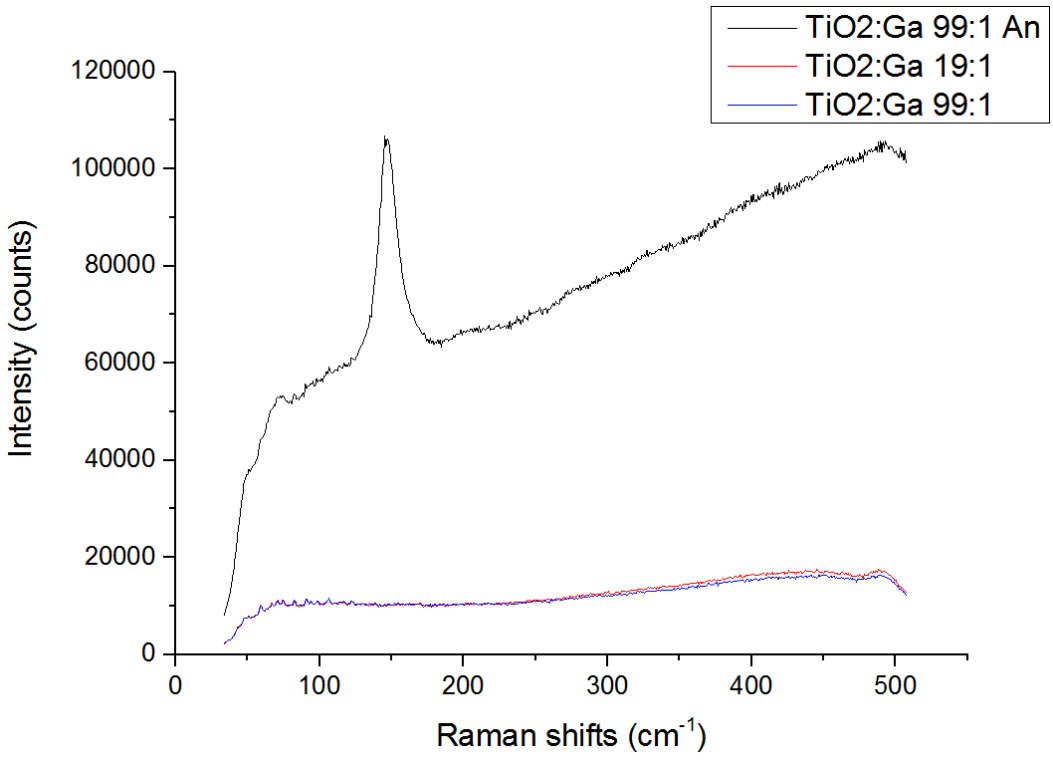

Figure 6.3: Raman spectra of as-grown and annealed (An) $Ti_{1-x}O_2:Ga_x$ (99:1) and as-grown $Ti_{1-x}O_2:Ga_x$ (19:1)

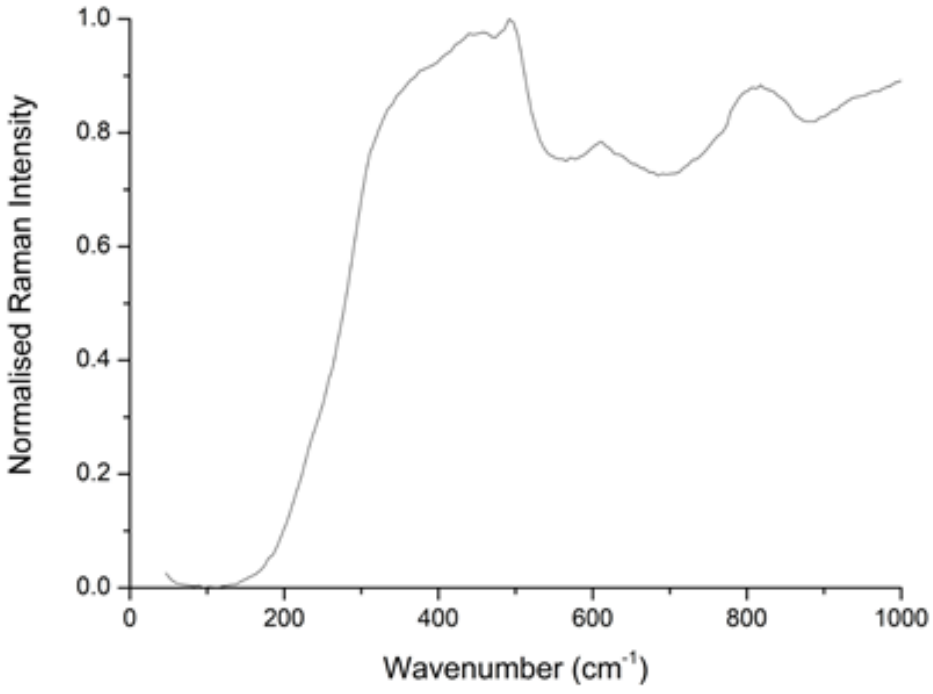

Figure 6.3: Raman spectra of an annealed $Ti_{1-x}O_2:Ga_x$ (19:1) film.

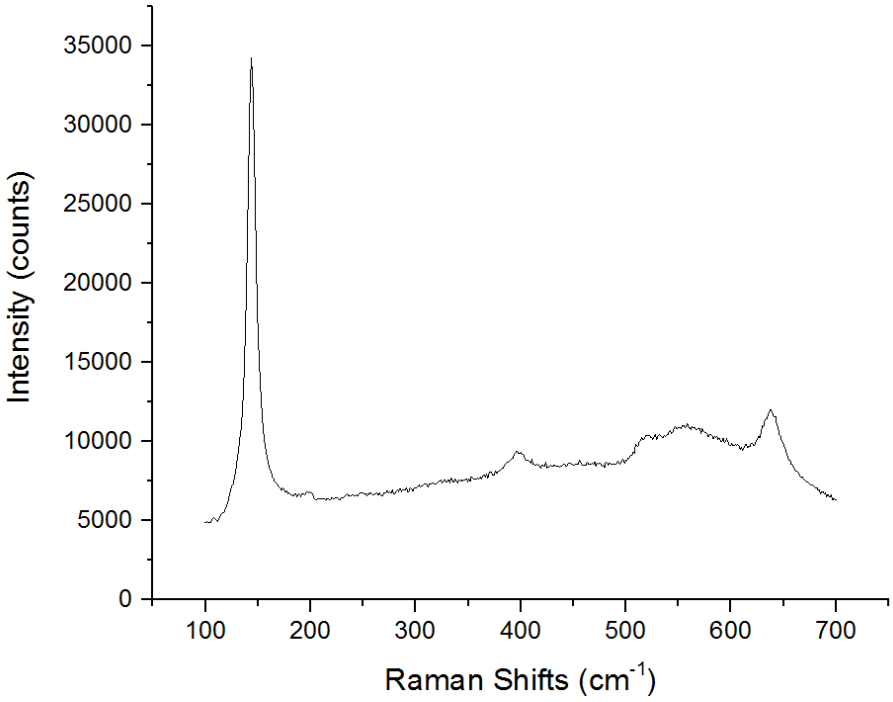

Figure 6.5 Raman spectra of an annealed nominally undoped TiO_2 film.

Furthermore, surface SEM was performed on $Ti_{1-x}O_2:Ga_x$ resulting in as-grown $Ti_{1-x}O_2:Ga_x$ indicating smooth, featureless surfaces (figure 6.6 a) and b)).

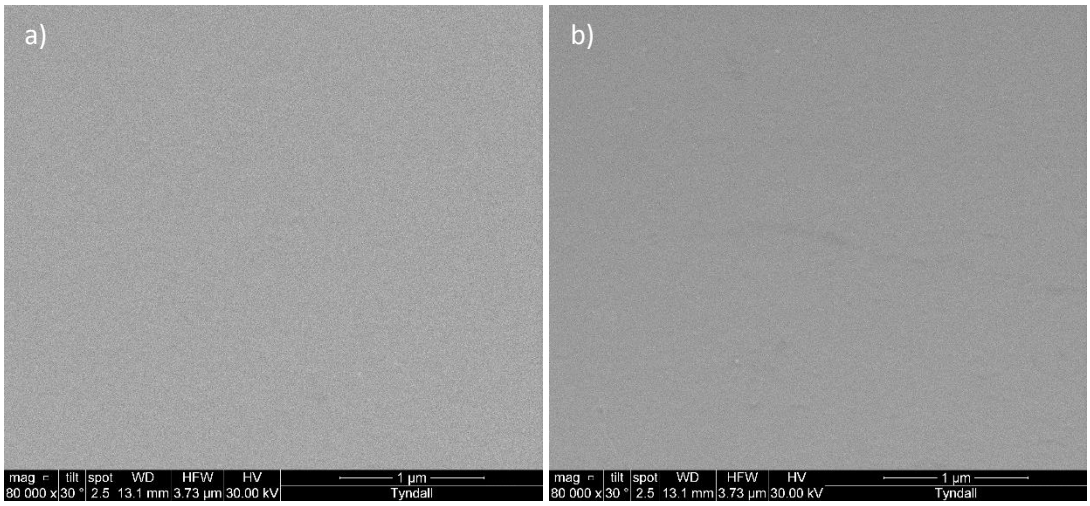

Figure 6.6 a) and b): Surface SEM of as-grown $Ti_{1-x}O_2:Ga_x$ (99:1 and 19:1).

In contrast, annealed $Ti_{1-x}O_2:Ga_x$ (99:1 and 19:1) (figures 6.7a) and b)) both indicate greater granulation density within a smoother film morphology, again suggestive of some crystallinity presence within amorphous morphology. Additionally, no obvious morphological disparity is detected between $Ti_{1-x}O_2:Ga_x$ with variable

gallium concentrations, suggesting crystallinity is independent of gallium concentration.

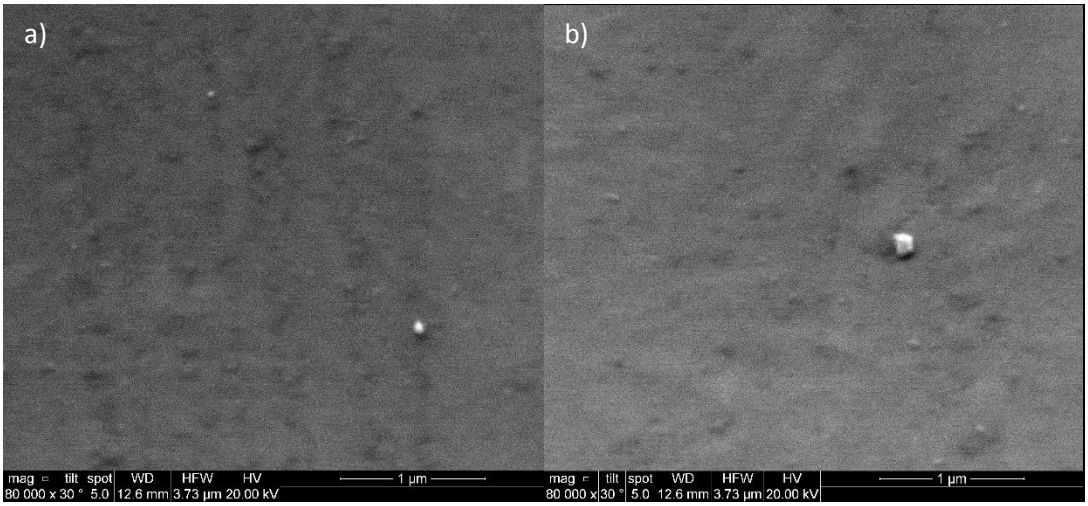

Figure 6.7 a) and b): Surface SEM of annealed $Ti_{1-x}O_2:Ga_x$ (99:1 and 19:1).

For comparison, figures 6.8a) and b) show SEM images of the as-grown and annealed nominally undoped thermally grown TiO_2 samples. In correlation with the $Ti_{1-x}O_2:Ga_x$ films, the as-grown surface possesses a smooth surface morphology as in figure 6.8 a). Annealed surfaces as in figure 6.8 b) indicate a much rougher, mixed surface morphology, suggestive of crystallinity together with amorphous morphology.

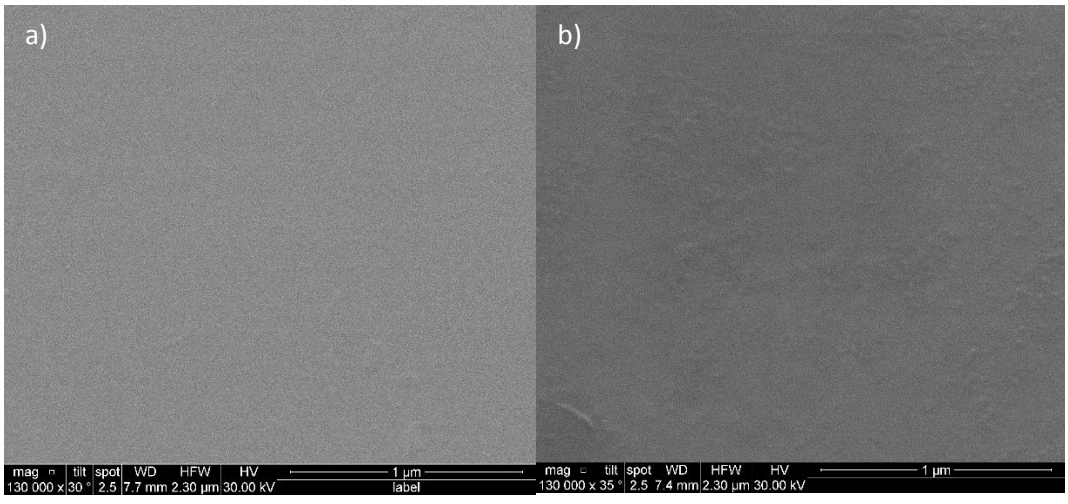

Figure 6.8: Surface SEM of a) as-grown and b) annealed nominally undoped TiO_2.

In summary, $Ti_{1-x}O_2:Ga_x$ grown through a thermal ALD process with subsequent annealing suggests minimal morphological disparity on incorporation of differing

gallium concentrations. Only $Ti_{1-x}O_2:Ga_x$ (99:1) indicates any anatase reflection from either Raman or XRD spectroscopy corresponding to a single 144 cm^{-1} peak. Additionally, annealing produces mixed surface morphologies for both $Ti_{1-x}O_2:Ga_x$ and nominally undoped TiO_2, suggesting minimal anatase crystallite production. Lower anatase creation is observed within the Raman spectra for $Ti_{1-x}O_2:Ga_x$ films on comparison with nominally undoped TiO_2.

XPS was performed on the annealed $Ti_{1-x}O_2:Ga_x$ (99:1) and (19:1) films (tables 6.1 and 6.2), as well as the annealed nominally undoped TiO_2 film (table 6.3), to determine composition and specific gallium concentrations.

	$Ti_{1-x}O_2:Ga_x$ (99:1)	$Ti_{1-x}O_2:Ga_x$ (99:1)	$Ti_{1-x}O_2:Ga_x$ (19:1)	$Ti_{1-x}O_2:Ga_x$ (19:1)
Peak	Position (eV)	Concentration (%)	Position (eV)	Concentration (%)
O 1s_1 (metal oxide)	530.3	45.6	530.4	50.0
O 1s_2 (organics, hydroxide)	531.5	6.1	531.5	18.6
O 1s_3 (organics, SiO_x)	533.5	19.1	533.0	2.5
Ti 2p_1 (Ti^{3+} $2p_{3/2}$)	457.2	1.9	457.2	1.8
Ti 2p (Ti^{3+} $2p_{1/2}$)	461.8	0.9	461.6	0.9
Ti 2p_1 (Ti^{4+} $2p_{3/2}$)	458.9	12.8	458.9	12.3
Ti 2p (Ti^{4+} $2p_{1/2}$)	464.6	6.4	464.5	6.2
C 1s_1 (C=C/C-C)	284.8	3.6	284.8	3.1
C 1s_2 (C-O)	286.5	1.5	286.6	0.8
C 1s_3 (O-C=O)	288.8	0.8	288.8	0.2
C 1s_4 (CO_3)	290.2	1.1	290.1	1.1

Table 6.1: High resolution XPS results for both $Ti_{1-x}O_2:Ga_x$ (99:1) and $Ti_{1-x}O_2:Ga_x$ (19:1) films.

	$Ti_{1-x}O_2:Ga_x$ (99:1)	$Ti_{1-x}O_2:Ga_x$ (99:1)	$Ti_{1-x}O_2:Ga_x$ (19:1)	$Ti_{1-x}O_2:Ga_x$ (19:1)
Peak	Position (eV)	Concentration (%)	Position (eV)	Concentration (%)
O 1s	530.1	63.0	530.4	60.2
Ti 2p	458.1	19.2	458.4	16.9
Ga 2p	1118.1	0.2	1117.4	1.4
C 1s	285.1	5.2	284.4	4.6
N 1s	397.1	1.0	396.4	5.5
Al 2p	-	-	74.4	11.4
Si 2p	104.1	11.5	-	-

Table 6.2: Low resolution XPS results for both $Ti_{1-x}O_2:Ga_x$ (99:1) and $Ti_{1-x}O_2:Ga_x$ (19:1) films.

Peak	Position (eV)	Concentration (%)
O 1s_1	530.6	58.8
O 1s_2	531.7	8.7
Ti^{3+} 2p_1	457.7	3.7
Ti^{3+} 2p	462.6	1.9
Ti^{4+} 2p_1	459.3	16.4
Ti^{4+} 2p	464.9	8.2
C 1s_1	284.7	1.6
C 1s_2	286.6	0.4
C 1s_3	289.4	0.3

Table 6.3: High resolution XPS results for the nominally undoped TiO_2 film.

From Table 6.1, the $Ti_{0.92}Ga_{0.08}O_2$ (19:1) and $Ti_{0.99}Ga_{0.01}O_2$ (99:1) films both showed a 2.9/2.8 % Ti^{3+} $2p_{3/2\ and\ 1/2}$ concentration (457.2/461.6 eV) equating to 13.1/12.7 % of detected titanium. Correspondingly, 19.2 % (86.9/87.2 % total) is retained as

$Ti^{4+}2p_{(3/2 \text{ and } 1/2)}$ (458.9/464.5 eV) [150, 573], indicating a lower Ti^{3+} concentration on comparison with nominally undoped TiO_2 (5.6 % of overall detected elements or 18.5 % of all detected titanium).

A 1:2 Ti:O ratio is clearly indicated through comparing the signals from titanium and lattice incorporated oxygen (O 1s_1: 530.4/530.3 eV) (50.1/45.6 %), suggesting the ALD process provides sufficient TiO_2 oxidation. In contrast, a bulk oxygen deficiency is indicated within lattice incorporated oxygen (O 1s_1 530.6 eV) concentrations (58.8 %) in a 1:2 ratio (Ti:O) for the nominally undoped TiO_2 film. This suggests a greater Ti^{3+} creation results from $V_O^{\cdot\cdot}$ defect generation on oxygen diffusion [574].

Some shifts in the titanium 2p peaks (0.3-1 eV) and an oxygen 1s_1 peak (530.3 eV) (0.3 eV) are observed for both $Ti_{1-x}O_2$:Ga_x films. This suggests a degree of electron enrichment of atomic titanium environments further increasing the stability of Ti^{4+}-O^{2-}-Ti^{4+} bonding in comparison to nominally undoped TiO_2 (figures 6.9 and 6.10), which contain greater Ti^{3+}.

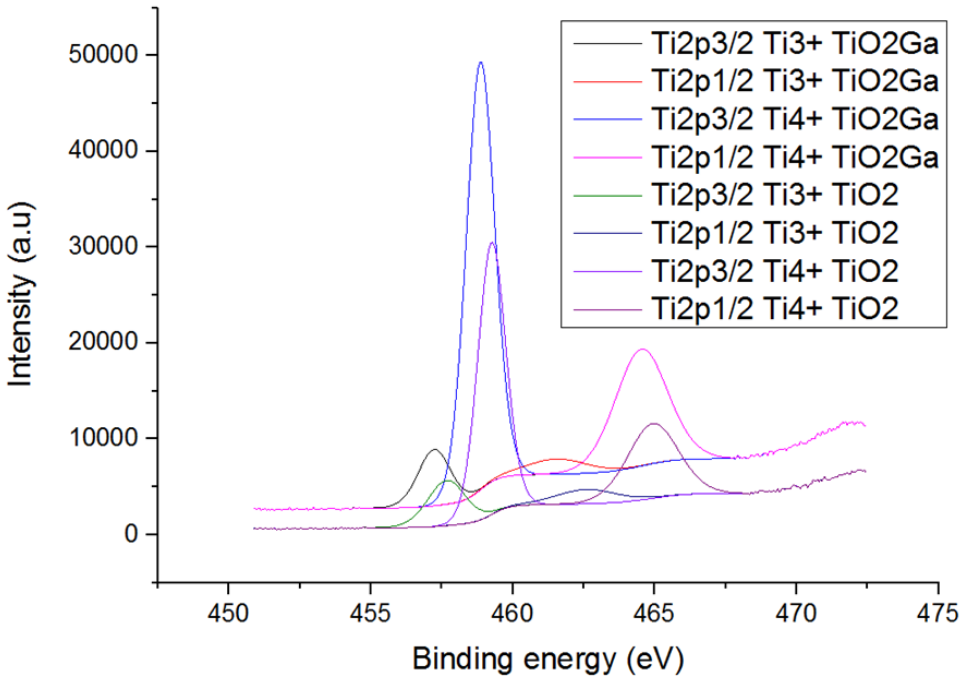

Figure 6.9: Titanium 2p peak shifts for $Ti_{1-x}O_2$:Ga_x (19:1) ($Ti_{1-x}O_2$:Ga_x (99:1) within error of (19:1)) and nominally undoped TiO_2.

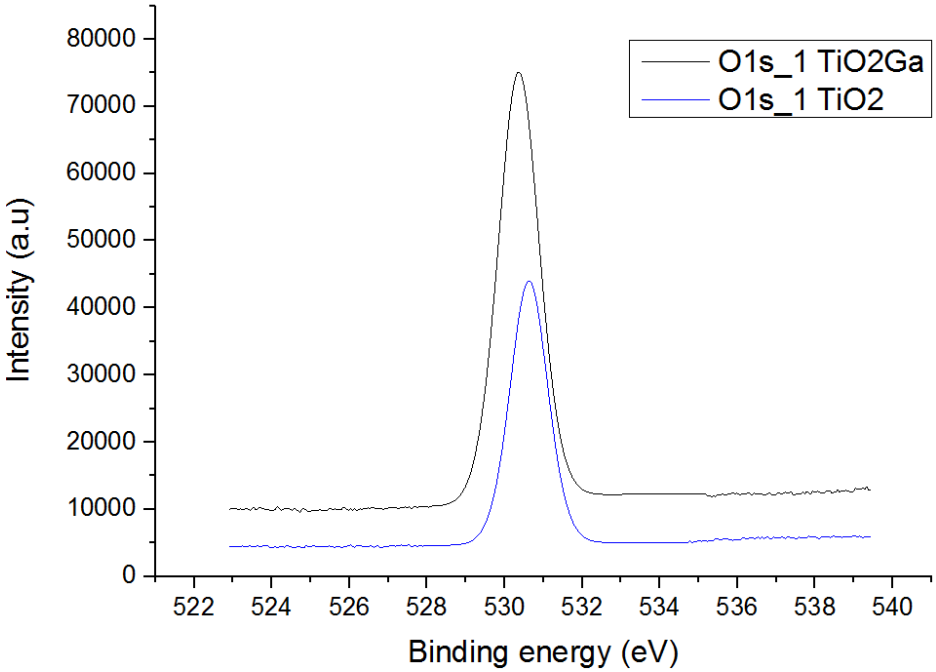

Figure 6.10: Oxygen 1s_1 peak shift between the $Ti_{1-x}O_2:Ga_x$ (19:1) film and nominally undoped TiO_2.

Disparities are also indicated between O 1s_1 environments for $Ti_{1-x}O_2:Ga_x$ (99:1) and $Ti_{1-x}O_2:Ga_x$ (19:1) films, corresponding to 0.5 eV O 1s_3 (533.5 eV) peak shifts respectively (figure 6.11).

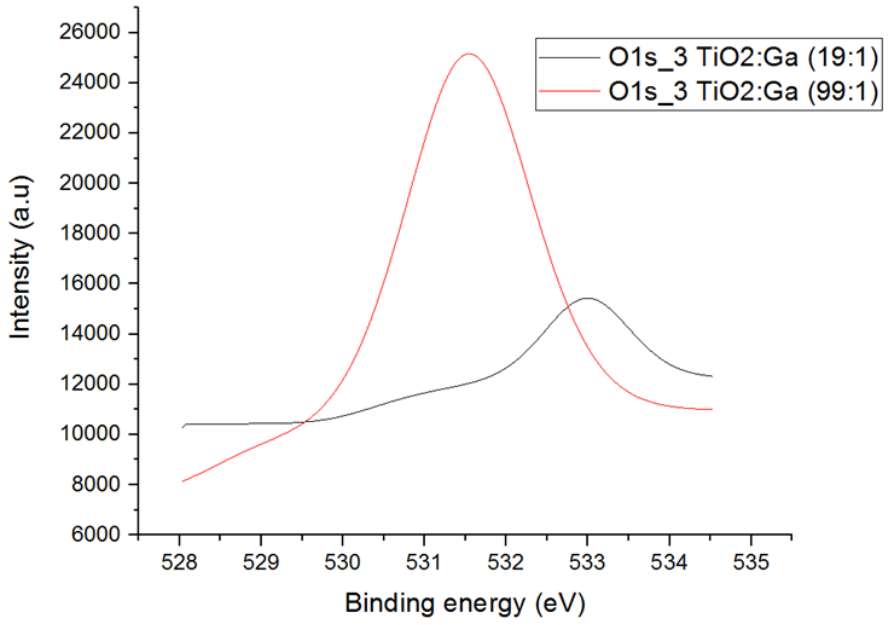

Figure 6.11: Oxygen 1s_3 peak shift between $Ti_{1-x}O_2:Ga_x$ (19:1) and (99:1) films.

Gallium concentrations for the $Ti_{1-x}O_2:Ga_x$ (19:1) film were not the 5 % expected from the precursor ratios utilized (table 6.2). The $Ti_{1-x}O_2:Ga_x$ (19:1) film contained 1.4 % gallium Ga^{3+} 2p (1117.4 eV) equating to 7.7 % when compared to the overall titanium percentage (22.3 %). However, the $Ti_{1-x}O_2:Ga_x$ (99:1) film contains 0.2 % gallium equating to an expected 1 % on comparison to the overall titanium percentage (19.2 %). Additionally, table 6.4 shows $Ti_{0.92}Ga_{0.08}O_2$ gallium concentrations remain at 1.4 % until 100 seconds sputtering with a gradual decrease to 0.8 % at 1500 seconds sputtering. Overall this equates to a 4.9 % bulk Ga^{3+} average concentration on comparison to equivalent titanium concentrations. Therefore, comparably greater surface Ga^{3+} concentrations could suggest accumulation resulting from diffusion during annealing [605, 606].

Peak	Concentration (%) at 100 seconds sputtering	Concentration (%) at 800 seconds sputtering	Concentration (%) at 1500 seconds sputtering
O 1s	62.5	62.5	63.0
Ti 2p	22.3	26.6	27.0
Ga 2p	1.3	0.9	0.8
C 1s	5.1	4.2	3.5
N 1s	0.9	-	-
Al 2p	7.8	5.8	3.2
Si 2s	-	-	2.6

Table 6.4: Concentrations of the $Ti_{0.99}Ga_{0.01}O_2$ film at 100, 800 and 1500 seconds sputtering

Furthermore, minimal nitrogen (1 %) and carbon (5.2 %) contamination is indicated in $Ti_{0.99}Ga_{0.01}O_2$ (table 6.1). This contamination primarily correlates to adventitious carbon [575] and TDMAT/TEGa precursor residue with both C-C (285.1 eV, 3.6 %) and C-N (397.1 eV) bonding detected. Some 11.5 % silicon, relating to either non-uniform substrate coverage or ion diffusion is also detected. In contrast, table 6.3

highlights lower (2.3 %) adventitious carbon contamination for undoped TiO_2, potentially suggesting a purer film with decreased precursor residues.

Table 6.2 also suggests electron enrichment of surface carbonate groups for both $Ti_{1-x}O_2$:Ga_x with decreasing peak (288.8 eV) binding energy (0.6 eV) indicated, as compared to nominally undoped TiO_2 (figure 6.12). Correspondingly, $Ti_{0.99}Ga_{0.01}O_2$ and $Ti_{0.92}Ga_{0.08}O_2$ also possess a 290.1 eV peak equatable to metal-carbonate (CO_3^-) bonding [440]. Additionally, a slight increase in atmospheric carbonate concentration (2.3 % compared to 1.1 %) is detected for $Ti_{0.99}Ga_{0.01}O_2$.

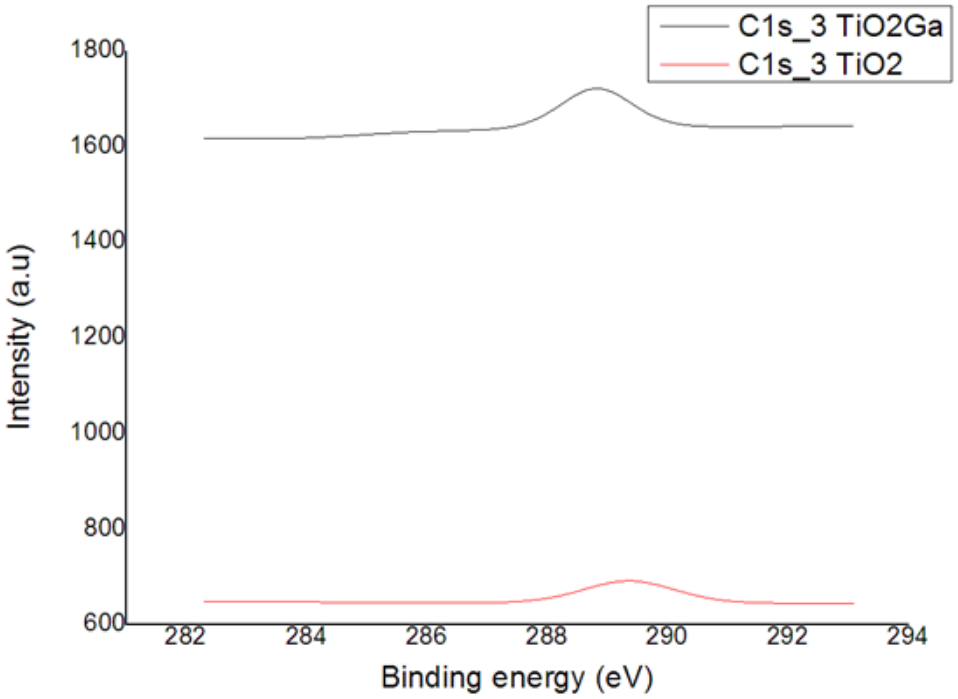

Figure 6.12: Nominally undoped TiO_2 and $Ti_{0.92}Ga_{0.08}O_2$ ($Ti_{0.99}Ga_{0.01}O_2$ within error) carbonate group peak shift.

Furthermore, the $Ti_{0.92}Ga_{0.08}O_2$ also displays evidence of significant contamination:

- Decreasing aluminium concentration on sputtering (11.4 to 3.2%) (table 6.4), initially present as Al-O bonding (74.4-74.6 eV) in Al_2O_3 [579]. Aluminium environments subsequently undergo a peak shift (73.4-73.7 eV) with increasing film depth (beyond 60 seconds sputtering) (table 6.4). However, in a separate study (figure 6.13) the aluminium contamination appears to be surface related (~7.5x10 atm%). This suggests either Al_2O_3 or

AlN particulate contamination from the ALD or oven chamber walls during synthesis or annealing, respectively.

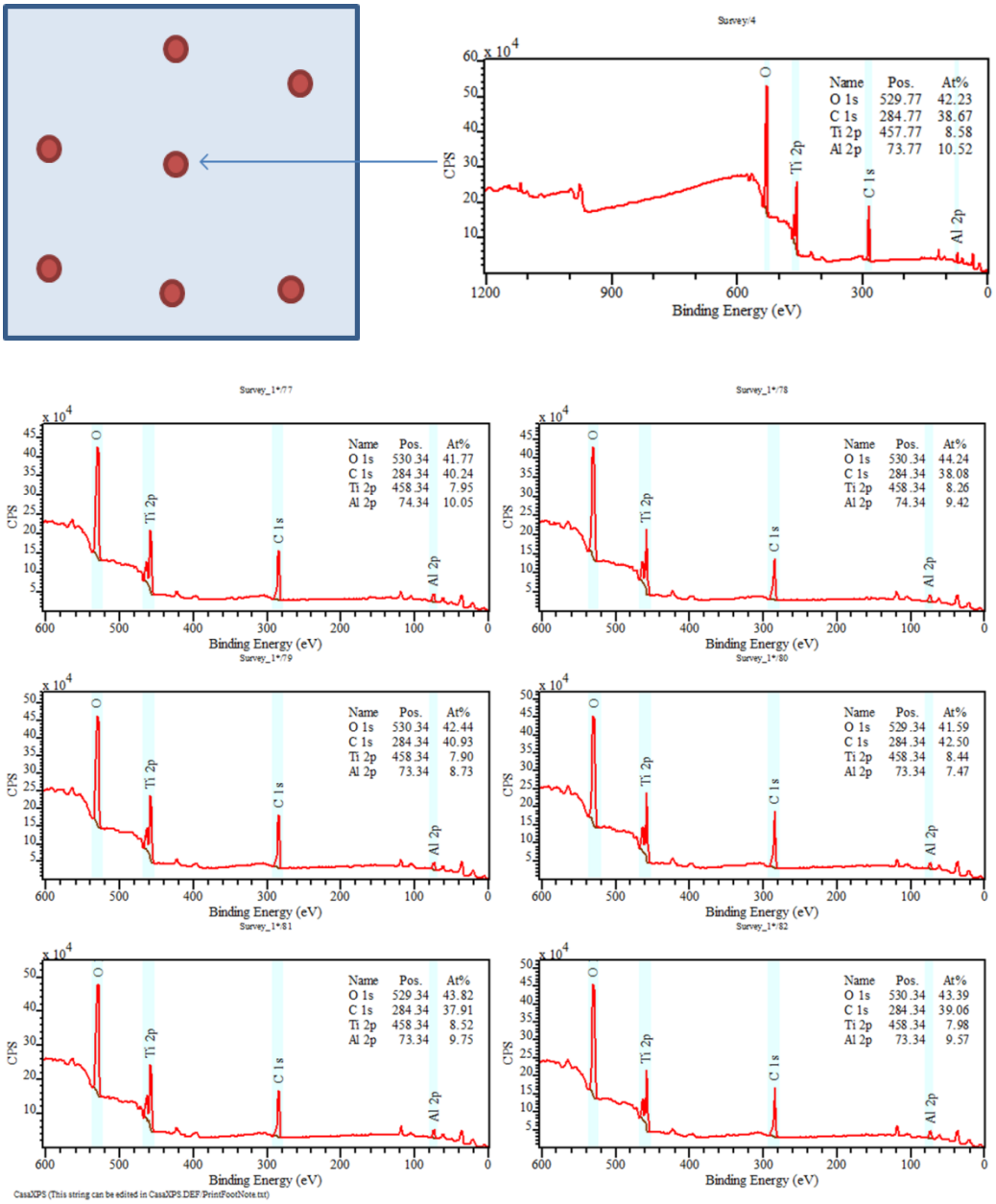

Figure 6.13: Analysis distribution across $Ti_{0.92}Ga_{0.08}O_2$ surface and correlating aluminium signals from generated spectra

Al_2O_3 particulate contamination was subsequently detected through surface SEM measurements (figure 6.14).

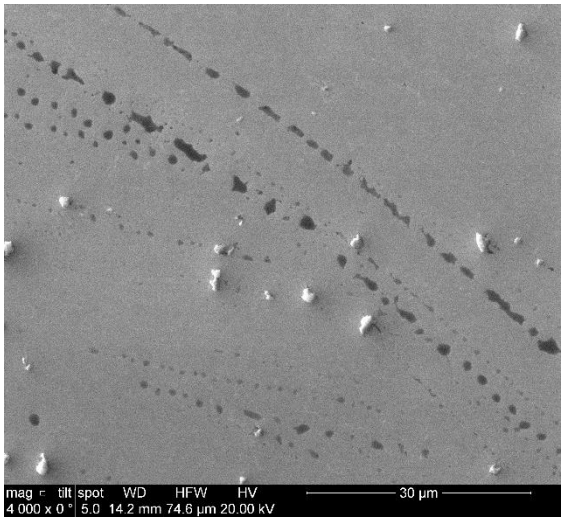

Figure 6.14: Particulates on the $Ti_{0.92}Ga_{0.08}O_2$ film.

- Adventitious carbon levels are initially stable (4.6-4 % for up to 15 seconds sputtering) and most probably arise from either atmospheric contamination or precursor reaction residues. Specifically, Table 6.4 indicates gradual concentration decrease on further sputtering (1.9-0.9 % up to 600 seconds). Peaks corresponding to both metal-carbonate (290.1 eV) [440] and metal-carbide (282.5 eV) bonding [440] were also evident from 100 seconds sputtering onwards. This suggests that carbon incorporation is most likely as interstitial and substitutional doping. Furthermore, negligible carbon contamination was detected subsequent to 600 seconds of sputtering.
- Surface nitrogen contamination was detected, suggestive of metal-nitrogen bonding (368.4 eV). These are generated through either precursor residues, which are unlikely to be Ti-N related with respect to titanium peak positions [607], or possibly Al-N (396.4 eV) [608], arising from surface particulate contamination.

Since $Ti_{0.92}Ga_{0.08}O_2$ contained significant amounts of aluminium, nitrogen and carbon, further research is ideally required in order to accurately gauge the photocatalytic activity.

In summary, both $Ti_{1-x}O_2$:Ga_x films exhibit lower levels of Ti^{3+} 13.1/12.7 % as compared to similarly grown nominally undoped TiO_2 (18.5 %). Additionally, the gallium concentrations are greater (1.3/8.6 %) than might be expected just from

the ALD ratio employed (1/5 %), probably correlating with an increased GaO_x growth rate [609]. However, the films also incorporates both nitrogen and carbon contamination as well as being influenced by aluminium containing particulates.

6.3.1 Optical and Photocatalytic activity

Photocatalytic basic blue 66 ink degradation was subsequently attempted under UV light irradiation. Initial results (figure 6.15) prepared using the 3 mm K hand coater™ show no evidence of degradation after two hours UV light irradiation for the unannealed $Ti_{1-x}O_2:Ga_x$ (99:1 and 19:1) samples. Furthermore no evidence of degradation was observed for the annealed $Ti_{0.92}Ga_{0.08}O_2$.

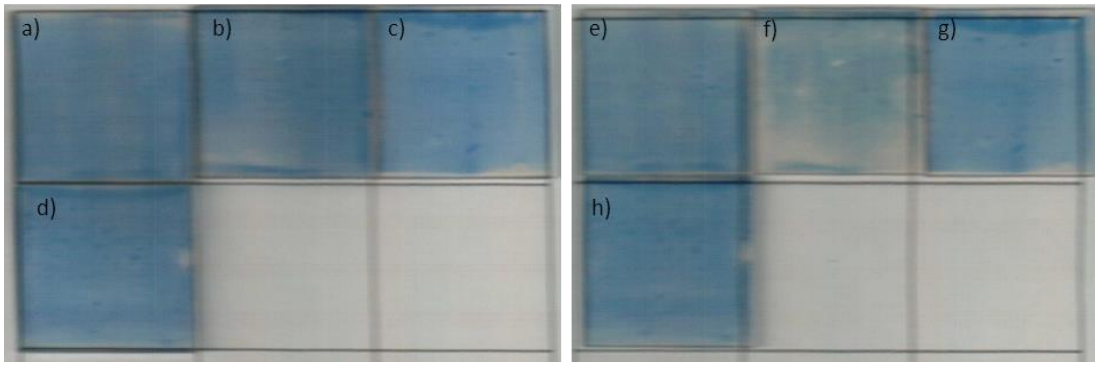

Figure 6.15): Initial basic blue 66 ink degradation before and after two hours UV irradiation on $Ti_{1-x}O_2:Ga_x$ films; a) and e) unannealed 99:1, b) and f) annealed 99:1, c) and g) unannealed 19:1, and d) and h) annealed 19:1.

Contrastingly, the annealed $Ti_{0.99}Ga_{0.01}O_2$ film exhibits some evidence of basic blue 66 ink degradation over two hours, suggesting sufficient charge carrier motion and reactive surface oxide species generation. Furthermore, photocatalytically active properties are proposed to arise through the presence of some anatase crystallites presumably containing lower levels of gallium and not being affected by surface particulate contamination. The observation was verified by performing basic blue 66 ink degradation on $Ti_{0.99}Ga_{0.01}O_2$ for six hours of UV irradiation, resulting in complete bleaching (ttb) after 4 hours and 22 minutes (figure 6.16).

Figure 6.16: Annealed $Ti_{0.99}Ga_{0.01}O_2$ film before and after six hours irradiation.

The annealed $Ti_{0.99}Ga_{0.01}O_2$ film exhibits a significantly increased ttb in contrast to annealed nominally undoped TiO_2 (11 minutes 4 seconds ±35 seconds) undergoing identical thermal ALD film syntheses. Thus further suggesting gallium addition to TiO_2 results in a reduction in photocatalytic activity.

To further examine the photocatalytic activity through surface reactive oxide species generation, average water contact angles were measured on the $Ti_{1-x}O_2:Ga_x$ (99:1 and 19:1 films, both unannealed and annealed) films (figure 6.17).

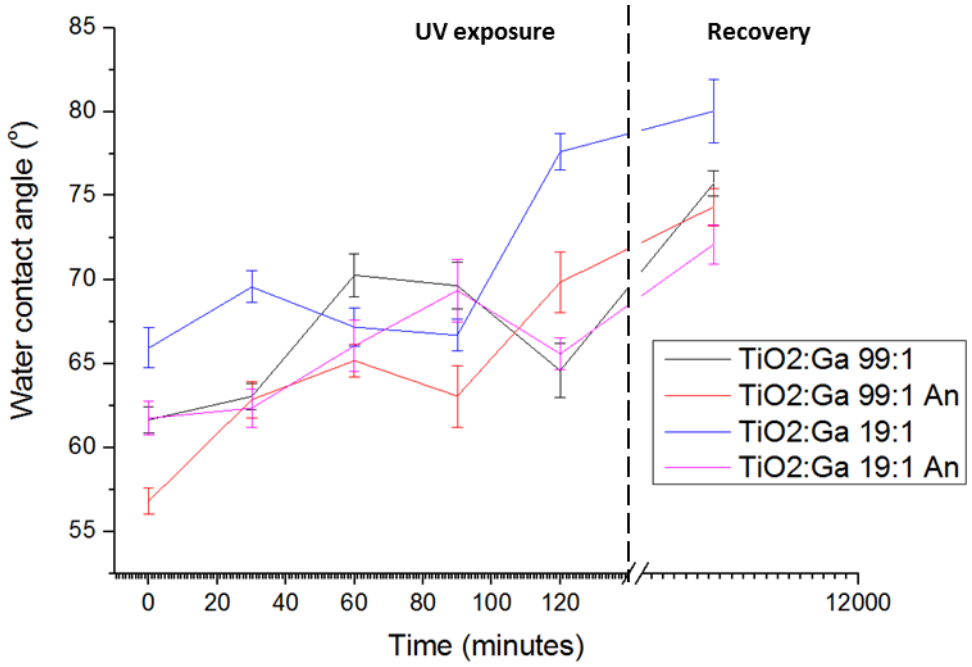

Figure 6.17: $Ti_{1-x}O_2:Ga_x$ (99:1 and 19:1, unannealed and annealed (An)) average water contact angles prior to, during and subsequent to UV irradiation.

From figure 6.16, remarkably $Ti_{1-x}O_2:Ga_x$ films become more hydrophobic upon UV irradiation (57-78 °) with increasing contact angle detected over 0 to 120 minutes of UV illumination. No obvious correlation is visible between UV light irradiation time and either gallium concentration or annealed/unannealed $Ti_{1-x}O_2:Ga_x$.

Additionally, all $Ti_{1-x}O_2:Ga_x$ films became more hydrophobic on darkness immersion.

Further experimentation showed UV light irradiation (up to five hours) on the annealed $Ti_{0.99}Ga_{0.01}O_2$ film had little or no effect on water contact angle, with the reasons for this behaviour not clear. However, it is possible to speculate that a lack of anatase crystallinity, combined with aluminium particulate contamination could result in high levels of recombination and prevent ROS formation. Furthermore, deliberately introduced GaO_x, or even AlO_x particulates, could provide electron trapping centres [610], increasing recombination.

UV/visible spectra were recorded from the unannealed and annealed nominally undoped TiO_2 and $Ti_{1-x}O_2:Ga_x$ films (figure 6.18). The samples exhibit 87-93 % transmission at 700 nm, gradually degrading on decreasing visible light wavelength to 61-73 % transmission at 390 nm. Subsequently, a rapid decrease in transmission is observed preceding 300 nm as a result of TiO_2 bandgap absorption [585] across all films.

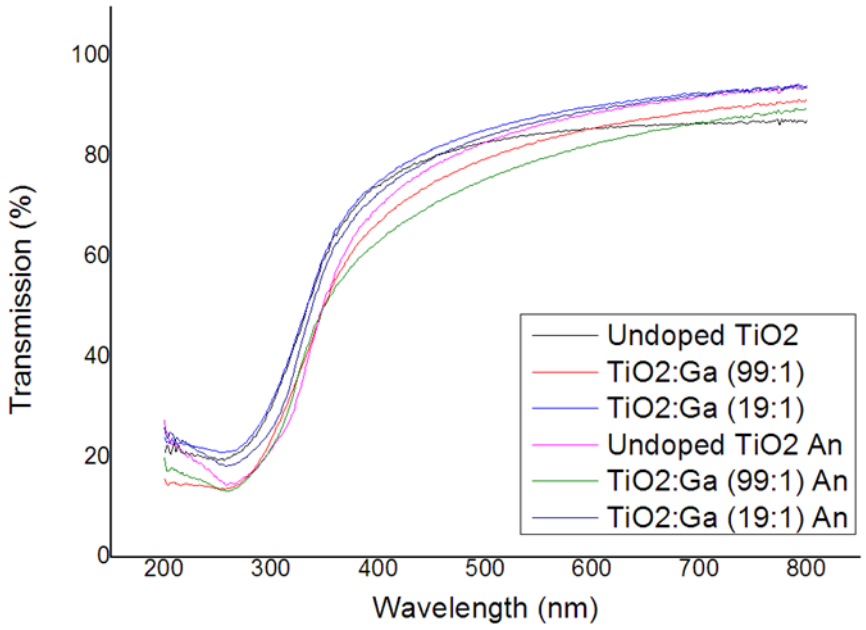

Figure 6.18: UV/Visible light transmission for nominally undoped TiO_2 and $Ti_{1-x}O_2:Ga_x$ films (unannealed and annealed (An)).

Both the $Ti_{0.99}Ga_{0.01}O_2$ films exhibit reduced visible wavelength transmission as compared to the $Ti_{0.92}Ga_{0.08}O_2$ film. This possibly relates to lower GaO_x nanolaminate levels and a reduction in Burstein-Moss effects which would arise if the TiO_2 was modified by a higher band gap material such as Ga_2O_3. Furthermore, a reduction in visible light transmission is detected upon annealing of the $Ti_{1-x}O_2$:Ga_x film (figure 6.18) possibly due to the formation of anatase (3.2 eV) from amorphous (3.37 eV), reducing the overall band gap.

The annealed $Ti_{0.99}Ga_{0.01}O_2$ film possesses lowest visible light transmission levels resulting from lower GaO_x nanolaminate concentration and the presence of some anatase. Correspondingly, both $Ti_{0.99}Ga_{0.01}O_2$ films possess lower visible light transmission in contrast to the nominally undoped TiO_2 film, possibly relating to the lower Ti^{3+} concentrations detected, suggesting the presence of mid-band gap states [44].

From the spectra shown in figure 6.18 band gaps were calculated (table 6.5) through Tauc plot creation (figure 6.19). Table 6.5 indicates minimal $Ti_{1-x}O_2$:Ga_x band gap variation as compared to nominally undoped annealed TiO_2 (2.82 eV). However, this value is low compared to reported band gaps for similar TiO_2 morphologies in literature [1, 2], but potentially this relates to significant mid-band gap Ti^{3+} state creation [44, 150].

	Band gap (eV)
TiO_2 (annealed)	2.82
$Ti_{0.99}Ga_{0.01}O_2$	2.85
$Ti_{0.99}Ga_{0.01}O_2$ (annealed)	2.80
$Ti_{0.92}Ga_{0.08}O_2$	2.76
$Ti_{0.92}Ga_{0.08}O_2$ (annealed)	2.90

Table 6.5: Calculated band gaps (direct) for nominally undoped TiO_2 and $Ti_{1-x}O_2$:Ga_x films.

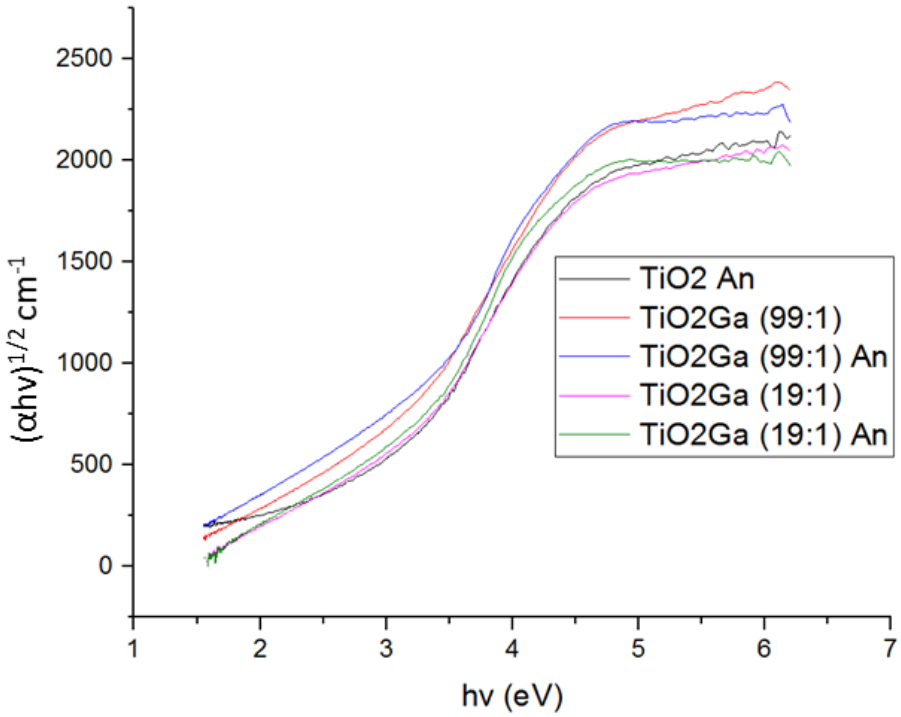

Figure 6.19: Equivalent Tauc plots of annealed (An) nominally undoped TiO_2 and as-grown and annealed (An) $Ti_{1-x}O_2$:Ga_x (19:1) and (99:1) films.

Thus it may be concluded that GaO_x nanolaminate addition provides only a minimal band gap variation (2.76-2.90 eV), as compared to nominally undoped TiO_2, which is possibly related to either;

- Varying levels of anatase between differing $Ti_{1-x}O_2$:Ga_x samples,
- Or varying amounts of Ti^{3+} defects resulting from Ga^{3+} inclusion.

To summarize, $Ti_{1-x}O_2$:Ga_x (99:1 and 19:1) films indicate lower photocatalytic activity with respect to basic blue 66 ink degradation. Additionally, greater water droplet hydrophobicity under UV light irradiation is detected for $Ti_{1-x}O_2$:Ga_x films (99:1 and 19:1), as compared to the nominally undoped TiO_2 film. Moreover, minimal band gap difference is generated on disparate gallium concentrations.

6.3.2 Electrical conduction

All $Ti_{1-x}O_2$:Ga_x samples grown by thermal ALD were highly resistive, irrespective of annealing status and dopant concentration.

6.4 Results from Ga-capped nanolaminate $Ti_{1-x}O_2:Ga_x$ film analysis

GIXRD was performed on Ga-capped $Ti_{1-x}O_2:Ga_x$ films. Figure 6.20 a) and b) shows representative data for the Ga-capped $Ti_{1-x}O_2:Ga_x$ (74:1) films on silicon and glass substrates, with additional data provided within appendix A. Additionally, figure 6.20a) and b) highlights a weak broad peak at 25.3 ^{o} 2θ, corresponding to the (101) anatase reflection [424]. This peak is found in the Ga-capped $Ti_{1-x}O_2:Ga_x$ (99:1) and (74:1) films on silicon and glass substrates, as well as for the Ga-capped $Ti_{1-x}O_2:Ga_x$ (49:1) and (39:1) films on the silicon substrate. In contrast, no weak peak at 25.3 ^{o} 2θ is observed for Ga-capped $Ti_{1-x}O_2:Ga_x$ films incorporating higher gallium concentrations, suggesting amorphous film natures.

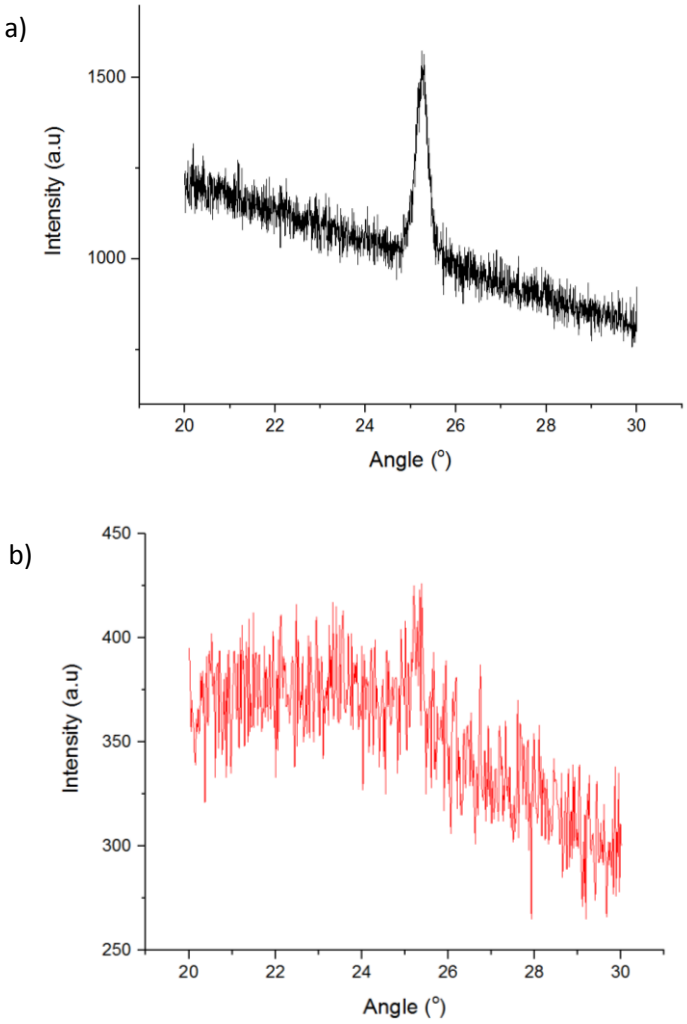

Figures: 6.20 a) and b), demonstrating typical (101) anatase reflection observed from Ga-capped $Ti_{1-x}O_2:Ga_x$ (74:1) on silicon and glass, respectively (remainder in appendix A).

Assumedly, other anatase reflections possess inadequate intensity for successful definition compared to background radiation, suggesting poor crystalline natures from weak titanium dioxide anatase (101) reflection intensity [611]. Rutile crystalline phase reflections [612], or deviation in (101) anatase reflection position (25.3^{o} 2θ) remained undetected on varied gallium dopant concentration. These results therefore suggest complete Ga_2O_3 nanolaminate inclusion into titanium dioxide matrices [178], and also lattice distortion on incorporation of Ti^{4+} site ($Ga_{Ti'}$) substitution, as detected from low peak intensity [177].

Absence of Ga_2O_3 polymorph (α, β, γ) reflections also confirms complete dopant inclusion [600, 613], suggestive of minimal gallium oxide diffusion to assemble larger Ga_2O_3 barrier layers/regions. However, additional Ga_2O_3 nanolaminate growth in $Ti_{1-x}O_2$:Ga_x films suggests an optimal gallium saturation effect [339, 614] with a major shift in crystallinity from anatase to amorphous after (74:1) on glass and (39:1) on silicon substrates. Significant reduction in overall $Ti_{1-x}O_2$:Ga_x film crystallinity is therefore subsequent to optimal dopant saturation. On reaching optimal dopant saturation, greater frequencies of Ga_2O_3 nanolaminates would prevent anatase generation and "fix" $Ti_{1-x}O_2$:Ga_x films into an amorphous morphology. With amorphous morphology occurring through either: diminished TiO_2 thickness between Ga_2O_3 nanolaminates [614] or alternatively, lattice strain or distortion intensification [177, 339].

However, reduced anatase crystallinity indicated could also result from either; $Ti_{1-x}O_2$:Ga_x film oxygen deficiency or XRD machine insensitivity. Oxygen deficient $Ti_{1-x}O_{<2}$:Ga_x would possess greater $V_{O}^{\cdot\cdot}$ concentrations from charge compensation on substitution of two Ti^{4+} for Ga^{3+} ($Ga_{Ti'}$) [603]. Possibly presenting a $Ti_2O_3/TiO_2/Ga_2O_3$ film environment with greater gallium concentrations, to result in amorphous morphology, however, confirmation is required through either XPS or SIMS analyses. Alternatively, XRD machine insensitivity towards synthesized $Ti_{1-x}O_2$:Ga_x possessing lower thicknesses, can also result in decreased reflection peak intensity, providing peak broadening and unobservance above detected background radiation. However, confirmation or negation of this phenomenon requires thicker film growth or utilization of differing microscopic or spectroscopic analyses.

Raman spectroscopy was performed on TiO_2 and Ga-capped $Ti_{1-x}O_2$:Ga_x films and provided more information (figures 6.21 and 6.22), as compared to the XRD results (figures 6.20a) and b)). Films grown on silicon substrates exhibit Raman vibrational modes equating to anatase crystallinity; 144 cm^{-1}, 199 cm^{-1}, 399 cm^{-1} and 636 cm^{-1} (E_g, E_g, B_{1g} and E_g) [1] for TiO_2 and Ga-capped TiO_2:Ga ((99:1), (74:1) and (39:1)) films. The remaining peaks equate to the substrates [567, 615] with the 517 cm^{-1} anatase peak being obscured by a large silicon substrate peak. An optimal dopant limit is suggested between ratios of (49:1) and (39:1) respectively indicating a transition between amorphous material and anatase crystallinity, with additional gallium concentration equating to amorphous morphology. This optimal dopant limit also correlates to the XRD results.

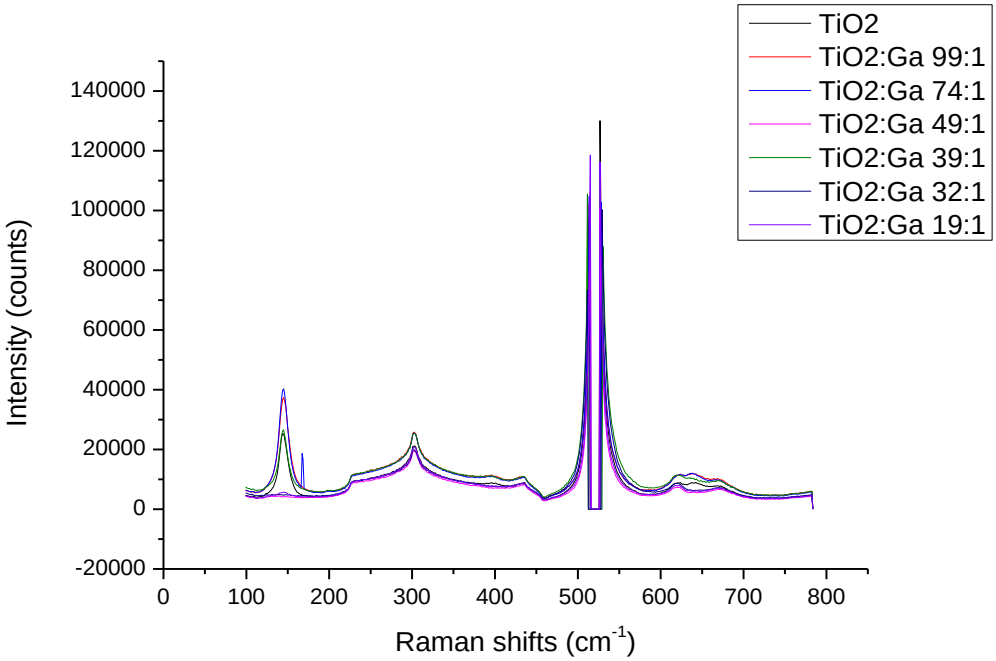

Figure 6.21: Showing TiO_2 and Ga-capped $Ti_{1-x}O_2$:Ga_x (99:1-19:1) vibrational mode peaks on silicon.

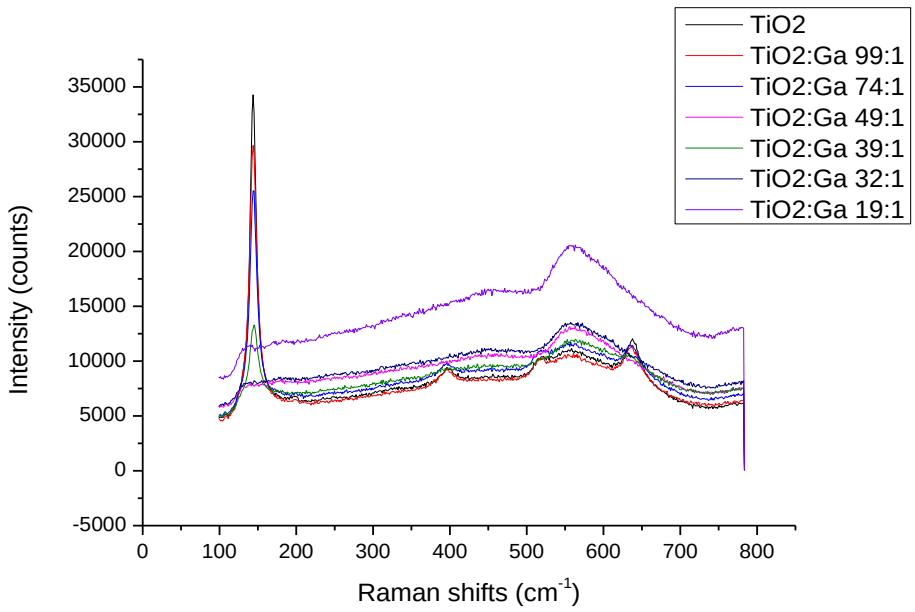

Figure 6.22: showing TiO_2 and Ga-capped $Ti_{1-x}O_2:Ga_x$ (99:1-19:1) vibrational mode peaks on glass substrates.

Spectra obtained for TiO_2 and Ga-capped $Ti_{1-x}O_2:Ga_x$ ((99:1), (74:1) and (39:1)) grown on glass substrates again exhibit anatase crystallinity. The corresponding vibrational modes for anatase are detected at; 144 cm^{-1}, 399 cm^{-1}, 514 cm^{-1} and 636 cm^{-1} (E_g, B_{1g}, $A_{1g}+B_{1g}$ and E_g) with a broad 530 cm^{-1} glass substrate peak [567]. Nominally undoped TiO_2 and (99:1) Ga-capped $Ti_{1-x}O_2:Ga_x$ also possessed a 199 cm^{-1} (E_g) vibrational mode, suggesting greater anatase character [1].

As previously indicated, increasing gallium concentration incorporation generates decreasing anatase character. This is particularly observed for both the 144 cm^{-1} peak intensity decrease from (99:1) to (39:1) Ga-capped $Ti_{1-x}O_2:Ga_x$, and the detection of the 199 cm^{-1} peak in TiO_2 and (99:1) Ga-capped $Ti_{1-x}O_2:Ga_x$. Therefore the optimal gallium incorporation is suggested prior to negatively affecting anatase morphology.

Furthermore, surface SEM was performed on Ga-capped $Ti_{1-x}O_2:Ga_x$ films to see if surface morphology could reinforce the hypothesis of decreasing film crystallinity with increasing gallium concentration. Surface SEM indicates flat, conformal Ga-capped $Ti_{1-x}O_2:Ga_x$ films were grown (figures 6.23a-d). However, for the growth of

Ga-capped $Ti_{1-x}O_2$:Ga_x exceeding 32:1 cycles ((19:1) and (9:1)), greater numbers of uneven features potentially corresponding to pinholes were observed (figure 6.23c)). The detected minor variation in layer texture may result from growth on differing substrates or varied gallium concentration.

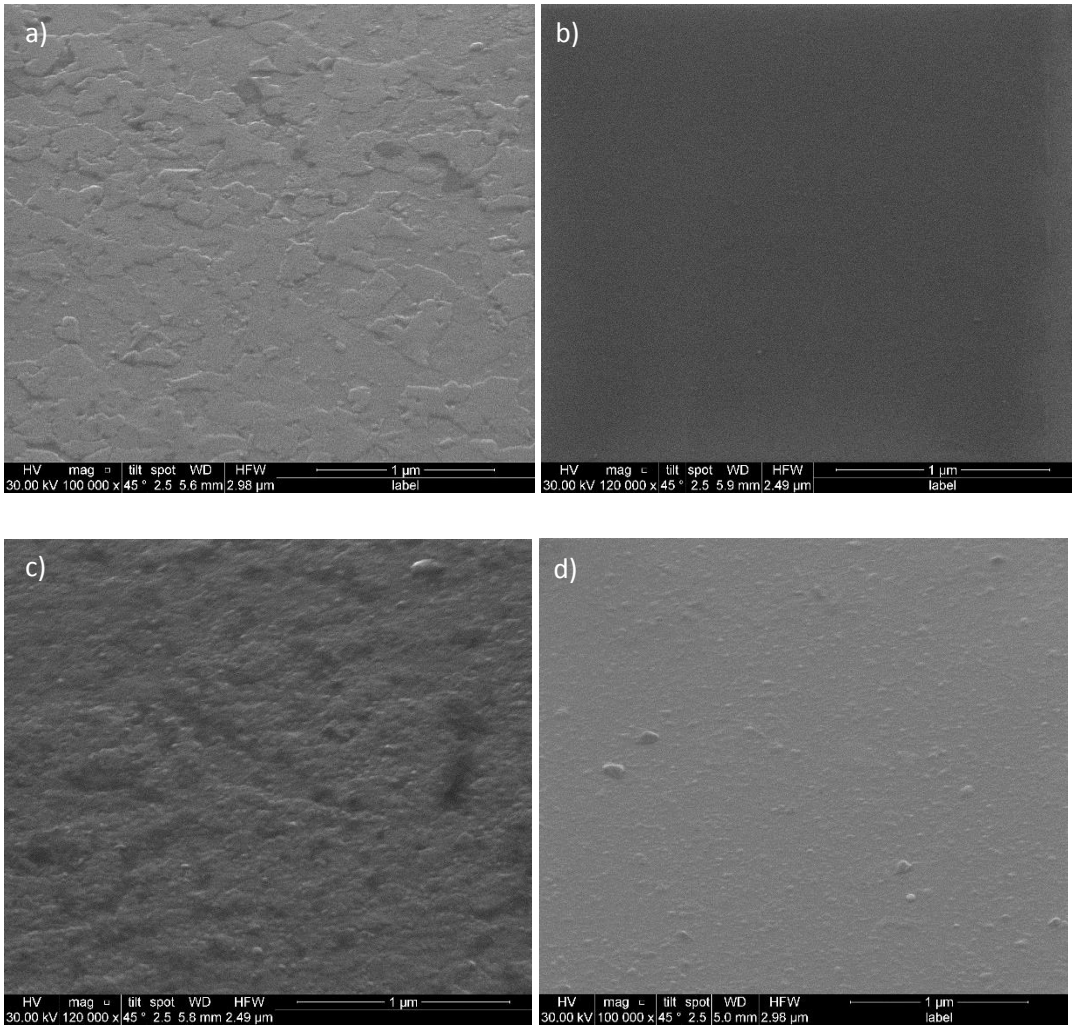

Figures 6.23a), b), c) and d): Surface SEM of (99:1) and (9:1) Ga-capped Ti_{1-x} O_2:Ga_x on silicon, and (99:1) and (9:1) Ga-capped $Ti_{1-x}O_2$:Ga_x on glass (remainder in appendix A), respectively.

The morphology of the Ga-capped $Ti_{1-x}O_2$:Ga_x (99:1) sample indicates a substrate dependence. Ga-capped $Ti_{1-x}O_2$:Ga_x films grown on silicon substrates possess flat lamellar growth and small granular structures (figure 6.23a)), and films grown on glass substrates are significantly granular (figure 6.23c)). Substrate growth selectivity, as seen in dip coated TiO_2 film growth [616] and related to surface

hydroxyl group density, as detected in ALD growth of tungsten [617], is therefore proposed in order to explain disparate Ga-capped $Ti_{1-x}O_2:Ga_x$ film surface structures. However, similar Ga-capped $Ti_{1-x}O_2:Ga_x$ (99:1) thicknesses, silicon: 36.5 nm and glass: 35 nm (as shown by TEM in the next section), also suggest otherwise.

Corresponding with previous analyses, significant Ga-capped $Ti_{1-x}O_2Ga_x$ surface morphology variation is seen to occur upon increasing the gallium concentration. On silicon substrates, flat lamellae structures diminish to generate rougher, granular Ga-capped $Ti_{1-x}O_2:Ga_x$ films (between (39:1) and (32:1)). Additionally, further granular dispersity and smoothening occur for greater gallium concentrations, resulting in the smoothest morphologies for the highest (Ga-capped $Ti_{1-x}O_2:Ga_x$ (9:1)) gallium concentrations (figure 6.23b)). Furthermore, scattered granules across Ga-capped $Ti_{1-x}O_2:Ga_x$ surfaces could result from the final Ga_2O_3 ALD cycle, which forms a "capping" Ga_2O_3 monolayer [618, 619]. On glass substrates, identical surface morphological variations are observed subsequent to Ga-capped $Ti_{1-x}O_2:Ga_x$ (49:1) synthesis, correlating with the detected anatase to amorphous transition as noted earlier. For improved resolution of $Ti_{1-x}O_2:Ga_x$ thicknesses and morphology, TEM was subsequently performed, as described in the following section.

TEM results suggest nominally undoped TiO_2 and all Ga-capped $Ti_{1-x}O_2:Ga_x$ films comprehensively incorporate separate polycrystalline anatase and amorphous morphology regions, independent of the disparate gallium concentrations and the utilized substrate (figure 6.24).

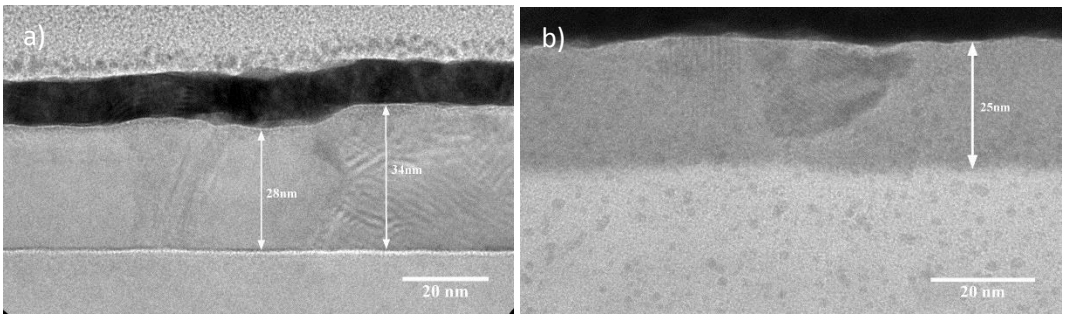

Figure 6.24: demonstrating thickness and crystalline morphology detected on each substrate, a) silicon (49:1) and b) glass (19:1), respectively (rest in appendix A).

Furthermore, TEM suggests that all samples were poor in terms of anatase crystallinity. However, variable Ga-capped $Ti_{1-x}O_2:Ga_x$ crystallinity with clearly observable grain boundaries (figure 6.24) between amorphous and anatase growth areas, suggests TiO_2 growth results from multiple hydroxyl nucleation sites on the substrate surface [617]. The fact that the Ga-capped $Ti_{1-x}O_2:Ga_x$ crystallinity decreases with increasing gallium concentrations suggests gallium incorporation hinders or deforms anatase crystal growth [177, 339].

The observable variation in Ga-capped $Ti_{1-x}O_2:Ga_x$ film thicknesses (table 6.6) shows no correlation with increasing gallium concentration, suggesting only the crystallinity and not the film growth rate is affected.

Dopant ratio cycles (Ti:Ga)	**silicon substrate**		**Glass Substrate**	
	Film thickness (nm)	**Film growth rate (nm/cycle)**	**Film thickness (nm)**	**Film growth rate (nm/cycle)**
Undoped	31	0.056	21	0.038
99:1	36.5	0.061	35	0.058
74:1	36	0.068	20	0.038
49:1	31	0.056	27	0.049
39:1	33.6	0.06	20	0.036
32:1	30	0.054	26	0.046
19:1	30	0.054	25	0.045
9:1	30	0.054	30	0.055
Average	**32.3**	**0.058**	**25.5**	**0.046**

Table 6.6: Average film thicknesses and growth per ALD cycle

Both nominally undoped TiO_2 and average Ga-capped $Ti_{1-x}O_2:Ga_x$ growth on silicon substrates (0.058 nm/cycle), are equal (within error) to the quoted literature growth rates (0.06 nm/cycle) [604]. In contrast, a reduced average growth rate is observed on glass substrates (0.046 nm/cycle), suggesting the postponement of

initial nucleation on glass is possibly generated as a result of reduction in active surface sites [617].

Furthermore, although Ga_2O_3 nanolaminate generation might be in Ga-capped $Ti_{1-x}O_2:Ga_x$ ALD synthesis, Ga^{3+} diffusion [605, 606] could generate increased dopant concentrations at grain boundaries and surface regions. Surface Ga_2O_3 or even Ga^{3+} distribution throughout $Ti_{1-x}O_2:Ga_x$ could result varying crystallinity and therefore also varying photocatalytic activity and electrical conduction properties. In order to attempt to investigate the possibility of nanolaminate GaO_x formation, TEM was utilized to study the $Ti_{1-x}O_2:Ga_x$ (39:1) film, figure 6.25.

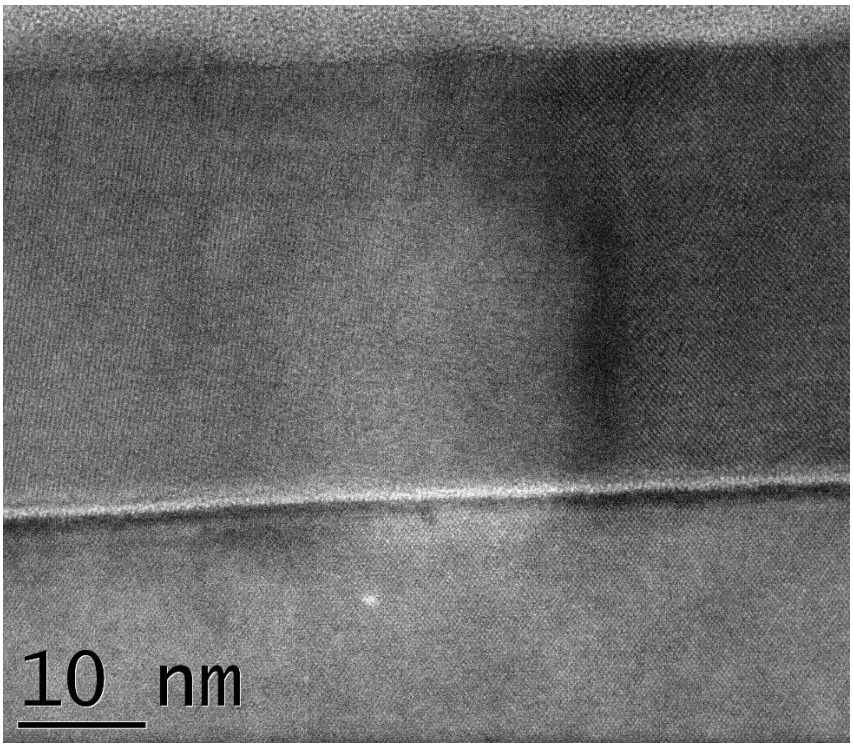

Figure 6.25: Attempting GaO_x nanolaminate detection with the $Ti_{1-x}O_2:Ga_x$ (39:1) film through TEM.

Figure 6.25 indicates no obvious GaO_x nanolaminate detection, suggesting gallium diffusion [605, 606] throughout $Ti_{1-x}O_2:Ga_x$ films. However, it is not reliable to draw conclusions from figure 6.25, due to gallium overexposure during sample cutting (FIB utilizes a gallium ion beam [432]) and/or the use of low magnification. Ideally high resolution TEM (HRTEM) with hydrogen beam cutting would be utilized to prepare samples for future analysis.

To summarize, all nominally TiO_2 and $Ti_{1-x}O_2:Ga_x$ samples prepared show minimal anatase crystallite formation from TEM, dependent on possessed gallium concentrations. Lower gallium concentrations allow for greatest anatase crystallite growth, with highest GaO_x nanolaminate concentrations to register anatase crystallites in Raman and XRD spectroscopy equalling ≤ (49:1)-(39:1) Ti:Ga growth cycle ratios. Alternatively, greater GaO_x nanolaminate concentrations in $Ti_{1-x}O_2:Ga_x$ films result in significant crystalline degradation towards an amorphous morphology with increasing concentrations, as suggested by the absence of discernible features in SEM.

Additionally, assumed GaO_x nanolaminate growth with or without Ga^{3+} diffusion is suggested to sterically hinder anatase generation. However, it was impossible to unambiguously identify the gallium sites by TEM.

Furthermore, $Ti_{1-x}O_2:Ga_x$ indicates anatase growth variability on differing substrates, with silicon and glass surfaces generating flat lamellae and granular growths, respectively. Disparate growths on differing substrates potentially result from variations in nucleation characteristics. However, polycrystalline growth could also result from utilizing synthesis temperatures above the ideal precursor ALD window to attempt simultaneous anatase growth, generating significant CVD-type synthesis. Nevertheless, nominally undoped TiO_2 and $Ti_{1-x}O_2:Ga_x$ composition is analysed through SEM energy dispersive X-ray spectroscopy (EDX) below.

Ga-capped $Ti_{1-x}O_2:Ga_x$ films grown on silicon substrates (figures 6.26 and 6.27) predominately indicate high purity with negligible contamination attributed to adventitious carbon (0.277 keV). However, the (39:1), (32:1) and (19:1) Ga-capped $Ti_{1-x}O_2:Ga_x$ films contain comparably greater carbon concentration. Additionally, the (39:1) Ga-capped $Ti_{1-x}O_2:Ga_x$ film also indicates minimal nitrogen contamination (0.392keV), possibly relating to TDMAT precursor decomposition [115]. Otherwise silicon (1.740 keV), oxygen (0.523 keV) and titanium (0.452, 4.510 and 4.95 keV) are detected, confirming TiO_2 growth.

Gallium is detected throughout the (9:1), (19:1) and (32:1) Ga-capped $Ti_{1-x}O_2:Ga_x$ films with the 1.028 keV peak intensity decreasing corresponding to lower gallium

nanolaminate incorporation. Furthermore, minimal or negligible 1.028 KeV peak intensity is detected for the (49:1) to (99:1) Ga-capped $Ti_{1-x}O_2:Ga_x$ films, suggesting the gallium concentrations are below the EDX detection limits [430]. Other peaks corresponding to gallium (10.27 and 9.250 keV), also remain undetected in most Ga-capped $Ti_{1-x}O_2:Ga_x$ films. Additionally, the 10.27 and 9.250 keV peaks are detected at highest gallium concentrations found in the (9:1) Ga-capped $Ti_{1-x}O_2:Ga_x$ films. However, due to identical process synthesis utilization across all Ga-capped $Ti_{1-x}O_2:Ga_x$, gallium incorporation into all Ga-capped $Ti_{1-x}O_2:Ga_x$ films is assumed.

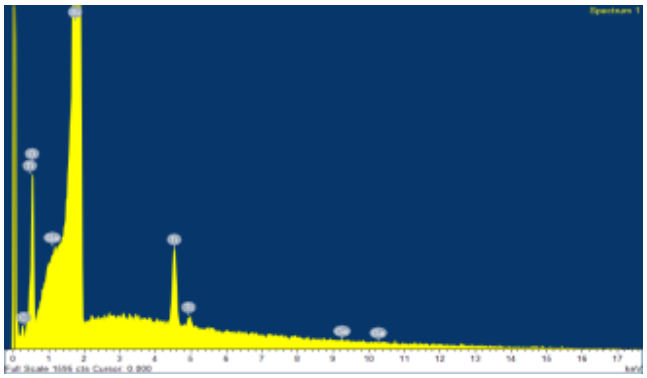

Figure 6.26: EDX of Ga-capped $Ti_{1-x}O_2:Ga_x$ (99:1) on silicon.

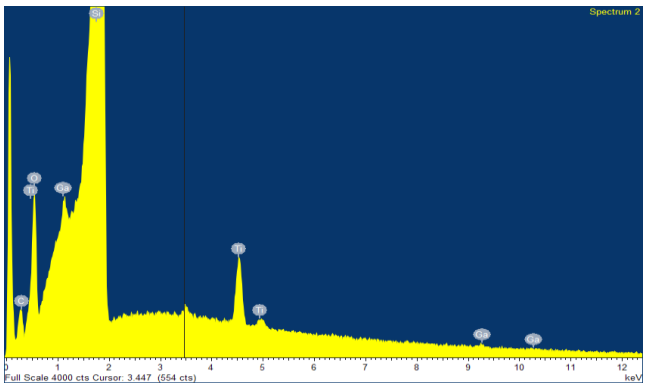

Figure 6.27: EDX of Ga-capped $Ti_{1-x}O_2:Ga_x$ (9:1) on silicon (remainder in appendix A).

Silicon, oxygen and glass impurity elements (bromine (1.48 keV), calcium (0.34, 3.69 keV), potassium (3.3 keV), magnesium (1.25 keV) and sodium (1.04 keV)) are indicated on Ga-capped $Ti_{1-x}O_2:Ga_x$ films on glass substrates (figures 6.28 and 6.29). Film growth is also confirmed through the detection of titanium peaks (0.452, 4.510 and 4.95 keV) with an indiscernible adventitious carbon contamination peak.

However, minimal surface concentrations are assumed as on silicon substrate samples.

The 9.250 keV gallium peak is only detected in both the (19:1) and (9:1) Ga-capped $Ti_{1-x}O_2:Ga_x$ films with 10.27 keV gallium peaks remaining undetected and 1.028 keV peaks smothered by a 1.04 keV sodium peak. However, as aforementioned on silicon substrates a gallium presence is assumed in all Ga-capped $Ti_{1-x}O_2:Ga_x$ films.

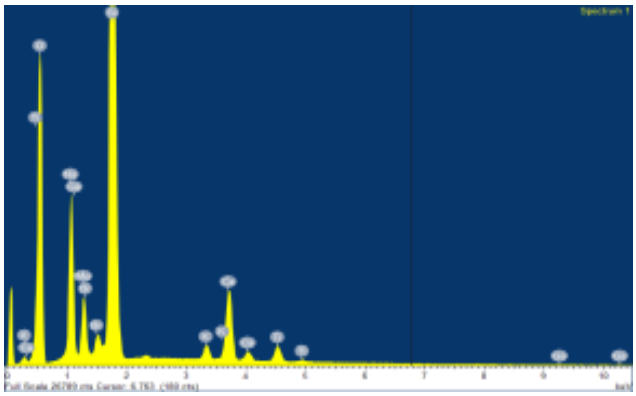

Figure 6.28: EDX of Ga-capped $Ti_{1-x}O_2:Ga_x$ (99:1) on glass.

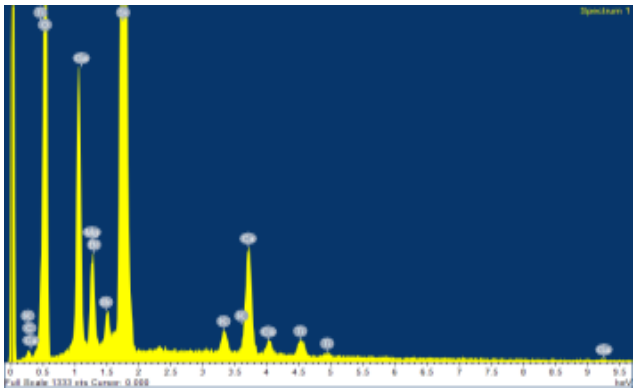

Figure 6.29: EDX of Ga-capped $Ti_{1-x}O_2:Ga_x$ (9:1) on glass (remainder in appendix A).

XPS was further performed on the Ga-capped $Ti_{1-x}O_2:Ga_x$ (99:1) film and the nominally undoped TiO_2 film, both grown on silicon and glass substrates, to generate surface region film composition.

Ga-capped $Ti_{0.93}Ga_{0.07}O_2$ (99:1) films on both glass and silicon substrates indicated only Ti^{4+} (Ti $2p_{3/2}$ and $_{1/2}$: 458.6 and 464.3 eV) peaks in a 2:1 ratio (13.7:6.9 % and 20.6 % total) and no evidence of Ti^{3+} formation. This suggests completely oxidized $Ti_{1-x}O_2:Ga_x$ and nominally undoped TiO_2 through PEALD synthesis. A 1:2 Ti:O ratio is

also clearly defined with corresponding lattice oxygen (O 1s_1; 530 eV) concentrations (42.8 %). Additionally, negligible variation is detected between growths on disparate substrates.

Furthermore, nominally undoped TiO_2 samples on both glass and silicon substrates grown under the same conditions show similar properties. These typically involve lacking Ti^{3+} concentrations (Ti^{4+}: 10.4 % (glass), 12.4 % (silicon) with a 1:2 Ti:O ratio, suggesting fully oxidized films. However, various disparate surface oxygen environments are detected between equivalently grown nominally undoped TiO_2 and Ga-capped $Ti_{1-x}O_2:Ga_x$ films, as shown by O 1s peak shift in figures 6.30 and 6.31.

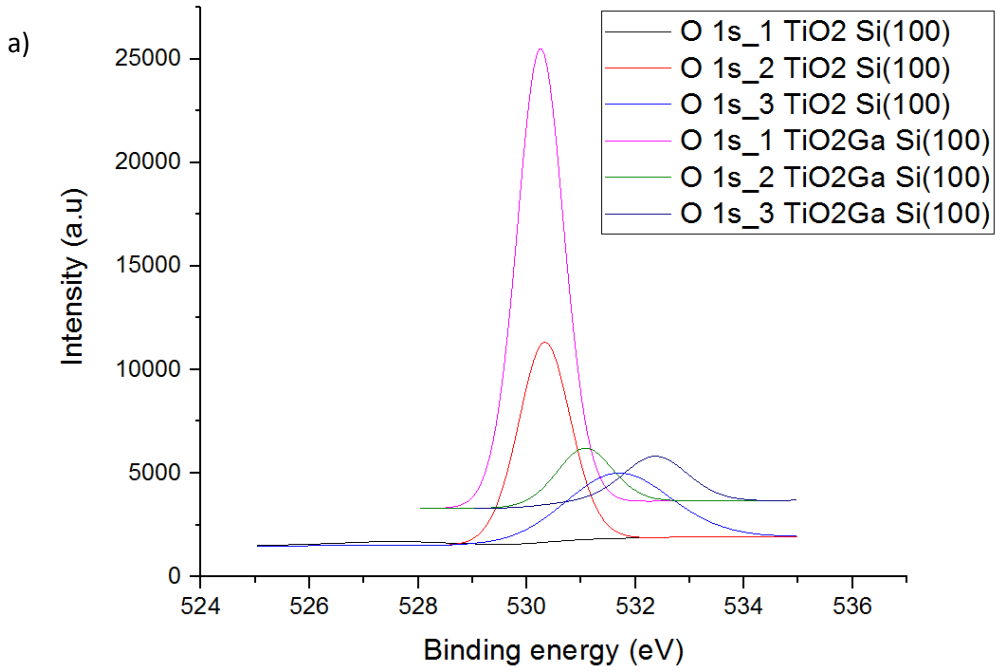

Figure 6.30: O 1s XPS for the nominally undoped TiO_2 film and the Ga-capped $Ti_{1-x}O_2:Ga_x$ films on silicon substrate.

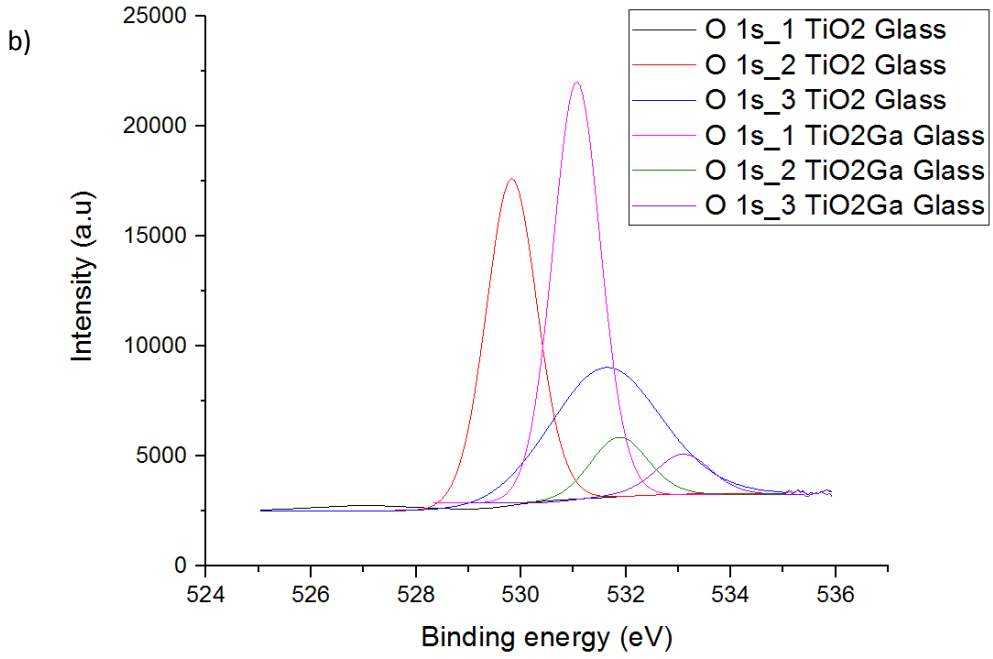

Figure 6.31: O 1s XPS for the nominally undoped TiO_2 film and the Ga-capped $Ti_{1-x}O_2$:Ga_x films on glass substrate.

Additionally; Ga^{3+} 2p (1117.9 eV) and (1117.5 eV) was detected for the Ga-capped $Ti_{0.93}Ga_{0.07}O_2$ films on glass and silicon substrates respectively. This generates 1.5-1.6 % of overall surface composition or 7 %, if assuming Ti^{4+} substitutional nanolaminate growth, suggesting a significantly higher GaO_x concentration than expected (1 %) [609].

Furthermore, between 21.8-23.1 % of adventitious carbon impurities are detected within the Ga-capped $Ti_{0.93}Ga_{0.07}O_2$ surface escape depth, due to a lack of surface sputtering. Typically, adventitious carbon either corresponds to;

- Atmospheric CO_2 capture by surface OH groups, generating water and surface carbonates [575].
- Contact sources, with C 1s peaks (284.8, 286.2 and 288.7 eV) resulting in C-C, C-O and O=C-O bonding, respectively.

The absence of any nitrogen contamination equating to C-N bonding suggests negligible TDMAT precursor decomposition and reaffirming the carbon arises from atmospheric or contact sourced carbon impurities.

From table 6.7, the PEALD grown Ga-capped $Ti_{1-x}O_2:Ga_x$ (99:1) films on glass and silicon and the thermal ALD grown $Ti_{0.92}Ga_{0.08}O_2$ films are shown to possess disparate O 1s, Ti 2p and C 1s_2 chemical environments.

	Ga-capped $Ti_{1-x}O_2:Ga_x$ (99:1) on glass	Ga-capped $Ti_{1-x}O_2:Ga_x$ (19:1) on silicon	$Ti_{1-x}O_2:Ga_x$ (99:1)
Peak	Position (eV)	Position (eV)	Position (eV)
O 1s_1 (metal oxide)	530.0	529.8	530.5
O 1s_2 (organics, hydroxide)	530.8	530.6	531.5
O 1s_3 (organics, SiO_x)	532.0	531.9	533.5
Ti 2p_1 (Ti^{4+} $2p_{3/2}$)	458.6	458.5	485.9
Ti 2p (Ti^{4+} $2p_{1/2}$)	464.3	464.3	464.6
C 1s_1 (C=C/C-C)	284.8	284.8	-
C 1s_2 (C-O)	286.2	286.2	286.5
C 1s_3 (O-C=O)	288.7	288.5	-

Table 6.7: High resolution XPS peaks for the Ga-capped $Ti_{0.93}Ga_{0.07}O_2$ film on glass and silicon and the $Ti_{0.99}Ga_{0.01}O_2$ film.

As shown in figures 6.32, 6.33 and 6.34, Ti 2p (458.9/464.6 eV), O 1s (530.4/531.2/533 eV) and carbonate C 1s_2 (286.6 eV) peaks possess increased binding energy (0.4/0.3 eV), (0.6/0.8/1.1 eV) and (0.4 eV), respectively. Ti-O bonding therefore suggests decreased free electron density. This possibly results from the formation of electron trapping Ti^{3+} sites (zero concentration of these sites in PEALD grown $Ti_{1-x}O_2:Ga_x$ (19:1)) and provides lower electron density for surface ROS creation.

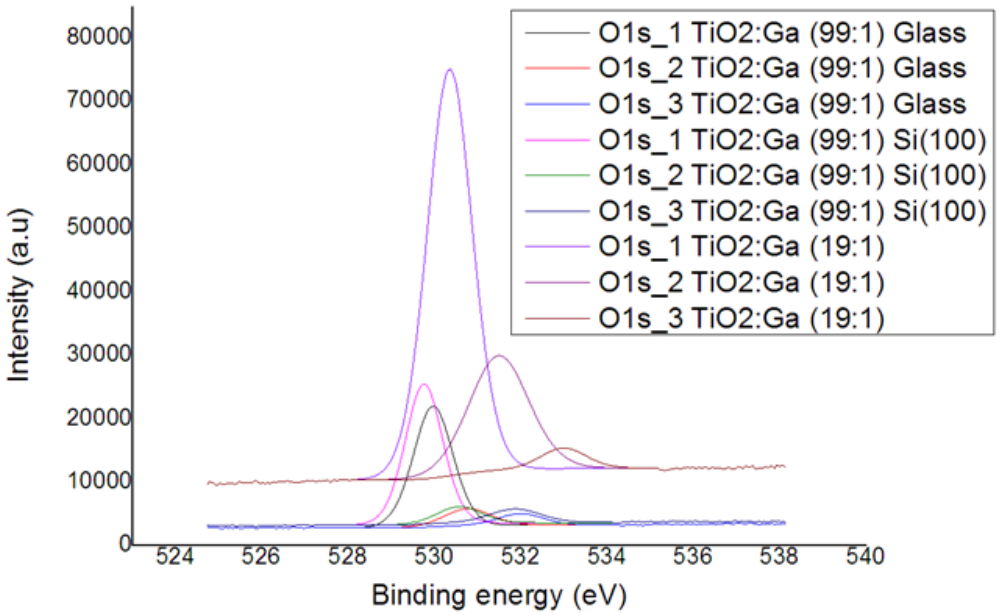

Figure 6.32: O 1s peak shifts for the PEALD grown Ga-capped $Ti_{1-x}O_2:Ga_x$ (99:1) films on glass and silicon as compared to thermal ALD grown $Ti_{1-x}O_2:Ga_x$ (99:1).

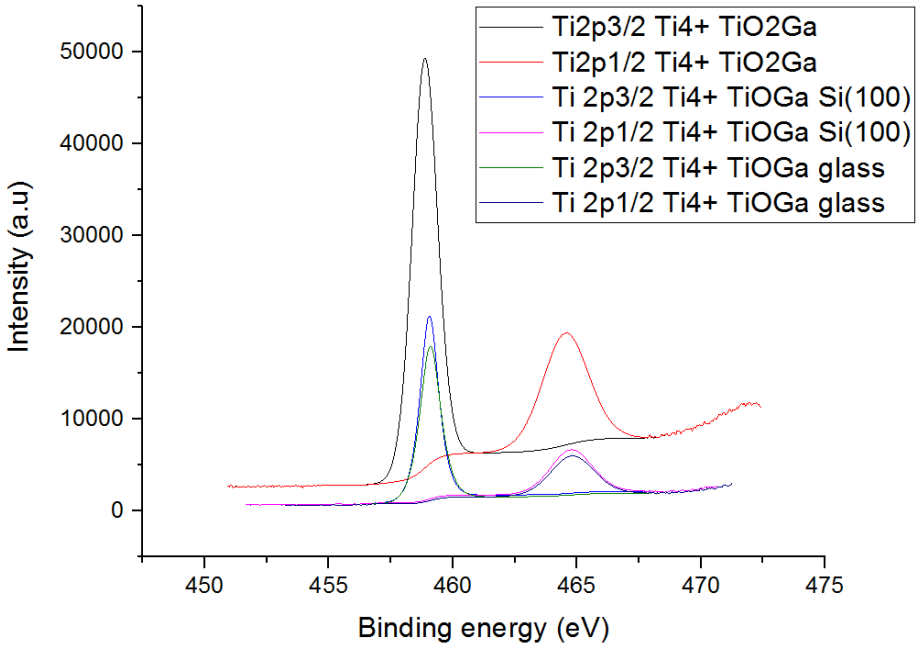

Figure 6.33: Ti^{4+} $2p_{3/2 \text{ and } 1/2}$ peaks shifts for the PEALD grown Ga-capped $Ti_{1-x}O_2:Ga_x$ (99:1) films on glass and silicon as compared to thermal ALD grown $Ti_{1-x}O_2:Ga_x$ (99:1).

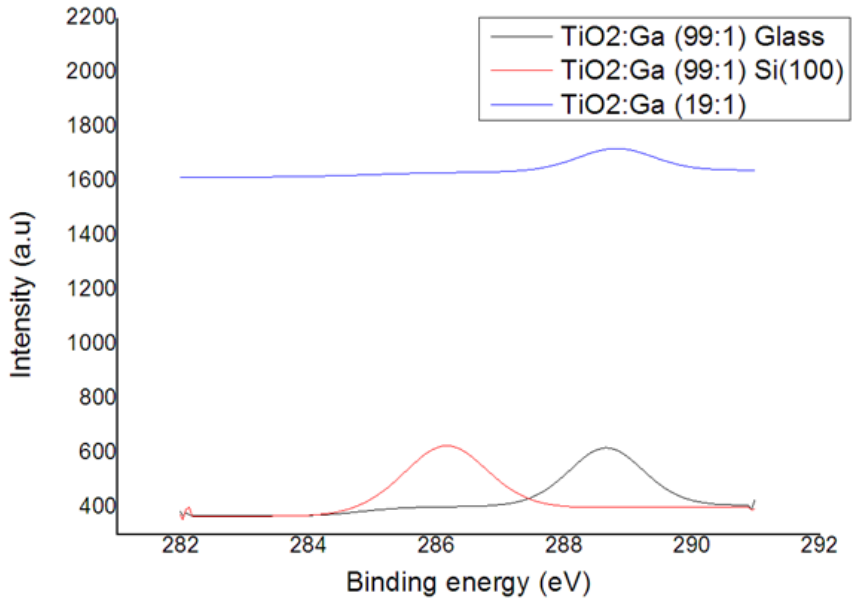

Figure 6.34: C 1s_2 peak shifts for the PEALD grown Ga-capped $Ti_{1-x}O_2:Ga_x$ (99:1) films on glass and silicon as compared to thermal ALD grown $Ti_{1-x}O_2:Ga_x$ (99:1).

Furthermore, SIMS was utilized to try to discern any compositional variations of the Ga-capped $Ti_{1-x}O_2:Ga_x$ (99:1) and (19:1). Figures 6.35 and 6.36 subsequently determine titanium, gallium, aluminium and silicon presence in both the Ga-capped $Ti_{1-x}O_2:Ga_x$ (99:1) and (19:1) films.

As expected, greater gallium concentrations are detected in the (9:1) film as compared to the (99:1) Ga-capped $Ti_{1-x}O_2:Ga_x$ films. Both films show a slight gallium decrease on depth profiling, in contrast to a titanium increase and correlate to surface GaO_x from the final ALD gallium pulse. Also as expected, the titanium concentrations plateau on continued depth profiling, before gradually decreasing (700 seconds) with majority Ga-capped $Ti_{1-x}O_2:Ga_x$ removal. Gallium concentrations also plateau, with a subsequent gradual decrease (1000 seconds). This suggests either homogeneous Ga^{3+} diffusion throughout the Ga-capped $Ti_{1-x}O_2:Ga_x$ film [605, 606] or aggressive sputtering from collisional cascading providing continuous elemental detection [446, 447]. Correspondingly, the TEM results suggest homogeneous Ga^{3+} diffusion, but as discussed, are rendered inconclusive from Ga^{3+} overexposure.

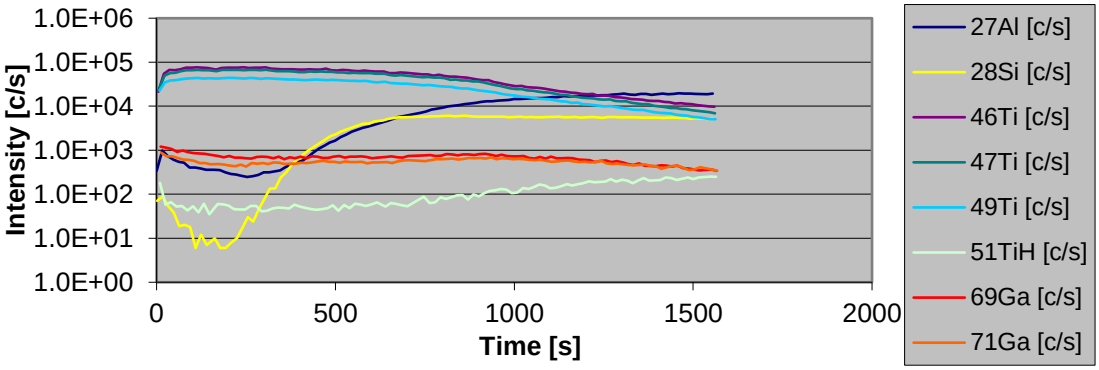

Figure 6.35: SIMS of the Ga-doped $Ti_{1-x}O_2:Ga_x$ (99:1).

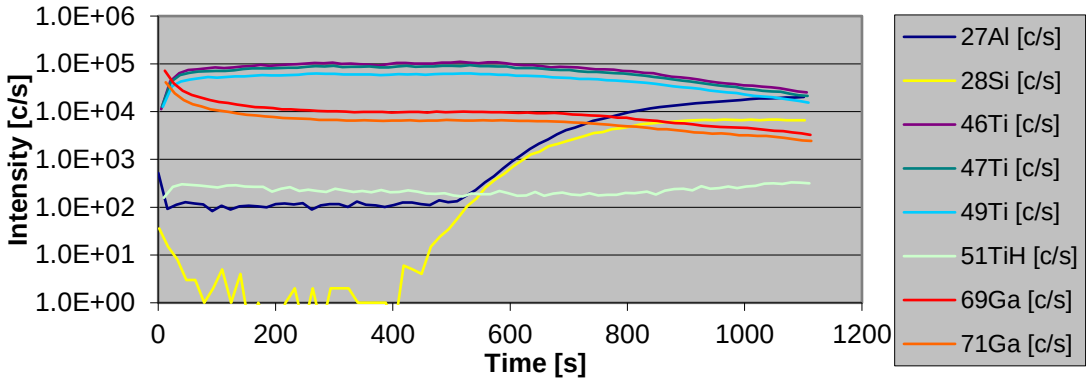

Figure 6.36: SIMS of the Ga-doped $Ti_{1-x}O_2:Ga_x$ (19:1).

It is suggested that the sample cutting processes utilized generates minimal silicon and aluminium surface contamination as detected in figures 6.35 and 6.36, with an initial decreasing trend in concentration from surface regions. Furthermore, with continued sputtering, both aluminium and silicon signals slowly increase and plateau whilst the titanium signal decreases, suggesting a majority of Ga-capped $Ti_{1-x}O_2:Ga_x$ film is removed after 1250 seconds.

Comparatively, both Ga-capped $Ti_{1-x}O_2:Ga_x$ films show a slight variation in average silicon and aluminium concentrations at $1.0e^2$ (~450 and 620 seconds, respectively). Therefore, some possible thickness variations are suggested, with the Ga-capped $Ti_{1-x}O_2:Ga_x$ (99:1) film being thinner. This is supported by the reduced sputtering time required prior to an increase in silicon and aluminium concentrations. In contrast, TEM measurements indicate the Ga-capped $Ti_{1-x}O_2:Ga_x$

(99:1) film possesses greater thickness as compared to the Ga-capped $Ti_{1-x}O_2:Ga_x$ (9:1) film.

To summarize, compositional analysis of nominally undoped TiO_2 and $Ti_{1-x}O_2:Ga_x$ typically indicate high purity with adventitious atmospherically or contact sourced surface carbonates with negligible precursor surface decomposition. Additionally, nominally undoped TiO_2 and Ga-capped $Ti_{1-x}O_2:Ga_x$ only showed Ti^{4+} concentration presence and a 1:2 Ti:O ratio, suggesting fully oxidized films with negligible $Ti^{3+}/V_O^{\cdot\cdot}$ defect generation.

Furthermore, gallium was detected throughout Ga-capped $Ti_{1-x}O_2:Ga_x$ with SIMS analysis suggesting homogeneous Ga^{3+} distribution and an expected order of magnitude concentration difference between the (9:1) and the (99:1) Ga-capped $Ti_{1-x}O_2:Ga_x$ films. Additionally, surface XPS analysis suggests greater gallium concentrations than expected for $Ti_{0.93}Ga_{0.07}O_2$ (99:1), correlating to either 7 % doping or 1.5/1.6 % of surface constitution. Therefore, assuming identical syntheses, Ga-capped $Ti_{1-x}O_2:Ga_x$ possess greater gallium surface concentrations than expected, probably resulting from Ga^{3+} surface accumulation [180] via the final "capping" TEGa pulse. Ga-capped $Ti_{1-x}O_2:Ga_x$ photocatalytic activity with respect to gallium addition is explored beneath.

6.4.1 Optical and Photocatalytic activity

Photocatalytic ink degradation was performed on pre-photocatalytically UV light activated nominally undoped TiO_2 and $Ti_{1-x}O_2:Ga_x$ films on glass substrates. This was accomplished to indicate the relative ttb of basic blue 66 ink, with both plain glass substrate and Pilkington Activ™ as reference samples (figures 6.37 and 6.38).

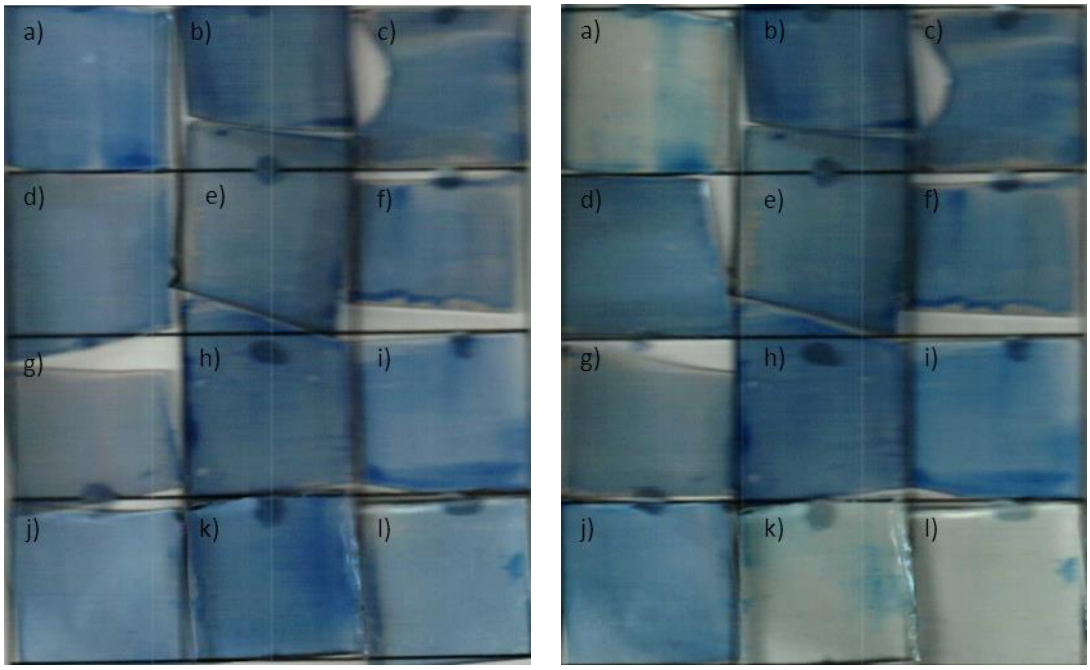

Figures 6.37 and 6.38: before and after 10 minutes of UV irradiation on a) nominally undoped TiO_2, and b) (99:1), c) (74:1), d) (49:1), e) (39:1), f) (32:1), g) (19:1), h) (9:1) $Ti_{1-x}O_2$:Ga_x on glass substrate, and i) and j) plain glass substrate and k) and l) Pilkington Activ™.

Figures 6.37 and 6.38, show no evidence of degradation after 10 minutes on the UV-activated Ga-capped $Ti_{1-x}O_2$:Ga_x film. In contrast, nominally undoped TiO_2 and Pilkington Activ™ both generate basic blue 66 ink degradation (blue colouration loss) and a ttb of 2-4 minutes under UV light irradiation. As expected, basic blue 66 ink is degraded with a ttb of 2-3 minutes under UV light irradiation by photocatalytically active films such as Pilkington Activ™ [483].

Additionally, nominally undoped TiO_2 indicates a similar ttb as Pilkington Activ™. This suggests typical photocatalytic activity generation from excition charge pair and subsequent hydroxyl radical creation [32], without generating any significant $Ti^{3+}/V_{O^{\cdot\cdot}}$ surface defects, as indicated in XPS. Correspondingly, negligible activity for the Ga-capped $Ti_{1-x}O_2$:Ga_x films subsequent to 10 minutes UV light irradiation, probably results from surface GaO_x.

Water contact angle analysis was subsequently performed on nominally undoped TiO_2 and Ga-capped $Ti_{1-x}O_2$:Ga_x films prior to irradiation, after four hours exposure

and subsequent to a week in darkness following UV activation (figures 6.39 and 6.40).

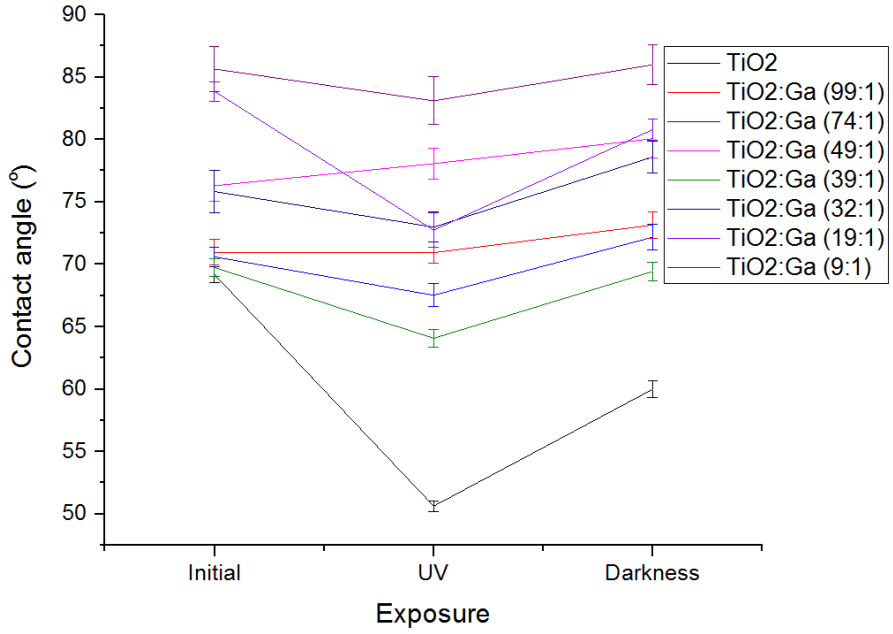

Figure 6.39: Average water contact angles at initial (0 minutes), after UV light exposure (60 minutes) and after darkness (10800 minutes) for nominally undoped TiO_2 and Ga-capped $Ti_{1-x}O_2:Ga_x$ on silicon substrates pre-coated with Al_2O_3.

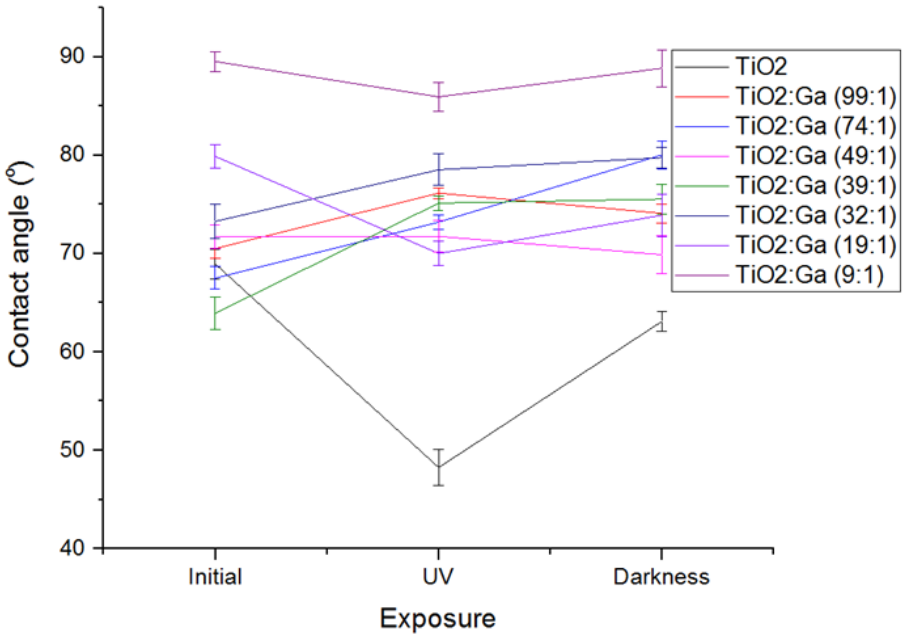

Figures 6.40: Average water contact angles at initial (0 minutes), after UV light exposure (60 minutes) and after darkness (10800 minutes) for nominally undoped TiO_2 and Ga-capped $Ti_{1-x}O_2:Ga_x$ on glass substrates pre coated with Al_2O_3.

A significant variation between nominally undoped TiO_2 and Ga-capped $Ti_{1-x}O_2:Ga_x$ films is detected, with nominally undoped TiO_2 films presenting decreased contact angle values on average (70/65 ^{o}, 52/55 ^{o}, 61/64 ^{o} silicon/glass). These decreased contact angles indicate both greater wetting capability and potential photoactivity compared to Ga-capped $Ti_{1-x}O_2:Ga_x$ films (75-86 ^{o}, 67-83 ^{o}, 72-86 ^{o} silicon/glass). Ga-capped $Ti_{1-x}O_2:Ga_x$ films therefore exhibit decreased wetting capability, suggesting diminished photocatalytic activity, both resulting from either an inability to generate or minimal creation of ROS.

Several Ga-capped $Ti_{1-x}O_2:Ga_x$ films ((74:1) on silicon, (49:1) on glass and both (32:1)) indicate hydrophobic behaviour subsequent to UV activation which further increases on darkness immersion. This is in contrast to the usual trends of decreasing hydrophobicity with subsequent recovery to the pre-irradiated state [620].

No discernible trend is detected between Ga-capped $Ti_{1-x}O_2:Ga_x$ films containing varied gallium concentrations with water contact angles ranging between 67 and 86 ^{o} after UV light irradiation. Additionally, nominally undoped TiO_2 and $Ti_{1-x}O_2:Ga_x$ films on glass consistently show slightly increased hydrophilicity (1-5 ^{o}) as compared to those films on silicon, suggesting minimal growth effects from differing substrates.

Interestingly, despite the GaO_x surface cap on the $Ti_{1-x}O_2:Ga_x$ film surface, some Ga-capped $Ti_{1-x}O_2:Ga_x$ films grown on silicon and the Ga-capped $Ti_{1-x}O_2:Ga_x$ (19:1) film grown on glass, actually indicate a hydrophilic increase outside of error upon UV light irradiation. This potentially suggests that the GaO_x surface cap does not completely remove ROS presence as first thought, with some retention of latent photocatalytic activity. Thus, Ga-capping of $Ti_{1-x}O_2:Ga_x$ films is suggested to deteriorate TiO_2 photocatalytic activity and hydrophilic wetting capabilities.

In the following section, the study of the influence of gallium incorporation on the TiO_2 band gap is presented. Figure 6.41 shows TiO_2 and Ga-capped $Ti_{1-x}O_2:Ga_x$ film, UV/visible light transmission spectra (200-800 nm) for a range of samples studied and furthermore table 6.8 contains corresponding band gap calculations. Figure

6.40 shows nominally undoped TiO_2 and Ga-capped $Ti_{1-x}O_2:Ga_x$ films initially generate between 76-82 % transmission at 700 nm, gradually decreasing with to 54-59 % transmission at 390 nm. The rapid transmission decrease preceding 300 nm occurs on TiO_2 bandgap UV light absorption with all films possessing decreased transmission compared to glass substrates, as expected.

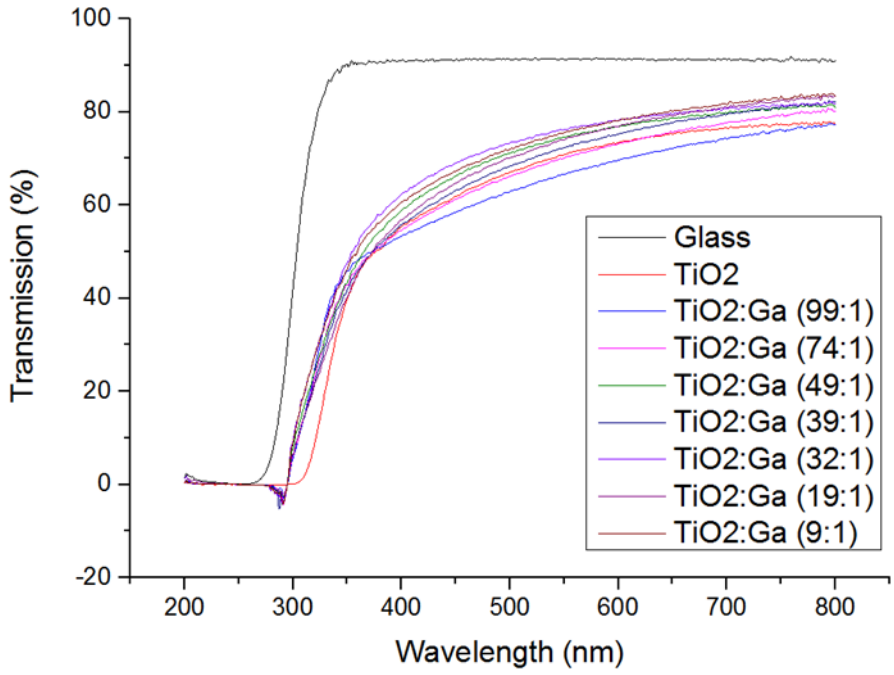

Figure 6.41: UV/Visible light transmission for nominally undoped TiO_2 and Ga-capped $Ti_{1-x}O_2:Ga_x$ films compared to glass substrate.

No obvious correlation is observed between transmission and previously observed crystalline morphology for the nominally undoped TiO_2 and Ga-capped $Ti_{1-x}O_2:Ga_x$ films. However, the nominally undoped TiO_2 film shows a significantly lower transmission at higher wavelengths with respect to that observed for Ga-capped $Ti_{1-x}O_2:Ga_x$ films, suggesting surface GaO_x presence slightly increases UV/visible light wavelength transmission.

The spectra recorded were processed utilizing the Tauc approach as described in Chapter 2 (figure 6.42) and band gaps were calculated (table 6.8) and compared to the literature values [621].

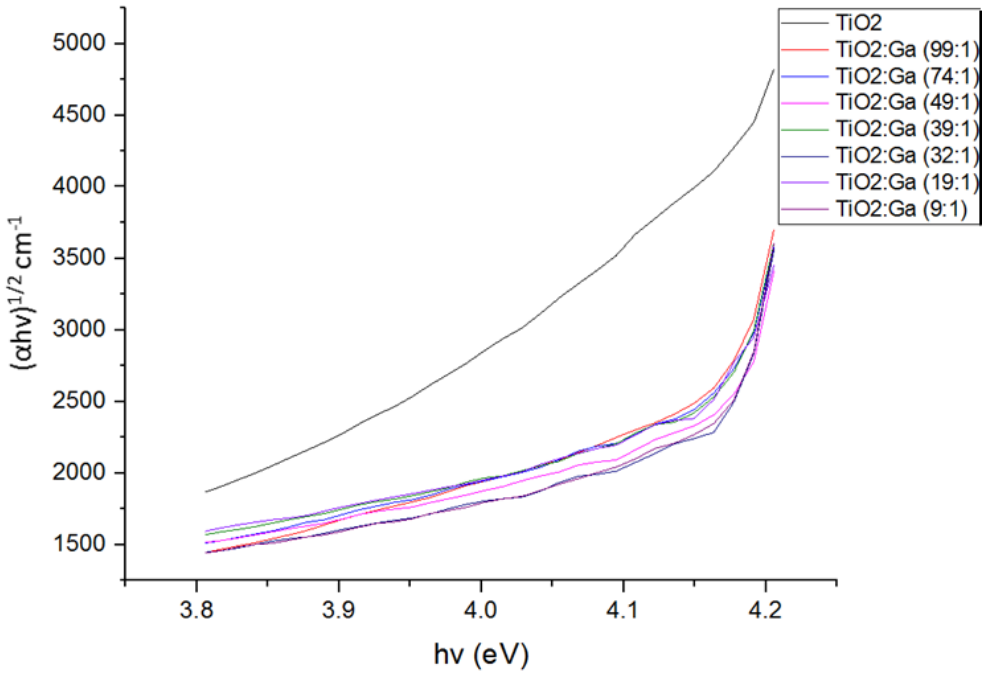

Figure 6.42: Tauc Plot of the nominally undoped TiO_2 film and the Ga-capped $Ti_{1-x}O_2:Ga_x$ (99:1), (74:1), (49:1), (39:1), (32:1), (19:1) and (9:1) films.

	Direct (eV) band gap
TiO_2	3.88
$Ti_{1-x}O_2:Ga_x$ (99:1)	4.03
$Ti_{1-x}O_2:Ga_x$ (74:1)	4.03
$Ti_{1-x}O_2:Ga_x$ (49:1)	4.03
$Ti_{1-x}O_2:Ga_x$ (39:1)	4.04
$Ti_{1-x}O_2:Ga_x$ (32:1)	4.05
$Ti_{1-x}O_2:Ga_x$ (19:1)	4.02
$Ti_{1-x}O_2:Ga_x$ (9:1)	4.05

Table 6.8: Calculated direct band gap values for nominally undoped TiO_2 and Ga-capped $Ti_{1-x}O_2:Ga_x$ (99:1), (74:1), (49:1), (39:1), (32:1), (19:1) and (9:1) films.

Gallium doping provides an increase in band gap (4.02-4.05 eV) as compared to nominally undoped TiO_2 (3.88 eV). Additionally greater band gap widths suggest Burstein-Moss effects with 3.15-3.37 eV TiO_2 and 4.9 eV Ga_2O_3 [175] band gap mixing inducing population of TiO_2 conduction band states or a combination of

both morphology and Burstein-Moss effects. However, no clear trend in Ga-capped $Ti_{1-x}O_2:Ga_x$ band gap variation with increasing GaO_x concentration is observed.

To summarize, Ga-capped $Ti_{1-x}O_2:Ga_x$ films indicate no photocatalytic activity with respect to basic blue 66 ink degradation under UV light, dissimilar to the nominally undoped TiO_2 film. However, despite the GaO_x surface cap on the $Ti_{1-x}O_2:Ga_x$ film surface, some films suggest a hydrophilic increase and show ROS presence. Additionally, the Ga-capped $Ti_{1-x}O_2:Ga_x$ films show a blue shift in band gap variation as compared to a nominally undoped TiO_2 film possibly relating to Burstein-Moss effects on GaO_x incorporation. However, no discernible trend between varied gallium concentrations and overall band gap size is detected.

6.4.2 Electrical conduction

Table 6.9 presents a summary of the electrical data for two different four point probe set ups. It may be seen that all films are essentially resistive. In table 6.09, the resistivity of the Ga-capped $Ti_{1-x}O_2:Ga_x$ films grown on glass are all much higher than the Ga-capped $Ti_{1-x}O_2:Ga_x$ films grown on silicon substrates. However, only the values recorded on the glass substrates are relevant due to potential influence of the silicon substrate for the other measurements.

	Silicon substrate	Silicon substrate	Glass substrate	Glass substrate
	Resistivity (Ω.cm)	Conductivity (Scm^{-1})	Resistivity (Ω.cm)	Conductivity (Scm^{-1})
TiO_2	3.75	0.267	2730	$3x10^{-4}$
Ga-capped $Ti_{1-x}O_2:Ga_x$ (99:1)	1.90	0.526	324	$3x10^{-3}$
Ga-capped $Ti_{1-x}O_2:Ga_x$ (74:1)	2.69	0.372	3310	$3x10^{-4}$
Ga-capped $Ti_{1-x}O_2:Ga_x$ (49:1)	2.18	0.459	84	0.0119
Ga-capped $Ti_{1-x}O_2:Ga_x$ (39:1)	11.6	0.0864	3840	$2x10^{-4}$
Ga-capped $Ti_{1-x}O_2:Ga_x$ (32:1)	10.9	0.0913	129	$7x10^{-3}$
Ga-capped $Ti_{1-x}O_2:Ga_x$ (19:1)	11.5	0.0871	43000	$2x10^{-5}$
Ga-capped $Ti_{1-x}O_2:Ga_x$ (9:1)	138	$7x10^{-3}$	367000	$2x10^{-6}$

Table 6.9: Cascade manual prober and HP1456 parameter analyser resistivity and conductivity values.

6.5 Discussion

From these results, it may be observed that the thermal ALD grown $Ti_{1-x}O_2:Ga_x$ films and the PEALD grown Ga-capped $Ti_{1-x}O_2:Ga_x$ films share similar morphology. However, greater gallium nanolaminate concentrations decreasing anatase crystallite formation, as shown in XRD and Raman spectroscopy results above. This could occur either during synthesis through GaO_x nanolaminates providing barrier layers to larger crystallite growth or during annealing, with Ga^{3+} diffusion preventing successful crystallite generation. Furthermore, the Ga-capped Ti_{1-}

$_xO_2$:Ga_x films were grown above the TDMAT ALD precursor temperature window [115, 622] to attempt anatase crystallinity formation, however, inadequately polycrystalline anatase resulted.

Additionally, with a reduction in anatase crystallite formation, namely the most photocatalytically active TiO_2 polymorph [30], the photocatalytic activity of both $Ti_{1-x}O_2$:Ga_x and Ga-capped $Ti_{1-x}O_2$:Ga_x films would be expected to decrease. However, this expected trend of photocatalytic reduction is only observed within thermal ALD grown $Ti_{1-x}O_2$:Ga_x films. Addition of the surface GaO_x capping layer is shown to completely remove any potential photocatalytic activity from the Ga-capped $Ti_{1-x}O_2$:Ga_x films. Though interestingly the water contact angle still suggests minimal surface ROS species formation under UV light for some Ga-capped $Ti_{1-x}O_2$:Ga_x films, with slight hydrophilic water droplet increases outside of error detected.

Furthermore, it can be inferred from the results above that gallium doping also provides a direct decrease in photocatalytic activity. The thermal ALD grown $Ti_{0.99}Ga_{0.01}O_2$ (99:1) film records a ttb of 4 hours 22 minutes for basic blue 66 ink, as compared to 11 minutes 4 seconds for nominally undoped TiO_2. However, other gallium-doped films present no photodegradation of basic blue 66 ink and hydrophobic water contact angle retention under UV light irradiation. In particular gallium doping decreases both the photocatalytic activity and hydrophilic wetting observed. This corresponds with GaO_x nanolaminates or diffused Ga^{3+}, providing deep hole dominated recombination centres for UV light excited excitons [177, 610], interrupting charge carrier surface diffusion and preventing surface ROS creation [127, 418, 623]. However, surface synthesized GaO_x on the PEALD grown Ga-capped $Ti_{1-x}O_2$:Ga_x films could hinder surface ROS creation and also prevent the accurate measurement of the photocatalytic and wetting properties by creating unfavourable surface reactions [180].

AlO_x particulate presence on the thermal ALD grown $Ti_{0.92}Ga_{0.08}O_2$ surface could also hinder surface wettability with Al_2O_3 incorporation suggesting previous reduced photocatalytic activity and surface reactive oxide species generation [624].

The differing synthesis techniques were also reflected through XPS analysis on both sets of $Ti_{1-x}O_2:Ga_x$ films with the thermal ALD grown $Ti_{1-x}O_2:Ga_x$ films showing presence of Ti^{3+} (12.7-13.1 %). This Ti^{3+} either naturally results during oxygen deficient synthesis [150] or from charge compensation on Ga^{3+} "substitution" for Ti^{4+} ($Ga_{Ti'}$) [150]. In contrast, the PEALD grown Ga-capped $Ti_{1-x}O_2:Ga_x$ films indicate only Ti^{4+} presence, suggesting fully oxidative films after utilizing highly oxidizing oxygen plasma, with possible bulk Ti^{3+} on gallium "substitution". Ti^{3+} presence in the thermal ALD grown $Ti_{1-x}O_2:Ga_x$ films would be beneficial towards photocatalysis [127, 625] and could also be the reason for the basic blue 66 ink photodegradation observed.

Furthermore, Ti^{3+} typically provides mid-band gap states, favourably reducing the overall band gap as observed for the thermal ALD grown $Ti_{1-x}O_2:Ga_x$ films (2.76-2.90 eV). This contrasts with both the PEALD grown Ga-capped $Ti_{1-x}O_2:Ga_x$ films (4.02-4.05 eV) and values in the literature (3-3.37 eV) [1]. However, Ga-capped $Ti_{1-x}O_2:Ga_x$ films are also effected by Burstein-Moss effects with possible surface GaO_x formation, blue shifting band gap size. Additionally, the significantly amorphous $Ti_{1-x}O_2:Ga_x$ film morphology would also increase band gap size, decreasing potential wavelength absorption.

6.6 Conclusions

In conclusion, annealed nominally undoped TiO_2 and $Ti_{1-x}O_2:Ga_x$ (19:1 and 99:1) films were successfully grown onto quartz substrates by thermal ALD. Additionally, nominally undoped TiO_2 and a range of Ga-capped $Ti_{1-x}O_2:Ga_x$ films were also successfully grown onto and glass substrates by PEALD. The influence of gallium doping concentration and specifically the presence of a capping gallium monolayer on the photocatalytic, structural, optical and electrical characteristics was investigated. Gallium doping was indicated to greatly decrease the photocatalytic activity of TiO_2 films with respect to basic blue 66 ink photodegradation under UV irradiation. A ttb of 4 hours 22 minutes for $Ti_{0.99}Ga_{0.01}O_2$ was reported, as compared to 11 minutes 4 seconds ± 35 seconds for nominally undoped TiO_2. Heavier doped $Ti_{0.92}Ga_{0.08}O_2$ films subsequently reported no basic blue 66 ink degradation. Additionally, water contact angle analysis also provided limited hydrophilic change

for both annealed $Ti_{1-x}O_2:Ga_x$ films under UV light irradiation. This decrease in photocatalytic activity and wetting effects possibly results from gallium ions acting as exciton recombination centres and the subsequent loss of surface ROS sites.

In comparison, Ga-capped $Ti_{1-x}O_2:Ga_x$ films suggested a complete destruction of photocatalytic activity irrespective of gallium concentration, reinforcing photocatalysis as a surface driven effect. However, the lack of Ti^{3+} detection from the highly oxidative synthesis environment may also contribute. Surprisingly, minimal hydrophilic increase was observed for water droplets on Ga-capped $Ti_{1-x}O_2:Ga_x$ surfaces under UV light irradiation. This suggests a single gallium ALD precursor pulse, equating to just under a monolayer of GaO_x material, is not enough to completely remove all titanium dioxide based surface ROS sites.

Furthermore, gallium doping for both sets of film showed decreasing anatase crystalline morphology for increasing gallium concentrations also reducing the potential photocatalytic activity of films.

Conclusions and Further Research

This research set out to study differences in photocatalytic, structural, optical and electrical properties of $Ti_{1-x}O_2:M_x$ films synthesized with a variety of dopants. Additionally, the examination of the photocatalytic activity of both standard Pilkington Activ™ samples and the synthesized $Ti_{1-x}O_2:M_x$ (19:1) films, after routine Irish hospital cleaning agent application was a priority, as was the study of antimicrobial properties of sufficiently photocatalytic films.

Initially, Pilkington Activ™ surfaces individually treated with a range of common Irish hospital cleaning agents (Actichlor Plus™, Chloraprep™, Stericlean™ and Virusolve™) showed a permanent decrease in photocatalytic activity. This photocatalytic activity decrease was in respect to resazurin ink and basic blue 66 ink photodegradation, as well as increased water contact angle hydrophobicity under UV irradiation. Typically, photocatalytic activity decrease resulted from cleaning agent residues, specifically from Actichlor Plus™ or Chloraprep™. However, the photocatalytic activity decrease was not incremental following multiple treatments for the non-residue creating cleaning agents (Stericlean™ and Virusolve^{+}™). This suggested that the development of cleaning agents of this nature would be beneficial towards utilizing photocatalytic TiO_2 films in environments subject to rigorous cleaning regimes.

Considering the above study, a range of nominally undoped TiO_2 and annealed $Ti_{1-x}O_2:M_x$ films synthesized through thermal ALD on quartz substrates showed disparate photocatalytic activities dependent on crystalline morphology, Ti^{3+} concentration and dopant utilized. An annealed nominally undoped TiO_2 film synthesized by thermal ALD was predominately amorphous, containing around 20 % Ti^{3+} concentrations, and provided a time to bleach of 11 minutes 4 seconds ±35 seconds with respect to basic blue 66 ink. In comparison, the highly anatase polycrystalline CVD-grown Pilkington Activ™ samples yield a time to bleach of 2 minutes 7 seconds ±19 seconds. This suggested that whilst ALD can produce

nominally undoped TiO_2 films possessing photocatalytic activity, the films are less active than Pilkington Activ™.

The $Ti_{1-x}O_2:M_x$ films separately incorporated aluminium, gallium, hafnium, silver, tin and vanadium as nanolaminate dopants, resulting in varying degrees of crystallinity and Ti^{3+} concentrations. Among these doped films, only the $Ti_{1-x}O_2$:Ag (19:1) and $Ti_{1-x}O_2$:Sn (19:1) films showed any photocatalytic improvement as compared to the nominally undoped TiO_2 film. Resulting in basic blue 66 ink time to bleach values of 6 minutes 4 seconds for $Ti_{1-x}O_2:Ag_x$ (19:1) and 6 minutes 42 seconds for $Ti_{1-x}O_2:Sn_x$ (19:1), nearly halving the time to bleach observed for the nominally undoped TiO_2 films. This reduced time to bleach is suggested to originate from higher bulk Ti^{3+} concentrations for the annealed $Ti_{1-x}O_2:Ag_x$ and $Ti_{1-x}O_2:Sn_x$ (19:1) films (52 and 31 %), respectively. However, in the case of $Ti_{1-x}O_2:Sn_x$ (19:1), Sn^{4+} could also provide an electron sink, with both Ti^{3+} and Sn^{4+} resulting in greater reactive oxide species concentrations.

Interestingly, although silver could not be detected in the $Ti_{1-x}O_2:Ag_x$ (19:1) films using XPS, along with $Ti_{1-x}O_2:Sn_x$ (19:1), it produced the most photocatalytic active ALD-grown films. The $Ti_{1-x}O_2:Sn_x$ (19:1) film was used for further photocatalytic analysis, which revealed a shorter average time to bleach for the $Ti_{1-x}O_2:Sn_x$ (19:1) films of 5 minutes 12 seconds ± 1 minute 13 seconds. After treatment with Chloraprep™ and Virusolve+™, the photocatalytic activity of this sample again decreased with respect to resazurin ink photodegradation. However, as with Pilkington Activ™ treated surfaces, the photocatalytic activity decrease was not incremental, suggesting permanent damage, but not complete destruction of the photocatalytic activity within the first two cleaning agent treatments. Unfortunately, further microbiological exposure of both Pilkington Activ™ and $Ti_{1-x}O_2:Sn_x$ (19:1) films were inconclusive with a complex interplay between bacterial attachment and antimicrobial activity suggested in the terms of the key parameters.

Conclusively, it can be inferred from this study that ALD is suitable for growing UV light active $Ti_{1-x}O_2:M_x$ films with respect to photocatalytic ink degradation.

However, such films would ideally require sustainable visible light activity to be useable within indoor environments. In addition, as also observed from this study, the photocatalytic activity needs to withstand repeat cleaning agent application to produce an ideal sterile environment. Therefore, further research is required in terms of synthesizing an increasingly resilient and ideally also visible light active TiO_2 films, or the synthesis of cleaning agents which do not impair the photocatalytic activity of the films.

From the above conclusions gathered, further research should focus on:

- Using FTIR analysis of cleaning agent exposed surfaces to reinforce the XPS results and identify the molecular nature of Ti-impurity or Ti-O-impurity bonding.
- Testing of Pilkington Activ^{TM} or synthesized (undoped/doped) TiO_2 in hospital environments.
- Utilizing atomic force microscopy (AFM) to establish whether or not any TiO_2 surface physical abrasion occurred during cleaning agent exposure, resulting in decreased photocatalytic activity.
- Improving both nominally undoped TiO_2 and $Ti_{1-x}O_2:M_x$ film morphology through annealing studies.
- Repeat the $Ti_{1-x}O_2:Ag_x$ film synthesis, including a growth study to detect how silver precursor exposure effects TiO_2 film growth and silver incorporation through solid solubility.
- Exploring variable dopant amounts, combinations and subsequent annealing processes to synthesize $Ti_{1-x}O_2:Sn_x$ films with greater photocatalytic activity.
- Further microbiological experimentation to determine if Pilkington Activ^{TM} and $Ti_{1-x}O_2:M_x$ (19:1) film activation generates *E.coli* colony photosterilization.
- The development and subsequent analysis of visible light photocatalytically activated TiO_2 films with microbiological properties.

References

1. Mo, S.D. and W.Y. Ching, Electronic and optical properties of 3 phases of titanium dioxide - Rutile, anatase and brookite. Physical Review B, 1995. 51(19): pages 13023-13032.
2. Lu, L., X.H. Xia, J.K. Luo, and G. Shao, Mn-doped TiO_2 thin films with significantly improved optical and electrical properties. Journal of Physics D-Applied Physics, 2012. 45(48): page 8.
3. Yamamoto, T. and H. Katayama-Yoshida, Unipolarity of ZnO with a wide-band gap and its solution using codoping method. Journal of Crystal Growth, 2000. 214: pages 552-555.
4. Hidaka, H., S. Horikoshi, N. Serpone, and J. Knowland, In vitro photochemical damage to DNA, RNA and their bases by an inorganic sunscreen agent on exposure to UVA and UVB radiation. Journal of Photochemistry and Photobiology a-Chemistry, 1997. 111(1-3): pages 205-213.
5. O'Connor, C., J. Powell, C. Finnegan, A. O'Gorman, S. Barrett, K.L. Hopkins, B. Pichon, R. Hill, L. Power, N. Woodford, J.C. Coffey, A. Kearns, N.H. O'Connell, and C.P. Dunne, Incidence, management and outcomes of the first cfr-mediated linezolid-resistant Staphylococcus epidermidis outbreak in a tertiary referral centre in the Republic of Ireland. Journal of Hospital Infection, 2015. 90(4): pages 316-321.
6. Ryan, L., E. O'Mahony, C. Wrenn, S. FitzGerald, U. Fox, B. Boyle, K. Schaffer, G. Werner, and I. Klare, Epidemiology and molecular typing of VRE bloodstream isolates in an Irish tertiary care hospital. Journal of Antimicrobial Chemotherapy, 2015. 70(10): pages 2718-2724.
7. Reuter, S., M.E. Toeroek, M.T.G. Holden, R. Reynolds, K.E. Raven, B. Blane, T. Donker, S.D. Bentley, D.M. Aanensen, H. Grundmann, E.J. Feil, B.G. Spratt, J. Parkhill, and S.J. Peacock, Building a genomic framework for prospective MRSA surveillance in the United Kingdom and the Republic of Ireland. Genome Research, 2016. 26(2): pages 263-270.

8. Evans, P. and D.W. Sheel, Photoactive and antibacterial TiO_2 thin films on stainless steel. Surface & Coatings Technology, 2007. 201(22-23): pages 9319-9324.
9. Cheng, H.E., W.J. Lee, C.M. Hsu, M.H. Hon, and C.L. Huang, Visible light activity of nitrogen-doped TiO_2 thin films grown by atomic layer deposition. Electrochemical and Solid State Letters, 2008. 11(10): pages D81-D84.
10. Kaariainen, M.L. and D.C. Cameron, The importance of the majority carrier polarity and p-n junction in titanium dioxide films to their photoactivity and photocatalytic properties. Surface Science, 2012. 606(3-4): pages L22-L25.
11. Lee, W.J. and M.H. Hon, Space limited crystal growth mechanism of TiO_2 films by Atomic Layer Deposition. Journal of Physical Chemistry C, 2010. 114(15): pages 6917-6921.
12. Reyes-Coronado, D., G. Rodriguez-Gattorno, M.E. Espinosa-Pesqueira, C. Cab, R. de Coss, and G. Oskam, Phase-pure TiO_2 nanoparticles: anatase, brookite and rutile. Nanotechnology, 2008. 19(14): p. 145605-145615.
13. Fujishima, A. and K. Honda, Electrochemical photolysis of water at a semiconductor electrode. Nature, 1972. 238(5358): pages 37-38.
14. Frank, S.N. and A.J. Bard, Heterogeneous photocatalytic oxidation of cyanide ion in aqueous solutions at TiO_2 powder. Journal of the American Chemical Society, 1977. 99(1): pages 303-304.
15. Frank, S.N. and A.J. Bard, Semiconductor electrodes. 12. Photoassisted oxidations and photoelectrosynthesis at polycrystalline TiO_2 electrodes. Journal of the American Chemical Society, 1977. 99(14): pages 4667-4675.
16. Mills, A., A. Lepre, N. Elliott, S. Bhopal, I.P. Parkin, and S.A. O'Neill, Characterisation of the photocatalyst Pilkington Activ (TM): a reference film photocatalyst? Journal of Photochemistry and Photobiology a-Chemistry, 2003. 160(3): pages 213-224.
17. Ohtani, B., O.O. Prieto-Mahaney, D. Li, and R. Abe, What is Degussa (Evonik) P25? Crystalline composition analysis, reconstruction from isolated pure particles and photocatalytic activity test. Journal of Photochemistry and Photobiology a-Chemistry, 2010. 216(2-3): pages 179-182.

18. Rehman, S., R. Ullah, A.M. Butt, and N.D. Gohar, Strategies of making TiO_2 and ZnO visible light active. Journal of Hazardous Materials, 2009. 170(2-3): pages 560-569.
19. Quesada-Cabrera, R., C. Sotelo-Vazqueza, M. Quesada-Gonzalez, E.P. Melian, N. Chadwick, and I.P. Parkin, On the apparent visible-light and enhanced UV-light photocatalytic activity of nitrogen-doped TiO_2 thin films. Journal of Photochemistry and Photobiology a-Chemistry, 2017. 333: pages 49-55.
20. Zhou, Y., C.H. Chen, N.N. Wang, Y.Y. Li, and H.M. Ding, Stable Ti^{3+} self-doped anatase rutile mixed TiO2 with enhanced visible light utilization and durability. Journal of Physical Chemistry C, 2016. 120(11): pages 6116-6124.
21. Yadav, H.M., S.V. Otari, V.B. Koli, S.S. Mali, C.K. Hong, S.H. Pawar, and S.D. Delekar, Preparation and characterization of copper-doped anatase TiO_2 nanoparticles with visible light photocatalytic antibacterial activity. Journal of Photochemistry and Photobiology a-Chemistry, 2014. 280: pages 32-38.
22. Wu, Q., J.J. Ouyang, K.P. Xiea, L. Sun, M.Y. Wang, and C.J. Lin, Ultrasound-assisted synthesis and visible-light-driven photocatalytic activity of Fe-incorporated TiO_2 nanotube array photocatalysts. Journal of Hazardous Materials, 2012. 199: pages 410-417.
23. El -Sheikh, S.M., T.M. Khedr, A. Hakki, A.A. Ismail, W.A. Badawy, and D.W. Bahnemann, Visible light activated carbon and co-doped mesoporous TiO_2 as efficient photocatalyst for degradation of ibuprofen. Separation and Purification Technology, 2017. 173: pages 258-268.
24. Bandaranayake, K.M.P., M.K.I. Senevirathna, P. Weligamuwa, and K. Tennakone, Dye-sensitized solar cells made from nanocrystalline TiO_2 films coated with outer layers of different oxide materials. Coordination Chemistry Reviews, 2004. 248(13-14): pages 1277-1281.
25. Tricoli, A., M. Righettoni, and S.E. Pratsinis, Anti-fogging nanofibrous SiO_2 and nanostructured SiO_2-TiO_2 films made by Rapid Flame Deposition and In Situ Annealing. Langmuir, 2009. 25(21): pages 12578-12584.

26. Jang, H.D., S.K. Kim, H. Chang, K.-M. Roh, J.-W. Choi, and J. Huang, A glucose biosensor based on TiO_2-Graphene composite. Biosensors & Bioelectronics, 2012. 38(1): pages 184-188.
27. Hitosugi, T., N. Yamada, S. Nakao, Y. Hirose, and T. Hasegawa, Properties of TiO_2 based transparent conducting oxides. Physica Status Solidi a-Applications and Materials Science, 2010. 207(7): pages 1529-1537.
28. Raulio, M., V. Pore, S. Areva, M. Ritala, M. Leskela, M. Linden, J.B. Rosenholm, K. Lounatmaa, and M. Salkinoja-Salonen, Destruction of Deinococcus geothermalis biofilm by photocatalytic ALD and sol-gel TiO_2 surfaces. Journal of Industrial Microbiology & Biotechnology, 2006. 33(4): pages 261-268.
29. Chabas, A., L. Gentaz, T. Lombardo, R. Sinegre, R. Falcone, M. Verita, and H. Cachier, Wet and dry atmospheric deposition on TiO_2 coated glass. Environmental Pollution, 2010. 158(12): pages 3507-3512.
30. Etacheri, V., C. Di Valentin, J. Schneider, D. Bahnemann, and S.C. Pillai, Visible-light activation of TiO_2 photocatalysts: Advances in theory and experiments. Journal of Photochemistry and Photobiology C-Photochemistry Reviews, 2015. 25: pages 1-29.
31. Scholes, G.D. and G. Rumbles, Excitons in nanoscale systems (vol 5, pg 683, 2006). Nature Materials, 2006. 5(11): pages 920-920.
32. Daimon, T., T. Hirakawa, M. Kitazawa, J. Suetake, and Y. Nosaka, Formation of singlet molecular oxygen associated with the formation of superoxide radicals in aqueous suspensions of TiO_2 photocatalysts. Applied Catalysis a-General, 2008. 340(2): pages 169-175.
33. Mills, G. and M.R. Hoffmann, Photocatalytic degradation of pentachlorophenol on TiO_2 particles - Identification of intermediates and mechanism of reaction. Environmental Science & Technology, 1993. 27(8): pages 1681-1689.
34. Bonch-Bruevich, V.L. and E.G. Landsberg, Recombination mechanisms. Physica Status Solidi, 1968. 29(1): pages 9-43.

35. Reddy, K.M., S.V. Manorama, and A.R. Reddy, Bandgap studies on anatase titanium dioxide nanoparticles. Materials Chemistry and Physics, 2003. 78(1): pages 239-245.

36. Posternak, M., A. Baldereschi, E.J. Walter, and H. Krakauer, Wannier functions and Born charge tensors of brookite TiO_2. Physical Review B, 2006. 74(12): pages 125113-125118.

37. Zhang, J.F., P. Zhou, J.J. Liu, and J.G. Yu, New understanding of the difference of photocatalytic activity among anatase, rutile and brookite TiO_2. Physical Chemistry Chemical Physics, 2014. 16(38): pages 20382-20386.

38. Chen, X. and S.S. Mao, Titanium dioxide nanomaterials: Synthesis, properties, modifications, and applications. Chemical Reviews, 2007. 107(7): pages 2891-2959.

39. Sclafani, A. and J.M. Herrmann, Comparison of the photoelectronic and photocatalytic activities of various anatase and rutile forms of titania in pure liquid organic phases and in aqueous solutions. Journal of Physical Chemistry, 1996. 100(32): pages 13655-13661.

40. He, J., R.K. Behera, M.W. Finnis, X. Li, E.C. Dickey, S.R. Phillpot, and S.B. Sinnott, Prediction of high-temperature point defect formation in TiO_2 from combined ab initio and thermodynamic calculations. Acta Materialia, 2007. 55(13): pages 4325-4337.

41. Hossain, F.M., G.E. Murch, L. Sheppard, and J. Nowotny, Reactivity of ideal and defected rutile TiO_2 (110) surface with oxygen. Advances in Applied Ceramics, 2007. 106(1-2): pages 95-100.

42. Peng, S.Q., Y.X. Li, F.Y. Jiang, G.X. Lu, and S.B. Li, Effect of Be^{2+} doping TiO_2 on its photocatalytic activity. Chemical Physics Letters, 2004. 398(1-3): pages 235-239.

43. Shao, G., Red shift in manganese- and iron-doped TiO_2: A DFT+U analysis. Journal of Physical Chemistry C, 2009. 113(16): pages 6800-6808.

44. Nowotny, J., Titanium dioxide-based semiconductors for solar-driven environmentally friendly applications: impact of point defects on performance. Energy & Environmental Science, 2008. 1(5): pages 565-572.

45. Choi, W.Y., A. Termin, and M.R. Hoffmann, The role of metal ion dopants in quantum sized TiO_2 - correlation between photoreactivity and charge carrier recombination dynamics. Journal of Physical Chemistry, 1994. 98(51): pages 13669-13679.

46. Serpone, N., Relative photonic efficiencies and quantum yields in heterogeneous photocatalysis. Journal of Photochemistry and Photobiology a-Chemistry, 1997. 104(1-3): pages 1-12.

47. Schneider, J., M. Matsuoka, M. Takeuchi, J. Zhang, Y. Horiuchi, M. Anpo, and D.W. Bahnemann, Understanding TiO_2 photocatalysis: Mechanisms and materials. Chemical Reviews, 2014. 114(19): pages 9919-9986.

48. Ollis, D.F., C.Y. Hsiao, L. Budiman, and C.L. Lee, Heterogeneous photoassisted catalysis - Conversions of perchloroethylene, dicholroethane, chloroacetic acids and chlorobenzenes. Journal of Catalysis, 1984. 88(1): pages 89-96.

49. Turchi, C.S. and D.F. Ollis, Mixed reactant photocatalysis - intermediates and mutual rate inhibition. Journal of Catalysis, 1989. 119(2): pages 483-496.

50. Hoffman, A.J., E.R. Carraway, and M.R. Hoffmann, Photocatalytic production of H_2O_2 and organic peroxides on quantum sized semiconductor colloids. Environmental Science & Technology, 1994. 28(5): pages 776-785.

51. Sakai, H., R. Baba, K. Hashimoto, A. Fujishima, and A. Heller, Local detection of photoelectrochemically produced H_2O_2 with a wired horseradish peroxidase microsensor. Journal of Physical Chemistry, 1995. 99(31): pages 11896-11900.

52. Ranjit, K.T., I. Willner, S.H. Bossmann, and A.M. Braun, Lanthanide oxide-doped titanium dioxide photocatalysts: Novel photocatalysts for the enhanced degradation of p-chlorophenoxyacetic acid. Environmental Science & Technology, 2001. 35(7): pages 1544-1549.

53. Nosaka, Y., T. Daimon, A.Y. Nosaka, and Y. Murakami, Singlet oxygen formation in photocatalytic TiO_2 aqueous suspension. Physical Chemistry Chemical Physics, 2004. 6(11): pages 2917-2918.

54. Ali, A.M., E.A.C. Emanuelsson, and D.A. Patterson, Photocatalysis with nanostructured zinc oxide thin films: The relationship between morphology

and photocatalytic activity under oxygen limited and oxygen rich conditions and evidence for a Mars Van Krevelen mechanism. Applied Catalysis B-Environmental, 2010. 97(1-2): pages 168-181.

55. Muggli, D.S. and J.L. Falconer, Role of lattice oxygen in photocatalytic oxidation on TiO_2. Journal of Catalysis, 2000. 191(2): p. 318-325.

56. Lee, G.D. and J.L. Falconer, Transient measurements of lattice oxygen in photocatalytic decomposition of formic acid on TiO_2. Catalysis Letters, 2000. 70(3-4): pages 145-148.

57. Chakrabarti, S. and B.K. Dutta, Photocatalytic degradation of model textile dyes in wastewater using ZnO as semiconductor catalyst. Journal of Hazardous Materials, 2004. 112(3): pages 269-278.

58. Etacheri, V., R. Roshan, and V. Kumar, Mg-doped ZnO nanoparticles for efficient sunlight driven photocatalysis. Acs Applied Materials & Interfaces, 2012. 4(5): pages 2717-2725.

59. Wu, D., M. Long, W. Cai, C. Chen, and Y. Wu, Low temperature hydrothermal synthesis of N-doped TiO_2 photocatalyst with high visible-light activity. Journal of Alloys and Compounds, 2010. 502(2): pages 289-294.

60. Moser, J., S. Punchihewa, P.P. Infelta, and M. Gratzel, Surface complexation of colloidal semiconductors strongly enhances interfacial electron-transfer rates. Langmuir, 1991. 7(12): pages 3012-3018.

61. Kormann, C., D.W. Bahnemann, and M.R. Hoffmann, Photolysis of chloroform and other organic molecules in aqueous TiO_2 suspensions. Environmental Science & Technology, 1991. 25(3): pages 494-500.

62. Petrik, N.G. and G.A. Kimmel, Reaction kinetics of water molecules with oxygen vacancies on rutile TiO_2 (110). Journal of Physical Chemistry C, 2015. 119(40): pages 23059-23067.

63. Sunada, K., T. Watanabe, and K. Hashimoto, Studies on photokilling of bacteria on TiO_2 thin film. Journal of Photochemistry and Photobiology a-Chemistry, 2003. 156(1-3): pages 227-233.

64. Takeuchi, M., K. Sakamoto, G. Martra, S. Coluccia, and M. Anpo, Mechanism of photoinduced superhydrophilicity on the TiO_2 photocatalyst surface. Journal of Physical Chemistry B, 2005. 109(32): pages 15422-15428.

65. Mills, A., N. Elliott, I.P. Parkin, S.A. O'Neill, and R.J.H. Clark, Novel TiO_2 CVD films for semiconductor photocatalysis. Journal of Photochemistry and Photobiology a-Chemistry, 2002. 151(1-3): pages 171-179.

66. Rengifo-Herrera, J.A. and C. Pulgarin, Photocatalytic activity of N, S co-doped and N-doped commercial anatase TiO_2 powders towards phenol oxidation and E.coli inactivation under simulated solar light irradiation. Solar Energy, 2010. 84(1): pages 37-43.

67. Byrne, J.A., P.A. Fernandez-Ibanez, P.S.M. Dunlop, D.M.A. Alrousan, and J.W.J. Hamilton, Photocatalytic enhancement for solar disinfection of water: A review. International Journal of Photoenergy, 2011: pages 1-12.

68. Fisher, M.B., D.A. Keane, P. Fernandez-Ibanez, J. Colreavy, S.J. Hinder, K.G. McGuigan, and S.C. Pillai, Nitrogen and copper doped solar light active TiO_2 photocatalysts for water decontamination. Applied Catalysis B-Environmental, 2013. 130: pages 8-13.

69. Podporska-Carroll, J., E. Panaitescu, B. Quilty, L. Wang, L. Menon, and S.C. Pillai, Antimicrobial properties of highly efficient photocatalytic TiO_2 nanotubes. Applied Catalysis B-Environmental, 2015. 176: pages 70-75.

70. Matsunaga, T., R. Tomoda, T. Nakajima, and H. Wake, Photoelectrochemical sterilization of microbial-cells by semiconductor powders. Fems Microbiology Letters, 1985. 29(1-2): pages 211-214.

71. Matsunaga, T., R. Tomoda, T. Nakajima, N. Nakamura, and T. Komine, Continuous sterilization system that uses photosemiconductor powders. Applied and Environmental Microbiology, 1988. 54(6): pages 1330-1333.

72. Kubacka, A., M.J. Munoz-Batista, M. Ferrer, and M. Fernandez-Garcia, UV and visible light optimization of anatase TiO_2 antimicrobial properties: Surface deposition of metal and oxide (Cu, Zn, Ag) species. Applied Catalysis B-Environmental, 2013. 140: pages 680-690.

73. Kubacka, A., M.S. Diez, D. Rojo, R. Bargiela, S. Ciordia, I. Zapico, J.P. Albar, C. Barbas, V.A.P.M. dos Santos, M. Fernandez-Garcia, and M. Ferrer,

Understanding the antimicrobial mechanism of TiO_2-based nanocomposite films in a pathogenic bacterium. Scientific Reports, 2014. 4: pages 1-10.

74. Kambala, V.S.R. and R. Naidu, Disinfection studies on TiO_2 thin films prepared by a sol-gel method. Journal of Biomedical Nanotechnology, 2009. 5(1): pages 121-129.
75. Foster, H.A., I.B. Ditta, S. Varghese, and A. Steele, Photocatalytic disinfection using titanium dioxide: spectrum and mechanism of antimicrobial activity. Applied Microbiology and Biotechnology, 2011. 90(6): pages 1847-1868.
76. Maness, P.C., S. Smolinski, D.M. Blake, Z. Huang, E.J. Wolfrum, and W.A. Jacoby, Bactericidal activity of photocatalytic TiO_2 reaction: Toward an understanding of its killing mechanism. Applied and Environmental Microbiology, 1999. 65(9): pages 4094-4098.
77. Hu, C., J. Guo, J. Qu, and X. Hu, Photocatalytic degradation of pathogenic bacteria with AgI/TiO_2 under visible light irradiation. Langmuir, 2007. 23(9): pages 4982-4987.
78. Gogniat, G., M. Thyssen, M. Denis, C. Pulgarin, and S. Dukan, The bactericidal effect of TiO_2 photocatalysis involves adsorption onto catalyst and the loss of membrane integrity. Fems Microbiology Letters, 2006. 258(1): pages 18-24.
79. Saito, T., T. Iwase, J. Horie, and T. Morioka, Mode of photocatalytic bactericidal action of powdered semiconductor TiO_2 on mutans streptococci. Journal of Photochemistry and Photobiology B-Biology, 1992. 14(4): pages 369-379.
80. Nadtochenko, V.A., A.G. Rincon, S.E. Stanca, and J. Kiwi, Dynamics of E.coli membrane cell peroxidation during TiO_2 photocatalysis studied by ATR-FTIR spectroscopy and AFM microscopy. Journal of Photochemistry and Photobiology a-Chemistry, 2005. 169(2): pages 131-137.
81. Nadtochenko, V., N. Denisov, O. Sarkisov, D. Gumy, C. Pulgarin, and J. Kiwi, Laser kinetic spectroscopy of the interfacial charge transfer between membrane cell walls of E.coli and TiO_2. Journal of Photochemistry and Photobiology a-Chemistry, 2006. 181(2-3): pages 401-407.

82. Nadtochenko, V.A., O.M. Sarkisov, V.V. Nikandrov, P.A. Chubukov, and N.N. Denisov, Inactivation of pathogenic microorganisms in the photocatalytic process on nanosized TiO_2 crystals. Russian Journal of Physical Chemistry B, 2008. 2(1): pages 105-114.

83. Brown, L., J.M. Wolf, R. Prados-Rosales, and A. Casadevall, Through the wall: extracellular vesicles in gram-positive bacteria, mycobacteria and fungi. Nature Reviews Microbiology, 2015. 13(10): pages 620-630.

84. Shah, R.R., S. Kaewgun, B.I. Lee, and T.-R.J. Tzeng, The antibacterial effects of biphasic brookite-anatase titanium dioxide nanoparticles on multiple-drug-resistant Staphylococcus aureus. Journal of Biomedical Nanotechnology, 2008. 4(3): pages 339-348.

85. Shah, R.R., S. Kaewgun, B.I. Lee, and T.r.J. Tzeng, The antibacterial effects of visible light activated titanium dioxide nanoparticles on Escherichia coli and Staphylococcus aureus. Abstracts of the General Meeting of the American Society for Microbiology, 2008. 108: pages 1-16.

86. Chung, C.-J., H.-I. Lin, C.-M. Chou, P.-Y. Hsieh, C.-H. Hsiao, Z.-Y. Shi, and J.-L. He, Inactivation of Staphylococcus aureus and Escherichia coli under various light sources on photocatalytic titanium dioxide thin film. Surface & Coatings Technology, 2009. 203(8): pages 1081-1085.

87. Gartner, M., C. Anastasescu, M. Zaharescu, M. Enache, L. Dumitru, T. Stoica, T.F. Stoica, and C. Trapalis. The simulation in the real conditions of antibacterial activity of TiO_2Fe films with optimized morphology. in 32nd International Conference on Advanced Ceramics and Composites. 2008. Daytona Beach, FL.

88. Vacaroiu, C., M. Enache, M. Gartner, G. Popescu, M. Anastasescu, A. Brezeanu, N. Todorova, T. Giannakopoulou, C. Trapalis, and L. Dumitru, The effect of thermal treatment on antibacterial properties of nanostructured TiO_2(N) films illuminated with visible light. World Journal of Microbiology & Biotechnology, 2009. 25(1): pages 27-31.

89. Barnes, R.J., R. Molina, J. Xu, P.J. Dobson, and I.P. Thompson, Comparison of TiO_2 and ZnO nanoparticles for photocatalytic degradation of methylene

blue and the correlated inactivation of gram-positive and gram-negative bacteria. Journal of Nanoparticle Research, 2013. 15(2): pages 1-11.

90. Lee, Y.W., H.D. Yoon, J.H. Park, and U.C. Ryu, Application of 265 nm UVC LED lighting to sterilization of typical gram negative and positive bacteria. Journal of the Korean Physical Society, 2018. 72(10): pages 1174-1178.
91. Fox, M.A. and M.T. Dulay, Heterogeneous photocatalysis. Chemical Reviews, 1993. 93(1): pages 341-357.
92. Linsebigler, A.L., G.Q. Lu, and J.T. Yates, Photocatalysis on TiO_2 surfaces - Principles, mechanisms and selected results. Chemical Reviews, 1995. 95(3): pages 735-758.
93. Muruganandham, M. and M. Swaminathan, Solar photocatalytic degradation of a reactive azo dye in TiO_2-suspension. Solar Energy Materials and Solar Cells, 2004. 81(4): pages 439-457.
94. Etacheri, V., G. Michlits, M.K. Seery, S.J. Hinder, and S.C. Pillai, A highly efficient $TiO_{2-x}C_x$ nano-heterojunction photocatalyst for visible light induced antibacterial applications. Acs Applied Materials & Interfaces, 2013. 5(5): pages 1663-1672.
95. Zhang, J. and Y. Nosaka, Mechanism of the OH radical generation in photocatalysis with TiO_2 of different crystalline types. Journal of Physical Chemistry C, 2014. 118(20): pages 10824-10832.
96. Etacheri, V., M.K. Seery, S.J. Hinder, and S.C. Pillai, Highly visible light active $TiO_{2-x}N_x$ heterojunction photocatalysts. Chemistry of Materials, 2010. 22(13): pages 3843-3853.
97. Balasubramanian, G., D.D. Dionysiou, M.T. Suidan, I. Baudin, B. Audin, and J.M. Laine, Evaluating the activities of immobilized TiO_2 powder films for the photocatalytic degradation of organic contaminants in water. Applied Catalysis B-Environmental, 2004. 47(2): pages 73-84.
98. Nakajima, H., T. Mori, Q. Shen, and T. Toyoda, Photoluminescence study of mixtures of anatase and rutile TiO_2 nanoparticles: Influence of charge transfer between the nanoparticles on their photo luminescence excitation bands. Chemical Physics Letters, 2005. 409(1-3): pages 81-84.

99. Miyagi, T., M. Kamei, T. Mitsuhashi, T. Ishigaki, and A. Yamazaki, Charge separation at the rutile/anatase interface: a dominant factor of photocatalytic activity. Chemical Physics Letters, 2004. 390(4-6): pages 399-402.

100. Kohan, A.F., G. Ceder, D. Morgan, and C.G. Van de Walle, First-principles study of native point defects in ZnO. Physical Review B, 2000. 61(22): pages 15019-15027.

101. Van de Walle, C.G., Defect analysis and engineering in ZnO. Physica B-Condensed Matter, 2001. 308: pages 899-903.

102. Ozgur, U., Y.I. Alivov, C. Liu, A. Teke, M.A. Reshchikov, S. Dogan, V. Avrutin, S.J. Cho, and H. Morkoc, A comprehensive review of ZnO materials and devices. Journal of Applied Physics, 2005. 98(4): pages 041301-041404.

103. Sheppard, L.R., M.K. Nowotny, T. Bak, and J. Nowotny, Effect of cooling on electrical conductivity of TiO_2. Physica Status Solidi B-Basic Solid State Physics, 2008. 245(9): pages 1816-1827.

104. Varley, J.B., A. Janotti, C. Franchini, and C.G. Van de Walle, Role of self-trapping in luminescence and p-type conductivity of wide-band-gap oxides. Physical Review B, 2012. 85(8): pages 081101-081109.

105. Pan, X., M.-Q. Yang, X. Fu, N. Zhang, and Y.-J. Xu, Defective TiO_2 with oxygen vacancies: synthesis, properties and photocatalytic applications. Nanoscale, 2013. 5(9): pages 3601-3614.

106. Won, S., S. Go, W. Lee, K. Jeong, H. Jung, C. Lee, E. Lee, and J. Lee, Effects of defects generated in ALD TiO_2 films on electrical properties and interfacial reaction in $TiO_2/SiO_2/Si$ system upon annealing in vacuum. Metals and Materials International, 2008. 14(6): pages 759-765.

107. Kong, M., Y. Li, X. Chen, T. Tian, P. Fang, F. Zheng, and X. Zhao, Tuning the relative concentration ratio of bulk defects to surface defects in TiO_2 nanocrystals leads to high photocatalytic efficiency. Journal of the American Chemical Society, 2011. 133(41): pages 16414-16417.

108. Wang, Q.L., O.K. Varghese, C.A. Grimes, and E.C. Dickey, Grain boundary blocking and segregation effects in yttrium-doped polycrystalline titanium dioxide. Solid State Ionics, 2007. 178(3-4): pages 187-194.

109. Nowotny, J., T. Bak, T. Burg, M.K. Nowotny, and L.R. Sheppard, Effect of grain boundaries on semiconducting properties of TiO_2 at elevated temperatures. Journal of Physical Chemistry C, 2007. 111(27): pages 9769-9778.

110. Shannon, R.D. and J.A. Pask, Kinetics of anatase-rutile transformation. Journal of the American Ceramic Society, 1965. 48(8): pages 391-398.

111. Etacheri, V., M.K. Seery, S.J. Hinder, and S.C. Pillai, Oxygen rich titania: A dopant free, high temperature stable and visible light active anatase photocatalyst. Advanced Functional Materials, 2011. 21(19): pages 3744-3752.

112. Zhao, L., X. Zhao, J. Liu, A. Zhang, D. Wang, and B. Wei, Fabrications of Nb-doped TiO_2 (TNO) transparent conductive oxide polycrystalline films on glass substrates by sol-gel method. Journal of Sol-Gel Science and Technology, 2010. 53(2): pages 475-479.

113. Saha, D., R.S. Ajimsha, K. Rajiv, C. Mukherjee, M. Gupta, P. Misra, and L.M. Kukreja, Spectroscopic ellipsometry characterization of amorphous and crystalline TiO_2 thin films grown by atomic layer deposition at different temperatures. Applied Surface Science, 2014. 315: pages 116-123.

114. Kruger, P., S. Bourgeois, B. Domenichini, H. Magnan, D. Chandesris, P. Le Fevre, A.M. Flank, J. Jupille, L. Floreano, A. Cossaro, A. Verdini, and A. Morgante, Defect states at the TiO_2 (110) surface probed by resonant photoelectron diffraction. Physical Review Letters, 2008. 100(5): pages 055501-055504.

115. Jin, C.Y., B. Liu, Z.X. Lei, and J.M. Sun, Structure and photoluminescence of the TiO2 films grown by atomic layer deposition using tetrakis-dimethylamino titanium and ozone. Nanoscale Research Letters, 2015. 10: pages 1-27.

116. Mathew, S., A.K. Prasad, T. Benoy, P.P. Rakesh, M. Hari, T.M. Libish, P. Radhakrishnan, V.P.N. Nampoori, and C.P.G. Vallabhan, UV-visible photoluminescence of TiO_2 nanoparticles prepared by hydrothermal method. Journal of Fluorescence, 2012. 22(6): pages 1563-1569.

117. Abazovic, N.D., M.I. Comor, M.D. Dramicanin, D.J. Jovanovic, S.P. Ahrenkiel, and J.M. Nedeljkovic, Photoluminescence of anatase and rutile TiO_2 particles. Journal of Physical Chemistry B, 2006. 110(50): pages 25366-25370.

118. Deak, P., B. Aradi, and T. Frauenheim, Oxygen deficiency in TiO_2: Similarities and differences between the Ti self-interstitial and the O vacancy in bulk rutile and anatase. Physical Review B, 2015. 92(4): pages 045204-045210.

119. Nakamura, I., N. Negishi, S. Kutsuna, T. Ihara, S. Sugihara, and E. Takeuchi, Role of oxygen vacancy in the plasma-treated TiO_2 photocatalyst with visible light activity for NO removal. Journal of Molecular Catalysis a-Chemical, 2000. 161(1-2): pages 205-212.

120. Liu, G., F. Li, D.-W. Wang, D.-M. Tang, C. Liu, X. Ma, G.Q. Lu, and H.-M. Cheng, Electron field emission of a nitrogen-doped TiO_2 nanotube array. Nanotechnology, 2008. 19(2): pages 025606-025612.

121. Bak, T., M.K. Nowotny, L.R. Sheppard, and J. Nowotny, Effect of prolonged oxidation on semiconducting properties of titanium dioxide. Journal of Physical Chemistry C, 2008. 112(34): pages 13248-13257.

122. von Oertzen, G.U. and A.R. Gerson, The effects of O deficiency on the electronic structure of rutile TiO_2. Journal of Physics and Chemistry of Solids, 2007. 68(3): pages 324-330.

123. Morgan, B.J. and G.W. Watson, Intrinsic n-type defect formation in TiO_2: A comparison of rutile and anatase from GGA plus U calculations. Journal of Physical Chemistry C, 2010. 114(5): pages 2321-2328.

124. Naldoni, A., M. Allieta, S. Santangelo, M. Marelli, F. Fabbri, S. Cappelli, C.L. Bianchi, R. Psaro, and V. Dal Santo, Effect of nature and location of defects on bandgap narrowing in black TiO_2 nanoparticles. Journal of the American Chemical Society, 2012. 134(18): pages 7600-7603.

125. Schaub, R., P. Thostrup, N. Lopez, E. Laegsgaard, I. Stensgaard, J.K. Norskov, and F. Besenbacher, Oxygen vacancies as active sites for water dissociation on rutile TiO_2 (110). Physical Review Letters, 2001. 87(26): pages 1-4.

126. Muhich, C.L., Y. Zhou, A.M. Holder, A.W. Weimer, and C.B. Musgrave, Effect of surface deposited Pt on the photoactivity of TiO_2. Journal of Physical Chemistry C, 2012. 116(18): pages 10138-10149.

127. Lira, E., S. Wendt, P. Huo, J.O. Hansen, R. Streber, S. Porsgaard, Y. Wei, R. Bechstein, E. Laegsgaard, and F. Besenbacher, The importance of bulk Ti^{3+} defects in the oxygen chemistry on titania surfaces. Journal of the American Chemical Society, 2011. 133(17): pages 6529-6532.

128. Zuo, F., L. Wang, T. Wu, Z. Zhang, D. Borchardt, and P. Feng, Self doped Ti^{3+} enhanced photocatalyst for hydrogen production under visible light. Journal of the American Chemical Society, 2010. 132(34): pages 11856-11857.

129. Wang, J., D.N. Tafen, J.P. Lewis, Z. Hong, A. Manivannan, M. Zhi, M. Li, and N. Wu, Origin of photocatalytic activity of nitrogen-doped TiO_2 nanobelts. Journal of the American Chemical Society, 2009. 131(34): pages 12290-12297.

130. Pan, X., N. Zhang, X. Fu, and Y.-J. Xu, Selective oxidation of benzyl alcohol over TiO_2 nanosheets with exposed {001} facets: Catalyst deactivation and regeneration. Applied Catalysis a-General, 2013. 453: pages 181-187.

131. Xie, T.-H. and J. Lin, Origin of photocatalytic deactivation of TiO_2 film coated on ceramic substrate. Journal of Physical Chemistry C, 2007. 111(27): pages 9968-9974.

132. Jing, L., B. Xin, F. Yuan, L. Xue, B. Wang, and H. Fu, Effects of surface oxygen vacancies on photophysical and photochemical processes of Zn-doped TiO_2 nanoparticles and their relationships. Journal of Physical Chemistry B, 2006. 110(36): pages 17860-17865.

133. Wang, G., H. Wang, Y. Ling, Y. Tang, X. Yang, R.C. Fitzmorris, C. Wang, J.Z. Zhang, and Y. Li, Hydrogen-treated TiO_2 nanowire arrays for photoelectrochemical water splitting. Nano Letters, 2011. 11(7): pages 3026-3033.

134. Zhuang, J., W. Dai, Q. Tian, Z. Li, L. Xie, J. Wang, P. Liu, X. Shi, and D. Wang, Photocatalytic degradation of RhB over TiO_2 bilayer films: Effect of defects and their location. Langmuir, 2010. 26(12): pages 9686-9694.

135. Kamat, P.V., Meeting the clean energy demand: Nanostructure architectures for solar energy conversion. Journal of Physical Chemistry C, 2007. 111(7): pages 2834-2860.

136. Oregan, B. and M. Gratzel, A low-cost, high efficiency solar cell based on dye sensitized colloidal TiO_2 films. Nature, 1991. 353(6346): pages 737-740.

137. Daneshvar, N., A. Niaei, S. Akbari, S. Aber, and N. Kazemian, Photocatalytic disinfection of water polluted by pseudomonas aeruginosa. Global Nest Journal, 2007. 9(2): pages 132-136.

138. Mohamed, A.E.R. and S. Rohani, Modified TiO_2 nanotube arrays (TNTAs): progressive strategies towards visible light responsive photoanode, a review. Energy & Environmental Science, 2011. 4(4): pages 1065-1086.

139. Li, X.Y., S.X. Wu, P. Hu, X.J. Xing, Y.J. Liu, Y.P. Yu, M. Yang, J.Q. Lu, S.W. Li, and W. Liu, Structures and magnetic properties of p-type Mn:TiO_2 dilute magnetic semiconductor thin films. Journal of Applied Physics, 2009. 106(4): pages 043913-043918.

140. Tong, H., S. Ouyang, Y. Bi, N. Umezawa, M. Oshikiri, and J. Ye, Nano-photocatalytic materials: Possibilities and challenges. Advanced Materials, 2012. 24(2): pages 229-251.

141. Zheleznov, V.V., E.I. Voit, Y.V. Sushkov, S.A. Sarin, V.G. Kuryavyi, D.P. Opra, S.V. Gnedenkov, S.L. Sinebryukhov, and A.A. Sokolov. Nanostructured microtubes based on TiO_2 doped by Zr and Hf oxides with the anatase structure. in 2nd International Symposium on Fundamental Aspects of Rare-Earth Elements Mining and Separation and Modern Materials Engineering (REES). 2015. Belokuriha, RUSSIA.

142. Shannon, R.D., Revised effective ionic radii and systematic studies of interatomic distances in halides and chalcogenides. Acta Crystallographica Section A, 1976. 32(SEP1): pages 751-767.

143. Otto, F., Y. Yang, H. Bei, and E.P. George, Relative effects of enthalpy and entropy on the phase stability of equiatomic high-entropy alloys. Acta Materialia, 2013. 61(7): pages 2628-2638.

144. Mizutani, U., Hume-Rothery rules for structurally complex alloy phases introduction. Hume-Rothery Rules for Structurally Complex Alloy Phases, 2011: pages 1-19.

145. Duan, Y.D., N.Q. Fu, Q.P. Liu, Y.Y. Fang, X.W. Zhou, J.B. Zhang, and Y. Lin, Sn-doped TiO_2 photoanode for Dye-Sensitized Solar Cells. Journal of Physical Chemistry C, 2012. 116(16): pages 8888-8893.

146. Niemela, J.-P., Y. Hirose, K. Shigematsu, M. Sano, T. Hasegawa, and M. Karppinen, Suppressed grain-boundary scattering in atomic layer deposited Nb:TiO_2 thin films. Applied Physics Letters, 2015. 107(19): pages 192102-192107.

147. Banerjee, S., D.D. Dionysiou, and S.C. Pillai, Self-cleaning applications of TiO_2 by photo-induced hydrophilicity and photocatalysis. Applied Catalysis B-Environmental, 2015. 176: pages 396-428.

148. Ollis, D.F., Photoreactors for purification and decontamination of air. Photocatalytic Purification and Treatment of Water and Air, 1993. 3: pages 481-494.

149. Koelsch, M., S. Cassaignon, C.T.T. Minh, J.F. Guillemoles, and J.P. Jolivet, Electrochemical comparative study of titania (anatase, brookite and rutile) nanoparticles synthesized in aqueous medium. Thin Solid Films, 2004. 451: pages 86-92.

150. Bharti, B., S. Kumar, H.N. Lee, and R. Kumar, Formation of oxygen vacancies and Ti^{3+} state in TiO_2 thin film and enhanced optical properties by air plasma treatment. Scientific Reports, 2016. 6: pages 1-13.

151. Emeline, A.V., Y. Furubayashi, X.T. Zhang, M. Jin, T. Murakami, and A. Fujishima, Photoelectrochemical behavior of Nb-doped TiO_2 electrodes. Journal of Physical Chemistry B, 2005. 109(51): pages 24441-24444.

152. Li, J.L., X.T. Xu, X.J. Liu, C.Y. Yu, D. Yan, Z. Sun, and L.K. Pan, Sn doped TiO_2 nanotube with oxygen vacancy for highly efficient visible light photocatalysis. Journal of Alloys and Compounds, 2016. 679: pages 454-462.

153. O'Rourke, C. and D.R. Bowler, Intrinsic oxygen vacancy and extrinsic aluminum dopant interplay: A route to the restoration of defective TiO_2. Journal of Physical Chemistry C, 2014. 118(14): pages 7261-7271.

154. Mohanty, P., N.C. Mishra, R.J. Choudhary, A. Banerjee, T. Shripathi, N.P. Lalla, S. Annapoorni, and C. Rath, Oxygen vacancy induced phase formation and room temperature ferromagnetism in undoped and Co-doped TiO_2 thin films. Journal of Physics D-Applied Physics, 2012. 45(32): pages 325301-325309.

155. Bloh, J.Z., R. Dillert, and D.W. Bahnemann, Designing optimal metal-doped photocatalysts: Correlation between photocatalytic activity, doping ratio, and particle size. Journal of Physical Chemistry C, 2012. 116(48): pages 25558-25562.

156. Wu, Q. and R. van de Krol, Selective photoreduction of nitric oxide to nitrogen by nanostructured TiO_2 photocatalysts: Role of oxygen vacancies and iron dopant. Journal of the American Chemical Society, 2012. 134(22): pages 9369-9375.

157. Periyat, P., S.C. Pillai, D.E. McCormack, J. Colreavy, and S.J. Hinder, Improved high-temperature stability and sun-light-driven photocatalytic activity of sulfur-doped anatase TiO_2. Journal of Physical Chemistry C, 2008. 112(20): pages 7644-7652.

158. Gamboa, J.A. and D.M. Pasquevich, Effect of chlorine atmosphere on the anatase rutile transformation. Journal of the American Ceramic Society, 1992. 75(11): pages 2934-2938.

159. Eppler, R.A., Effect of antimony oxide on the anatase-rutile transformation in titanium dioxide. Journal of the American Ceramic Society, 1987. 70(4): pages C64-C66.

160. Wu, N.L., M.S. Lee, Z.J. Pon, and J.Z. Hsu, Effect of calcination atmosphere on TiO_2 photocatalysis in hydrogen production from methanol/water solution. Journal of Photochemistry and Photobiology a-Chemistry, 2004. 163(1-2): pages 277-280.

161. Liao, M.C., H. Niu, and G.S. Chen, Effect of sputtering pressure and post-annealing on hydrophilicity of TiO_2 thin films deposited by reactive magnetron sputtering. Thin Solid Films, 2010. 518(24): pages 7258-7262.

162. Luka, G., B.S. Witkowski, L. Wachnicki, M. Andrzejczuk, M. Lewandowska, and M. Godlewski, Kinetics of anatase phase formation in TiO_2 films during atomic layer deposition and post-deposition annealing. Crystengcomm, 2013. 15(46): pages 9949-9954.

163. Choi, G.J., S.K. Kim, S.J. Won, H.J. Kim, and C.S. Hwang, Plasma-Enhanced Atomic Layer Deposition of TiO_2 and Al-doped TiO_2 films using N_2O and O_2 reactants. Journal of the Electrochemical Society, 2009. 156(9): pages G138-G143.

164. Kim, S.K., G.J. Choi, J.H. Kim, and C.S. Hwang, Growth behavior of Al-doped TiO_2 thin films by atomic layer deposition. Chemistry of Materials, 2008. 20(11): pages 3723-3727.

165. Kim, S.K., S.W. Lee, J.H. Han, B. Lee, S. Han, and C.S. Hwang, Capacitors with an equivalent oxide thickness of < 0.5 nm for nanoscale electronic semiconductor memory. Advanced Functional Materials, 2010. 20(18): pages 2989-3003.

166. Kim, S.K., G.J. Choi, and C.S. Hwang, Controlling the composition of doped materials by ALD: A case study for Al-doped TiO_2 films. Electrochemical and Solid State Letters, 2008. 11(7): pages G27-G29.

167. Navas, J., J.M. Iglesias-Arnaiz, C. Fernandez-Lorenzo, R. Alcantara, G. Blanco, D.M. De Los Santos, A. Sanchez-Coronilla, and J. Martin-Calleja, Synthesis and characterization of gel derived, highly Al-doped TiO_2 ($Al_xTi_{1-x}O_{2-x/2}$; x=0.083, 0.154, 0.2) nanoparticles: Improving the photocatalytic activity. Science of Advanced Materials, 2014. 6(10): pages 2134-2145.

168. de los Santos, D.M., T. Aguilar, A. Sanchez-Coronilla, J. Navas, N. Cruz Hernandez, R. Alcantara, C. Fernandez-Lorenzo, and J. Martin-Calleja, Electronic and structural properties of highly aluminum ion doped TiO_2 nanoparticles: A combined experimental and theoretical study. Chemphyschem, 2014. 15(11): pages 2267-2280.

169. Liu, S., G. Liu, and Q. Feng, Al-doped TiO_2 mesoporous materials: synthesis and photodegradation properties. Journal of Porous Materials, 2010. 17(2): pages 197-206.

170. Murashkina, A.A., P.D. Murzin, A.V. Rudakova, V.K. Ryabchuk, A.V. Emeline, and D.W. Bahnemann, Influence of the dopant concentration on the photocatalytic activity: Al-Doped TiO_2. Journal of Physical Chemistry C, 2015. 119(44): pages 24695-24703.

171. Gesenhues, U., Al-doped TiO_2 pigments: influence of doping on the photocatalytic degradation of alkyd resins. Journal of Photochemistry and Photobiology a-Chemistry, 2001. 139(2-3): pages 243-251.

172. Maeda, M. and T. Yamada. Photocatalytic activity of metal-doped titanium oxide films prepared by sol-gel process. in International Conference on Nanoscience and Technology. 2006. Basel, SWITZERLAND.

173. Paulauskas, I.E., D.R. Modeshia, T.T. Ali, E.H. El-Mossalamy, A.Y. Obaid, S.N. Basahel, A.A. Al-Ghamdi, and F.K. Sartain, Photocatalytic activity of doped and undoped titanium dioxide nanoparticles synthesised by flame spray pyrolysis platinum-doped TiO_2 composites show improved activity compared to commercially available product. Platinum Metals Review, 2013. 57(1): pages 32-43.

174. Tsai, C.-Y., T.-H. Kuo, and H.-C. Hsi, Fabrication of Al-doped TiO_2 visible light photocatalyst for low concentration mercury removal. International Journal of Photoenergy, 2012: pages 639-648.

175. Chandiran, A.K., N. Tetreault, R. Humphry-Baker, F. Kessler, E. Baranoff, C.Y. Yi, M.K. Nazeeruddin, and M. Gratzel, Subnanometer Ga_2O_3 tunnelling layer by Atomic Layer Deposition to achieve 1.1 V open-circuit potential in Dye-Sensitized Solar Cells. Nano Letters, 2012. 12(8): pages 3941-3947.

176. Reddy, L.S., Y.H. Ko, and J.S. Yu, Hydrothermal synthesis and photocatalytic property of beta-Ga_2O_3 nanorods. Nanoscale Research Letters, 2015. 10: pages 1-7.

177. Banerjee, A.N., S.W. Joo, and B.-K. Min, Photocatalytic degradation of organic dye by sol-gel-derived gallium-doped anatase titanium oxide

nanoparticles for environmental remediation. Journal of Nanomaterials, 2012: pages 1-14.

178. Liu, X., M. Khan, W. Liu, W. Xiang, M. Guan, P. Jiang, and W. Cao, Synthesis of nanocrystalline Ga-TiO_2 powders by mild hydrothermal method and their visible light photoactivity. Ceramics International, 2015. 41(2): pages 3075-3080.

179. Umare, S.S., A. Charanpahari, and R. Sasikala, Enhanced visible light photocatalytic activity of Ga, N and S codoped TiO_2 for degradation of azo dye. Materials Chemistry and Physics, 2013. 140(2-3): pages 529-534.

180. Zhou, J.K., Y.X. Zhang, X.S. Zhao, and A.K. Ray, Photodegradation of benzoic acid over metal-doped TiO_2. Industrial & Engineering Chemistry Research, 2006. 45(10): pages 3503-3511.

181. Ranjit, K.T. and B. Viswanathan, Synthesis, characterization and photocatalytic properties of iron-doped TiO_2 catalysts. Journal of Photochemistry and Photobiology a-Chemistry, 1997. 108(1): pages 79-84.

182. Fang, Q., J.Y. Zhang, Z.M. Wang, J.X. Wu, B.J. O'Sullivan, P.K. Hurley, T.L. Leedham, H. Davies, M.A. Audier, C. Jimenez, J.P. Senateur, and I.W. Boyd, Investigation of TiO_2-doped HfO_2 thin films deposited by photo-CVD. Thin Solid Films, 2003. 428(1-2): pages 263-268.

183. Pan, J.W., C. Li, Y.F. Zhao, R.X. Liu, Y.Y. Gong, L.Y. Niu, X.J. Liu, and B.Q. Chi, Electronic properties of TiO_2 doped with Sc, Y, La, Zr, Hf, V, Nb and Ta. Chemical Physics Letters, 2015. 628: pages 43-48.

184. Li, C., Y.F. Zhao, Y.Y. Gong, T. Wang, and C.Q. Sun, Band gap engineering of early transition-metal-doped anatase TiO_2: first principles calculations. Physical Chemistry Chemical Physics, 2014. 16(39): pages 21446-21451.

185. Meng, X.Y., L. Wang, D.Y. Liu, X.H. Wen, Q. Zhu, W.A. Goddard, and Q. An, Discovery of Fe_2 P-Type $Ti(Zr/Hf)_2O_6$ Photocatalysts toward Water Splitting. Chemistry of Materials, 2016. 28(5): pages 1335-1342.

186. Seery, M.K., R. George, P. Floris, and S.C. Pillai, Silver doped titanium dioxide nanomaterials for enhanced visible light photocatalysis. Journal of Photochemistry and Photobiology a-Chemistry, 2007. 189(2-3): pages 258-263.

187. Xin, B.F., L.Q. Jing, Z.Y. Ren, B.Q. Wang, and H.G. Fu, Effects of simultaneously doped and deposited Ag on the photocatalytic activity and surface states of TiO_2. Journal of Physical Chemistry B, 2005. 109(7): pages 2805-2809.

188. Kariniemi, M., J. Niinisto, T. Hatanpaa, M. Kemell, T. Sajavaara, M. Ritala, and M. Leskela, Plasma-Enhanced Atomic Layer Deposition of silver thin films. Chemistry of Materials, 2011. 23(11): pages 2901-2907.

189. Xin, B.F., Z.Y. Ren, H.Y. Hu, X.Y. Zhang, C.L. Dong, K.Y. Shi, L.Q. Jing, and H.G. Fu, Photocatalytic activity and interfacial carrier transfer of Ag-TiO_2 nanoparticle films. Applied Surface Science, 2005. 252(5): pages 2050-2055.

190. Wu, P., R. Xie, K. Imlay, and J.K. Shang, Visible light induced bactericidal activity of titanium dioxide codoped with nitrogen and silver. Environmental Science & Technology, 2010. 44(18): pages 6992-6997.

191. Veres, A., L. Janovak, T. Bujdoso, T. Rica, E. Fodor, S. Tallosy, N. Buzas, E. Nagy, and I. Dekany, Silver and phosphate functionalized reactive TiO_2/polymer composite films for destructions of resistent bacteria using visible light. Journal of Advanced Oxidation Technologies, 2012. 15(1): pages 205-216.

192. Feng, Q.L., J. Wu, G.Q. Chen, F.Z. Cui, T.N. Kim, and J.O. Kim, A mechanistic study of the antibacterial effect of silver ions on Escherichia coli and Staphylococcus aureus. Journal of Biomedical Materials Research, 2000. 52(4): pages 662-668.

193. Yamanaka, M., K. Hara, and J. Kudo, Bactericidal actions of a silver ion solution on Escherichia coli, studied by energy-filtering transmission electron microscopy and proteomic analysis. Applied and Environmental Microbiology, 2005. 71(11): pages 7589-7593.

194. Greil, J., T. Spies, M. Boswald, T. Bechert, S. Lugauer, A. Regenfus, and J.P. Guggenbichler, Analysis of the acute cytotoxicity of the Erlanger silver catheter. Infection, 1999. 27: pages S34-S37.

195. Davies, R.L. and S.F. Etris, The development and functions of silver in water purification and disease control. Catalysis Today, 1997. 36(1): pages 107-114.

196. Dorman, J.A., J. Weickert, J.B. Reindl, M. Putnik, A. Wisnet, M. Noebels, C. Scheu, and L. Schmidt-Mende, Control of recombination pathways in TiO_2 nanowire hybrid solar cells using Sn^{4+} dopants. Journal of Physical Chemistry C, 2014. 118(30): pages 16672-16679.

197. Sayilkan, F., M. Asilturk, P. Tatar, N. Kiraz, E. Arpac, and H. Sayilkan, Photocatalytic performance of Sn-doped TiO_2 nanostructured mono and double layer thin films for Malachite Green dye degradation under UV and vis-lights. Journal of Hazardous Materials, 2007. 144(1-2): pages 140-146.

198. Harunsani, M.H., F.E. Oropeza, R.G. Palgrave, and R.G. Egdell, Electronic and structural properties of $Sn_xTi_{1-x}O_2$ ($0.0 < x < 0.1$) solid solutions. Chemistry of Materials, 2010. 22(4): pages 1551-1558.

199. Nguyen-Phan, T.D., V.H. Pham, J.S. Chung, M. Chhowalla, T. Asefa, W.J. Kim, and E.W. Shin, Photocatalytic performance of Sn-doped TiO_2/reduced graphene oxide composite materials. Applied Catalysis a-General, 2014. 473: pages 21-30.

200. Li, X., R.C. Xiong, and G. Wei, Preparation and photocatalytic activity of nanoglued Sn-doped TiO_2. Journal of Hazardous Materials, 2009. 164(2-3): pages 587-591.

201. Oropeza, F.E., B. Mei, I. Sinev, A.E. Becerikli, M. Muhler, and J. Strunk, Effect of Sn surface states on the photocatalytic activity of anatase TiO_2. Applied Catalysis B-Environmental, 2013. 140: pages 51-59.

202. Brook, L.A., P. Evans, H.A. Foster, M.E. Pemble, D.W. Sheel, A. Steele, and H.M. Yates, Novel multifunctional films. Surface & Coatings Technology, 2007. 201(22-23): pages 9373-9377.

203. Ramirez-Ortega, D., P. Acevedo-Pena, F. Tzompantzi, R. Arroyo, F. Gonzalez, and I. Gonzalez, Energetic states in SnO_2-TiO_2 structures and their impact on interfacial charge transfer process. Journal of Materials Science, 2017. 52(1): pages 260-275.

204. Yu, C.Y., Y. Bai, D. Yan, X.G. Li, and W.F. Zhang, Improved electrochemical properties of Sn-doped TiO_2 nanotube as an anode material for lithium ion battery. Journal of Solid State Electrochemistry, 2014. 18(7): pages 1933-1940.

205. Shen, Y.D., T.R.B. Foong, and X. Hu, Towards atomic level vanadium doping of TiO_2 via liquid-phase atomic layer deposition. Applied Catalysis a-General, 2011. 409: pages 87-90.

206. Niemela, J.-P., H. Yamauchi, and M. Karppinen, Conducting Nb-doped TiO_2 thin films fabricated with an atomic layer deposition technique. Thin Solid Films, 2014. 551: pages 19-22.

207. Pehlivan, E., F.Z. Tepehan, and G.G. Tepehan, Effect of TiO_2 mixtures on the optical, structural and electrochromic properties of Nb_2O_5 thin films. Solar Energy Materials and Solar Cells, 2005. 87(1-4): pages 317-322.

208. Shimizu, H., H. Sato, S. Nishimura, and M. Honda, Electrical properties of anodically oxidized Nb_2O_5 and Si-doped Nb_2O_5 films. Japanese Journal of Applied Physics Part 1-Regular Papers Brief Communications & Review Papers, 2005. 44(9A): pages 6664-6666.

209. Wang, G.Q., W. Lan, M.L. Yu, G.J. Han, Y. Wang, Q. Su, and X.Q. Liu, Optical and structural properties of TiO_2 films as a function of Nb doping concentration. Journal of Materials Science-Materials in Electronics, 2011. 22(5): pages 463-466.

210. O'Hara, A., T.N. Nunley, A.B. Posadas, S. Zollner, and A.A. Demkov, Electronic and optical properties of NbO_2. Journal of Applied Physics, 2014. 116(21): pages 213705-213717.

211. Posadas, A.B., A. O'Hara, S. Rangan, R.A. Bartynski, and A.A. Demkov, Band gap of epitaxial in-plane-dimerized single-phase NbO_2 films. Applied Physics Letters, 2014. 104(9): pages 092901-092906.

212. Fleming, R.M., D.V. Lang, C.D.W. Jones, M.L. Steigerwald, D.W. Murphy, G.B. Alers, Y.H. Wong, R.B. van Dover, J.R. Kwo, and A.M. Sergent, Defect dominated charge transport in amorphous Ta_2O_5 thin films. Journal of Applied Physics, 2000. 88(2): pages 850-862.

213. Kukli, K., J. Aarik, A. Aidla, O. Kohan, T. Uustare, and V. Sammelselg, Properties of tantalum oxide thin films grown by atomic layer deposition. Thin Solid Films, 1995. 260(2): pages 135-142.

214. Ramprasad, R., M. Sadd, D. Roberts, T. Remmel, M. Raymond, E. Luckowski, S. Kalpat, C. Barron, and M. Miller, Oxygen vacancy defects in tantalum

pentoxide: a density functional study. Microelectronic Engineering, 2003. 69(2-4): pages 190-194.

215. Sawada, H. and K. Kawakami, Electronic structure of oxygen vacancy in Ta_2O_5. Journal of Applied Physics, 1999. 86(2): pages 956-959.

216. Choi, J.H., S.H. Kwon, Y.K. Jeong, I. Kim, and K.H. Kim, Atomic Layer Deposition of Ta-doped TiO_2 electrodes for Dye-Sensitized Solar Cells. Journal of the Electrochemical Society, 2011. 158(6): pages B749-B753.

217. Abdullah, M.M., F.M. Rajab, and S.M. Al-Abbas, Structural and optical characterization of Cr_2O_3 nanostructures: Evaluation of its dielectric properties. Aip Advances, 2014. 4(2): pages 027121-027132.

218. Hones, P., M. Diserens, and F. Levy, Characterization of sputter-deposited chromium oxide thin films. Surface & Coatings Technology, 1999. 120: pages 277-283.

219. Borgarello, E., J. Kiwi, M. Gratzel, E. Pelizzetti, and M. Visca, Visible light induced water cleavage in colloidal solutions of chromium doped titanium dioxide particles. Journal of the American Chemical Society, 1982. 104(11): pages 2996-3002.

220. Lyson-Sypien, B., A. Czapla, M. Lubecka, P. Gwizdz, K. Schneider, K. Zakrzewska, K. Michalow, T. Graule, A. Reszka, M. Rekas, A. Lacz, and M. Radecka, Nanopowders of chromium doped TiO_2 for gas sensors. Sensors and Actuators B-Chemical, 2012. 175: pages 163-172.

221. Ivanova, T., A. Szekeres, M. Gartner, D. Gogova, and K.A. Gesheva, Spectroscopic characterization of CVD-molybdenum oxide films. Electrochimica Acta, 2001. 46(13-14): pages 2215-2219.

222. Szekeres, A., T. Ivanova, and K. Gesheva, Spectroscopic ellipsometry study of CVD molybdenum oxide films: effect of temperature. Journal of Solid State Electrochemistry, 2002. 7(1): pages 17-20.

223. Xiang, D., C. Han, J. Zhang, and W. Chen, Gap states assisted MoO_3 nanobelt photodetector with wide spectrum response. Scientific Reports, 2014. 4: pages 1-6.

224. Zollfrank, C., K. Gutbrod, P. Wechsler, and J.P. Guggenbichler, Antimicrobial activity of transition metal acid MoO_3 prevents microbial growth on

material surfaces. Materials Science & Engineering C-Materials for Biological Applications, 2012. 32(1): pages 47-54.

225. Kwon, K.D., K. Refson, and G. Sposito, Defect-induced photoconductivity in layered manganese oxides: A density functional theory study. Physical Review Letters, 2008. 100(14): pages 146601-146604.

226. Leblanc, S.E. and H.S. Fogler, The role of conduction valence bands and redox potential in accelerated mineral dissolution. Aiche Journal, 1986. 32(10): pages 1702-1709.

227. Thirumalairajan, S., K. Girija, M. Sudha, P. Maadeswaran, and J. Chandrasekaran, Structural and optical investigation of manganese oxide thin films by spray pyrolysis technique. Optoelectronics and Advanced Materials-Rapid Communications, 2008. 2(12): pages 779-781.

228. Sellers, M.C.K. and E.G. Seebauer, Structural and magnetic properties of Mn-doped anatase TiO_2 films synthesized by atomic layer deposition. Applied Physics a-Materials Science & Processing, 2011. 104(2): pages 583-586.

229. Al-Kuhaili, M.F., M. Saleem, and S.M.A. Durrani, Optical properties of iron oxide (alpha-Fe_2O_3) thin films deposited by the reactive evaporation of iron. Journal of Alloys and Compounds, 2012. 521: pages 178-182.

230. Gilbert, B., C. Frandsen, E.R. Maxey, and D.M. Sherman, Band-gap measurements of bulk and nanoscale hematite by soft x-ray spectroscopy. Physical Review B, 2009. 79(3): pages 035101-035108.

231. Iwamoto, M., T. Abe, and Y. Tachibana, Control of bandgap of iron oxide through its encapsulation into SiO_2-based mesoporous materials. Journal of Molecular Catalysis a-Chemical, 2000. 155(1-2): pages 143-153.

232. Yu, H., H. Irie, Y. Shimodaira, Y. Hosogi, Y. Kuroda, M. Miyauchi, and K. Hashimoto, An efficient visible light sensitive Fe(III)-grafted TiO_2 photocatalyst. Journal of Physical Chemistry C, 2010. 114(39): pages 16481-16487.

233. Chen, J., X. Wu, and A. Selloni, Electronic structure and bonding properties of cobalt oxide in the spinel structure. Physical Review B, 2011. 83(24): pages 1-24.

234. Irwin, M.D., B. Buchholz, A.W. Hains, R.P.H. Chang, and T.J. Marks, p-type semiconducting nickel oxide as an efficiency-enhancing anode interfacial layer in polymer bulk-heterojunction solar cells. Proceedings of the National Academy of Sciences of the United States of America, 2008. 105(8): pages 2783-2787.

235. Das, N.S., B. Saha, R. Thapa, G.C. Das, and K.K. Chattopadhyay, Band gap widening of nanocrystalline nickel oxide thin films via phosphorus doping. Physica E-Low-Dimensional Systems & Nanostructures, 2010. 42(5): pages 1377-1382.

236. Sasi, B. and K.G. Gopchandran, Nanostructured mesoporous nickel oxide thin films. Nanotechnology, 2007. 18(11): pages 115613-115622.

237. Tian, J., H. Gao, H. Deng, L. Sun, H. Kong, P. Yang, and J. Chu, Structural, magnetic and optical properties of Ni-doped TiO_2 thin films deposited on silicon (100) substrates by sol-gel process. Journal of Alloys and Compounds, 2013. 581: pages 318-323.

238. Hosny, N.M., Synthesis, characterization and optical band gap of NiO nanoparticles derived from anthranilic acid precursors via a thermal decomposition route. Polyhedron, 2011. 30(3): pages 470-476.

239. Santra, K., C.K. Sarkar, M.K. Mukherjee, and B. Ghosh, Copper oxide thin films grown by plasma evaporation method. Thin Solid Films, 1992. 213(2): pages 226-229.

240. Ray, S.C., Preparation of copper oxide thin film by the sol-gel-like dip technique and study of their structural and optical properties. Solar Energy Materials and Solar Cells, 2001. 68(3-4): pages 307-312.

241. Hashimoto, K., H. Irie, and A. Fujishima, TiO_2 photocatalysis: A historical overview and future prospects. Japanese Journal of Applied Physics Part 1-Regular Papers Brief Communications & Review Papers, 2005. 44(12): pages 8269-8285.

242. Thurman, R.B. and C.P. Gerba, The molecular mechanisms of copper and silver ion disinfection of bacteria and viruses. Crc Critical Reviews in Environmental Control, 1988. 18(4): pages 295-315.

243. Stafford, S.L., N.J. Bokil, M.E.S. Achard, R. Kapetanovic, M.A. Schembri, A.G. McEwan, and M.J. Sweet, Metal ions in macrophage antimicrobial pathways: emerging roles for zinc and copper. Bioscience Reports, 2013. 33: pages 541-554.

244. Zhao, Y., C. Li, X. Liu, F. Go, H.L. Du, and L. Shi, Zn-doped TiO_2 nanoparticles with high photocatalytic activity synthesized by hydrogen-oxygen diffusion flame. Applied Catalysis B-Environmental, 2008. 79(3): pages 208-215.

245. Thanh Binh, N., M.-J. Hwang, and K.-S. Ryu, Synthesis and high photocatalytic activity of Zn-doped TiO_2 nanoparticles by sol-gel and ammonia-evaporation method. Bulletin of the Korean Chemical Society, 2012. 33(1): pages 243-247.

246. Chauhan, R., A. Kumar, and R.P. Chaudhary, Structural and optical characterization of Zn doped TiO_2 nanoparticles prepared by sol-gel method. Journal of Sol-Gel Science and Technology, 2012. 61(3): pages 585-591.

247. Wattanawikkam, C. and W. Pecharapa, Synthesis and Characterization of Zn-Doped TiO_2 Nanoparticles via Sonochemical Method. Integrated Ferroelectrics, 2015. 165(1): pages 167-175.

248. Arunachalam, A., S. Dhanapandian, C. Manoharan, and G. Sivakumar, Physical properties of Zn doped TiO_2 thin films with spray pyrolysis technique and its effects in antibacterial activity. Spectrochimica Acta Part a-Molecular and Biomolecular Spectroscopy, 2015. 138: pages 105-112.

249. Wang, L., X. Xue, F. Shi, D. Zhao, D. Zhang, K. Zheng, G. Wang, C. He, R. Kim, and W. Qin, Ultraviolet and violet upconversion fluorescence of europium (III) doped in YF_3 nanocrystals. Optics Letters, 2009. 34(18): pages 2781-2783.

250. Wakefield, G., H.A. Keron, P.J. Dobson, and J.L. Hutchison, Synthesis and properties of sub-50-nm europium oxide nanoparticles. Journal of Colloid and Interface Science, 1999. 215(1): pages 179-182.

251. Hansen, P.-A., H. Fjellvag, T.G. Finstad, and O. Nilsen, Luminescence properties of europium titanate thin films grown by atomic layer deposition. Rsc Advances, 2014. 4(23): pagges 11876-11883.

252. Hansen, P.-A., H. Fjellvag, T.G. Finstad, and O. Nilsen, Luminescent properties of multilayered Eu_2O_3 and TiO_2 grown by Atomic Layer Deposition. Chemical Vapor Deposition, 2014. 20(7-9): pages 274-281.

253. Auzel, F., Upconversion and anti-stokes processes with f and d ions in solids. Chemical Reviews, 2004. 104(1): pages 139-173.

254. Haase, M. and H. Schaefer, Upconverting nanoparticles. Angewandte Chemie-International Edition, 2011. 50(26): pages 5808-5829.

255. Park, D.J., H.H. Nahm, and C.H. Park, Microscopic properties of interstitial hydrogen impurity in TiO_2. Journal of the Korean Physical Society, 2006. 49: pages S473-S476.

256. Mehta, M., N. Kodan, S. Kumar, A. Kaushal, L. Mayrhofer, M. Walter, M. Moseler, A. Dey, S. Krishnamurthy, S. Basu, and A.P. Singh, Hydrogen treated anatase TiO_2: a new experimental approach and further insights from theory. Journal of Materials Chemistry A, 2016. 4(7): pages 2670-2681.

257. Mo, L.B., Y. Wang, Y. Bai, Q.Y. Xiang, Q. Li, W.Q. Yao, J.O. Wang, K. Ibrahim, H.H. Wang, C.H. Wan, and J.L. Cao, Hydrogen impurity defects in rutile TiO_2. Scientific Reports, 2015. 5: pages 1-7.

258. Ataei, S.S., M.R. Mohammadizadeh, and N. Seriani, Excitonic effects in the optical properties of hydrogenated anatase TiO_2. Physical Review B, 2017. 95(15): pages 155201-155206.

259. Deng, X.Q., X.B. Zhu, Z.G. Sun, X.S. Li, J.L. Liu, C. Shi, and A.M. Zhu, Exceptional activity for photocatalytic mineralization of formaldehyde over amorphous titania nanofilms. Chemical Engineering Journal, 2016. 306: pages 1001-1009.

260. Di Valentin, C., G. Pacchioni, and A. Selloni, Theory of carbon doping of titanium dioxide. Chemistry of Materials, 2005. 17(26): pages 6656-6665.

261. Sakthivel, S. and H. Kisch, Daylight photocatalysis by carbon-modified titanium dioxide. Angewandte Chemie-International Edition, 2003. 42(40): pages 4908-4911.

262. Asahi, R., T. Morikawa, T. Ohwaki, K. Aoki, and Y. Taga, Visible-light photocatalysis in nitrogen-doped titanium oxides. Science, 2001. 293(5528): pages 269-271.

263. Khan, S.U.M., M. Al-Shahry, and W.B. Ingler, Efficient photochemical water splitting by a chemically modified n-TiO_2. Science, 2002. 297(5590): pages 2243-2245.

264. Irie, H., Y. Watanabe, and K. Hashimoto, Carbon-doped anatase TiO_2 powders as a visible-light sensitive photocatalyst. Chemistry Letters, 2003. 32(8): pages 772-773.

265. Vilhunen, S.H. and M.E.T. Sillanpaa, Atomic layer deposited TiO_2 and $TiO_{2-x}N_x$ thin film photocatalysts in salicylic acid decomposition. Water Science and Technology, 2009. 60(10): pages 2471-2475.

266. Kaariainen, M.L. and D.C. Cameron, Nitrogen doping in atomic layer deposition grown titanium dioxide films by using ammonium hydroxide. Thin Solid Films, 2012. 526: pages 212-217.

267. Pore, V., M. Heikkila, M. Ritala, M. Leskela, and S. Areva, Atomic layer deposition of $TiO_{2-x}N_x$ thin films for photocatalytic applications. Journal of Photochemistry and Photobiology a-Chemistry, 2006. 177(1): pages 68-75.

268. Sato, S., Photocatalytic activity of NO_x doped TiO_2 in the visible light region. Chemical Physics Letters, 1986. 123(1-2): pages 126-128.

269. Torres, G.R., T. Lindgren, J. Lu, C.G. Granqvist, and S.E. Lindquist, Photoelectrochemical study of nitrogen-doped titanium dioxide for water oxidation. Journal of Physical Chemistry B, 2004. 108(19): pages 5995-6003.

270. Barolo, G., S. Livraghi, M. Chiesa, M.C. Paganini, and E. Giamello, Mechanism of the photoactivity under visible light of N-Doped titanium dioxide. Charge carriers migration in irradiated N-TiO_2 investigated by electron paramagnetic resonance. Journal of Physical Chemistry C, 2012. 116(39): pages 20887-20894.

271. Kongkanand, A., K. Tvrdy, K. Takechi, M. Kuno, and P.V. Kamat, Quantum dot solar cells. Tuning photoresponse through size and shape control of CdSe-TiO_2 architecture. Journal of the American Chemical Society, 2008. 130(12): pages 4007-4015.

272. Irie, H., S. Washizuka, N. Yoshino, and K. Hashimoto, Visible-light induced hydrophilicity on nitrogen-substituted titanium dioxide films. Chemical Communications, 2003(11): pages 1298-1299.

273. Irie, H., Y. Watanabe, and K. Hashimoto, Nitrogen-concentration dependence on photocatalytic activity of $TiO_{2-x}N_x$ powders. Journal of Physical Chemistry B, 2003. 107(23): pages 5483-5486.

274. Morikawa, T., R. Asahi, T. Ohwaki, K. Aoki, and Y. Taga, Band-gap narrowing of titanium dioxide by nitrogen doping. Japanese Journal of Applied Physics Part 2-Letters, 2001. 40(6A): pages L561-L563.

275. Ihara, T., M. Miyoshi, Y. Iriyama, O. Matsumoto, and S. Sugihara, Visible-light-active titanium oxide photocatalyst realized by an oxygen-deficient structure and by nitrogen doping. Applied Catalysis B-Environmental, 2003. 42(4): pages 403-409.

276. Livraghi, S., M.C. Paganini, E. Giamello, A. Selloni, C. Di Valentin, and G. Pacchioni, Origin of photoactivity of nitrogen-doped titanium dioxide under visible light. Journal of the American Chemical Society, 2006. 128(49): pages 15666-15671.

277. Triantis, T.M., T. Fotiou, T. Kaloudis, A.G. Kontos, P. Falaras, D.D. Dionysiou, M. Pelaez, and A. Hiskia, Photocatalytic degradation and mineralization of microcystin-LR under UV-A, solar and visible light using nanostructured nitrogen doped TiO_2. Journal of Hazardous Materials, 2012. 211: pages 196-202.

278. Diwald, O., T.L. Thompson, E.G. Goralski, S.D. Walck, and J.T. Yates, The effect of nitrogen ion implantation on the photoactivity of TiO_2 rutile single crystals. Journal of Physical Chemistry B, 2004. 108(1): pages 52-57.

279. Diwald, O., T.L. Thompson, T. Zubkov, E.G. Goralski, S.D. Walck, and J.T. Yates, Photochemical activity of nitrogen-doped rutile TiO_2 (111) in visible light. Journal of Physical Chemistry B, 2004. 108(19): pages 6004-6008.

280. Nolan, N.T., D.W. Synnott, M.K. Seery, S.J. Hinder, A. Van Wassenhoven, and S.C. Pillai, Effect of N-doping on the photocatalytic activity of sol-gel TiO_2. Journal of Hazardous Materials, 2012. 211: pages 88-94.

281. Graciani, J., L.J. Alvarez, J.A. Rodriguez, and J.F. Sanz, N doping of rutile TiO_2 (110) surface. A theoretical DFT study. Journal of Physical Chemistry C, 2008. 112(7): pages 2624-2631.

282. Yates, H.M., M.G. Nolan, D.W. Sheel, and M.E. Pemble, The role of nitrogen doping on the development of visible light-induced photocatalytic activity in thin TiO_2 films grown on glass by chemical vapour deposition. Journal of Photochemistry and Photobiology a-Chemistry, 2006. 179(1-2): pages 213-223.

283. Dunnill, C.W.H., Z.A. Aiken, J. Pratten, M. Wilson, D.J. Morgan, and I.P. Parkin, Enhanced photocatalytic activity under visible light in N-doped TiO_2 thin films produced by APCVD preparations using t-butylamine as a nitrogen source and their potential for antibacterial films. Journal of Photochemistry and Photobiology a-Chemistry, 2009. 207(2-3): pages 244-253.

284. Dunnill, C.W. and I.P. Parkin, N-doped titania thin films prepared by Atmospheric Pressure CVD using t-butylamine as the nitrogen source: enhanced photocatalytic activity under visible light. Chemical Vapor Deposition, 2009. 15(7-9): pages 171-174.

285. Ananpattarachai, J. and P. Kajitvichyanukul, Photocatalytic degradation of p,p '-DDT under UV and visible light using interstitial N-doped TiO_2. Journal of Environmental Science and Health Part B-Pesticides Food Contaminants and Agricultural Wastes, 2015. 50(4): pages 247-260.

286. Azami, M.S., W.I. Nawawi, and D.S.M. Shukri, Formation of predominant interstitial N-TiO_2 using physical preparation under microwave irradiation for Reactive Red 4 dye removal. Desalination and Water Treatment, 2017. 92: pages 172-180.

287. Iwase, M., K. Yamada, T. Kurisaki, B. Ohtani, and H. Wakita, A study on the active sites for visible-light photocatalytic activity of phosphorus-doped titanium(IV) oxide particles prepared using a phosphide compound. Applied Catalysis B-Environmental, 2013. 140: pages 327-332.

288. Iwase, M., K. Yamada, T. Kurisaki, O.O. Prieto-Mahaney, B. Ohtani, and H. Wakita, Visible-light photocatalysis with phosphorus-doped titanium(IV) oxide particles prepared using a phosphide compound. Applied Catalysis B-Environmental, 2013. 132: pages 39-44.

289. Han, Z., J. Wang, L. Liao, H. Pan, S. Shen, and J. Chen, Phosphorus doped TiO_2 as oxygen sensor with low operating temperature and sensing mechanism. Applied Surface Science, 2013. 273: pages 349-356.

290. Do, Y.R., W. Lee, K. Dwight, and A. Wold, The effect of WO_3 on the photocatalytic activity of TiO_2. Journal of Solid State Chemistry, 1994. 108(1): pages 198-201.

291. Ohno, T., M. Akiyoshi, T. Umebayashi, K. Asai, T. Mitsui, and M. Matsumura, Preparation of S-doped TiO_2 photocatalysts and their photocatalytic activities under visible light. Applied Catalysis a-General, 2004. 265(1): pages 115-121.

292. Nishijima, K., H. Naitoh, T. Tsubota, and T. Ohno, Visible-light-induced hydrophilic conversion of an S-doped TiO_2 thin film and its photocatalytic activity for decomposition of acetaldehyde in gas phase. Journal of the Ceramic Society of Japan, 2007. 115(1341): pages 310-314.

293. Dong, F., W. Zhao, and Z. Wu, Characterization and photocatalytic activities of C, N and S co-doped TiO_2 with 1D nanostructure prepared by the nano-confinement effect. Nanotechnology, 2008. 19(36): pages 365607-365617.

294. Cui, Y., H. Du, and L. Wen, Origin of visible-light-induced photocatalytic properties of S-doped anatase TiO_2 by first-principles investigation. Solid State Communications, 2009. 149(15-16): pages 634-637.

295. Umebayashi, T., T. Yamaki, H. Itoh, and K. Asai, Band gap narrowing of titanium dioxide by sulfur doping. Applied Physics Letters, 2002. 81(3): pages 454-456.

296. Feng, N.D., F. Liu, M. Huang, A.M. Zheng, Q. Wang, T.H. Chen, G.Y. Cao, J. Xu, J. Fan, and F. Deng, Unravelling the efficient photocatalytic activity of boron-induced Ti^{3+} species in the surface layer of TiO_2. Scientific Reports, 2016. 6: pages 1-9.

297. Finazzi, E., C. Di Valentin, and G. Pacchioni, Boron-Doped Anatase TiO_2: Pure and Hybrid DFT Calculations. Journal of Physical Chemistry C, 2009. 113(1): pages 220-228.

298. Chen, D., D. Yang, Q. Wang, and Z.Y. Jiang, Effects of boron doping on photocatalytic activity and microstructure of titanium dioxide nanoparticles.

Industrial & Engineering Chemistry Research, 2006. 45(12): pages 4110-4116.

299. In, S., A. Orlov, R. Berg, F. Garcia, S. Pedrosa-Jimenez, M.S. Tikhov, D.S. Wright, and R.M. Lambert, Effective visible light-activated B-doped and B,N-codoped TiO_2 photocatalysts. Journal of the American Chemical Society, 2007. 129(45): pages 13790-13791.

300. Stengl, V., V. Houskova, S. Bakardjieva, and N. Murafa, Photocatalytic activity of boron modified titania under UV and visible light illumination. Acs Applied Materials & Interfaces, 2010. 2(2): pages 575-580.

301. Xu, J., Y. Ao, M. Chen, and D. Fu, Low-temperature preparation of Boron-doped titania by hydrothermal method and its photocatalytic activity. Journal of Alloys and Compounds, 2009. 484(1-2): pages 73-79.

302. Li, D., H. Haneda, S. Hishita, and N. Ohashi, Visible-light-driven N-F-codoped TiO_2 photocatalysts. 2. Optical characterization, photocatalysis, and potential application to air purification. Chemistry of Materials, 2005. 17(10): pages 2596-2602.

303. Li, D., H. Haneda, S. Hishita, and N. Ohashi, Visible-light-driven N-F-codoped TiO_2 photocatalysts. 1. Synthesis by spray pyrolysis and surface characterization. Chemistry of Materials, 2005. 17(10): pages 2588-2595.

304. Li, D., H. Haneda, N.K. Labhsetwar, S. Hishita, and N. Ohashi, Visible-light-driven photocatalysis on fluorine-doped TiO_2 powders by the creation of surface oxygen vacancies. Chemical Physics Letters, 2005. 401(4-6): pages 579-584.

305. Dozzi, M.V., C. D'Andrea, B. Ohtani, G. Valentini, and E. Selli, Fluorine doped TiO_2 materials: Photocatalytic activity vs time resolved photoluminescence. Journal of Physical Chemistry C, 2013. 117(48): pages 25586-25595.

306. Dozzi, M.V. and E. Selli, Effects of phase composition and surface area on the photocatalytic paths on fluorinated titania. Catalysis Today, 2013. 206: pages 26-31.

307. Ho, W., J.C. Yu, and S. Lee, Synthesis of hierarchical nanoporous F-doped TiO_2 spheres with visible light photocatalytic activity. Chemical Communications, 2006(10): pages 1115-1117.

308. Yu, J.C., J.G. Yu, W.K. Ho, Z.T. Jiang, and L.Z. Zhang, Effects of F- doping on the photocatalytic activity and microstructures of nanocrystalline TiO_2 powders. Chemistry of Materials, 2002. 14(9): pages 3808-3816.

309. Xu, J., Y. Ao, D. Fu, and C. Yuan, Low-temperature preparation of F-doped TiO_2 film and its photocatalytic activity under solar light. Applied Surface Science, 2008. 254(10): pages 3033-3038.

310. Yu, J., J. Fan, and K. Lv, Anatase TiO_2 nanosheets with exposed (001) facets: improved photoelectric conversion efficiency in dye-sensitized solar cells. Nanoscale, 2010. 2(10): pages 2144-2149.

311. Dozzi, M.V. and E. Selli, Specific facets-dominated anatase TiO_2: Fluorine-mediated synthesis and photoactivity. Catalysts, 2013. 3(2): pages 455-485.

312. Hong, X.T., Z.P. Wang, W.M. Cai, F. Lu, J. Zhang, Y.Z. Yang, N. Ma, and Y.J. Liu, Visible-light-activated nanoparticle photocatalyst of iodine-doped titanium dioxide. Chemistry of Materials, 2005. 17(6): pages 1548-1552.

313. Liu, G., C. Sun, X. Yan, L. Cheng, Z. Chen, X. Wang, L. Wang, S.C. Smith, G.Q. Lu, and H.-M. Cheng, Iodine doped anatase TiO_2 photocatalyst with ultra-long visible light response: correlation between geometric/electronic structures and mechanisms. Journal of Materials Chemistry, 2009. 19(18): pages 2822-2829.

314. Su, W., Y. Zhang, Z. Li, L. Wu, X. Wang, J. Li, and X. Fu, Multivalency iodine doped TiO_2: Preparation, characterization, theoretical studies, and visible-light photocatalysis. Langmuir, 2008. 24(7): pages 3422-3428.

315. Tojo, S., T. Tachikawa, M. Fujitsuka, and T. Majima, Iodine-doped TiO_2 photocatalysts: Correlation between band structure and mechanism. Journal of Physical Chemistry C, 2008. 112(38): pages 14948-14954.

316. Zhang, Q., Y. Li, E.A. Ackerman, M. Gajdardziska-Josifovska, and H. Li, Visible light responsive iodine-doped TiO_2 for photocatalytic reduction of CO_2 to fuels. Applied Catalysis a-General, 2011. 400(1-2): pages 195-202.

317. Li, X., Q. Liu, X. Jiang, and J. Huang, Enhanced photocatalytic activity of Ga-N Co-doped anatase TiO_2 for water decomposition to hydrogen. International Journal of Electrochemical Science, 2012. 7(11): pages 11519-11527.

318. Li, Y.-F., D. Xu, J.I. Oh, W. Shen, X. Li, and Y. Yu, Mechanistic study of codoped titania with nonmetal and metal ions: A case of C plus Mo codoped TiO_2. Acs Catalysis, 2012. 2(3): pages 391-398.

319. Periyat, P., D.E. McCormack, S.J. Hinder, and S.C. Pillai, One-pot synthesis of anionic (nitrogen) and cationic (sulfur) codoped high-temperature stable, visible light active, anatase photocatalysts. Journal of Physical Chemistry C, 2009. 113(8): pages 3246-3253.

320. Xiang, Q., J. Yu, and M. Jaroniec, Nitrogen and sulfur co-doped TiO_2 nanosheets with exposed {001} facets: synthesis, characterization and visible-light photocatalytic activity. Physical Chemistry Chemical Physics, 2011. 13(11): pages 4853-4861.

321. Rengifo-Herrera, J.A., E. Mielczarski, J. Mielczarski, N.C. Castillo, J. Kiwi, and C. Pulgarin, Escherichia coli inactivation by N, S co-doped commercial TiO_2 powders under UV and visible light. Applied Catalysis B-Environmental, 2008. 84(3-4): pages 448-456.

322. Rengifo-Herrera, J.A., J. Kiwi, and C. Pulgarin, N, S co-doped and N-doped Degussa P-25 powders with visible light response prepared by mechanical mixing of thiourea and urea. Reactivity towards E.coli inactivation and phenol oxidation. Journal of Photochemistry and Photobiology a-Chemistry, 2009. 205(2-3): pages 109-115.

323. Rengifo-Herrera, J.A., K. Pierzchala, A. Sienkiewicz, L. Forro, J. Kiwi, and C. Pulgarin, Abatement of organics and Escherichia coli by N, S co-doped TiO_2 under UV and visible light. Implications of the formation of singlet oxygen (O^{-12}) under visible light. Applied Catalysis B-Environmental, 2009. 88(3-4): pages 398-406.

324. Xing, M., Y. Wu, J. Zhang, and F. Chen, Effect of synergy on the visible light activity of B, N and Fe co-doped TiO_2 for the degradation of MO. Nanoscale, 2010. 2(7): pages 1233-1239.

325. Xu, Q.C., D.V. Wellia, S. Yan, D.W. Liao, T.M. Lim, and T.T.Y. Tan, Enhanced photocatalytic activity of C-N-codoped TiO_2 films prepared via an organic-free approach. Journal of Hazardous Materials, 2011. 188(1-3): pages 172-180.

326. Wang, J., B. Huang, Z. Wang, X. Qin, and X. Zhang, Synthesis and characterization of C, N-codoped TiO_2 nanotubes/nanorods with visible-light activity. Rare Metals, 2011. 30: pages 161-165.

327. Liu, G., C. Han, M. Pelaez, D. Zhu, S. Liao, V. Likodimos, A.G. Kontos, P. Falaras, and D.D. Dionysiou, Enhanced visible light photocatalytic activity of C-N-codoped TiO_2 films for the degradation of microcystin-LR. Journal of Molecular Catalysis a-Chemical, 2013. 372: pages 58-65.

328. Wang, X. and T.-T. Lim, Solvothermal synthesis of C-N codoped TiO_2 and photocatalytic evaluation for bisphenol A degradation using a visible-light irradiated LED photoreactor. Applied Catalysis B-Environmental, 2010. 100(1-2): pages 355-364.

329. Zhao, C., M. Pelaez, D.D. Dionysiou, S.C. Pillai, J.A. Byrne, and K.E. O'Shea, UV and visible light activated TiO_2 photocatalysis of 6-hydroxymethyl uracil, a model compound for the potent cyanotoxin cylindrospermopsin. Catalysis Today, 2014. 224: pages 70-76.

330. Hamilton, J.W.J., J.A. Byrne, P.S.M. Dunlop, D.D. Dionysiou, M. Pelaez, K. O'Shea, D. Synnott, and S.C. Pillai, Evaluating the mechanism of visible light activity for N,F-TiO_2 using photoelectrochemistry. Journal of Physical Chemistry C, 2014. 118(23): pages 12206-12215.

331. Pelaez, M., P. Falaras, V. Likodimos, A.G. Kontos, A.A. de la Cruz, K. O'Shea, and D.D. Dionysiou, Synthesis, structural characterization and evaluation of sol-gel-based NF-TiO_2 films with visible light-photoactivation for the removal of microcystin-LR. Applied Catalysis B-Environmental, 2010. 99(3-4): pages 378-387.

332. Barndok, H., M. Pelaez, C. Han, W.E. Platten, III, P. Campo, D. Hermosilla, A. Blanco, and D.D. Dionysiou, Photocatalytic degradation of contaminants of concern with composite NF-TiO_2 films under visible and solar light. Environmental Science and Pollution Research, 2013. 20(6): pages 3582-3591.

333. Andersen, J., M. Pelaez, L. Guay, Z. Zhang, K. O'Shea, and D.D. Dionysiou, NF-TiO_2 photocatalysis of amitrole and atrazine with addition of oxidants under simulated solar light: Emerging synergies, degradation intermediates,

and reusable attributes. Journal of Hazardous Materials, 2013. 260: pages 569-575.

334. Lim, M., Y. Zhou, B. Wood, Y. Guo, L. Wang, V. Rudolph, and G. Lu, Fluorine and carbon codoped macroporous titania microspheres: Highly effective photocatalyst for the destruction of airborne styrene under visible light. Journal of Physical Chemistry C, 2008. 112(49): pages 19655-19661.

335. Liu, G., L.-C. Yin, J. Wang, P. Niu, C. Zhen, Y. Xie, and H.-M. Cheng, A red anatase TiO_2 photocatalyst for solar energy conversion. Energy & Environmental Science, 2012. 5(11): pages 9603-9610.

336. Wang, P., A.G. Fane, and T.-T. Lim, Evaluation of a submerged membrane vis-LED photoreactor (sMPR) for carbamazepine degradation and TiO_2 separation. Chemical Engineering Journal, 2013. 215: pages 240-251.

337. Breault, T.M. and B.M. Bartlett, Lowering the band gap of anatase structured TiO_2 by coalloying with Nb and N: Electronic structure and photocatalytic degradation of methylene blue dye. Journal of Physical Chemistry C, 2012. 116(10): pages 5986-5994.

338. Hirano, M. and T. Ito, Titania solid solution nanoparticles co-doped with niobium and gallium. Journal of the Ceramic Society of Japan, 2010. 118(1384): pages 1170-1175.

339. Song, S., C. Wang, F. Hong, Z. He, Q. Cai, and J. Chen, Gallium- and iodine-co-doped titanium dioxide for photocatalytic degradation of 2-chlorophenol in aqueous solution: Role of gallium. Applied Surface Science, 2011. 257(8): pages 3427-3432.

340. Depero, L.E., A. Marino, B. Allieri, E. Bontempi, L. Sangaletti, C. Casale, and M. Notaro, Morphology and microstructural properties of TiO_2 nanopowders doped with trivalent Al and Ga cations. Journal of Materials Research, 2000. 15(10): pages 2080-2086.

341. Deng, Q., X. Han, Y. Gao, and G. Shao, Remarkable optical red shift and extremely high optical absorption coefficient of V-Ga co-doped TiO_2. Journal of Applied Physics, 2012. 112(1).

342. Leyland, N.S., J. Podporska-Carroll, J. Browne, S.J. Hinder, B. Quilty, and S.C. Pillai, Highly efficient F, Cu doped TiO_2 anti-bacterial visible light active

photocatalytic coatings to combat hospital-acquired infections. Scientific Reports, 2016. 6: pages 1-10.

343. Korner, W. and C. Elsasser, Density functional theory study of dopants in polycrystalline TiO_2. Physical Review B, 2011. 83(20): pages 205311-205315.

344. Stadler, A., Transparent Conducting Oxides-An up-to-date overview. Materials, 2012. 5(4): pages 661-683.

345. Elam, J.W., D.A. Baker, A.B.F. Martinson, M.J. Pellin, and J.T. Hupp, Atomic layer deposition of indium tin oxide thin films using nonhalogenated precursors. Journal of Physical Chemistry C, 2008. 112(6): pages 1938-1945.

346. Muslih, E.Y., K.H. Kim, and Iop. Preparation of zinc oxide (ZnO) thin film as Transparent Conductive Oxide (TCO) from zinc complex compound on thin film solar cells: A study of O_2 effect on annealing process. in 2nd Materials-Research-Society-of-Indonesia Meeting (MRS-Id). 2016. Bandung, INDONESIA.

347. Steinhauser, J., S. Fay, N. Oliveira, E. Vallat-Sauvain, and C. Ballif, Transition between grain boundary and intragrain scattering transport mechanisms in boron-doped zinc oxide thin films. Applied Physics Letters, 2007. 90(14): pages 142101-142107.

348. Ellmer, K., Past achievements and future challenges in the development of optically transparent electrodes. Nature Photonics, 2012. 6(12): pages 808-816.

349. Edwards, P.P., A. Porch, M.O. Jones, D.V. Morgan, and R.M. Perks, Basic materials physics of transparent conducting oxides. Dalton Transactions, 2004(19): pages 2995-3002.

350. Pergament, A. and A. Morak, Photoinduced metal-insulator transitions: critical concentration and coherence length. Journal of Physics a-Mathematical and General, 2006. 39(17): pages 4619-4623.

351. Li, T.C., M.S. Goes, F. Fabregat-Santiago, J. Bisquert, P.R. Bueno, C. Prasittichai, J.T. Hupp, and T.J. Marks, Surface passivation of nanoporous TiO_2 via Atomic Layer Deposition of ZrO_2 for solid-state Dye-Sensitized Solar Cell applications. Journal of Physical Chemistry C, 2009. 113(42): pages 18385-18390.

352. Hojo, M. and K. Okimura, Effect of annealing with Ar plasma irradiation for transparent conductive Nb-doped TiO_2 films on glass substrate. Japanese Journal of Applied Physics, 2009. 48(8): pages 08HK06-01-08HK06-07.

353. Kim, H., G.P. Kushto, R.C.Y. Auyeung, and A. Pique, Optimization of F-doped SnO_2 electrodes for organic photovoltaic devices. Applied Physics a-Materials Science & Processing, 2008. 93(2): pages 521-526.

354. Kim, Y.J., Y.H. Lee, M.H. Lee, H.J. Kim, J.H. Pan, G.I. Lim, Y.S. Choi, K. Kim, N.-G. Park, C. Lee, and W.I. Lee, Formation of efficient Dye-Sensitized Solar Cells by introducing an interfacial layer of long-range ordered mesoporous TiO_2 thin film. Langmuir, 2008. 24(22): pages 13225-13230.

355. Sheehan, S., P.K. Surolia, O. Byrne, S. Garner, P. Cimo, X. Li, D.P. Dowling, and K.R. Thampi, Flexible glass substrate based dye sensitized solar cells. Solar Energy Materials and Solar Cells, 2015. 132: pages 237-244.

356. Wang, Y., Y.C. Wu, Y.Q. Qin, Z.H. Zhang, C.W. Shi, Q.F. Zhang, C.H. Li, X.H. Xia, S. Sun, and L. Chen, Large-area SnO_2: F thin films by offline APCVD. Materials Research Bulletin, 2011. 46(8): pages 1262-1265.

357. Zardetto, V., T.M. Brown, A. Reale, and A. Di Carlo, Substrates for flexible electronics: A practical investigation on the electrical, film flexibility, optical, temperature, and solvent resistance properties. Journal of Polymer Science Part B-Polymer Physics, 2011. 49(9): pages 638-648.

358. Suh, S.G., Z.H. Zhang, W.K. Chu, and D.M. Hoffman, Atmospheric-pressure chemical vapor deposition of fluorine-doped tin oxide thin films. Thin Solid Films, 1999. 345(2): pages 240-243.

359. Proscia, J. and R.G. Gordon, Properties of fluorine-doped tin oxide-films produced by atmospheric-pressure chemical vapor-deposition from tetramethyl tin, bromotrifluoromethane and oxygen. Thin Solid Films, 1992. 214(2): pages 175-187.

360. Maruyama, T. and K. Tabata, Fluorine-doped tin dioxide thin-films prepared by chemical vapor-deposition. Journal of Applied Physics, 1990. 68(8): pages 4282-4285.

361. Wang, Y., T. Brezesinski, M. Antonietti, and B. Smarsly, Ordered mesoporous Sb-, Nb-, and Ta-doped SnO_2 thin films with adjustable doping

levels and high electrical conductivity. Acs Nano, 2009. 3(6): pages 1373-1378.

362. Lin, Y.C., T.Y. Chen, L.C. Wang, and S.Y. Lien, Comparison of AZO, GZO, and AGZO Thin Films TCOs Applied for a-Si Solar Cells. Journal of the Electrochemical Society, 2012. 159(6): pages H599-H604.

363. Na, J.S., Q. Peng, G. Scarel, and G.N. Parsons, Role of gas doping sequence in surface reactions and dopant incorporation during Atomic Layer Deposition of Al-Doped ZnO. Chemistry of Materials, 2009. 21(23): pages 5585-5593.

364. Na, J.S., G. Scarel, and G.N. Parsons, In situ analysis of dopant incorporation, activation, and film growth during thin film ZnO and ZnO:Al Atomic Layer Deposition. Journal of Physical Chemistry C, 2010. 114(1): pages 383-388.

365. Kim, S., J. Seo, H.W. Jang, J. Bang, W. Lee, T. Lee, and J.-M. Myoung, Effects of H_2 ambient annealing in fully 0 0 2-textured ZnO:Ga thin films grown on glass substrates using RF magnetron co-sputter deposition. Applied Surface Science, 2009. 255(8): pages 4616-4622.

366. Kang, J., H.W. Kim, and C. Lee, Electrical resistivity and transmittance properties of Al- and Ga-codoped ZnO thin films. Journal of the Korean Physical Society, 2010. 56(2): pages 576-579.

367. Steglich, M., A. Bingel, G. Jia, and F. Falk, Atomic layer deposited ZnO:Al for nanostructured silicon heterojunction solar cells. Solar Energy Materials and Solar Cells, 2012. 103: pages 62-68.

368. Dhakal, T., D. Vanhart, R. Christian, A. Nandur, A. Sharma, and C.R. Westgate, Growth morphology and electrical/optical properties of Al-doped ZnO thin films grown by atomic layer deposition. Journal of Vacuum Science & Technology A, 2012. 30(2): pages 021201-021210.

369. Maeng, W.J., J.W. Lee, J.H. Lee, K.B. Chung, and J.S. Park, Studies on optical, structural and electrical properties of atomic layer deposited Al-doped ZnO thin films with various Al concentrations and deposition temperatures. Journal of Physics D-Applied Physics, 2011. 44(44): pages 445305-445312.

370. Myong, S.Y., S.J. Baik, C.H. Lee, W.Y. Cho, and K.S. Lim, Extremely transparent and conductive ZnO:Al thin films prepared by photo-assisted metalorganic chemical vapor deposition (photo-MOCVD) using $AlCl_3(6H_2O)$

as new doping material. Japanese Journal of Applied Physics Part 2-Letters, 1997. 36(8B): pages L1078-L1081.

371. Kato, H., M. Sano, K. Miyamoto, and T. Yao, Growth and characterization of Ga-doped ZnO layers on a-plane sapphire substrates grown by molecular beam epitaxy. Journal of Crystal Growth, 2002. 237: pages 538-543.

372. Ataev, B.M., A.M. Bagamadova, A.M. Djabrailov, V.V. Mamedov, and R.A. Rabadanov, Highly conductive and transparent Ga-doped epitaxial ZnO films on sapphire by CVD. Thin Solid Films, 1995. 260(1): pages 19-20.

373. Assuncao, V., E. Fortunato, A. Marques, H. Aguas, I. Ferreira, M.E.V. Costa, and R. Martins, Influence of the deposition pressure on the properties of transparent and conductive ZnO : Ga thin-film produced by r.f. sputtering at room temperature. Thin Solid Films, 2003. 427(1-2): pages 401-405.

374. Gabas, M., P. Diaz-Carrasco, F. Agullo-Rueda, P. Herrero, A.R. Landa-Canovas, and J.R. Ramos-Barrado, High quality ZnO and Ga:ZnO thin films grown onto crystalline Si (100) by RF magnetron sputtering. Solar Energy Materials and Solar Cells, 2011. 95(8): pages 2327-2334.

375. Gabas, M., A. Landa-Canovas, J. Luis Costa-Kraemer, F. Agullo-Rueda, A.R. Gonzalez-Elipe, P. Diaz-Carrasco, J. Hernandez-Moro, I. Lorite, P. Herrero, P. Castillero, A. Barranco, and J. Ramon Ramos-Barrado, Differences in n-type doping efficiency between Al- and Ga-ZnO films. Journal of Applied Physics, 2013. 113(16): pages 163701-163709.

376. Gabas, M., P. Torelli, N.T. Barrett, M. Sacchi, and J.R.R. Barrado, Electronic structure of Al- and Ga-doped ZnO films studied by hard X-ray photoelectron spectroscopy. Apl Materials, 2014. 2(1): pages 012111-012116.

377. Wang, T., Y. Liu, Q. Fang, M. Wu, X. Sun, and F. Lu, Low temperature synthesis wide optical band gap Al and (Al, Na) co-doped ZnO thin films. Applied Surface Science, 2011. 257(6): pages 2341-2345.

378. Lin, Y.C., B.L. Wang, W.T. Yen, C.T. Ha, and C. Peng, Effect of process conditions on the optoelectronic characteristics of ZnO:Mo thin films prepared by pulsed direct current magnetron sputtering. Thin Solid Films, 2010. 518(17): pages 4928-4934.

379. Bak, T., M.K. Nowotny, L.R. Sheppard, and J. Nowotny, Mobility of electronic charge carriers in titanium dioxide. Journal of Physical Chemistry C, 2008. 112(33): pages 12981-12987.

380. Aarik, J., A. Aidla, H. Mandar, T. Uustare, M. Schuisky, and A. Harsta, Atomic layer growth of epitaxial TiO_2 thin films from $TiCl_4$ and H_2O on alpha-Al_2O_3 substrates. Journal of Crystal Growth, 2002. 242(1-2): pages 189-198.

381. Hamann, T.W., A.B.F. Martinson, J.W. Elam, M.J. Pellin, and J.T. Hupp, Atomic layer deposition of TiO_2 on aerogel templates: New photoanodes for dye-sensitized solar cells. Journal of Physical Chemistry C, 2008. 112(27): pages 10303-10307.

382. Furubayashi, Y., T. Hitosugi, Y. Yamamoto, K. Inaba, G. Kinoda, Y. Hirose, T. Shimada, and T. Hasegawa, A transparent metal: Nb-doped anatase TiO_2. Applied Physics Letters, 2005. 86(25): pages 252101-252103.

383. Furubayashi, Y., T. Hitosugi, Y. Yamamoto, Y. Hirose, G. Kinoda, K. Inaba, T. Shimada, and T. Hasegawa, Novel transparent conducting oxide: Anatase $Ti_{1-x}Nb_xO_2$. Thin Solid Films, 2006. 496(1): pages 157-159.

384. Yamada, N., T. Hitosugi, N.L.H. Hoang, Y. Furubayashi, Y. Hirose, T. Shimada, and T. Hasegawa, Fabrication of low resistivity Nb-doped TiO_2 transparent conductive polycrystalline films on glass by reactive sputtering. Japanese Journal of Applied Physics Part 1-Regular Papers Brief Communications & Review Papers, 2007. 46(8A): pages 5275-5277.

385. Hitosugi, T., A. Ueda, S. Nakao, N. Yamada, Y. Furubayashi, Y. Hirose, T. Shimada, and T. Hasegawa, Fabrication of highly conductive Ti1-xNbxO2 polycrystalline films on glass substrates via crystallization of amorphous phase grown by pulsed laser deposition. Applied Physics Letters, 2007. 90(21).

386. Hung, K.-H., P.-W. Lee, W.-C. Hsu, H.C. Hsing, H.-T. Chang, and M.-S. Wong, Transparent conducting oxide films of heavily Nb-doped titania by reactive co-sputtering. Journal of Alloys and Compounds, 2011. 509(42): pages 10190-10194.

387. Hitosugi, T., Y. Furubayashi, A. Ueda, K. Itabashi, K. Inaba, Y. Hirose, G. Kinoda, Y. Yamamoto, T. Shimada, and T. Hasegawa, Ta-doped anatase TiO_2

epitaxial film as transparent conducting oxide. Japanese Journal of Applied Physics Part 2-Letters & Express Letters, 2005. 44(33-36): pages L1063-L1065.

388. Lee, D.-K. and H.-I. Yoo, Electrical conductivity and oxygen nonstoichiometry of acceptor (Ga)-doped titania. Physical Chemistry Chemical Physics, 2008. 10(45): pages 6890-6898.

389. Takeuchi, U., A. Chikamatsu, T. Hitosugi, H. Kumigashira, M. Oshima, Y. Hirose, T. Shimada, and T. Hasegawa, Transport properties and electronic states of anatase Ti1-xWxO2 epitaxial thin films. Journal of Applied Physics, 2010. 107(2): pages 023701-023705.

390. Coutts, T.J., D.L. Young, X. Li, W.P. Mulligan, and X. Wu, Search for improved transparent conducting oxides: A fundamental investigation of CdO, Cd_2SnO_4, and Zn_2SnO_4. Journal of Vacuum Science & Technology a-Vacuum Surfaces and Films, 2000. 18(6): pages 2646-2660.

391. Dakhel, A.A., Influence of hydrogenation on the electrical and optical properties of CdO:Ti thin films. Thin Solid Films, 2008. 517(2): pages 886-890.

392. Dakhel, A.A., Influence of dysprosium doping on the electrical and optical properties of CdO thin films. Solar Energy, 2009. 83(6): pages 934-939.

393. Prathap, P., G.G. Devi, Y.P.V. Subbaiah, V. Ganesan, K.T.R. Reddy, and J. Yi, Preparation and characterization of sprayed In_2O_3:Mo films. Physica Status Solidi a-Applications and Materials Science, 2008. 205(8): pages 1947-1951.

394. Kumar, S.R.S., P. Malar, T. Osipowicz, S.S. Banerjee, and S. Kasiviswanathan, Ion beam studies on reactive DC sputtered manganese doped indium tin oxide thin films. Nuclear Instruments & Methods in Physics Research Section B-Beam Interactions with Materials and Atoms, 2008. 266(8): pages 1421-1424.

395. Giurgola, S., A. Rodriguez, L. Martinez, P. Vergani, F. Lucchi, S. Benchabane, and V. Pruneri, Ultra thin nickel transparent electrodes. Journal of Materials Science-Materials in Electronics, 2009. 20: pages 181-184.

396. Lin, C., F.Y. Tsai, M.H. Lee, C.H. Lee, T.C. Tien, L.P. Wang, and S.Y. Tsai, Enhanced performance of dye-sensitized solar cells by an Al_2O_3 charge-

recombination barrier formed by low-temperature atomic layer deposition. Journal of Materials Chemistry, 2009. 19(19): pages 2999-3003.

397. Danks, A.E., S.R. Hall, and Z. Schnepp, The evolution of 'sol-gel' chemistry as a technique for materials synthesis. Materials Horizons, 2016. 3(2): pages 91-112.

398. Ahn, J., J.Y. Lee, J. Kim, J. Yoo, and C. Ryu. Comparison study from sputtering, sol-gel, and ALD processes developing embedded thin film capacitors. in 8th Electronics Packaging Technology Conference. 2006. Singapore, SINGAPORE.

399. Hodgkinson, J.L. and D.W. Sheel, Advances in atmospheric pressure PECVD: The influence of plasma parameters on film morphology. Surface & Coatings Technology, 2013. 230: pages 73-76.

400. Sato, N., K. Nakajima, N. Usami, H. Takahashi, A. Muramatsu, and E. Matsubara, Preparation of a TiO_2 film coated Si device for photo-decomposition of water by CVD method using $Ti(OPri)_4$. Materials Transactions, 2002. 43(7): pages 1533-1536.

401. Ding, Z., X.J. Hu, G.Q. Lu, P.L. Yue, and P.F. Greenfield, Novel silica gel supported TiO_2 photocatalyst synthesized by CVD method. Langmuir, 2000. 16(15): pages 6216-6222.

402. Diesen, V., M. Jonsson, and I.P. Parkin, Improved texturing and photocatalytic efficiency in TiO_2 films grown Using Aerosol-Assisted CVD and Atmospheric Pressure CVD. Chemical Vapor Deposition, 2013. 19(10-12): pages 355-362.

403. Simcock, M.N., Thin film growth of TiO_2 and Ti_2O_3 by the new method of liquid injection CVD investigated using optical interferometry, XRD and AFM. Surface and Interface Analysis, 2006. 38(7): pages 1122-1129.

404. Liu, J., Y. Hu, F. Gu, and C. Li, Large-scale synthesis of hollow titania spheres via flame combustion. Particuology, 2011. 9(6): pages 632-636.

405. Coleman, J.J., Metalorganic chemical vapor deposition for optoelectronic devices. Proceedings of the Ieee, 1997. 85(11): pages 1715-1729.

406. Miikkulainen, V., M. Leskela, M. Ritala, and R.L. Puurunen, Crystallinity of inorganic films grown by atomic layer deposition: Overview and general trends. Journal of Applied Physics, 2013. 113(2): pages 021101-021301.

407. Leskela, M. and M. Ritala, Atomic layer deposition (ALD): from precursors to thin film structures. Thin Solid Films, 2002. 409(1): pages 138-146.

408. van Delft, J.A., D. Garcia-Alonso, and W.M.M. Kessels, Atomic layer deposition for photovoltaics: applications and prospects for solar cell manufacturing. Semiconductor Science and Technology, 2012. 27(7): pages 1-13.

409. Frijters, C.H., P. Poodt, and A. Illiberi, Atmospheric spatial atomic layer deposition of Zn(O,S) buffer layer for Cu(In,Ga)Se_2 solar cells. Solar Energy Materials and Solar Cells, 2016. 155: pages 356-361.

410. Illiberi, A., R. Scherpenborg, F. Roozeboom, and P. Poodt, Atmospheric Spatial Atomic Layer Deposition of In-Doped ZnO. Ecs Journal of Solid State Science and Technology, 2014. 3(5): pages P111-P114.

411. Dunlop, L., A. Kursumovic, and J.L. MacManus-Driscoll, Reproducible growth of p-type ZnO:N using a modified atomic layer deposition process combined with dark annealing. Applied Physics Letters, 2008. 93(17): pages 172111-172113.

412. Scheuermann, A.G., J.D. Prange, M. Gunji, C.E.D. Chidsey, and P.C. McIntyre, Effects of catalyst material and atomic layer deposited TiO_2 oxide thickness on the water oxidation performance of metal-insulator-silicon anodes. Energy & Environmental Science, 2013. 6(8): pages 2487-2496.

413. Lin, J.H., D.T. Ma, Y.L. Li, P.X. Zhang, H.W. Mi, L.B. Deng, L.N. Sun, and X.Z. Ren, In situ nitrogen doping of TiO_2 by plasma enhanced atomic layer deposition for enhanced sodium storage performance. Dalton Transactions, 2017. 46(38): pages 13101-13107.

414. Brahimi, R., Y. Bessekhouad, and M. Trari, Physical properties of N_xTiO_2 prepared by sol-gel route. Physica B-Condensed Matter, 2012. 407(18): pages 3897-3904.

415. Palomares, E., J.N. Clifford, S.A. Haque, T. Lutz, and J.R. Durrant, Control of charge recombination dynamics in dye sensitized solar cells by the use of

conformally deposited metal oxide blocking layers. Journal of the American Chemical Society, 2003. 125(2): pages 475-482.

416. Chang, W.T., Y.C. Hsueh, S.H. Huang, K.I. Liu, C.C. Kei, and T.P. Perng, Fabrication of Ag-loaded multi-walled TiO_2 nanotube arrays and their photocatalytic activity. Journal of Materials Chemistry A, 2013. 1(6): pages 1987-1991.

417. Peng, T.C., X.H. Xiao, F. Ren, J.X. Xu, X.D. Zhou, F. Mei, and C.Z. Jiang, Influence of annealing temperature on the properties of TiO_2 films annealed by ex situ and in situ TEM. Journal of Wuhan University of Technology-Materials Science Edition, 2012. 27(6): pages 1014-1019.

418. Chen, W.F., P. Koshy, Y. Huang, E. Adabifiroozjaei, Y. Yao, and C.C. Sorrell, Effects of precipitation, liquid formation, and intervalence charge transfer on the properties and photocatalytic performance of cobalt- or vanadium-doped TiO_2 thin films. International Journal of Hydrogen Energy, 2016. 41(42): pages 19025-19056.

419. Battiston, G.A., R. Gerbasi, M. Porchia, R. Bertoncello, and F. Caccavale, Chemical vapour deposition and characterization of gallium oxide thin films. Thin Solid Films, 1996. 279(1-2): pages 115-118.

420. Lynch, J., C. Giannini, J.K. Cooper, A. Loiudice, I.D. Sharp, and R. Buonsanti, Substitutional or interstitial site-selective nitrogen doping in TiO_2 nanostructures. Journal of Physical Chemistry C, 2015. 119(13): pages 7443-7452.

421. Aubry, E., J. Lambert, V. Demange, and A. Billard, Effect of Na diffusion from glass substrate on the microstructural and photocatalytic properties of post-annealed TiO_2 films synthesised by reactive sputtering. Surface & Coatings Technology, 2012. 206(23): pages 4999-5005.

422. Ma, W., Z. Lu, and M. Zhang, Investigation of structural transformations in nanophase titanium dioxide by Raman spectroscopy. Applied Physics a-Materials Science & Processing, 1998. 66(6): pages 621-627.

423. Song, K.N., X.P. Han, and G.S. Shao, Electronic properties of rutile TiO_2 doped with 4d transition metals: First-principles study. Journal of Alloys and Compounds, 2013. 551: pages 118-124.

424. Lin, C.P., H. Chen, A. Nakaruk, P. Koshy, and C.C. Sorrell, Effect of annealing temperature on the photocatalytic activity of TiO_2 thin films. 10th Eco-Energy and Materials Science and Engineering Symposium, 2013. 34: pages 627-636.

425. Giannini, C., M. Ladisa, D. Altamura, D. Siliqi, T. Sibillano, and L. De Caro, X-ray diffraction: a powerful technique for the multiple length scale structural analysis of nanomaterials. Crystals, 2016. 6(8): pages 1-22.

426. Ambrus, Z., N. Balazs, T. Alapi, G. Wittmann, P. Sipos, A. Dombi, and K. Mogyorosi, Synthesis, structure and photocatalytic properties of Fe(III)-doped TiO_2 prepared from $TiCl_3$. Applied Catalysis B-Environmental, 2008. 81(1-2): pages 27-37.

427. Lee, J., S.J. Lee, W.B. Han, H. Jeon, J. Park, W. Jang, and C.S. Yoon, Deposition temperature dependence of titanium oxide thin films grown by remote-plasma atomic layer deposition. Physica Status Solidi a-Applications and Materials Science, 2013. 210(2): pages 276-284.

428. Hwu, J.J. and D.C. Joy, Dynamic charging in the low voltage SEM. Electron Microscopy 1998, Vol 1: General Interest and Instrumentation, 1998: pages 467-468.

429. Leslie, S.A. and J.C. Mitchell, Removing gold coating from SEM samples. Palaeontology, 2007. 50: pages 1459-1461.

430. Statham, P.J., Limitations to accuracy in extracting characteristic line intensities from x-ray spectra. Journal of Research of the National Institute of Standards and Technology, 2002. 107(6): pages 531-546.

431. Choel, M., K. Deboudt, J. Osan, P. Flament, and R. Van Grieken, Quantitative determination of low-Z elements in single atmospheric particles on boron substrates by automated scanning electron microscopy - Energy-dispersive X-ray spectrometry. Analytical Chemistry, 2005. 77(17): pages 5686-5692.

432. Unocic, K.A., M.J. Mills, and G.S. Daehn, Effect of gallium focused ion beam milling on preparation of aluminium thin foils. Journal of Microscopy, 2010. 240(3): pages 227-238.

433. Bendersky, L.A. and F.W. Gayle, Electron diffraction using transmission electron microscopy. Journal of Research of the National Institute of Standards and Technology, 2001. 106(6): pages 997-1012.

434. Zhou, W.Z. and H.F. Greer, What can electron microscopy tell us beyond crystal structures? European Journal of Inorganic Chemistry, 2016(7): pages 941-950.

435. Tian, F., Y.P. Zhang, J. Zhang, and C.X. Pan, Raman spectroscopy: A new approach to measure the percentage of anatase TiO_2 exposed (001) facets. Journal of Physical Chemistry C, 2012. 116(13): pages 7515-7519.

436. Hammes, G.G., Spectroscopy for the biological sciences. Spectroscopy for the Biological Sciences, 2005: pages 1-180.

437. Jablonski, A. and C.J. Powell, Effective attenuation lengths for quantitative determination of surface composition by Auger-electron spectroscopy and X-ray photoelectron spectroscopy. Journal of Electron Spectroscopy and Related Phenomena, 2017. 218: pages 1-12.

438. Ivanov, S., A. Barylyak, K. Besaha, A. Dimitrova, S. Krischok, A. Bund, and J. Bobitski, Enhanced lithium ion storage in TiO_2 nanoparticles, induced by sulphur and carbon co-doping. Journal of Power Sources, 2016. 326: pages 270-278.

439. Kerber, S.J., J.J. Bruckner, K. Wozniak, S. Seal, S. Hardcastle, and T.L. Barr, The nature of hydrogen in x-ray photoelectron spectroscopy: General patterns from hydroxides to hydrogen bonding. Journal of Vacuum Science & Technology a-Vacuum Surfaces and Films, 1996. 14(3): pages 1314-1320.

440. Liu, J.M., L. Han, N. An, L. Xing, H.Y. Ma, L. Cheng, J.C. Yang, and Q.C. Zhang, Enhanced visible-light photocatalytic activity of carbonate-doped anatase TiO_2 based on the electron-withdrawing bidentate carboxylate linkage. Applied Catalysis B-Environmental, 2017. 202: pages 642-652.

441. Georgios, P. and S.M. Wolfgang, X-ray photoelectron spectroscopy of anatase-TiO_2 coated carbon nanotubes. Solid State Chemistry and Photocatalysis of Titanium Dioxide, 2010. 162: pages 163-177.

442. Shard, A.G., R. Havelund, M.P. Seah, S.J. Spencer, I.S. Gilmore, N. Winograd, D. Mao, T. Miyayama, E. Niehuis, D. Rading, and R. Moellers, Argon cluster

ion beams for organic depth profiling: results from a VAMAS interlaboratory study. Analytical Chemistry, 2012. 84(18): pages 7865-7873.

443. Hernandez-Arriaga, H., E. Lopez-Luna, E. Martinez-Guerra, M.M. Turrubiartes, A.G. Rodriguez, and M.A. Vidal, Growth of HfO_2/TiO_2 nanolaminates by atomic layer deposition and HfO_2-TiO_2 by atomic partial layer deposition. Journal of Applied Physics, 2017. 121(6): pages 064301-064312.

444. Huang, N.K., D.Z. Wang, Z. Lu, and L.B. Lin, X-ray photoelectron spectroscopy characterization of TiO_2 films deposited by dynamic ion beam mixing. Surface & Coatings Technology, 1994. 70(1): pages 69-71.

445. Wang, Q.G., J. Biener, X.C. Guo, E. Farfan-Arribas, and R.J. Madix, Reactivity of stoichiometric and defective TiO_2 (110) surfaces toward DCOOD decomposition. Journal of Physical Chemistry B, 2003. 107(42): pages 11709-11720.

446. Fletcher, J.S. and J.C. Vickerman, Secondary Ion Mass Spectrometry: characterizing complex samples in two and three dimensions. Analytical Chemistry, 2013. 85(2): pages 610-639.

447. Wagner, M.S., S.L. McArthur, M.C. Shen, T.A. Horbett, and D.G. Castner, Limits of detection for time of flight secondary ion mass spectrometry (ToF-SIMS) and X-ray photoelectron spectroscopy (XPS): detection of low amounts of adsorbed protein. Journal of Biomaterials Science-Polymer Edition, 2002. 13(4): pages 407-428.

448. Viezbicke, B.D., S. Patel, B.E. Davis, and D.P. Birnie, Evaluation of the Tauc method for optical absorption edge determination: ZnO thin films as a model system. Physica Status Solidi B-Basic Solid State Physics, 2015. 252(8): pages 1700-1710.

449. Kang, H., C.S. Lee, D.Y. Kim, J. Kim, W. Choi, and H. Kim, Photocatalytic effect of thermal atomic layer deposition of TiO_2 on stainless steel. Applied Catalysis B-Environmental, 2011. 104(1-2): pages 6-11.

450. Kim, K.-D., W.S. Tai, Y.D. Kim, S.-J. Cho, I.-S. Bae, J.-H. Boo, B.C. Lee, K.H. Yang, and O.K. Park, Change in water contact angle of carbon contaminated

TiO_2 surfaces by high-energy electron beam. Bulletin of the Korean Chemical Society, 2009. 30(5): pages 1067-1070.

451. Sakai, N., A. Fujishima, T. Watanabe, and K. Hashimoto, Quantitative evaluation of the photoinduced hydrophilic conversion properties of TiO_2 thin film surfaces by the reciprocal of contact angle. Journal of Physical Chemistry B, 2003. 107(4): pages 1028-1035.
452. Zhang, L.W., R. Dillert, D. Bahnemann, and M. Vormoor, Photo-induced hydrophilicity and self-cleaning: models and reality. Energy & Environmental Science, 2012. 5(6): pages 7491-7507.
453. Kaariainen, M.L., T.O. Kaariainen, and D.C. Cameron, Titanium dioxide thin films, their structure and its effect on their photoactivity and photocatalytic properties. Thin Solid Films, 2009. 517(24): pages 6666-6670.
454. Toh, A.G.G., M.G. Nolan, R. Cai, and D.L. Butler, Reversible wetting of titanium dioxide films, in Device and Process Technologies for Microelectronics, Mems, Photonics and Nanotechnology Iv, H.H. Tan, J.C. Chiao, L. Faraone, C. Jagadish, J. Williams, and A.R. Wilson, Editors. 2008. pages 80004-80004.
455. Gao, L.C. and T.J. McCarthy, Contact angle hysteresis explained. Langmuir, 2006. 22(14): pages 6234-6237.
456. Chhasatia, V.H., A.S. Joshi, and Y. Sun, Effect of relative humidity on contact angle and particle deposition morphology of an evaporating colloidal drop. Applied Physics Letters, 2010. 97(23): pages 231901-231909.
457. Wenzel, R.N., Surface roughness and contact angle. Journal of Physical and Colloid Chemistry, 1949. 53(9): pages 1466-1467.
458. Evans, P., S. Mantke, A. Mills, A. Robinson, and D.W. Sheel, A comparative study of three techniques for determining photocatalytic activity. Journal of Photochemistry and Photobiology a-Chemistry, 2007. 188(2-3): pages 387-391.
459. Ferrari-Lima, A.M., R.P. de Souza, S.S. Mendes, R.G. Marques, M.L. Gimenes, and N.R.C. Fernandes-Machado, Photodegradation of benzene, toluene and xylenes under visible light applying N-doped mixed TiO_2 and ZnO catalysts. Catalysis Today, 2015. 241: pages 40-46.

460. Smirnova, N., T. Fesenko, M. Zhukovsky, J. Goworek, and A. Eremenko, Photodegradation of stearic acid adsorbed on superhydrophilic TiO_2 surface: In situ FT-IR and LDI study. Nanoscale Research Letters, 2015. 10: pages 1-7.

461. Mills, A. and J. Wang, Simultaneous monitoring of the destruction of stearic acid and generation of carbon dioxide by self-cleaning semiconductor photocatalytic films. Journal of Photochemistry and Photobiology a-Chemistry, 2006. 182(2): pages 181-186.

462. Mills, A. and M. McFarlane, Current and possible future methods of assessing the activities of photocatalyst films. Catalysis Today, 2007. 129(1-2): pages 22-28.

463. Remillard, J.T., J.R. McBride, K.E. Nietering, A.R. Drews, and X. Zhang, Real time in situ spectroscopic ellipsometry studies of the photocatalytic oxidation of stearic acid on titania films. Journal of Physical Chemistry B, 2000. 104(18): pages 4440-4447.

464. Deegan, R.D., O. Bakajin, T.F. Dupont, G. Huber, S.R. Nagel, and T.A. Witten, Capillary flow as the cause of ring stains from dried liquid drops. Nature, 1997. 389(6653): pages 827-829.

465. Bauer, C., P. Jacques, and A. Kalt, Photooxidation of an azo dye induced by visible light incident on the surface of TiO_2. Journal of Photochemistry and Photobiology a-Chemistry, 2001. 140(1): pages 87-92.

466. Bandara, J., K. Tennakone, and J. Kiwi, Surface mechanism of molecular recognition between aminophenols and iron oxide surfaces. Langmuir, 2001. 17(13): pages 3964-3969.

467. Epling, G.A. and C. Lin, Investigation of retardation effects on the titanium dioxide photodegradation system. Chemosphere, 2002. 46(6): pages 937-944.

468. Epling, G.A. and C. Lin, Photoassisted bleaching of dyes utilizing TiO_2 and visible light. Chemosphere, 2002. 46(4): pages 561-570.

469. Arslan, I., I.A. Balcioglu, and D.W. Bahnemann, Heterogeneous photocatalytic treatment of simulated dyehouse effluents using novel TiO_2-

photocatalysts. Applied Catalysis B-Environmental, 2000. 26(3): pages 193-206.

470. Sokmen, M. and A. Ozkan, Decolourising textile wastewater with modified titania: the effects of inorganic anions on the photocatalysis. Journal of Photochemistry and Photobiology a-Chemistry, 2002. 147(1): pages 77-81.

471. Binas, V.D., K. Sambani, T. Maggos, A. Katsanaki, and G. Kiriakidis, Synthesis and photocatalytic activity of Mn-doped TiO_2 nanostructured powders under UV and visible light. Applied Catalysis B-Environmental, 2012. 113: pages 79-86.

472. Dey, N.K., M.J. Kim, K.-D. Kim, H.O. Seo, D. Kim, Y.D. Kim, D.C. Lim, and K.H. Lee, Adsorption and photocatalytic degradation of methylene blue over TiO_2 films on carbon fiber prepared by atomic layer deposition. Journal of Molecular Catalysis a-Chemical, 2011. 337(1-2): pages 33-38.

473. Kerkez, O. and I. Boz, Efficient removal of methylene blue by photocatalytic degradation with TiO_2 nanorod array thin films. Reaction Kinetics Mechanisms and Catalysis, 2013. 110(2): pages 543-557.

474. Rashad, M.M., E.M. Elsayed, M.S. Al-Kotb, and A.E. Shalan, The structural, optical, magnetic and photocatalytic properties of transition metal ions doped TiO_2 nanoparticles. Journal of Alloys and Compounds, 2013. 581: pages 71-78.

475. Yogi, C., K. Kojima, N. Wada, H. Tokumoto, T. Takai, T. Mizoguchi, and H. Tamiaki, Photocatalytic degradation of methylene blue by TiO_2 film and Au particles-TiO_2 composite film. Thin Solid Films, 2008. 516(17): pages 5881-5884.

476. Xu, X., J. Wang, J. Tian, X. Wang, J. Dai, and X. Liu, Hydrothermal and post-heat treatments of TiO_2/ZnO composite powder and its photodegradation behavior on methyl orange. Ceramics International, 2011. 37(7): pages 2201-2206.

477. Zhang, J., S. Yan, L. Fu, F. Wang, M. Yuan, G. Luo, Q. Xu, X. Wang, and C. Li, Photocatalytic degradation of rhodamine B on anatase, rutile, and brookite TiO_2. Chinese Journal of Catalysis, 2011. 32(6): pages 983-991.

478. Bae, S., S. Kim, S. Lee, and W. Choi, Dye decolorization test for the activity assessment of visible light photocatalysts: Realities and limitations. Catalysis Today, 2014. 224: pages 21-28.
479. Mills, A. and M. McGrady, A study of new photocatalyst indicator inks. Journal of Photochemistry and Photobiology a-Chemistry, 2008. 193(2-3): pages 228-236.
480. Mills, A., A. Cusick, and J. Hepburn, The kinetics of semiconductor photocatalysis in activity-indicator films. Journal of Advanced Oxidation Technologies, 2009. 12(2): pages 152-157.
481. Photocatalyst activity measuring inks. 2018 [cited 2018 07/01/2018]; Available from: http://www.fp7-intec.eu/inks.html.
482. Kafizas, A., D. Adriaens, A. Mills, and I.P. Parkin, Simple method for the rapid simultaneous screening of photocatalytic activity over multiple positions of self-cleaning films. Physical Chemistry Chemical Physics, 2009. 11(37): pages 8367-8375.
483. Mills, A., C. O'Rourke, and N. Wells, A smart ink for the assessment of low activity photocatalytic surfaces. Analyst, 2014. 139(21): pages 5409-5414.
484. Donlan, R.M., Biofilms: Microbial life on surfaces. Emerging Infectious Diseases, 2002. 8(9): pages 881-890.
485. Johnson, M.B. and A.K. Criss, Fluorescence microscopy methods for determining the viability of bacteria in association with mammalian cells. Jove-Journal of Visualized Experiments, 2013(79): pages 1-9.
486. Netuschil, L., T.M. Auschill, A. Sculean, and N.B. Arweiler, Confusion over live/dead stainings for the detection of vital microorganisms in oral biofilms - which stain is suitable? Bmc Oral Health, 2014. 14: pages 1-12.
487. Bak, T., J. Nowotny, N.J. Sucher, and E.D. Wachsman, Photocatalytic water disinfection on oxide semiconductors: Part 1-basic concepts of TiO_2 photocatalysis. Advances in Applied Ceramics, 2012. 111(1-2): pages 4-15.
488. Yu, J.C., W.K. Ho, J.G. Yu, H. Yip, P.K. Wong, and J.C. Zhao, Efficient visible-light-induced photocatalytic disinfection on sulfur-doped nanocrystalline titania. Environmental Science & Technology, 2005. 39(4): pages 1175-1179.

489. Sauer, M.L. and D.F. Ollis, Photocatalyzed oxidation of ethanol and acetaldehyde in humidified air. Journal of Catalysis, 1996. 158(2): pages 570-582.

490. Schwitzgebel, J., J.G. Ekerdt, H. Gerischer, and A. Heller, Role of the oxygen molecule and of the photogenerated electron in TiO_2 photocatalyzed air oxidation reactions. Journal of Physical Chemistry, 1995. 99(15): pages 5633-5638.

491. Brigden, C.T., S. Poulston, M.V. Twigg, A.P. Walker, and A.J.J. Wilkins, Photo-oxidation of short-chain hydrocarbons over titania. Applied Catalysis B-Environmental, 2001. 32(1-2): pages 63-71.

492. Augugliaro, V., S. Coluccia, V. Loddo, L. Marchese, G. Martra, L. Palmisano, and M. Schiavello, Photocatalytic oxidation of gaseous toluene on anatase TiO_2 catalyst: mechanistic aspects and FT-IR investigation. Applied Catalysis B-Environmental, 1999. 20(1): pages 15-27.

493. Ameen, M.M. and G.B. Raupp, Reversible catalyst deactivation in the photocatalytic oxidation of dilute o-xylene in air. Journal of Catalysis, 1999. 184(1): pages 112-122.

494. Ahmed, M.S. and Y.A. Attia, Aerogel materials for photocatalytic detoxification of cyanide wastes in water. Journal of Non-Crystalline Solids, 1995. 186: pages 402-407.

495. Piccinini, P., C. Minero, M. Vincenti, and E. Pelizzetti, Photocatalytic mineralization of nitrogen-containing benzene derivatives. Catalysis Today, 1997. 39(3): pages 187-195.

496. Maurino, V., C. Minero, E. Pelizzetti, P. Piccinini, N. Serpone, and H. Hidaka, The fate of organic nitrogen under photocatalytic conditions: degradation of nitrophenols and aminophenols on irradiated TiO_2. Journal of Photochemistry and Photobiology a-Chemistry, 1997. 109(2): pages 171-176.

497. Bhatkhande, D.S., V.G. Pangarkar, and A. Beenackers, Photocatalytic degradation of nitrobenzene using titanium dioxide and concentrated solar radiation: chemical effects and scaleup. Water Research, 2003. 37(6): pages 1223-1230.

498. Low, G.K.C., S.R. McEvoy, and R.W. Matthews, Formation of nitrate and ammonium ions in titanium dioxide mediated photocatalytic degradation of organic compounds containing nitrogen atoms. Environmental Science & Technology, 1991. 25(3): pages 460-467.

499. Nohara, K., H. Hidaka, E. Pelizzetti, and N. Serpone, Dependence on chemical structure of the production of NH^{4+} and or NO^{3-} ions during the photocatalyzed oxidation of nitrogen-containing substances at the titania water interface. Catalysis Letters, 1996. 36(1-2): pages 115-118.

500. Jaiswal, R., N. Patel, D.C. Kothari, and A. Miotello. Visible light photocatalytic degradation of 4-chlorophenol using vanadium and nitrogen co-doped TiO_2. in 57th DAE Solid State Physics Symposium. 2012. Indian Inst Technol, Bombay, INDIA.

501. Ho, W.K., J.C. Yu, and S.C. Lee, Low-temperature hydrothermal synthesis of S-doped TiO_2 with visible light photocatalytic activity. Journal of Solid State Chemistry, 2006. 179(4): pages 1171-1176.

502. Krijgsheld, K.R. and A. Vandergen, Assessment of the impact of the emission of certain organochlorine compounds on the aquatic environment 1. monochlorophenols and 2,4-dichlorophenol. Chemosphere, 1986. 15(7): pages 825-860.

503. Manilal, V.B., A. Haridas, R. Alexander, and G.D. Surender, Photocatalytic treatment of toxic organics in waste water - toxicity of photodegradation products. Water Research, 1992. 26(8): pages 1035-1038.

504. Dibble, L.A. and G.B. Raupp, Fludized bed photocatalytic oxidation of trichloroethylene in contaminated airstreams. Environmental Science & Technology, 1992. 26(3): pages 492-495.

505. Zaleska, A., E. Grabowska, J.W. Sobczak, M. Gazda, and J. Hupka, Photocatalytic activity of boron-modified TiO_2 under visible light: The effect of boron content, calcination temperature and TiO_2 matrix. Applied Catalysis B-Environmental, 2009. 89(3-4): pages 469-475.

506. Chowdhury, P., J. Moreira, H. Gomaa, and A.K. Ray, Visible solar light driven photocatalytic degradation of phenol with dye-sensitized TiO_2: Parametric

and kinetic study. Industrial & Engineering Chemistry Research, 2012. 51(12): pages 4523-4532.

507. Wang, K.H., Y.H. Hsieh, M.Y. Chou, and C.Y. Chang, Photocatalytic degradation of 2-chloro and 2-nitrophenol by titanium dioxide suspensions in aqueous solution. Applied Catalysis B-Environmental, 1999. 21(1): pages 1-8.

508. Stafford, U., K.A. Gray, and P.V. Kamat, Photocatalytic degradation of 4-chlorophenol: The effects of varying TiO_2 concentration and light wavelength. Journal of Catalysis, 1997. 167(1): pages 25-32.

509. Zhang, R.B., L. Gao, and Q.H. Zhang, Photodegradation of surfactants on the nanosized TiO_2 prepared by hydrolysis of the alkoxide titanium. Chemosphere, 2004. 54(3): pages 405-411.

510. Dalton, J.S., P.A. Janes, N.G. Jones, J.A. Nicholson, K.R. Hallam, and G.C. Allen, Photocatalytic oxidation of NO_x gases using TiO_2: a surface spectroscopic approach. Environmental Pollution, 2002. 120(2): pages 415-422.

511. Yu, J.G., H.G. Yu, C.H. Ao, S.C. Lee, J.C. Yu, and W.K. Ho, Preparation, characterization and photocatalytic activity of in situ Fe-doped TiO_2 thin films. Thin Solid Films, 2006. 496(2): pages 273-280.

512. ASTM International, W.C., PA, USA, ASTM F0390-11, in Standard Test Method for Sheet Resistance of Thin Metallic Films With a Collinear Four-Probe Array. 2011, ASTM International: ASTM International, West Conshohocken, PA, USA.

513. Li, M.Y., M.C. Yang, E. Vargas, K. Neff, A. Vanli, and R. Liang, Analysis of variance on thickness and electrical conductivity measurements of carbon nanotube thin films. Measurement Science and Technology, 2016. 27(9): pages 1-13.

514. Paz, Y., Z. Luo, L. Rabenberg, and A. Heller, Photooxidative self-cleaning transparent titanium dioxide films on glass. Journal of Materials Research, 1995. 10(11): pages 2842-2848.

515. Mills, A., J. Wang, and M. McGrady, Method of rapid assessment of photocatalytic activities of self-cleaning films. Journal of Physical Chemistry B, 2006. 110(37): pages 18324-18331.

516. Fagan, R., D.E. McCormack, D.D. Dionysiou, and S.C. Pillai, A review of solar and visible light active TiO_2 photocatalysis for treating bacteria, cyanotoxins and contaminants of emerging concern. Materials Science in Semiconductor Processing, 2016. 42: pages 2-14.

517. Activ, P. Pilkington Activ. 2018 [cited 2018 05/08/2018]; Available from: http://www.pilkington.com/products/bp/bybenefit/selfcleaning/activ/default.htm.

518. Saint-Gobain. Saint-Gobain world leader of habitat. 2018 [cited 2018 05/08/2018]; Available from: https://www.saint-gobain.com/en.

519. Serpone, N., Is the band gap of pristine TiO_2 narrowed by anion- and cation-doping of titanium dioxide in second-generation photocatalysts? Journal of Physical Chemistry B, 2006. 110(48): pages 24287-24293.

520. Kernazhitsky, L., V. Shymanovska, T. Gavrilko, V. Naumov, L. Fedorenko, V. Kshnyakin, and J. Baran, Room temperature photoluminescence of anatase and rutile TiO_2 powders. Journal of Luminescence, 2014. 146: pages 199-204.

521. Lafjah, M., A. Mayoufi, E. Schaal, F. Djafri, A. Bengueddach, N. Keller, and V. Keller, TiO_2 nanorods for gas phase photocatalytic applications. Catalysis Today, 2014. 235: pages 193-200.

522. Ashkarran, A.A., H. Hamidinezhad, H. Haddadi, and M. Mahmoudi, Double-doped TiO_2 nanoparticles as an efficient visible-light-active photocatalyst and antibacterial agent under solar simulated light. Applied Surface Science, 2014. 301: pages 338-345.

523. Khan, J.A., C. Han, N.S. Shah, H.M. Khan, M.N. Nadagouda, V. Likodimos, P. Falaras, K. O'Shea, and D.D. Dionysiou, Ultraviolet visible light sensitive high surface area phosphorous-fluorine-co-doped TiO_2 nanoparticles for the degradation of atrazine in water. Environmental Engineering Science, 2014. 31(7): pages 435-446.

524. Mohamed, R.M. and E. Aazam, Synthesis and characterization of P-doped TiO_2 thin-films for photocatalytic degradation of butyl benzyl phthalate under visible-light irradiation. Chinese Journal of Catalysis, 2013. 34(6): pages 1267-1273.

525. Sun, M.X., X.Y. Zhang, J. Li, X.L. Cui, D.L. Sun, and Y.H. Lin, Thermal formation of silicon-doped TiO_2 thin films with enhanced visible light photoelectrochemical response. Electrochemistry Communications, 2012. 16(1): pages 26-29.

526. Gurunathan, K., P. Maruthamuthu, and M.V.C. Sastri, Photocatalytic hydrogen production by dye-sensitized Pt/SnO_2 and $Pt/SnO_2/RuO_2$ in aqueous methyl viologen solution. International Journal of Hydrogen Energy, 1997. 22(1): pages 57-62.

527. Tamiolakis, I., I.N. Lykakis, and G.S. Armatas, Mesoporous CdS-sensitized TiO_2 nanoparticle assemblies with enhanced photocatalytic properties: Selective aerobic oxidation of benzyl alcohols. Catalysis Today, 2015. 250: pages 180-186.

528. Yao, H., X. Li, L. Liu, J. Niu, D. Ding, Y. Mu, P. Su, G. Wang, W. Fu, and H. Yang, Photoelectrolchemical performance of PbS/CdS quantum dots co-sensitized TiO_2 nanosheets array film photoelectrodes. Journal of Alloys and Compounds, 2015. 647: pages 402-406.

529. Sakthivel, S., M.V. Shankar, M. Palanichamy, B. Arabindoo, D.W. Bahnemann, and V. Murugesan, Enhancement of photocatalytic activity by metal deposition: characterisation and photonic efficiency of Pt, Au and Pd deposited on TiO_2 catalyst. Water Research, 2004. 38(13): pages 3001-3008.

530. Bamwenda, G.R., S. Tsubota, T. Nakamura, and M. Haruta, Photoassisted hydrogen production from a water-ethanol solution - A comparison of activities of $Au-TiO_2$ and $Pt-TiO_2$. Journal of Photochemistry and Photobiology a-Chemistry, 1995. 89(2): pages 177-189.

531. Subramanian, V., E. Wolf, and P.V. Kamat, Semiconductor-metal composite nanostructures. To what extent do metal nanoparticles improve the photocatalytic activity of TiO_2 films? Journal of Physical Chemistry B, 2001. 105(46): pages 11439-11446.

532. Jakob, M., H. Levanon, and P.V. Kamat, Charge distribution between UV-irradiated TiO_2 and gold nanoparticles: Determination of shift in the fermi level. Nano Letters, 2003. 3(3): pages 353-358.

533. Kastus. Kastus. 2017 [cited 2017 20/07/2017]; Available from: http://www.kastus.com/.

534. Pelaez, M., N.T. Nolan, S.C. Pillai, M.K. Seery, P. Falaras, A.G. Kontos, P.S.M. Dunlop, J.W.J. Hamilton, J.A. Byrne, K. O'Shea, M.H. Entezari, and D.D. Dionysiou, A review on the visible light active titanium dioxide photocatalysts for environmental applications. Applied Catalysis B-Environmental, 2012. 125: pages 331-349.

535. Szabo-Bardos, E., Z. Zsilak, and O. Horvath, Photocatalytic degradation of anionic surfactant in titanium dioxide suspension, in Colloids for Nano- and Biotechnology, Z.D. Horvolgyi and E. Kiss, Editors. 2008. pages 21-28.

536. Patel, N., R. Jaiswal, T. Warang, G. Scarduelli, A. Dashora, B.L. Ahuja, D.C. Kothari, and A. Miotello, Efficient photocatalytic degradation of organic water pollutants using V-N-codoped TiO_2 thin films. Applied Catalysis B-Environmental, 2014. 150: pages 74-81.

537. Xu, B., J.-H. Wu, L.-Q. Fan, M.-L. Huang, and J.-M. Lin, Effect of surfactant on photoelectric properties of dye-sensitized solar cell. Chinese Journal of Inorganic Chemistry, 2008. 24(11): pages 1900-1906.

538. Tamilarasan, T.R., R. Rajendran, G. Rajagopal, and J. Sudagar, Effect of surfactants on the coating properties and corrosion behaviour of Ni-P-nano-TiO_2 coatings. Surface & Coatings Technology, 2015. 276: pages 320-326.

539. International Organization for Standardization, G., Switzerland, ISO 10545:2016, in Ceramic tiles -- Part 13: Determination of chemical resistance. 2016, International Organization for Standardization: International Organization for Standardization, Geneva, Switzerland. page 9.

540. Soares, J.M.C., M. Hall, M. Cristofolini, and M. Bowker, The role of impurities on the low temperature CO oxidation on Au/TiO_2. Catalysis Letters, 2006. 109(1-2): pages 103-108.

541. Cao, S., H.Q. Wang, F.X. Yu, M.P. Shi, S. Chen, X.L. Weng, Y. Liu, and Z.B.A. Wu, Catalyst performance and mechanism of catalytic combustion of

dichloromethane (CH_2Cl_2) over Ce doped TiO_2. Journal of Colloid and Interface Science, 2016. 463: pages 233-241.

542. Beamson, G. and D. Briggs, High-resolution monochromated x-ray photoelectron-spectroscopy of organic polymers - a comparison between solid-state data for organic polymers and gas-phase data for small molecules. Molecular Physics, 1992. 76(4): pages 919-936.

543. Hart, J.N., P.W. May, N.L. Allan, K.R. Hallam, F. Claeyssens, G.M. Fuge, M. Ruda, and P.J. Heard, Towards new binary compounds: Synthesis of amorphous phosphorus carbide by pulsed laser deposition. Journal of Solid State Chemistry, 2013. 198: pages 466-474.

544. Yamanaka, H., K. Nakahata, and R. Terai, Structure of Na_2O-TiO_2-SiO_2 glasses from the viewpoint of non-binding oxygen measured by XPS. Journal of Non-Crystalline Solids, 1987. 95-6: pages 405-410.

545. Mekki, A., D. Holland, C.F. McConville, and M. Salim, An XPS study of iron sodium silicate glass surfaces. Journal of Non-Crystalline Solids, 1996. 208(3): pages 267-276.

546. Fujishima, A. and T.N. Rao, Recent advances in heterogeneous TiO_2 photocatalysis. Proceedings of the Indian Academy of Sciences-Chemical Sciences, 1997. 109(6): pages 471-486.

547. Kurtoglu, M.E., T. Longenbach, and Y. Gogotsi, Preventing sodium poisoning of photocatalytic TiO_2 films on glass by metal doping. International Journal of Applied Glass Science, 2011. 2(2): pages 108-116.

548. Syrgiannis, Z., V. La Parola, C. Hadad, M. Lucio, E. Vazquez, F. Giacalone, and M. Prato, An atom-economical approach to functionalized single-walled carbon nanotubes: reaction with disulfides. Angewandte Chemie-International Edition, 2013. 52(25): pages 6480-6483.

549. Berger, F., E. Beche, R. Berjoan, D. Klein, and A. Chambaudet, An XPS and FTIR study of SO_2 adsorption on SnO_2 surfaces. Applied Surface Science, 1996. 93(1): pages 9-16.

550. Moser, M., A.P. Amrute, and J. Perez-Ramirez, Impact of feed impurities on catalysts for chlorine recycling. Applied Catalysis B-Environmental, 2015. 162: pages 602-609.

551. Cantau, C., S. Larribau, T. Pigot, M. Simon, M.T. Maurette, and S. Lacombe, Oxidation of nauseous sulfur compounds by photocatalysis or photosensitization. Catalysis Today, 2007. 122(1-2): pages 27-38.

552. Thompson, T.L., D.A. Panayotov, and J.T. Yates, Adsorption and thermal decomposition of 2-chloroethyl ethyl sulfide on TiO_2 surfaces. Journal of Physical Chemistry B, 2004. 108(43): pages 16825-16833.

553. Papirer, E., R. Lacroix, J.B. Donnet, G. Nanse, and P. Fioux, XPS study of the halogenation of carbon black 2. chlorination. Carbon, 1995. 33(1): pages 63-72.

554. Li, J.W., P. Zhao, and S.T. Liu, SnO_x-MnO_x-TiO_2 catalysts with high resistance to chlorine poisoning for low-temperature chlorobenzene oxidation. Applied Catalysis a-General, 2014. 482: pages 363-369.

555. Ohsaka, T., F. Izumi, and Y. Fujiki, Raman spectrum of anatase TiO_2. Journal of Raman Spectroscopy, 1978. 7(6): pages 321-324.

556. Beard, M.A., O.R. Ghita, and K.E. Evans, Using Raman spectroscopy to monitor surface finish and roughness of components manufactured by selective laser sintering. Journal of Raman Spectroscopy, 2011. 42(4): pages 744-748.

557. Wang, Y., M.Z. Huang, K.H. Wang, X. Liu, Y. Zou, B. Song, and J. Chen, Raman enhancement in metal-cladding waveguide and the influence of the metal film surface roughness. Journal of Lightwave Technology, 2016. 34(15): pages 3616-3621.

558. Marin, E., L. Guzman, A. Lanzutti, W. Ensinger, and L. Fedrizzi, Multilayer Al_2O_3/TiO_2 Atomic Layer Deposition coatings for the corrosion protection of stainless steel. Thin Solid Films, 2012. 522: pages 283-288.

559. Neumark, G.F., Achievement of well conducting wide band gap semiconductors - Role of solubility and nonequilibrium impurity incorporation. Physical Review Letters, 1989. 62(15): pages 1800-1803.

560. Weissmann, M. and L.A. Errico, The role of vacancies, impurities and crystal structure in the magnetic properties of TiO_2. Physica B-Condensed Matter, 2007. 398(2): pages 179-183.

561. Liu, Y., C.Y. Liu, Q.H. Rong, Z. Zhang, and C.Y. Wang, Effects of silver ion doping on the surface defect characteristics of TiO_2. Research on Chemical Intermediates, 2004. 30(4-5): pages 569-577.

562. Diebold, U., The surface science of titanium dioxide. Surface Science Reports, 2003. 48(5-8): pages 53-229.

563. Moon, J., H. Takagi, Y. Fujishiro, and M. Awano, Preparation and characterization of the Sb-doped TiO_2 photocatalysts. Journal of Materials Science, 2001. 36(4): pages 949-955.

564. Iancu, A.T., M. Logar, J. Park, and F.B. Prinz, Atomic layer deposition of undoped TiO_2 exhibiting p-type conductivity. Acs Applied Materials & Interfaces, 2015. 7(9): pages 5134-5140.

565. Li, L., C.F. Xia, W.S. Li, A.M. Ji, C.Y. Zhu, L.J. Zhang, Z.O. Wang, J.F. Yang, and L.F. Mao, Nature of the interstitials in titanium dioxide and their impact on transmission coefficient: ab initio calculations. Journal of Nanomaterials, 2015: pages 1-9.

566. Komaguchi, K., T. Maruoka, H. Nakano, I. Imae, Y. Ooyama, and Y. Harima, Electron transfer reaction of oxygen species on TiO_2 nanoparticles induced by sub-band-gap illumination. Journal of Physical Chemistry C, 2010. 114(2): pages 1240-1245.

567. Vukelic, S., P. Kongsuwan, S. Ryu, and Y.L. Yao, Ultrafast laser induced structural modification of fused silica part II: Spatially resolved and decomposed Raman spectral analysis. Journal of Manufacturing Science and Engineering-Transactions of the Asme, 2010. 132(6): pages 061013-061021.

568. Trzcinski, K., A. Borowska-Centkowska, M. Sawczak, and A. Lisowska-Oleksiak, Photoelectrochemical properties of BIMEVOX (ME = Cu, Zn, Mn) electrodes in contact with aqueous electrolyte. Solid State Ionics, 2015. 271: pages 63-68.

569. Carter, E.A., M.D. Hargreaves, T.P. Kee, M.A. Pasek, and H.G.M. Edwards, A Raman spectroscopic study of a fulgurite. Philosophical Transactions of the Royal Society a-Mathematical Physical and Engineering Sciences, 2010. 368(1922): pages 3087-3097.

570. Park, M.S., G.X. Wang, Y.M. Kang, D. Wexler, S.X. Dou, and H.K. Liu, Preparation and electrochemical properties of SnO_2 nanowires for application in lithium-ion batteries. Angewandte Chemie-International Edition, 2007. 46(5): pages 750-753.

571. Chu, L., Z.F. Qin, J.P. Yang, and X.A. Li, Anatase TiO_2 nanoparticles with exposed {001} facets for efficient Dye-Sensitized Solar Cells. Scientific Reports, 2015. 5: pages 1-11.

572. Miao, L., P. Jin, K. Kaneko, A. Terai, N. Nabatova-Gabain, and S. Tanemura, Preparation and characterization of polycrystalline anatase and rutile TiO_2 thin films by rf magnetron sputtering. Applied Surface Science, 2003. 212: pages 255-263.

573. Chen, P., A novel synthesis of Ti^{3+} self-doped Ag_2O/TiO_2 (p-n) nanoheteroj unctions for enhanced visible photocatalytic activity. Materials Letters, 2016. 163: pages 130-133.

574. Zhang, Y., Z.P. Xing, X.F. Liu, Z.Z. Li, X.Y. Wu, J.J. Jiang, M. Li, Q. Zhu, and W. Zhou, Ti^{3+} self doped blue TiO_2 single-crystalline nanorods for efficient solar driven photocatalytic performance. Acs Applied Materials & Interfaces, 2016. 8(40): pages 26851-26859.

575. Wu, W.Q., K. Bhattacharyya, K. Gray, and E. Weitz, Photoinduced reactions of surface bound species on titania nanotubes and platinized titania nanotubes: an in Situ FTIR study. Journal of Physical Chemistry C, 2013. 117(40): pages 20643-20655.

576. Murray, B.J., O. Li, J.T. Newberg, E.J. Menke, J.C. Hemminger, and R.M. Penner, Shape- and size-selective electrochemical synthesis of dispersed silver (I) oxide colloids. Nano Letters, 2005. 5(11): pages 2319-2324.

577. Veal, B.W., D.J. Lam, A.P. Paulikas, and W.Y. Ching, XPS study of CaO in sodium silicate glass. Journal of Non-Crystalline Solids, 1982. 49(1-3): pages 309-320.

578. U. UQG optics Fused Quartz Vitreosil 077. 2017 [cited 2017 19/05/2017]; Available from: http://www.uqgoptics.com/pdf/Fused%20Quartz%20-%20Vit%20077.pdf.

579. Haeberle, J., K. Henkel, H. Gargouri, F. Naumann, B. Gruska, M. Arens, M. Tallarida, and D. Schmeisser, Ellipsometry and XPS comparative studies of thermal and plasma enhanced atomic layer deposited Al_2O_3 films. Beilstein Journal of Nanotechnology, 2013. 4: pages 732-742.

580. Lewis, W.K., A.T. Rosenberger, J.R. Gord, C.A. Crouse, B.A. Harruff, K.A.S. Fernando, M.J. Smith, D.K. Phelps, J.E. Spowart, E.A. Guliants, and C.E. Bunker, Multispectroscopic (FTIR, XPS, and TOFMS-TPD) Investigation of the Core-Shell Bonding in Sonochemically Prepared Aluminum Nanoparticles Capped with Oleic Acid. Journal of Physical Chemistry C, 2010. 114(14): pages 6377-6380.

581. Xu, K., A.P. Milanov, M. Winter, D. Barreca, A. Gasparotto, H.W. Becker, and A. Devi, Heteroleptic guanidinate- and amidinate-based complexes of hafnium as new precursors for MOCVD of HfO2. European Journal of Inorganic Chemistry, 2010(11): pages 1679-1688.

582. Wang, S.L., C.G. Li, Z.L. Xiao, T. Chen, and G.Y. Wang, Highly efficient and stable PbO-ZrO_2 catalyst for the disproportionation of methyl phenyl carbonate to synthesize diphenyl carbonate. Journal of Molecular Catalysis a-Chemical, 2016. 420: pages 26-33.

583. Price, N.J., J.B. Reitz, R.J. Madix, and E.I. Solomon, A synchrotron XPS study of the vanadia-titania system as a model for monolayer oxide catalysts. Journal of Electron Spectroscopy and Related Phenomena, 1999. 98: pages 257-266.

584. Matsubara, M., R. Saniz, B. Partoens, and D. Lamoen, Doping anatase TiO_2 with group V-b and VI-b transition metal atoms: a hybrid functional first-principles study. Physical Chemistry Chemical Physics, 2017. 19(3): pages 1945-1952.

585. Mathews, N.R., E.R. Morales, M.A. Cortes-Jacome, and J.A.T. Antonio, TiO_2 thin films - Influence of annealing temperature on structural, optical and photocatalytic properties. Solar Energy, 2009. 83(9): pages 1499-1508.

586. Di Valentin, C., G. Pacchioni, and A. Selloni, Reduced and n-type doped TiO_2: Nature of Ti^{3+} species. Journal of Physical Chemistry C, 2009. 113(48): pages 20543-20552.

587. Shard, A.G., Detection limits in XPS for more than 6000 binary systems using Al and Mg Ka X-rays. Surface and Interface Analysis, 2014. 46(3): pages 175-185.

588. Liu, G., H.G. Yang, X. Wang, L. Cheng, H. Lu, L. Wang, G.Q. Lu, and H.-M. Cheng, Enhanced photoactivity of oxygen-deficient anatase TiO_2 sheets with dominant {001} facets. Journal of Physical Chemistry C, 2009. 113(52): pages 21784-21788.

589. Fei, C.X., H.X. Liu, X. Wang, and X.J. Fan, The influence of process parameters and pulse ratio of precursors on the characteristics of $La_{1-x}Al_xO_3$ films deposited by atomic layer deposition. Nanoscale Research Letters, 2015. 10: pages 1-9.

590. Jiang, H.B., J. Xing, Z.P. Chen, F. Tian, Q. Cuan, X.Q. Gong, and H.G. Yang, Enhancing photocatalytic activity of Sn doped TiO_2 dominated with {105} facets. Catalysis Today, 2014. 225: pages 18-23.

591. Jiang, G., Z. Lin, C. Chen, L. Zhu, Q. Chang, N. Wang, W. Wei, and H. Tang, TiO_2 nanoparticles assembled on graphene oxide nanosheets with high photocatalytic activity for removal of pollutants. Carbon, 2011. 49(8): pages 2693-2701.

592. Kim, Y., H.M. Hwang, L. Wang, I. Kim, Y. Yoon, and H. Lee, Solar-light photocatalytic disinfection using crystalline/amorphous low energy bandgap reduced TiO_2. Scientific Reports, 2016. 6: pages 1-12.

593. Wang, Z.P., X. Jun, W.M. Cai, B.X. Zhou, Z.G. He, C.G. Cai, and X.T. Hong, Visible light induced photodegradation of organic pollutants on nitrogen and fluorine co-doped TiO_2 photocatalyst. Journal of Environmental Sciences, 2005. 17(1): pages 76-80.

594. Mills, A., J. Hepburn, D. Hazafy, C. O'Rourke, J. Krysa, M. Baudys, M. Zlamal, H. Bartkova, C.E. Hill, K.R. Winn, M.E. Simonsen, E.G. Sogaard, S.C. Pillai, N.S. Leyland, R. Fagan, F. Neumann, C. Lampe, and T. Graumann, A simple, inexpensive method for the rapid testing of the photocatalytic activity of self-cleaning surfaces. Journal of Photochemistry and Photobiology a-Chemistry, 2013. 272: pages 18-20.

595. Mills, A., J. Hepburn, D. Hazafy, C. O'Rourke, N. Wells, J. Krysa, M. Baudys, M. Zlamal, H. Bartkova, C.E. Hill, K.R. Winn, M.E. Simonsen, E.G. Sogaard, S. Banerjee, R. Fagan, and S.C. Pillai, Photocatalytic activity indicator inks for probing a wide range of surfaces. Journal of Photochemistry and Photobiology a-Chemistry, 2014. 290: pages 63-71.

596. Junkar, I., M. Kulkarni, B. Drasler, N. Rugelj, N. Recek, D. Drobne, J. Kovac, P. Humpolicek, A. Iglic, and M. Mozetic, Enhanced biocompatibility of TiO_2 surfaces by highly reactive plasma. Journal of Physics D-Applied Physics, 2016. 49(24).

597. Nam, S.H. and J.H. Boo, Growth and surface treatment of TiO_2 nanorods using stearic acid solution. Thin Solid Films, 2013. 546: pages 35-37.

598. Broqvist, P., L.M. Molina, H. Gronbeck, and B. Hammer, Promoting and poisoning effects of Na and Cl coadsorption on CO oxidation over MgO-supported Au nanoparticles. Journal of Catalysis, 2004. 227(1): pages 217-226.

599. Kollu, K. and B. Ormeci, UV-induced self-aggregation of E-coli after low and medium pressure ultraviolet irradiation. Journal of Photochemistry and Photobiology B-Biology, 2015. 148: pages 310-321.

600. Whang, C.M., J.G. Kim, E.Y. Kim, Y.H. Kim, and W.I. Lee, Effect of Co, Ga, and Nd additions on the photocatalytic properties of TiO_2 nanopowders. Glass Physics and Chemistry, 2005. 31(3): pages 390-395.

601. Liu, G.-A., J. Zhang, and X.-M. He, Ga-doped nano-TiO_2 thin films: Preparation, optical and electrical properties. Chinese Journal of Inorganic Chemistry, 2009. 25(11): pages 1939-1946.

603. Lee, E.J. and S.O. Ryu, Characterization of ALD processed gallium doped TiO_2 Hole blocking layer in an inverted organic solar cell. Journal of Electronic Materials, 2017. 46(2): pages 961-966.

604. Xie, Q., J. Musschoot, D. Deduytsche, R.L. Van Meirhaeghe, C. Detavernier, S. Van den Berghe, Y.-L. Jiang, G.-P. Ru, B.-Z. Li, and X.-P. Qu, Growth kinetics and crystallization behavior of TiO_2 films prepared by plasma enhanced atomic layer deposition. Journal of the Electrochemical Society, 2008. 155(9): pages H688-H692.

605. Henegar, A.J., A.J. Cook, P. Dang, and T. Gougousi, Native oxide transport and removal during Atomic Layer Deposition of TiO_2 films on GaAs(100) surfaces. Acs Applied Materials & Interfaces, 2016. 8(3): pages 1667-1675.

606. Yang, Y., T. Kitashima, T. Hara, Y. Hara, Y. Yamabe-Mitarai, M. Hagiwara, and S. Iwasaki, Effects of Ga, Sn addition and microstructure on oxidation behavior of near-alpha Ti alloy. Oxidation of Metals, 2017. 88(5-6): pages 583-598.

607. Jiang, N., H.J. Zhang, S.N. Bao, Y.G. Shen, and Z.F. Zhou, XPS study for reactively sputtered titanium nitride thin films deposited under different substrate bias. Physica B-Condensed Matter, 2004. 352(1-4): pages 118-126.

608. Rosenberger, L., R. Baird, E. McCullen, G. Auner, and G. Shreve, XPS analysis of aluminum nitride films deposited by plasma source molecular beam epitaxy. Surface and Interface Analysis, 2008. 40(9): pages 1254-1261.

609. Okumura, H., M. Kita, K. Sasaki, A. Kuramata, M. Higashiwaki, and J.S. Speck, Systematic investigation of the growth rate of beta-Ga_2O_3 (010) by plasma-assisted molecular beam epitaxy. Applied Physics Express, 2014. 7(9): pages 095501-095505.

610. Choudhury, B., M. Dey, and A. Choudhury, Shallow and deep trap emission and luminescence quenching of TiO_2 nanoparticles on Cu doping. Applied Nanoscience, 2014. 4(4): pages 499-506.

611. Ohtani, B., Y. Ogawa, and S. Nishimoto, Photocatalytic activity of amorphous-anatase mixture of titanium(IV) oxide particles suspended in aqueous solutions. Journal of Physical Chemistry B, 1997. 101(19): pages 3746-3752.

612. Santos, D.M.D., J. Navas, A. Sanchez-Coronilla, R. Alcantara, C. Fernandez-Lorenzo, and J. Martin-Calleja, Highly Al-doped TiO_2 nanoparticles produced by Ball Mill Method: structural and electronic characterization. Materials Research Bulletin, 2015. 70: pages 704-711.

613. Wang, X., Q. Xu, M. Li, S. Shen, X. Wang, Y. Wang, Z. Feng, J. Shi, H. Han, and C. Li, Photocatalytic overall water splitting promoted by an alpha-beta phase junction on Ga_2O_3. Angewandte Chemie-International Edition, 2012. 51(52): pages 13089-13092.

614. Kim, Y.S. and S.J. Yun, Nanolaminated Al_2O_3-TiO_2 thin films grown by atomic layer deposition. Journal of Crystal Growth, 2005. 274(3-4): p. 585-593.

615. Dey, S., C. Roy, A. Pradhan, and S. Varma, Raman scattering characterization of Si(100) implanted with mega-electron-volt Sb. Journal of Applied Physics, 2000. 87(3): pages 1110-1117.

616. Ma, Y., J.B. Qiu, Y.A. Cao, Z.S. Guan, and J.N. Yao, Photocatalytic activity of TiO_2 films grown on different substrates. Chemosphere, 2001. 44(5): pages 1087-1092.

617. Lemaire, P.C., M. King, and G.N. Parsons, Understanding inherent substrate selectivity during atomic layer deposition: effect of surface preparation, hydroxyl density, and metal oxide composition on nucleation mechanisms during tungsten ALD. Journal of Chemical Physics, 2017. 146(5): pages 052811-052820.

618. Ferrari, S., F. Perissinotti, E. Peron, L. Fumagalli, D. Natali, and M. Sampietro, Atomic layer deposited Al_2O_3 as a capping layer for polymer based transistors. Organic Electronics, 2007. 8(4): pages 407-414.

619. Jevasuwan, W., T. Maeda, N. Miyata, M. Oda, T. Irisawa, T. Tezuka, and T. Yasuda, Self-limiting growth of ultrathin Ga_2O_3 for the passivation of Al_2O_3/InGaAs interfaces. Applied Physics Express, 2014. 7(1): pages 011201-011205.

620. Mills, A. and M. Crow, A study of factors that change the wettability of titania films. International Journal of Photoenergy, 2008: pages 1-6.

621. Lopez, R. and R. Gomez, Band-gap energy estimation from diffuse reflectance measurements on sol-gel and commercial TiO_2: a comparative study. Journal of Sol-Gel Science and Technology, 2012. 61(1): pages 1-7.

622. Katamreddy, R., V. Omarjee, B. Feist, and C. Dussarrat, Ti source precursors for Atomic Layer Deposition of TiO_2, STO and BST. Atomic Layer Deposition Applications 4, 2008. 16(4): pages 113-122.

623. Zhang, J., M. Steigerwald, L. Brus, and R.A. Friesner, Covalent O-H bonds as electron traps in proton-rich rutile TiO_2 nanoparticles. Nano Letters, 2014. 14(4): pages 1785-1789.

624. Li, Y., W. Zhang, J.F. Niu, and Y.S. Chen, Mechanism of photogenerated reactive oxygen species and correlation with the antibacterial properties of engineered metal-oxide nanoparticles. Acs Nano, 2012. 6(6): pages 5164-5173.

625. Bowker, M. and R.A. Bennett, The role of Ti^{3+} interstitials in TiO_2 (110) reduction and oxidation. Journal of Physics-Condensed Matter, 2009. 21(47): pages 474224-474234.

626. Nepal, J., S.S. Mottaghian, A.V. Iefanova, V. Mallam, M. Biesecker, M.F. Baroughi, and Ieee. Modeling trap assisted recombination in Dye Sensitized Solar Cells. in 39th IEEE Photovoltaic Specialists Conference (PVSC). 2013. Tampa, FL.

Appendix A

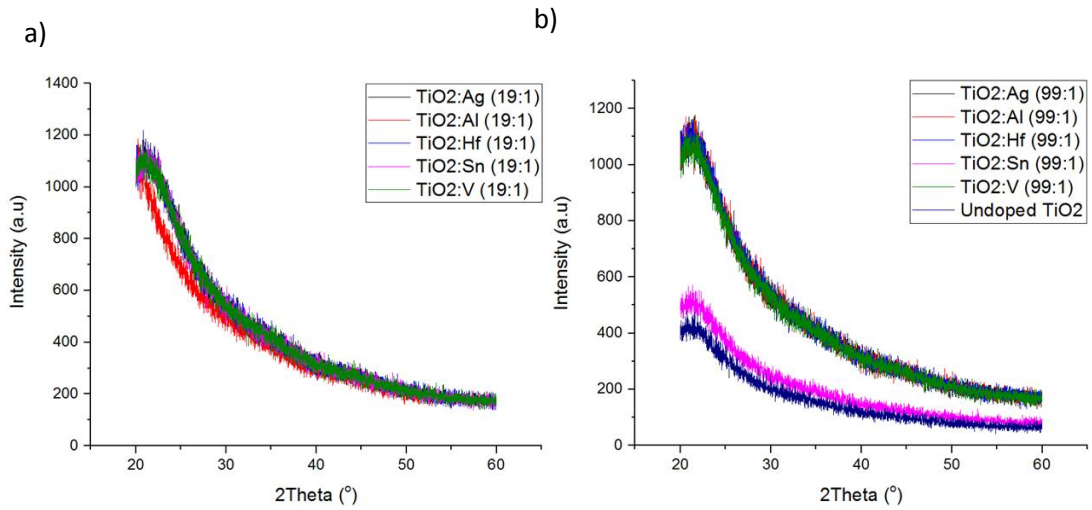

Figure 1: XRD of a) the as-grown doped TiO_2 (19:1) films and b) the as-grown nominally undoped TiO_2 and doped TiO_2 (99:1) films.

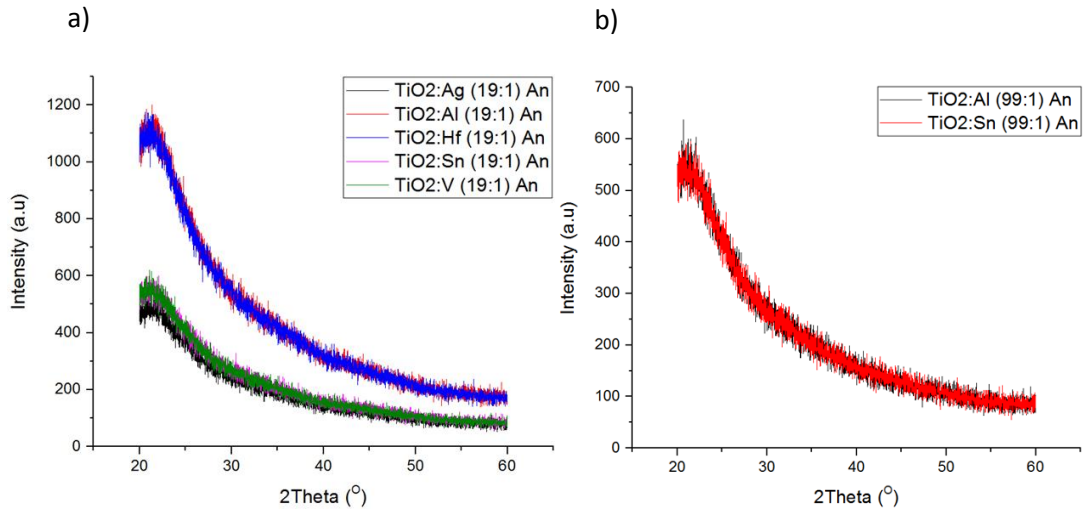

Figure 2: XRD of a) the annealed doped TiO_2 (99:1) films and b) the annealed $Ti_{1-x}O_2:Al_x$ (99:1) and $Ti_{1-x}O_2:Sn_x$ (99:1) films.

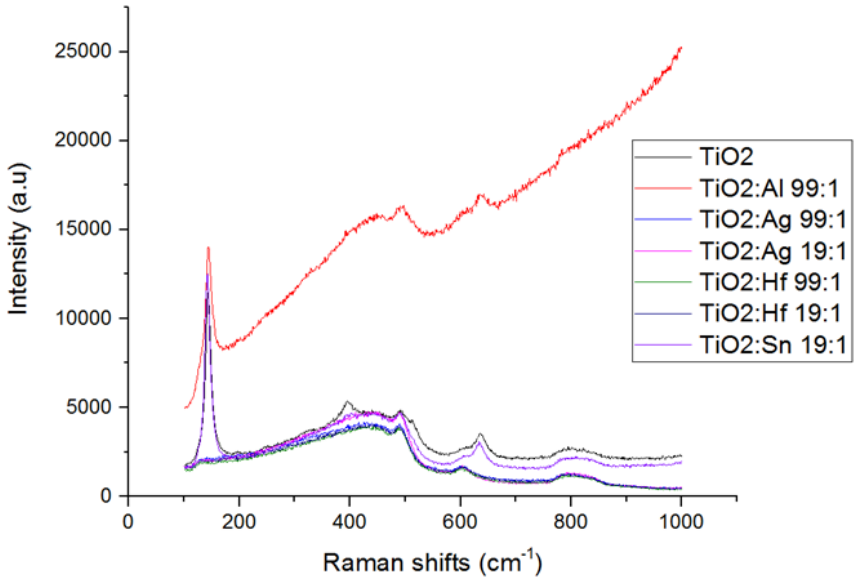

Figure 3: Raman spectra of the annealed nominally undoped TiO_2 film and the annealed $Ti_{1-x}O_2:Al_x$ (99:1), $Ti_{1-x}O_2:Ag_x$ (99:1 and 19:1), $Ti_{1-x}O_2:Hf_x$ (99:1 and 19:1) and $Ti_{1-x}O_2:Sn_x$ (19:1) films.

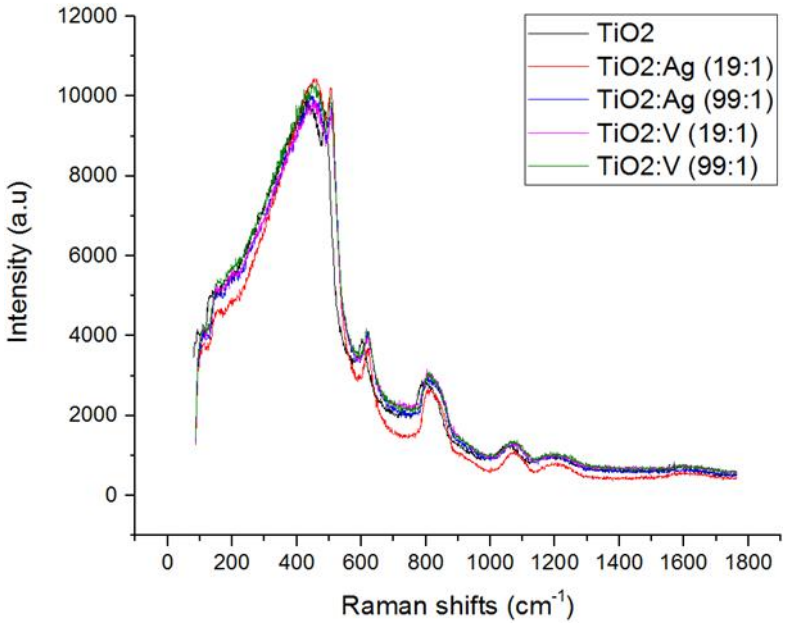

Figure 4: Raman spectra of the as-grown nominally undoped TiO_2 film and the as-grown $Ti_{1-x}O_2:Ag_x$ (99:1 and 19:1) and $Ti_{1-x}O_2:V_x$ (99:1 and 19:1) films.

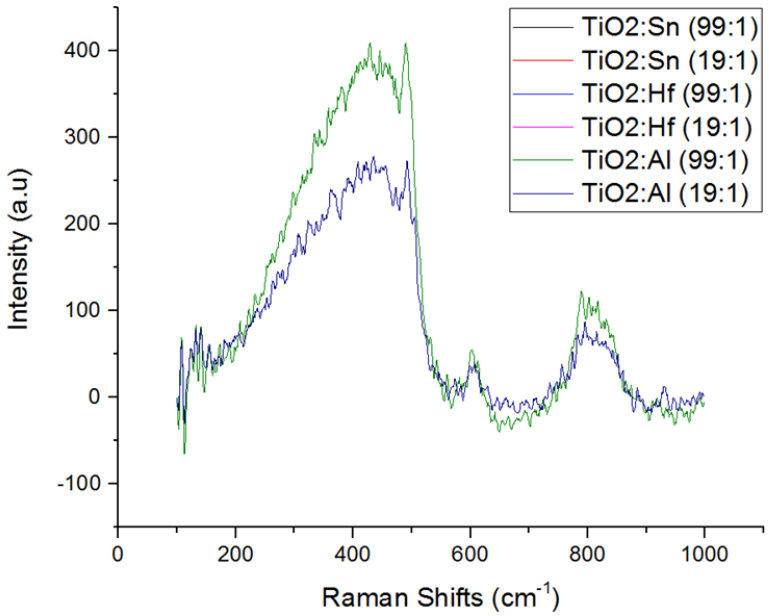

Figure 5: Raman spectra of the as-grown $Ti_{1-x}O_2:Sn_x$ (99:1 and 19:1), $Ti_{1-x}O_2:Hf_x$ (99:1 and 19:1) and $Ti_{1-x}O_2:Al_x$ (99:1 and 19:1) films.

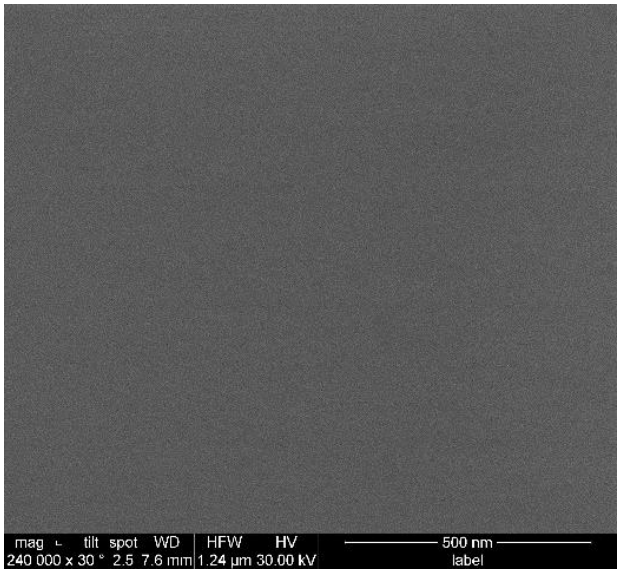

Figure 6: Example smooth surface SEM of the as-grown doped TiO_2 films.

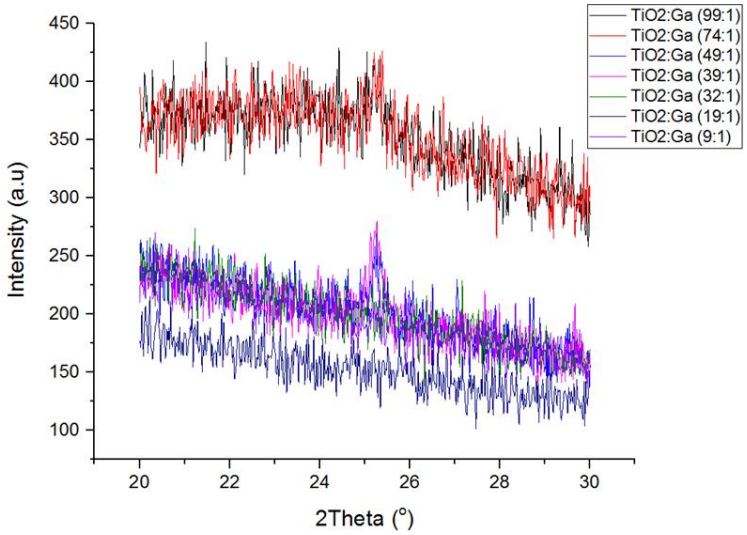

Figure 7: XRD of 20-30 ° 2θ spectra of the Ga-capped $Ti_{1-x}O_2$:Ga_x films on silicon substrates, indicating 25.3 ° 2θ peak corresponding to an anatase (101) miller plane for Ga-capped $Ti_{1-x}O_2$:Ga_x (99:1, 74:1, 49:1 and 39:1) films.

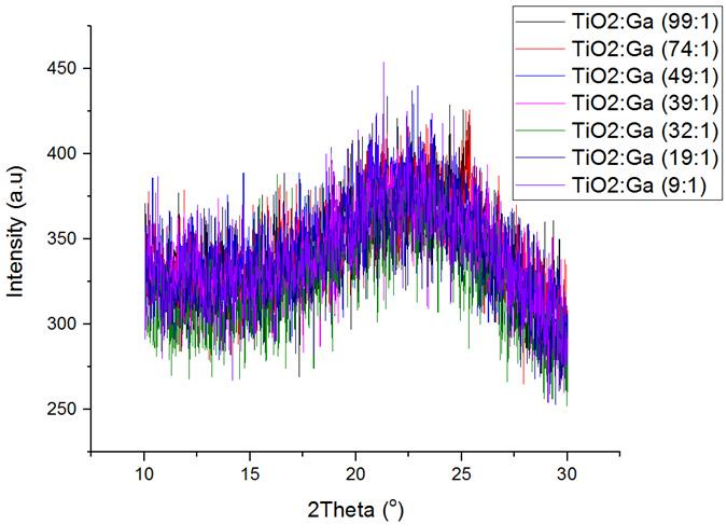

Figure 8: XRD of 10-30 ° 2θ spectra of the Ga-capped $Ti_{1-x}O_2$:Ga_x films on glass substrates, indicating 25.3 ° 2θ peak corresponding to an anatase (101) miller plane for Ga-capped $Ti_{1-x}O_2$:Ga_x (99:1 and 74:1) samples.

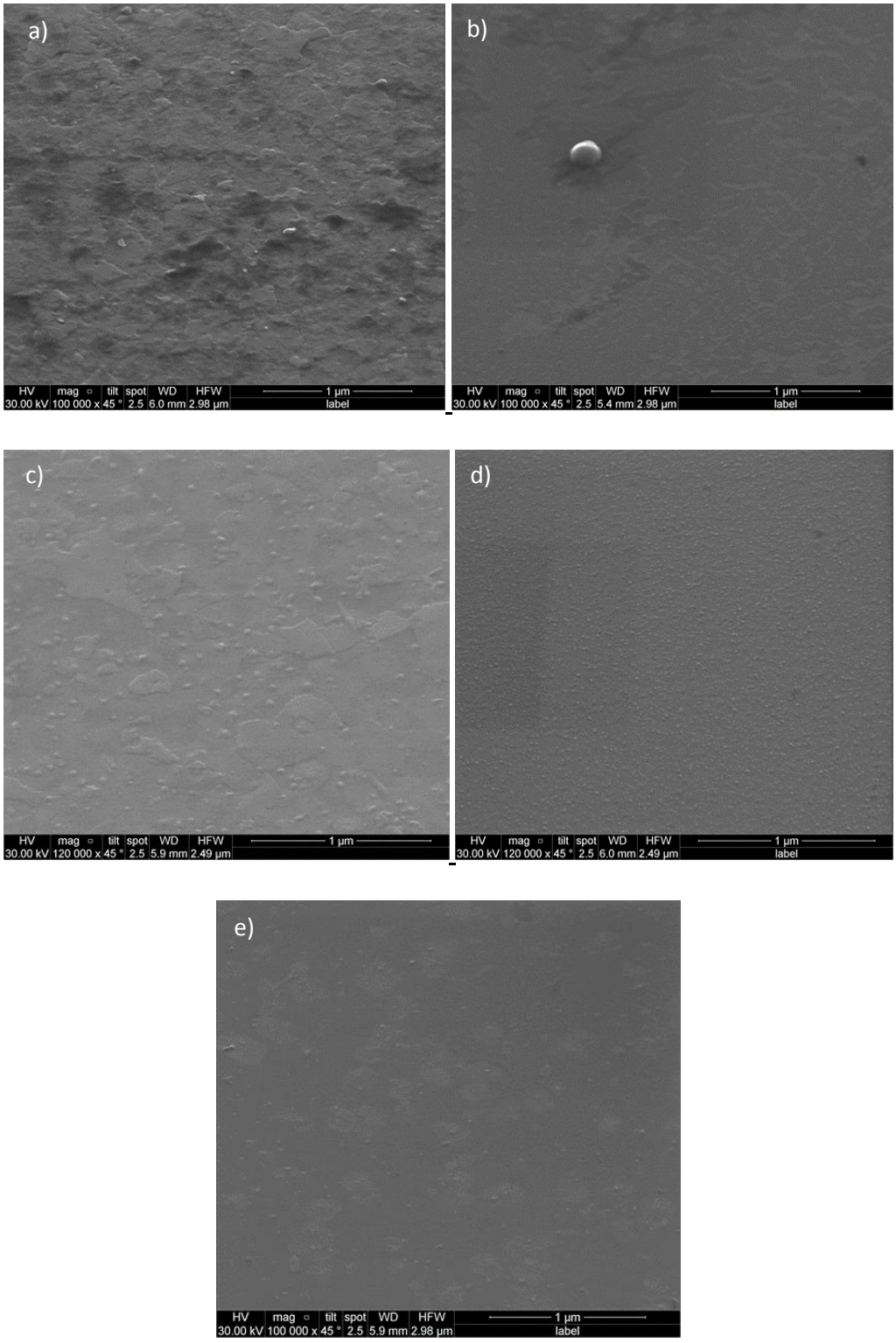

Figure 9: Surface SEM of Ga-capped $Ti_{1-x}O_2$:Ga_x a) (74:1), b) (49:1), c) (39:1), d) (32:1) and e) (19:1) on silicon substrates.

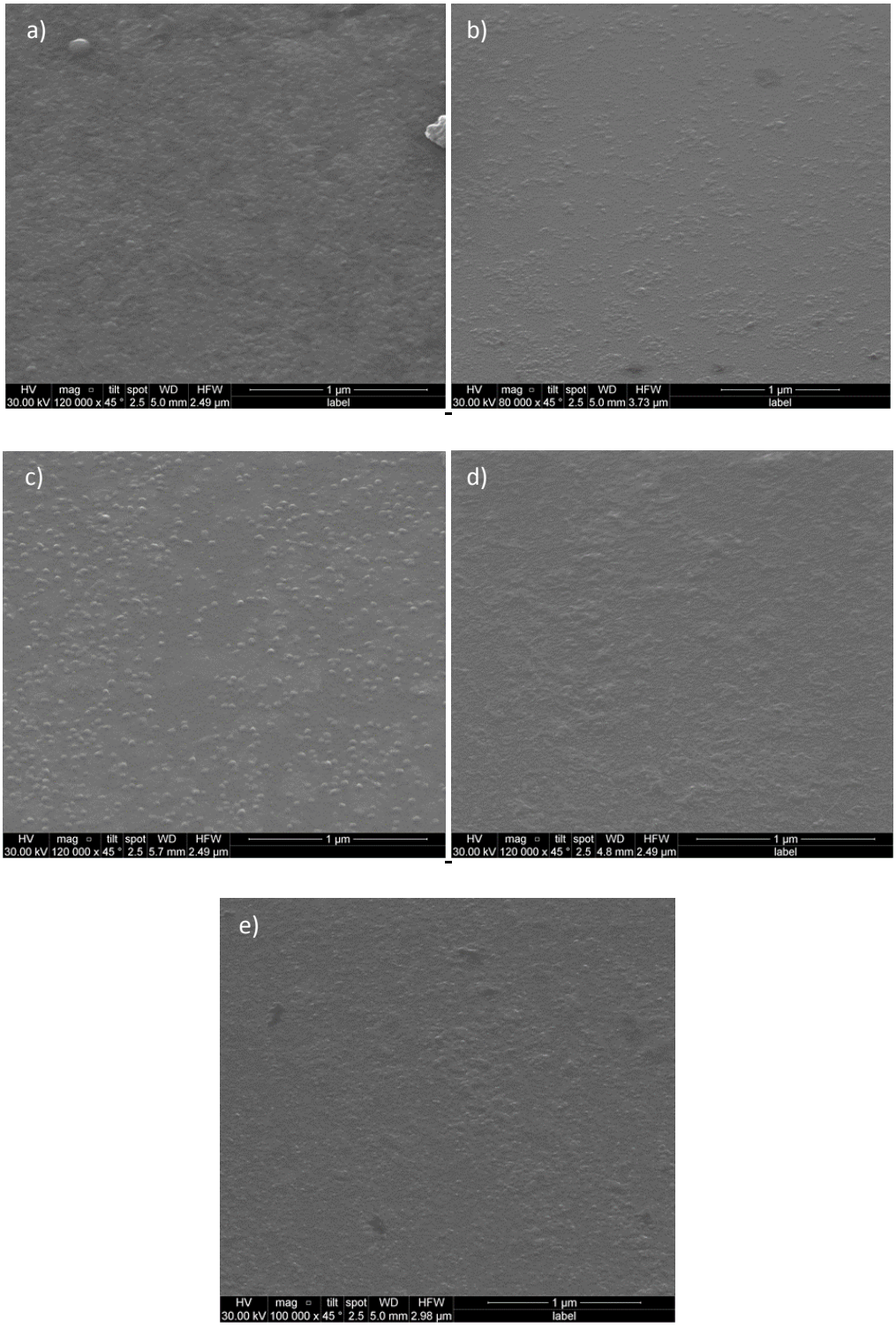

Figure 10: Surface SEM of Ga-capped $Ti_{1-x}O_2:Ga_x$ a) (74:1), b) (49:1), c) (39:1), d) (32:1) and e) (19:1) on glass substrates.

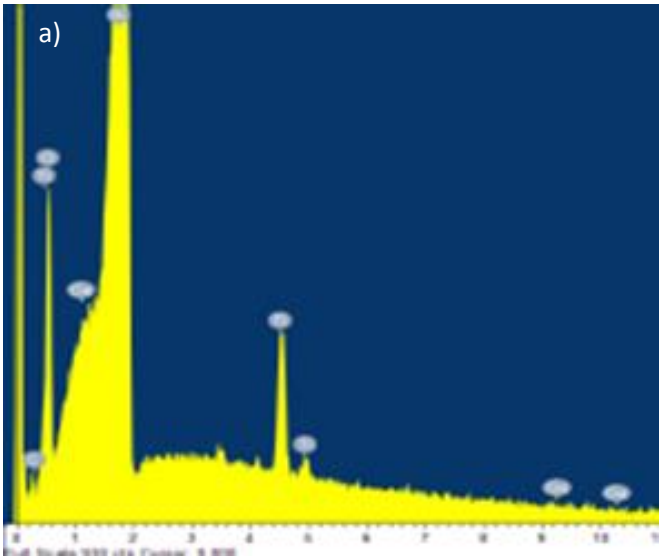
a)

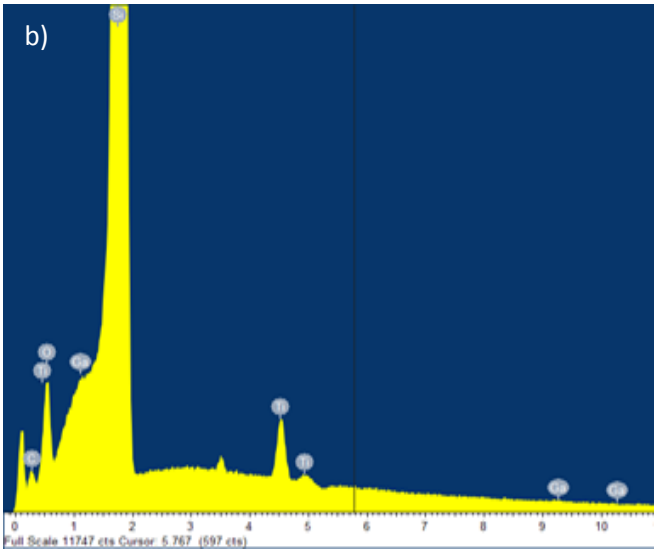
b)
0 1 2 3 4 5 6 7 8 9 10
Full Scale 11747 cts Cursor: 5.767 (597 cts)

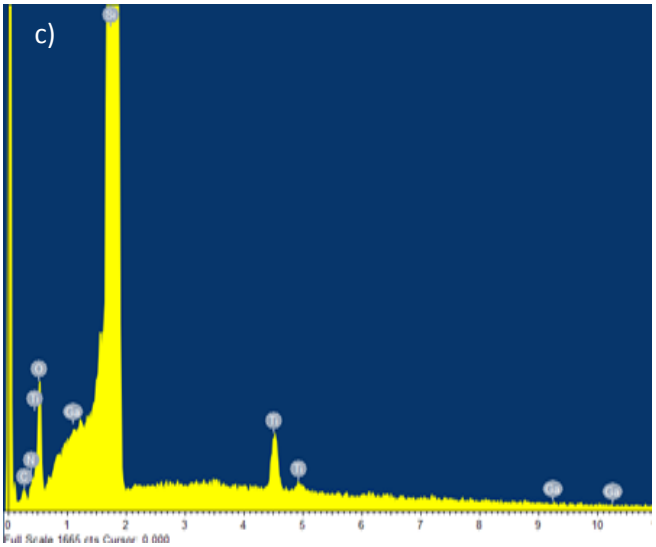
c)
0 1 2 3 4 5 6 7 8 9 10

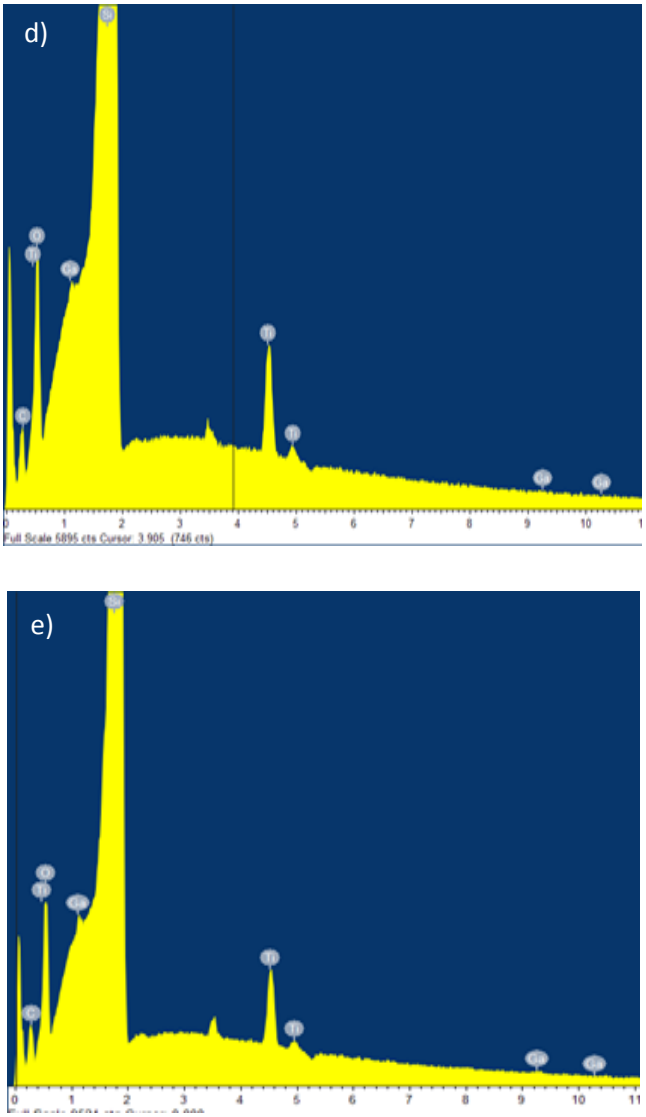

Figure 11: Surface EDX of Ga-capped $Ti_{1-x}O_2$:Ga_x a) (74:1), b) (49:1), c) (39:1), d) (32:1), e) (19:1) on silicon substrates.

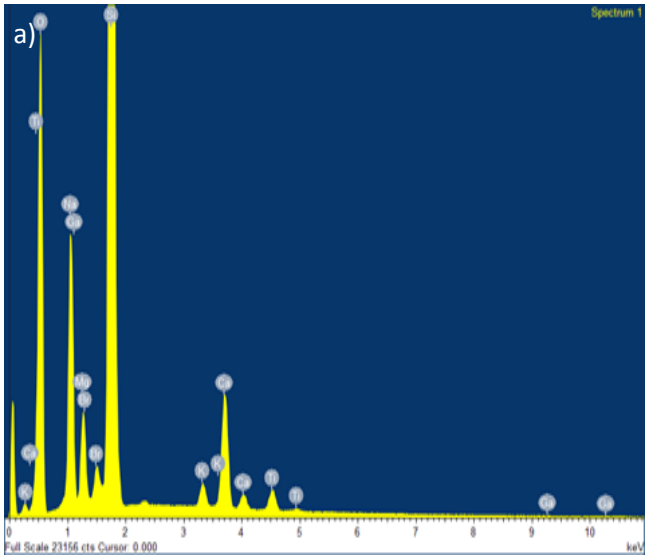
a)
Spectrum 1
0 1 2 3 4 5 6 7 8 9 10
Full Scale 23156 cts Cursor: 0.000
keV

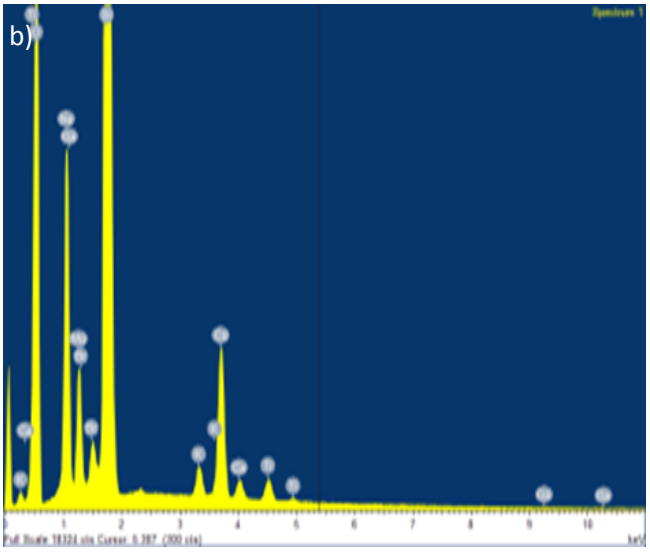
b)
0 1 2 3 4 5 6 7 8 9 10
keV

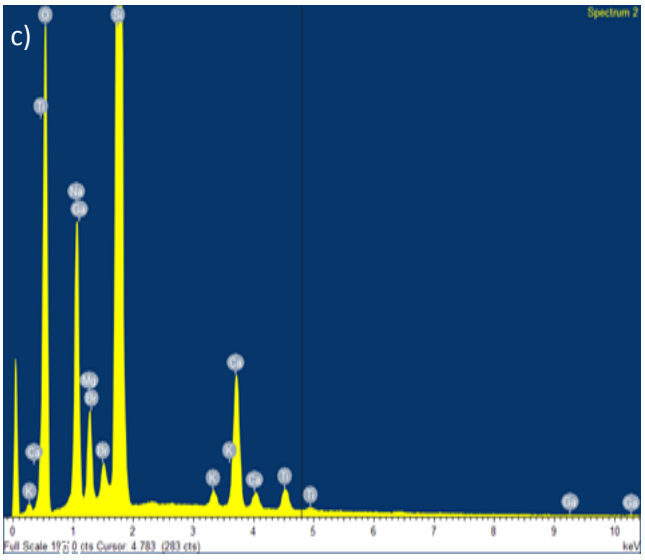
c)
Spectrum 2
0 1 2 3 4 5 6 7 8 9 10
keV

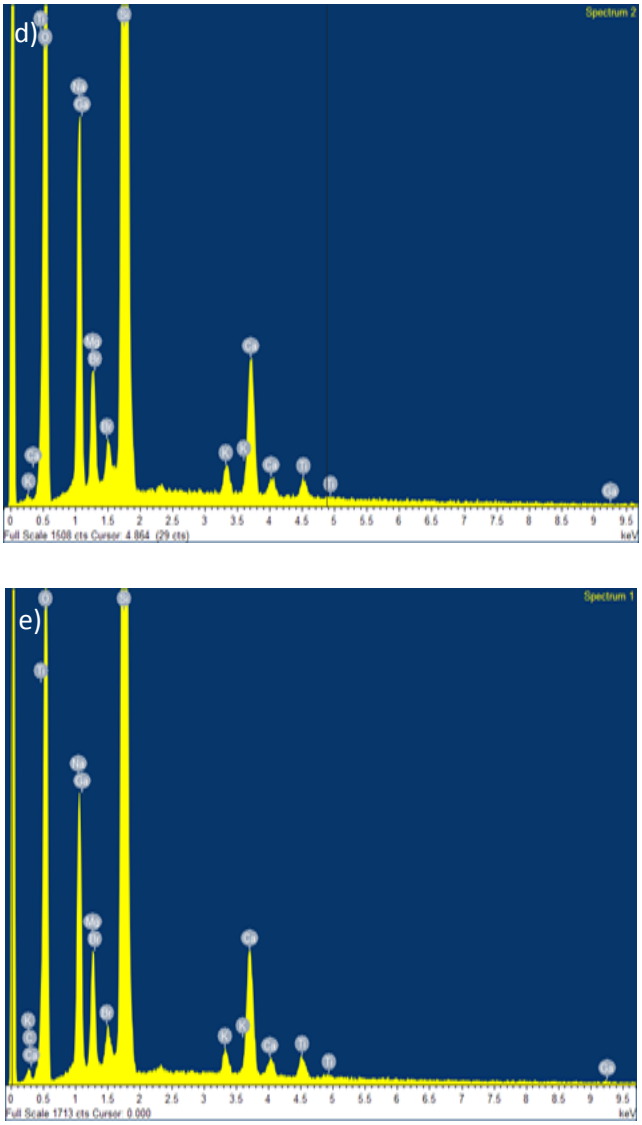

Figure 12: Surface EDX of Ga-capped $Ti_{1-x}O_2$:Ga_x a) (74:1), b) (49:1), c) (39:1), d) (32:1), e) (19:1) on glass substrates.

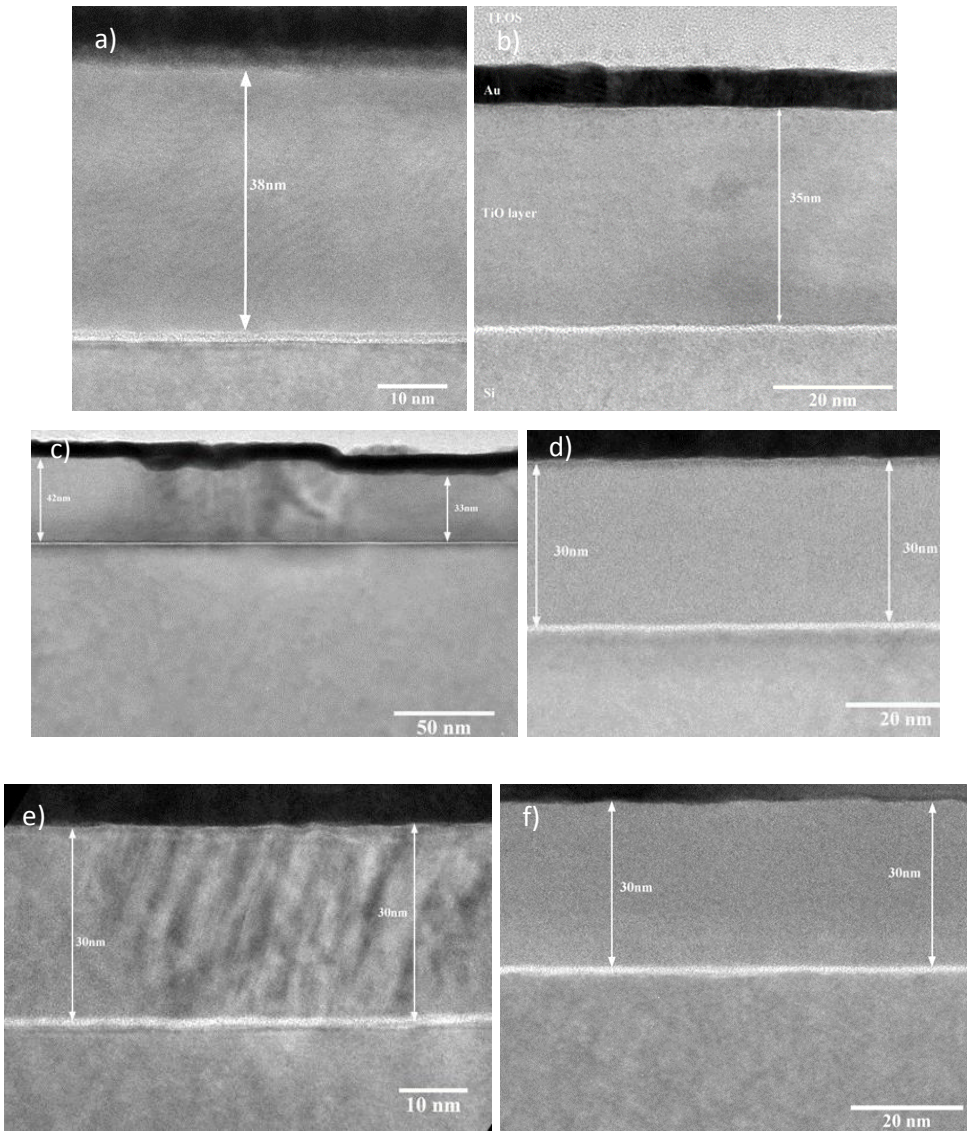

Figure 13: TEM of Ga-capped $Ti_{1-x}O_2:Ga_x$ a) (99:1), b) (74:1), c) (39:1), d) (32:1), e) (19:1) and f) (9:1) on silicon substrates.

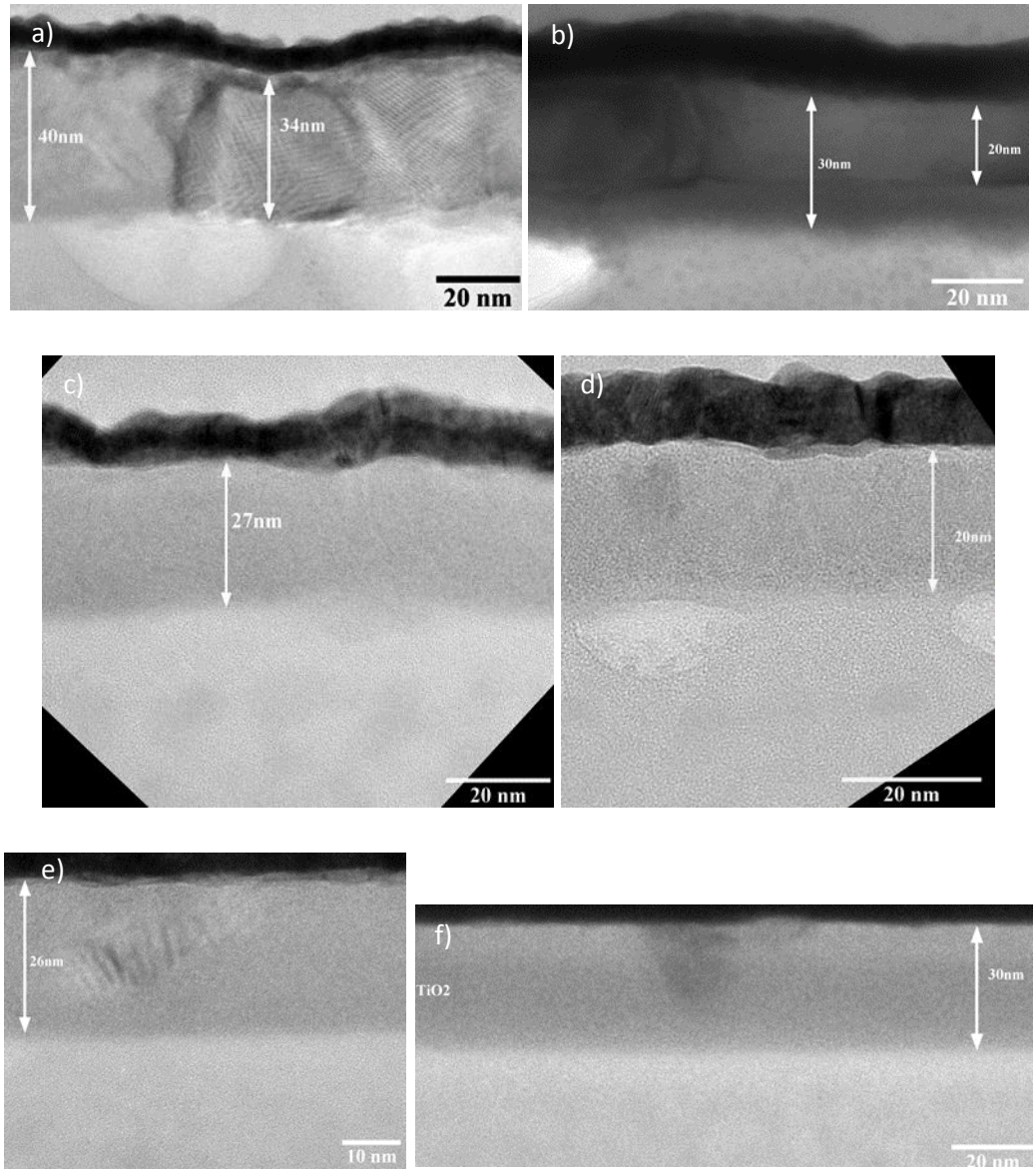

Figure 14: TEM of the Ga-capped $Ti_{1-x}O_2:Ga_x$ a) (99:1), b) (74:1), c) (49:1), d) (39:1), e) (32:1), f) (9:1) films.